Thin Films on Copper for Superconducting RF Cavities within the Future Circular Collider Study

DISSERTATION
zur Erlangung des Grades eines
Doktors der Naturwissenschaften

vorgelegt von
M. Sc. Dorothea FONNESU

eingereicht bei der Naturwissenschaftlich-Technischen Fakultät
der Universität Siegen
Siegen 2023

Betreuung und Erstgutachten:
Prof. Dr. Jens Knobloch
Universität Siegen, HZB – Helmholtz-Zentrum Berlin

Externe Betreuung:
Dr. Sergio Calatroni
CERN – European Organisation for Nuclear Research

Zweitgutachten:
HDR Dr. Claire Zylberajch Antoine
CEA – French Alternative Energies and Atomic Energy Commission

Weitere Mitglieder der Promotionskommission:
Prof. Dr. Alexander Lenz – Universität Siegen
Prof. Dr. Xin Jiang – Universität Siegen
Prof. Dr. Roberto Passante – University of Palermo

Tag der mündlichen Prüfung:
28 Februar 2024

"Now I'm a scientific expert;
that means I know nothing about absolutely everything."

— A. C. Clarke, *2001: A space Odissey*

Abstract

The Future Circular Collider (FCC) Study is a collaborative international initiative led by the European Organisation for Nuclear Research (CERN). Its primary objective is to assess the feasibility of a new circular collider intended to explore physics beyond the Standard Model. Toward this goal, developing superconducting radio-frequency (SRF) accelerating cavities that offer the required performance in terms of acceleration while maintaining cost-effectiveness represents a significant challenge. The baseline option being explored involves the niobium-on-copper (Nb/Cu) technology, which consists in coating the inner surface of the copper cavities with a superconducting thin film of niobium. The feasibility of using A15 compounds, particularly Nb_3Sn, as coating materials is also being investigated, although this approach is still in its early developmental stages.

This thesis work is focused on the initial phases of the Research and Development (R&D) of superconducting thin films produced at CERN for coating SRF copper cavities, namely when the coatings are produced and tested on their substrates in the form of small samples.

To evaluate the quality of the films and study the impact of the chosen coating parameters, it is important to analyze their superconducting properties. The critical temperature (T_c) is a key parameter of interest, serving as an early indicator of the film's superconducting performance. For this, a dedicated experimental test station designed for the inductive measurement of the T_c of superconducting thin films on copper, now permanently installed at the CERN's Central Cryogenic Laboratory, is developed and described in this work. A non-contact method is chosen to avoid any direct, and possibly destructive, manipulation of the sample, which allows for further characterization tests to be performed on the same sample. On top of this, the inductive measurement via a two-coil setup represents a fast, cheap and reliable way of measuring T_c.

Additionally, this work presents a feasibility study of a new method called "reverse-coating" technique, aimed at producing seamless copper substrates for Nb/Cu SRF cavities. The technique involves depositing a niobium layer on a mandrel shaped like the final cavity, followed by electro-forming the copper cavity around it. The mandrel is then removed, leaving behind a copper cavity with a functional niobium layer. This technique also eliminates the need for the usual copper surface preparation prior to superconducting layer coating. Preliminary results from flat disk samples suggest the technique's feasibility.

Finally, this work investigates the use of bipolar High Power Impulse Magnetron Sputtering (HiPIMS) as a coating method for Nb_3Sn films on copper. The study aims to understand potential correlations between T_c, deposition parameters, and film morphology data. The focus is on investigating if HiPIMS, as energetic deposition technique already demonstrated for niobium, can provide dense Nb_3Sn films on copper which also exhibit the expected T_c and a correct stoichiometry. The study, still ongoing, offers insights for optimizing the deposition process of Nb_3Sn films on copper.

Zusammenfassung

Die Future-Circular-Collider-Studie (FCC-Studie) ist eine gemeinschaftliche, internationale Initiative, die von der Europäischen Organisation für Kernforschung (CERN) angeführt wird. Ihr vorrangiges Ziel ist die Beurteilung der Machbarkeit eines neuen Speicherrings, dessen Zweck die Erforschung der Physik jenseits des Standardmodells der Teilchenphysik ist. Eine erhebliche Herausforderung auf dem Weg zu diesem Ziel stellt die Entwicklung supraleitender Hochfrequenz-Beschleunigerkavitäten (SRF-Beschleunigerkavitäten) dar, welche die erforderliche Beschleunigungsleistung bei gleichzeitiger Wahrung der Kosteneffizienz bieten. Bei der untersuchten Basisoption handelt es sich um die Niob-auf-Kupfer-Technologie (Nb/Cu-Technologie), bei welcher die Innenflächen der Kupferkavitäten mit einer supraleitenden Niob- Dünnschicht beschichtet werden. Die Machbarkeit der Verwendung von A15-Verbindungen, insbesondere Nb_3Sn, als Beschichtungsmaterialien wird ebenfalls untersucht, auch wenn sich dieser Ansatz noch in einem frühen Entwicklungsstadium befindet.

Die vorliegende Dissertation konzentriert sich auf die erste Phase der Forschung und Entwicklung (F&E) supraleitender Dünnschichten, welche am CERN zur Beschichtung von SRF-Kupferkavitäten hergestellt werden, nämlich auf die Herstellung und Charakterisierung der Dünnschichten in Form kleiner Proben auf ihren Substraten.

Zur Beurteilung der Qualität der Dünnschichten und zur Untersuchung des Einflusses der gewählten Beschichtungsparameter ist eine Analyse der Supraleitereigenschaften der Dünnschichten unerlässlich. Die kritische Temperatur (T_c) ist ein Schlüsselparameter, welcher als ein Frühindikator der Supraleitereigenschaften der Dünnschichten dient. Daher wurde im Rahmen dieser Arbeit ein spezieller experimenteller Prüfstand entwickelt und beschrieben, welcher zur induktiven Vermessung der kritischen Temperatur T_c der Dünnschichten auf Kupfer entworfen wurde und welcher nun dauerhaft im Kryogenen Zentrallabor des CERN installiert ist. Um eine direkte und möglicherweise destruktive Manipulation der Probe zu vermeiden, wird eine berührungslose Methode gewählt, was die Durchführung weiterer Charakterisierungstests an derselben Probe ermöglicht. Darüber hinaus stellt die induktive Messung, mithilfe eines Aufbaus bestehend aus zwei Spulen, eine schnelle, preiswerte und zuverlässige Messmethode dar.

Weiterhin stellt diese Arbeit eine Machbarkeitsstudie einer neuen Methode namens "Reverse-Coating"-Technik vor, welche auf die Herstellung nahtloser Kupfersubstrate für Nb/Cu-SRF-Kavitäten abzielt. Die Technik besteht darin, eine Niob-Dünnschicht auf einem Aufspanndorn abzuscheiden, der wie der endgültige Hohlraum geformt ist, und anschließend den Kupferhohlraum darum herum galvanisch zu formen. Anschließend wird der Aufspanndorn entfernt, wobei ein Kupferhohlraum mit einer funktionellen Niob- Dünnschicht zurückbleibt. Diese Technik macht auch die übliche Vorbereitung der Kupferoberfläche vor der Beschichtung mit der supraleitenden Dünnschicht überflüssig. Vorläufige Ergebnisse von flachen, scheibenförmigen Proben legen die Machbarkeit dieser Technik nahe.

Abschließend untersucht diese Arbeit den Einsatz des bipolaren Hochleistungsimpulsmagnetronsputtern (HiPIMS) als Beschichtungsverfahren für Nb_3Sn-Dünnschichten auf Kupfer. Ziel der Studie ist es, mögliche Korrelationen zwischen T_c, den Dünnschichtabscheidungsparametern und den Dünnschichtmorphologiedaten zu verstehen. Der Schwerpunkt liegt auf der Untersuchung, ob mit HiPIMS, einer bereits für Niob demonstrierten energetischen Abscheidungstechnik, dichte Nb_3Sn-Dünnschichten auf Kupfer erzeugt werden können, welche die erwartete kritische Temperatur $T_c$und eine korrekte Stöchiometrie aufweisen. Die noch laufende Studie liefert Erkenntnisse zur Optimierung des Abscheidungsprozesses von Nb_3Sn-Dünnschichten auf Kupfer.

Contents

List of Figures

List of Tables

Introduction

Resonant cavities are the component employed in particle accelerators and colliders to impart energy to the particle beam. In the simplest terms, a resonant cavity consists of an enclosure made of conductor material, within which an electromagnetic field, typically in the radio-frequency (RF) range, conveys energy to the charged particles passing through it.

Despite the working principle being still the same today as its first applications in the 1950's [1], the technology developed for the construction and operation as well as the variety of such devices have come a long way ever since [2], [3]. Superconducting materials entered the field in the 1960's [4] to meet the need for higher beam energy while containing the cavity power losses [5], which represented the main limitation in copper cavities. An important advantage introduced by superconductors was, in fact, their much smaller surface resistance in the RF regime compared to normal conductors. Niobium is nowadays the most employed material for cavity production together with copper. It is an elemental superconductor particularly suitable to the scope, as its superconducting transition temperature (9.2 K) is the highest among the superconducting elements and it exhibits values for the surface resistance several orders of magnitude smaller than copper (e.g. at 1.5 GHz, bulk niobium shows a surface resistance of about 10^2 nΩ at 4.2 K and 10 nΩ at 2 K, against the about 10^6 nΩ at 300 K and 10^5 nΩ at 10 K of bulk copper). However niobium, as all conventional superconductors, requires to be operated at cryogenic temperatures, therefore the choice on whether to employ it or copper depends on the specific application. Superconducting materials are beneficial, for example, for accelerators operating in continuous-wave mode or at high RF duty cycles, mitigating the power dissipated by the cavity during operation (discussions about the pros and cons for the two materials can be found at [6], [7]).

The intrinsic quality factor Q_0 represents an index of the number of RF cycles it takes a cavity to dissipate the energy stored in it. Tremendous progress was made in the last decades in improving the Q_0 of bulk niobium cavities, typically operated at 2 K, to the point that the bulk niobium technology is reaching its theoretical limits in terms of accelerating fields [8]. Bulk niobium cavities can nowadays deliver up to 50 MV/m at 2 K with $Q_0 \geq 10^{10}$, as in the case of the 1.3 GHz single-cell TESLA type cavities upon custom temperature treatment [9].

Other than in its bulk form, niobium can be employed in the form of thin film as the inner coating of bulk copper cavities [10], [11]. The niobium-coated copper (Nb/Cu) technology for the production of SRF cavities offers several advantages compared to bulk niobium: copper is much cheaper; it is easier to work; its thermal conductivity is generally higher at liquid helium temperature. After this technology was successfully introduced for the upgrade of Large Electron-Proton collider (LEP) [12], 400 MHz Nb/Cu cavities are still being employed for the Large Hadron Collider (LHC), at the European Organisation for Nuclear Research (CERN), for which they provide a baseline accelerating gradient of 5 MV/m with $Q_0 \geq 10^9$ at 4.5 K operating temperature [13]. The operation of Nb/Cu cavities at 4.5 K benefits

from the optimised surface resistance of the niobium film [14] and offers a substantial cost-saving profit in contexts requiring a large number of cavities, as is the case for colliders such as the LEP, the LHC and the Future Circular Collider (FCC). However, a degradation of Q_0 with increasing accelerating field (the so-called "Q-slope") is observed in Nb/Cu cavities. This issue is known to be related to the surface resistance of the niobium film and is not observed in the bulk niobium case [14]. For this reason, the research and development (R&D) efforts in the field of Nb/Cu cavities are primarily addressed toward solving the Q-slope problem, which is, to this day, not fully understood yet.

The next particle accelerators intended for fundamental research such as the FCC proposed by CERN, introduce new challenges in the development of the SRF cavities. For the first stage of the FCC programme, namely the lepton collider FCC-ee, the updated target with respect to what indicated in the conceptual design report (CDR) [15] foresees the production of up to 280 400 MHz Nb/Cu SRF cavities which should deliver a maximum accelerating gradient of 12 MV/m with $Q_0 > 3 \times 10^9$ at 4.5 K, which will require a maximum surface resistance of 65 nΩ for 2-cell elliptical cavity geometry at 4.5 K [16]. Developing niobium films on copper capable of overcoming the Q-slope to reach the required accelerating field is not a straightforward task, and will constitute the central activity of the SRF R&D program at CERN for the next years.

It is known that the purity, the lattice defect density, the surface morphology, the adhesion to the substrate are film properties affecting its surface resistance, and the film production technique plays a substantial role on these properties. Progress in the mitigation of the Q-slope in Nb/Cu films was made in the last years [17] by switching from the classically employed physical vapour deposition (PVD) technique of DC magnetron sputtering (DCMS) to the energetic condensation PVD technique of high power impulse magnetron sputtering (HiPIMS), which proved to allow better control than DCMS on the final properties of the film and to provide denser coatings on complex surfaces [18], [19].

The fabrication process of the copper cavity structure and the preparation of the substrate's surface prior to the film deposition are also known to have an impact on the surface resistance, therefore new paths are being investigated with regard to these aspects too. One representative example is given by the efforts directed toward the development of effective fabrication methods for seamless copper cavities, which might promote a lower substrate roughness and reduce the losses directly connected to the substrate's critical areas [20] by removing seams and welds [21]–[23].

Superconducting materials other than niobium are also being investigated in the quest for coated copper cavities providing high accelerating fields with high Q_0 values. The main focus is on the A15 compound Nb_3Sn, because of its critical temperature (18.3 K) twice as high as the one of niobium. Remarkably high fields larger than 20 MV/m at 4.5 K have been obtained with 1.3 GHz Nb_3Sn cavities produced out of bulk niobium cavities by vapour tin diffusion, whose performance main limitation was the difficulty in maintaining thermal stability and preventing quenches [24]. This, in addition to the fact that the brittleness of Nb_3Sn makes it only employable in the form of thin film, is encouraging the investigation of PVD methods to form the Nb_3Sn A15 phase on a high thermal conductivity substrate like copper. The development of Nb_3Sn films is also motivated by the possibility of cooling the cavities by conduction methods rather than using liquid helium, thanks to the availability of cryocoolers exhibiting high cooling capacity at 4 K [25].

Nb_3Sn films on copper have been object of study at CERN since the launch of the R&D studies for the FCC programme, first via DCMS [26] and more recently via

HiPIMS [27]. The technique is still in its early stage of development, with the R&D strategy currently being the optimisation of the A15 phase formation and of some key superconducting parameters, such as the critical temperature, on small samples. Achieving good Nb_3Sn films on copper, however, comes with its own challenges. First of all, the temperature needed for the formation of the Nb_3Sn A15 phase ($\geq$ 930 °C) is well above the temperature at which copper starts weakening ($\sim$ 600 °C), making it impossible for a large structure such as a cavity to sustain the coating process without undergoing significant mechanical stresses. The mismatch between the thermal expansion coefficients of Nb_3Sn and copper also represents an issue, affecting the strain status of the film, as well as the known phenomenon of copper-tin inter-diffusion which can heavily affect the film stoichiometry. The introduction of an intermediate layer between the copper and the Nb_3Sn film, generally tantalum or niobium, is being investigated as a solution to mitigate the last two.

The variety of factors affecting the film performance and their interdependence make the identification of the problem and the implementation of a tackling strategy a complex and often time-consuming task. As a consequence, it is crucial to establish a systematic and reproducible set of standardized characterisation techniques for the quality assessment of the films. This should consist of structured checks of the superconducting, thermal, morphological and RF properties of the film on its substrate. Fast techniques for the early assessment of the superconducting properties of the film, such as the induction measurement of the critical temperature, are helpful on this side and can save time and resources with respect to other techniques, e.g. magnetometry measurements, which are undoubtedly necessary yet could be saved for the samples which already demonstrated certain basic quality levels.

In the following, the content of this thesis work is introduced, with emphasis given to the parts contributing to the activities needed for the advancement of the thin film on copper technology discussed above, in the context of the R&D ongoing at CERN for the SRF cavities of the FCC programme.

Content of the thesis

This thesis work is part of the R&D effort on materials and fabrication techniques for SRF copper cavities being carried on at CERN, in the search for a cost effective, reliable and reproducible recipe for the coating of the SRF accelerating cavities proposed for the FCC.

In particular, this work is involved in the early stages of the development of the superconducting thin films produced at CERN, namely in the activities which are preliminary to the fabrication of the cavity itself, when the coatings and substrates are still produced and tested in the form of small samples. The small-sample approach grants faster procedures and data collection, in addition to cost avoidance, and possibly shortens the next phase of cavity prototype testing, which is usually more demanding and time-consuming.

The first four Chapters of this thesis can be considered introductory: the basics of the theory of conventional superconductivity and the figures of merit of RF superconductivity are presented in Chapter 1; the general properties of SRF cavities are discussed in Chapter 2, with focus on the Nb/Cu case; the description of the FCC study is given in Chapter 3; in Chapter 4 the basic concepts of magnetron sputtering are introduced.

The key R&D works carried on for this thesis are then topic for Chapters 5, 6 and 7.

The establishment at the CERN Central Cryogenic Laboratory of a permanent test station for the contactless measurement of the superconducting transition temperature of thin films for SRF cavity applications, as part of the film quality control chain, is presented in Chapter 5. The working principle, design and characterisation of the test station are discussed. The induction coil technique chosen for this test station offers a fast and cheap mean for the measurement of the T_c of the superconducting films on different substrate materials, with the advantage of being contactless, hence the sample is not damaged by the procedure and can undergo more characterisation measurements.

Chapter 6 is dedicated to the introduction of the novel "reverse-coating" technique [28], inspired by the work on the production of small diameter beam vacuum chambers [29], as a potential method for the production of seamless Nb/Cu cavities. The results of the first dedicated feasibility study are presented to demonstrate the applicability of the technique to the case of niobium HiPIMS coatings on copper up to the first stage, i.e. the production in small samples of healthy niobium films from the point of view of the purity and morphology.

A study of the features of Nb_3Sn films deposited on copper via HiPIMS, to pursue the parallel route of A15 compounds as alternative materials to niobium for the production of coated SRF copper cavities, is presented in Chapter 7. The emphasis is on the relation between the superconducting transition temperature of the films, the deposition parameters and other properties as, for example, the film composition and surface morphology. The study intends to highlight the progress achieved so far with the first development of HiPIMS coatings of Nb_3Sn/Cu and to compare it to the results obtained in the past with the more established DCMS deposition technique [26].

At last, the thesis is wrapped up in the final Conclusions.

Chapter 1

Theoretical background

This chapter is dedicated to the notions required for a basic understanding of conventional superconductivity. To guide the reader through the main developments of the theory, Section 1.1 will follow a chronological approach, whenever possible. The basics of RF superconductivity are then introduced in Section 1.2. The main sources of reference for this Chapter are [30]–[32].

1.1 Essentials of superconductivity

The most striking indication that a conductor has entered the superconducting state is the sudden and complete loss of electrical resistivity when cooled down below its critical temperature T_c. This was first observed in 1911 by H. Kamerling Onnes in mercury, a few years after he succeeded at liquefying helium [33] (Fig. 1.1a). Experimenting with superconducting wires, he then discovered a magnetic field can destroy the superconducting state of pure metals if it exceeds a certain critical value, known as the critical field H_c [34]. This was in turn related to the maximum electrical current a superconductor can carry without electrical resistance, named critical current or J_c. Twenty-two years later in 1933, W. Meissner and R. Ochsenfeld discovered that an externally applied magnetic field is expelled from the interior of a superconductor when cooled below T_c [35], [36] (Fig. 1.1b), provided that the applied field does not exceed the critical value H_c. However, according to Faraday's law of induction a conductor with infinite electrical conductivity is expected to conserve its interior magnetic field: remarkably, a superconductor was found to behave as a perfect conductor only from the electrical point of view, while magnetically it would rather behave as a perfect diamagnet. Nowadays, the loss of electrical resistivity and the expulsion of magnetic fields (addressed as "Meissner effect") are still the defining features of superconductivity, and both need to be observed in order to claim that a new superconducting material has been discovered.

A first attempt to a phenomenological description of the experimental observations was proposed in 1935 by the London brothers [37]. To explain the absence of electrical resistivity they reformulated the electromagnetic equations of a superconductor under the assumption that the electrons in it would move without the presence of an electric field. This is represented in the first London equation:

$$\vec{E} = \frac{m}{n_s e^2} \cdot \frac{\mathrm{d}\vec{j}}{\mathrm{d}t}\,, \tag{1.1}$$

where m, $-e$ and n_s are the mass, electric charge and the number density of the superconducting electrons. From Eq. 1.1 it is possible to see that, when the electric field $\vec{E}$ is zero the electric current $\vec{j}$ is constant. Applying the local Maxwell equations to Eq. 1.1 and using the expression for the magnetic flux density $\vec{B} = \mu_0 \vec{H}$ (where μ_0

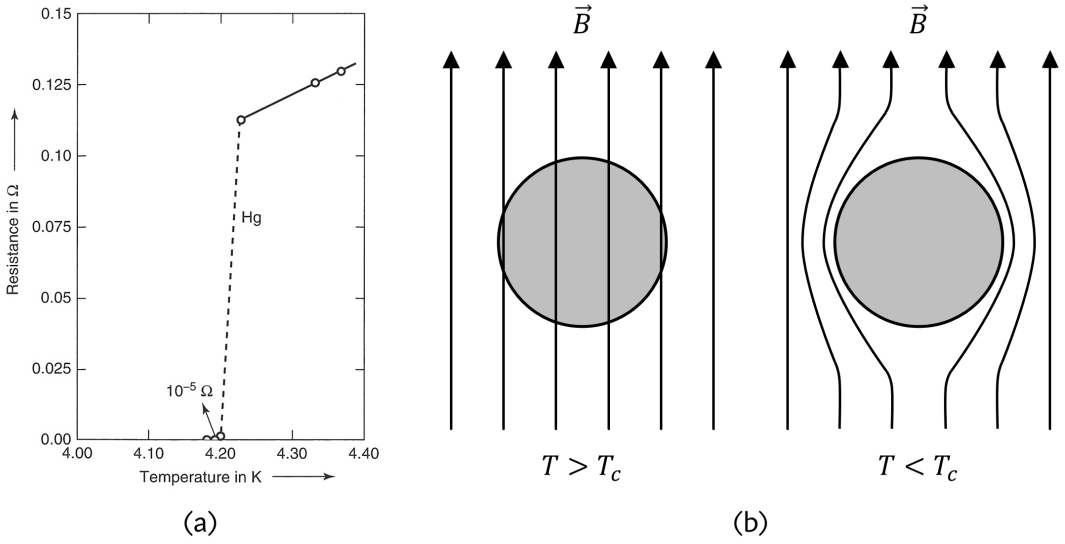

FIGURE 1.1: (a) Discovery of superconductivity in mercury (Reproduced from [31] with permission of John Wiley and Sons). (b) Schematic representation of the Meissner effect, where $\vec{B}$ is the externally applied magnetic field, T is the temperature of the sphere and T_c is the superconducting transition temperature.

is the magnetic permeability of vacuum and $\vec{H}$ is the magnetic field) one obtains the second London equation:

$$\vec{B} = -\mu_0 \lambda_L^2 \nabla \times \vec{j}\,, \tag{1.2}$$

for which the displacement currents originally included in Maxwell equations have been neglected. Equation 1.2 can be manipulated further to obtain its differential form, known as Helmholtz equation:

$$\nabla^2 \vec{B} = \frac{1}{\lambda_L^2} \vec{B}\,, \tag{1.3}$$

where λ_L, also appearing in Eq. 1.2, has the dimensions of a length and is defined as:

$$\lambda_L = \left(\frac{m}{\mu_0 n_s e^2} \right)^{1/2}. \tag{1.4}$$

The solution of Eq. 1.3 predicts the Meissner effect: the magnetic field is expelled from a superconductor due to the screening effect of the currents flowing without resistance near its surface. These *supercurrents* generate a magnetic field in the direction opposite to that of the applied field. Equations 1.1 and 1.2 show that the magnetic field and the current density decay exponentially within a distance λ_L below the surface of the superconductor. Everywhere else inside the material perfect diamagnetism is observed. The length λ_L is a characteristic quantity of superconductors and takes the name of London penetration depth.

While this macroscopic interpretation of the electromagnetism of superconducting phenomena was being developed, a description of superconductivity as a thermodynamical phase transition was proposed by C. Gorter and H. Casimir and published in 1934 [38]. In parallel, several uncommon properties of liquid helium were

being observed experimentally when it was cooled below 2.2 K. Below this temperature, the liquid would abruptly stop boiling [39] and it would show a peak in the specific heat [40], a surprisingly high thermal conductivity [41], [42] and the nearly complete absence of viscosity [43]. This series of discoveries culminated in 1938, with the separate works by P. Kapitza [44] and J. F. Allen and A. D. Misener [45], in which the new concept of superfluidity was introduced. In the effort to explain the properties of superfluid helium, F. London proposed that helium could be undergoing the phenomenon of Bose-Einstein condensation[46], [47] when cooled down below 2.2 K [48], [49], and, starting from his ideas, L. Tisza developed the so-called two-fluid model [50], [51]. According to the model, superfluid helium is described as consisting of two distinct, mutually permeating fluids, the normal fluid and the superfluid, each one having its own velocity and inertia, and between which there is little to no exchange of momentum. The superfluid is characterised by frictionless motion, while the normal fluid behaves like a regular, viscous liquid.

Following the observation of resistive losses in the surface screening layer of superconductors under the effect of a high frequency electromagnetic field [52], the assumption was made that normal conducting electrons were also present in the superconducting phase, especially at temperatures close to T_c. Therefore, the two-fluid model was also applied to describe superconductors [53], with the normal fluid being associated to the electron gas in the metal and the superfluid to the ensemble of electrons responsible for the supercurrents. The charge carrier density associated to each fluid is expressed as n_n and n_s for the normal conducting and superconducting carriers respectively, so that the total carrier density is expressed as the sum of the two:

$$n = n_n + n_s \, . \tag{1.5}$$

The normal and superfluid fractions, x_n and x_s, can also be introduced so that $x_n + x_s = 1$ and the total carrier density can be reformulated as:

$$n = n(x_n + x_s) \, . \tag{1.6}$$

The model also assumes the following temperature dependence for the superconducting carrier density:

$$n_s = n \left[1 - \left(\frac{T}{T_c} \right)^4 \right] \, . \tag{1.7}$$

The total current in the superconductor is hence described as the sum of two separate and independent components:

$$\vec{j} = \sigma \vec{E} = \vec{j}_n + \vec{j}_s \, , \tag{1.8}$$

where σ corresponds to the sum of the conductivities associated to the normal conducting and superconducting electrons respectively, that is:

$$\sigma = \sigma_n + \sigma_s \, . \tag{1.9}$$

This way one has $\vec{j}_n = \sigma_n \vec{E} = -n_n e \vec{v}$ associated to the normal conducting electrons, and $\vec{j}_s = \sigma_s \vec{E} = -n_s e \vec{v}$ associated to the superconducting electrons. The expressions for σ_n and σ_s in the harmonic regime will be derived later on in Section 1.2.

The first successful attempts at a microscopic understanding of superconductivity came with the phenomenological model proposed by V. Ginzburg and L. Landau in 1950 [54]. The Ginzburg-Landau (GL) theory succeeded at combining elements

of the London theory with the robust theory previously developed by Landau on phase transitions of second order [55], [56]. The theory starts from the assumption that, in the absence of an applied magnetic field, the transition from the normal conducting to the superconducting state represents a second-order phase transition, characterised by the absence of latent heat. This was supported by the experimental observation of the discontinuity in the specific heat of the superconductor, which would exhibit a jump at T_c [57]. A change in the symmetry of the system is associated to such transitions, so that with lowering temperature the order of the system increases. The reversibility of the Meissner effect as well suggested the superconducting phase to be characterised by lower entropy than the normal conducting one, also pointing in the direction of a more ordered state. To describe the new phase the order parameter Ψ, a physical quantity of extensive character, is defined so that:

$$\begin{aligned} \Psi(\vec{r}) &= 0 \qquad \text{for} \quad T \geq T_c \,, \\ \Psi(\vec{r}) &= 1 \qquad \text{for} \quad T = 0 \,, \end{aligned} \tag{1.10}$$

with $\vec{r}$ the position vector. It will be seen later that, within the microscopic theory of superconductivity, the order parameter represents the wave function of the collective system of superconducting electrons, so that the quantity $|\Psi(\vec{r})|^2 = n_s$ is interpreted as the density of the superconducting charge carriers. By minimising the thermodynamic free energy of the system, the GL theory shows that Ψ is governed by a Schrödinger-like equation into which magnetic effects can be included via a vector potential, whose solution not only accounts for the thermodynamic aspects of the normal-to-superconducting phase transition, but also for the spatial behaviour of the system at the normal-to-superconducting phase boundary.

Many physical concepts are introduced by the GL theory which help with the understanding of the phenomenon of superconductivity. Due to the structure of the theory, most of these are only valid in the limit $T \to T_c$, like, for example, the temperature dependency of the equilibrium density of superconducting electrons and of the thermodynamic critical field, respectively:

$$n_s(T) = n_s(0) \left(1 - \frac{T}{T_c}\right) \tag{1.11}$$

and

$$B_{cth}(T) = B_{cth}(0) \left(1 - \frac{T}{T_c}\right) \,, \tag{1.12}$$

the latter representing the largest energy perturbation that the system can withstand in the superconducting state before the transition to the normal conducting state is triggered. The London penetration depth λ_L (Eq. 1.4) is also derived by the GL theory, within which it assumes the same meaning. Another relevant length scale introduced by the GL theory is the Ginzburg-Landau coherence length ξ_{GL}, representing the spatial extension within which the order parameter Ψ can change. By introducing the definitions of these two lengths, which, in the limit $T \to T_c$, are given by:

$$\lambda_L = \frac{\lambda_L(0)}{\sqrt{1 - \frac{T}{T_c}}} \,, \tag{1.13}$$

$$\xi_{GL} = \frac{\xi_{GL}(0)}{\sqrt{1 - \frac{T}{T_c}}} \,, \tag{1.14}$$

it is possible to define the Ginzburg-Landau parameter, independent of the temperature and of the magnetic field, as the ratio of the two:

$$\kappa = \frac{\lambda_{\mathrm{L}}}{\xi_{\mathrm{GL}}}. \tag{1.15}$$

Later on in this chapter κ will be used as criterion for the distinction between type-I and type-II superconductors. At $T \ll T_{\mathrm{c}}$, λ_{L} is found to be approximately constant ($\lambda_{\mathrm{L}} \approx \lambda_{\mathrm{L}}(0)$), while its temperature dependence, inferred empirically, can be well approximated by:

$$\frac{\lambda_{\mathrm{L}}}{\lambda_L(0)} \propto \left[1 - \left(\frac{T}{T_{\mathrm{c}}}\right)^4\right]^{-1/2}, \tag{1.16}$$

which again yields Eq. 1.13 for $T \to T_{\mathrm{c}}$ [31]. The temperature dependence of the critical field is well described by the empirical expression:

$$B_{\mathrm{c}}(T) = B_{\mathrm{c}}(0)\left[1 - \left(\frac{T}{T_{\mathrm{c}}}\right)^2\right], \tag{1.17}$$

valid at $T < T_{\mathrm{c}}$. The critical field B_{c} is known to coincide with B_{cth} for type-I superconductors, and indeed, for $T \to T_{\mathrm{c}}$, takes the same linear temperature dependence predicted by the GL theory. Because of the dependence in Eq. 1.17, the superconducting transition happens at exactly $T = T_{\mathrm{c}}$ only in the absence of an applied magnetic field, otherwise T_{c} is lowered.

In 1952 A. Pippard proposed a modification of the London theory [58], in which the expression for the supercurrent is related to the average of the vector potential calculated over an extended region around the point considered, i. e. it made the London equations no longer local. The extension of the non-locality region, expressed by the parameter ξ, is assumed to depend on the purity of the material in an analogous way to that of the mean free path l of normal conducting electrons in a metal, and is connected to the latter via:

$$\frac{1}{\xi} = \frac{1}{\xi'} + \frac{1}{l}, \tag{1.18}$$

where ξ' represents the extension of the non-locality region in the limit of a very pure, ideal material, i. e. for $l \to \infty$. It will be shown later how ξ and ξ' are connected to ξ_{GL} and to ξ_0, the coherence length arising from the microscopic theory of superconductivity.

Inspired by the work of L. Shubnikov, V. Khotkevich, G. Shepelev and Y. Rjabinin on the critical field of alloys [59], A. Abrikosov noticed that the GL theory not only provided a description of the type-I superconductors for which it was meant, but it also explained the type-II superconductivity discovered by Shubnikov: below a certain critical concentration of its minor constituent, an alloy would behave like a pure superconductor in the Meissner state and suddenly lose its superconductivity at a critical field B_{c}; above this critical concentration, the external field would start penetrating the alloy in the form of magnetic flux lines at a value $B_{\mathrm{c1}} < B_{\mathrm{c}}$, thus disrupting the Meissner state, while superconductivity would only cease at a higher value of the field $B_{\mathrm{c2}} > B_{\mathrm{c}}$. The concept is well represented in Fig. 1.2a, with a practical case of an indium + 4 At% bismuth alloy [60] given in Fig. 1.2b. Further increasing the bismuth concentration would lower the value of the lower critical field B_{c1} and extend that of the upper critical field B_{c2}.

The *mixed state* of the superconductor resulting from the partial penetration of the field before the disruption of superconductivity is also known as the Shubnikov phase, schematically represented in Fig. 1.3a. For type-II superconductors, as proposed by Abrikosov in 1957 [61], it is energetically favourable to let the magnetic field enter the superconducting region in the form of magnetic flux lines, often addressed as Abrikosov vortices. The prediction that the vortices would carry a well defined, quantized amount of magnetic flux was inspired by, and immediately followed, R. Feynman's work on the quantization of vortex lines in liquid helium, published in 1955 [62]. The understanding of superconductivity was progressively pointing towards its interpretation as a macroscopic quantum phenomenon. Later

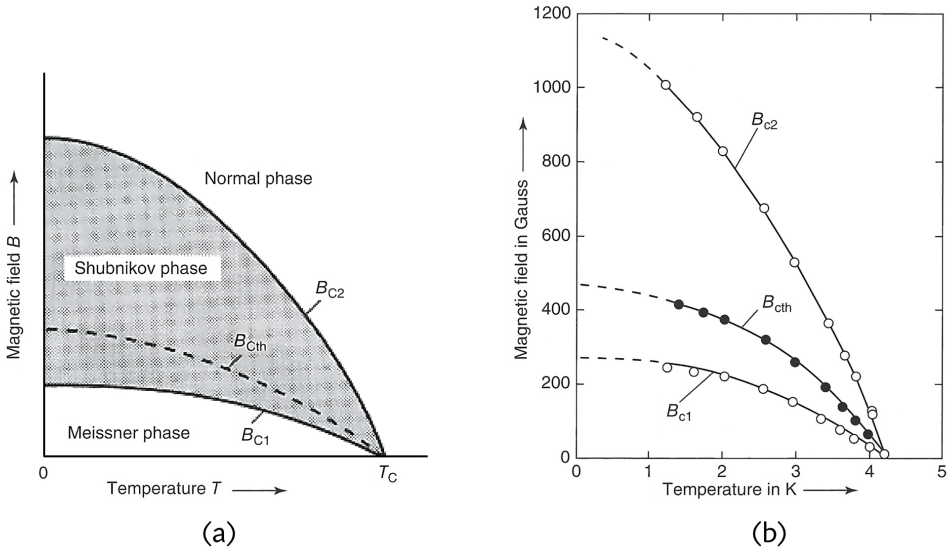

FIGURE 1.2: (a) Schematic representation of the temperature dependence of the critical fields and phase diagram of a type-II superconductor. (b) Critical fields of an In+4%Bi alloy. (Both reproduced from [31] with permission of John Wiley and Sons).

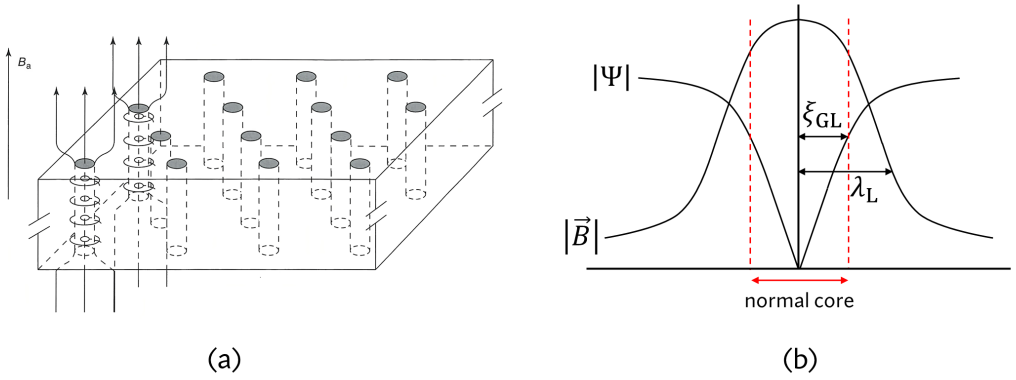

FIGURE 1.3: (a) Schematic representation of the Shubnikov phase (reproduced from [31] with permission of John Wiley and Sons). (b) Spatial distribution of the magnetic flux and of the order parameter for an Abrikosov vortex. The normal core of the magnetic flux line is indicated in red dashed lines.

on in 1961, the experimental evidence for the quantization of the magnetic flux in type-II superconductors came from B. Deaver and W. Fairbank [63]: a continuously increased applied magnetic flux was observed to penetrate a hollow cylinder made of tin by only discrete, well-defined amounts. A single vortex is today known to carry a magnetic flux equal to $\Phi_0 = h/2e = 2.07 \times 10^{-15}\,\mathrm{T\,m^2}$, the so-called magnetic flux quantum, where h is Planck's constant and e the electron charge. Each vortex consist of a tube-like system of circulating supercurrents which, in addition to the external magnetic field, generate the magnetic flux within the vortex. The more the external magnetic field is increased above B_{c1}, the greater the number of vortices entering the superconductor. The diameter of a single vortex is found to correspond to λ_L, while its "core", that is the normal conducting region in which the order parameter Ψ has zero amplitude, has the size of ξ_{GL} (Fig. 1.3b).

For a homogeneous superconductor in the Shubnikov phase, the vortices are known to evenly position themselves according to a triangular lattice (the Abrikosov lattice) representing the minimum energy configuration for the magnetic flux lines inside the superconductor. The full analogy between this lattice and the 3D crystal lattice of a solid can be made, to the point that a temperature dependent solid/liquid lattice state transition is observed. The vortex system is strongly correlated at low temperature ($T \ll T_c$). When the temperature is increased to the point that the the solid/liquid state line is crossed, the lattice "melts" and vortices can move freely. This is, in general, considered as a disturbance of the superconducting state, as it results in energy dissipation [64], hence a resistive behaviour. Eventually, this leads to the disruption of the superconducting phase, as the critical current that the superconductor can withstand approaches zero. Impurities and structural defects in the material can "pin" the vortices, preventing their flow. For this reason, pinning centers in the material can be actively exploited to prevent vortex flow. However, depending on the application this can be an advantage (e.g. for superconducting magnet, for which pinning points represent a stabilising factor for the critical current of the superconductor).

The foundations for a microscopic theory were already being established in the early 1950's, when H. Frölich and J. Bardeen, independently, emphasized the observation that many good normal conductors, such as gold or copper, did not become superconductors, suggesting that superconductivity might result from the strong interaction between conduction electrons and phonons (the lattice vibrations) of those metals which did not exhibit good normal conductivity [65], [66]. Based on these assumptions, their work predicted that the transition temperature of different isotopes of the same superconductor should scale inversely to the square root of the atomic mass, thus: $T_c \propto M^{-1/2}$. This was experimentally observed in the following years and confirmed the role of the electron-lattice interaction proposed by Frölich and Bardeen [67]–[69].

The first complete microscopic interpretation of superconductivity was presented in 1957 by J. Bardeen, L. Cooper and J. Schrieffer (the BCS theory) [70]. In this work, a quantum mechanical, attractive interaction is assumed to take place between the conduction electrons of the superconductor, with the interaction being mediated by virtual phonons[1]. This interaction results from the polarisation of the lattice of positive ions, induced by a negatively charged electron passing nearby, so that for another electron in the vicinity it can become energetically favourable to move along

[1]The phonons only exist in their transfer between correlated electrons, and are not transferred to the lattice as real phonons. This process would result in an energy transfer and, therefore, electrical resistance.

the polarisation "track" left by the previous one[2]. This electron-phonon interaction results in the formation of electron pairs. Each pair, named "Cooper-pair" and indicated as $\{\vec{k}\uparrow, -\vec{k}\downarrow\}$, consists of two electrons having opposite wave-vector $\vec{k}$ (or momentum $\vec{p}$) and spin, which are now correlated as a single system (the pair) whose relevant motion is that of its center of mass and total spin the sum of the two. The change from half-integer (single electrons are fermions with spin 1/2) to a total integer spin (the pair is a boson and has spin 0) is crucial for the collective behaviour of the Cooper pairs, which can now condense into a state whose physical quantities, and in particular the center of mass momentum, are the same for all pairs. This is the reason for the macroscopical manifestation of superconductivity. The size of a Cooper pair is expressed as the BCS coherence length ξ_0 and represents the distance within which the pair correlation is active.

The electrons taking part into superconductivity are only a small fraction, those whose energy falls within $\pm\hbar\omega_D$ of the Fermi energy E_F, with ω_D being the Debye frequency, the highest possible phonon frequency characteristic of the material. The usual Fermi distribution of the electronic energy levels is affected by the attractive interaction, so that the energy states near the Fermi level are redistributed (Fig. 1.4a). It is found that, for a superconductor, there are no available states within an interval of about $E_F \pm \Delta_0$, with the energy Δ_0 depending on the cumulative properties of the Cooper pair states. If a Cooper pair is broken, it yields two independent electrons, or *quasiparticles*, whose energy can be expressed as:

$$E_{QP} = \sqrt{(\epsilon_n - E_F)^2 + \Delta_0^2}\,, \tag{1.19}$$

where ϵ_n is the energy of the same electron in the normal state. Equation 1.19 shows the energy of a quasiparticle (Fig. 1.4b) has its minimum at Δ_0: the Cooper pair interaction still has an influence on the unpaired electrons as they cannot be into states corresponding to E_F, differently from what would be possible for single electrons in the normal conducting state. For this reason, the quantity $2\Delta_0$ not only represents the minimum energy needed to break a Cooper pair, but also the energy *gap* of the pair-quasiparticle density of states which is distinctive of superconductors. At $T > 0$ a Cooper pair can be broken due to thermal fluctuations, resulting in quasiparticles occupying the states available for Cooper pair condensation, hence reducing their total number and their binding energy. At finite temperatures, it is observed that Δ_0 approaches zero for $T \to T_c$. The energy gap is related to the critical temperature of a superconductor via [72]:

$$2\frac{\Delta_0}{k_B T_c} = 3.528\,, \tag{1.20}$$

where k_B is the Boltzmann's constant, for the superconducting energy gap at $T \ll T_c$. A good approximation of the temperature dependence of the superconducting gap is given by:

$$\Delta(T) = \Delta_0 \left[\cos\left(\frac{\pi}{2}\left(\frac{T}{T_c}\right)^2\right)\right]^{1/2}\,. \tag{1.21}$$

[2] A good human analogy to explain the phenomenon was proposed by P. Schmuser in a lecture about superconductivity [71]: "*Suppose you are cross-country skiing in very deep snow. You will find this quite cumbersome, there is a lot of 'resistance'. Now you discover a track made by another skier [...] and you will immediately realize that it is much more comfortable to ski along this track than in any other direction*".

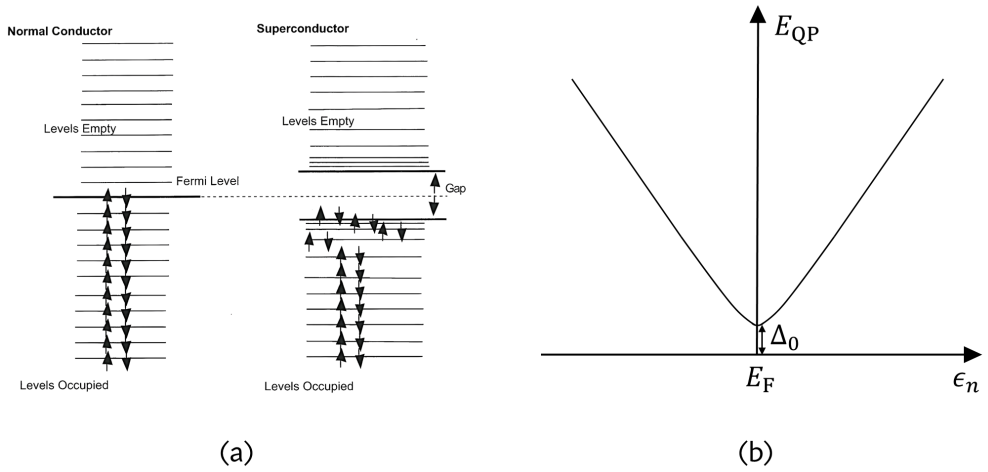

FIGURE 1.4: (a) Energy levels of the electrons in the normal conducting and superconducting state (reproduced from [32] with permission of John Wiley and Sons). (b) Qualitative trend of the quasiparticle energy as a function of the free electron energy.

The coherence length ξ_0 is found to be nearly temperature independent, and related to energy gap via:

$$\xi_0 = \frac{\hbar v_F}{\Delta_0} , \tag{1.22}$$

with v_F being the Fermi velocity. Another relation introduced by the BCS theory is that between ξ_0 and the electron mean free path l, such that:

$$\begin{aligned} \xi_0 &\simeq l && \text{for} \quad l \to 0 , \\ \xi_0 &= 0.18 \frac{\pi \hbar v_F}{2 k_B T_c} && \text{for} \quad l \to \infty . \end{aligned} \tag{1.23}$$

This suggests that ξ_0 is closely related to the coherence length ξ' introduced in Eq. 1.18, where one can see that $\xi \to \xi'$ for $l \to \infty$. Thus it is possible to classify superconductors into *clean* and *dirty* ones via the relative size of l with respect to ξ_0. One talks about:

$$\begin{aligned} &\textit{clean} \text{ superconductor} \quad \text{for} \quad l \gg \xi_0 \quad \text{and} \\ &\textit{dirty} \text{ superconductor} \quad \text{for} \quad l \ll \xi_0 , \end{aligned} \tag{1.24}$$

referring to the amount of impurities in it affecting the size of l. Many parameters derived from the London and GL theories are either obtained also within the BCS theory, or in many cases connected to the BCS ones under certain assumptions. For example, the real physical meaning of the GL order parameter Ψ becomes clear within the BCS theory as it can be interpreted as the macroscopic wave function associated with the collective system of Cooper pairs. λ_L and ξ_{GL} depend on the density of Cooper pairs and are also put in relation (in the limit $T \ll T_c$) to the electron mean free path l by the BCS theory as follows:

$$\lambda_L(l) = \lambda_L(l \to \infty) \left[1 + \frac{\xi_{GL}(l \to \infty)}{l} \right]^{1/2} , \tag{1.25}$$

$$\xi_{GL}(l) = [\xi_{GL}(l \to \infty)l]^{1/2} \ . \tag{1.26}$$

This dependence was not yet taken into account in Eqs. 1.13, 1.14 and 1.16. From Eqs. 1.25 and 1.26 one can see that, for decreasing l, λ_L increases and ξ_{GL} decreases. This also translates into a strong dependence on l of the GL parameter κ. Again, since l depends on the purity of the metal and can be regulated by controlling the amount of impurities, a type-I superconductor can be changed into a type-II superconductor as shown in the research by Shubnikov *et al.* [59], and κ is found [61] to perfectly describe (and somehow quantify) such a transition. In particular it is shown that:

$$\begin{aligned} &\text{for} \quad \kappa < \frac{1}{\sqrt{2}} \quad \text{the superconductor is of type-I} \quad \text{and} \\ &\text{for} \quad \kappa \geq \frac{1}{\sqrt{2}} \quad \text{the superconductor is of type-II} \ . \end{aligned} \tag{1.27}$$

The lower and upper critical fields of type-II superconductors can be also expressed in terms of ξ_{GL} and λ_L:

$$B_{c1} = \frac{\Phi_0}{4\pi\lambda_L^2}(\ln\kappa + 0.08) \ , \tag{1.28}$$

$$B_{c2} = \frac{\Phi_0}{4\pi\xi_{GL}^2} \ , \tag{1.29}$$

and due to their connection to B_{cth} their temperature dependence exhibits the same trend as B_c in Eq. 1.17. From the GL theory the following quantitative relation is found for $T \to T_c$:

$$B_{c2} = \sqrt{2}\kappa B_{cth} \ , \tag{1.30}$$

and in the limit $\kappa \gg 1/\sqrt{2}$ one finds [61]:

$$B_{c1} = \frac{1}{2\kappa}(\ln\kappa + 0.08)B_{cth} \ . \tag{1.31}$$

The relations in 1.27 somehow summarize the deep difference between type-I and type-II superconductors, which becomes clear in their response to an applied magnetic field B_a. To a superconductor of volume V in the pure Meissner state, with fully developed shielding (that is its dimensions are all much larger than λ_L), a magnetic moment m can be associated to the screening currents, so that one can speak of magnetization $M = m/V$ of the superconductor. For a special sample geometry such that no demagnetization effects can occur, one can also associate the magnetic susceptibility $\chi = -1$ of an ideal diamagnet, to which corresponds a magnetization:

$$M = \chi\frac{B_a}{\mu_0} = -\frac{B_a}{\mu_0} \ . \tag{1.32}$$

In general, demagnetization effects are due to the enhancement of the magnetic field at the sample surface due to the modification of the applied field lines which follows the Meissner field expulsion. The field enhancement is promoted by the surface roughness and features in the sample geometry such as, for example, sharp edges, so that even if the homogeneous applied field B_a does not exceed B_c, it will at those points at the sample surface where field enhancement occurs. The demagnetization effects are accounted for by the demagnetization coefficient N_M, which is only zero for infinitely long rod-shaped samples or ellipsoids with their major axis oriented parallel to the applied field. For any other shape, usually $N_M \neq 0$ and depends on the specific shape and the applied field orientation. As a consequence, in the latter

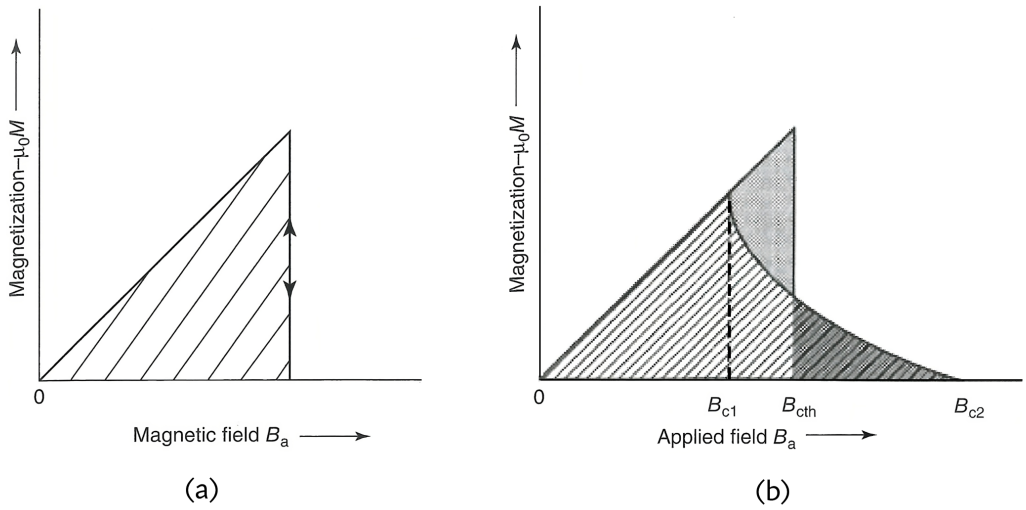

FIGURE 1.5: Magnetization as a function of an applied magnetic field for a type-I (a) and a type-II (b) superconductor. (Both reproduced from [31] with permission of John Wiley and Sons).

case, rather than B_a, one needs to consider the effective field at the sample surface:

$$B_{eff} = \frac{1}{1 - N_M} B_a \, . \tag{1.33}$$

The theoretical magnetization of the superconductor as a function of the applied magnetic field B_a is shown in Fig. 1.5a for type-I and in Fig. 1.5b for type-II. In the first case, $-M$ increases linearly until $B_a = B_c$ and the transition to the normal state takes place. However, for values of $B_a < B_c$ such that $B_{eff} > B_c$ at certain spots on the superconductor's surface, superconductivity must be destroyed at least locally. The superconductor cannot turn completely to the normal conducting state, since in this case the field in the interior would be equal to the external field and, hence, would be smaller than B_c. This situation will cause the superconductor to enter the *intermediate state*, a state in which it becomes energetically favourable for it to split up into superconducting and normal conducting domains, existing next to each other, with the normal conducting fraction in the interior of the superconductor increasing in such a way that the remaining field expulsion yields the value B_c at the surface spots where initially $B_{eff} > B_c$.

In the case of the type-II superconductor, the magnetization $-M$ increases linearly with increasing applied field only until $B_a = B_{c1}$. At this point, as already discussed, magnetic flux lines start entering the superconductor, with their number increasing with increasing B_a, resulting in a decreased $-M$. Flux penetration increases until $B_a = B_{c2}$, when superconductivity breaks off.

The crucial differences in the behaviour described above result from the complex balance between the magnetic field expulsion energy $\mathcal{E}_M$ and the Cooper pair condensation energy $\mathcal{E}_C$ at the normal to superconducting interface for the two different superconductor types.

A layer within which $\mathcal{E}_C$ and $\mathcal{E}_M$ can change is associated to the interface, and the wall energy $\mathcal{E}_W$ is associated to the layer itself, given by the difference between

the variations of $\mathcal{E}_C$ and $\mathcal{E}_M$:

$$\mathcal{E}_W = \Delta\mathcal{E}_C - \Delta\mathcal{E}_M = (\xi_{GL} - \lambda_L) A \frac{B_a^2}{2\mu_0} , \tag{1.34}$$

where A is the area of the interface.

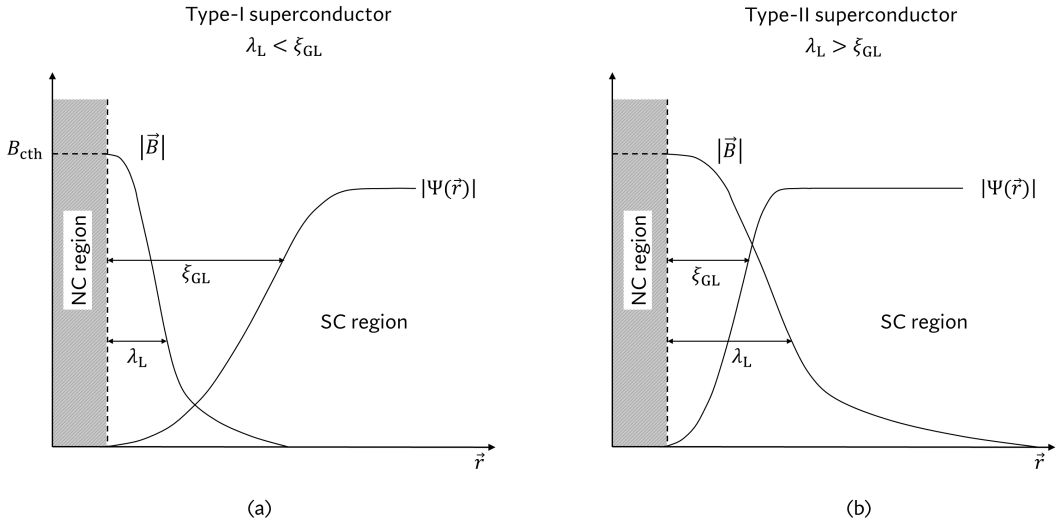

FIGURE 1.6: Schematic representation of the spatial variation of the magnetic field density and Cooper pair density at the interface between the normal conducting and superconducting regions for (a) a type-I superconductor and (b) a type-II superconductor.

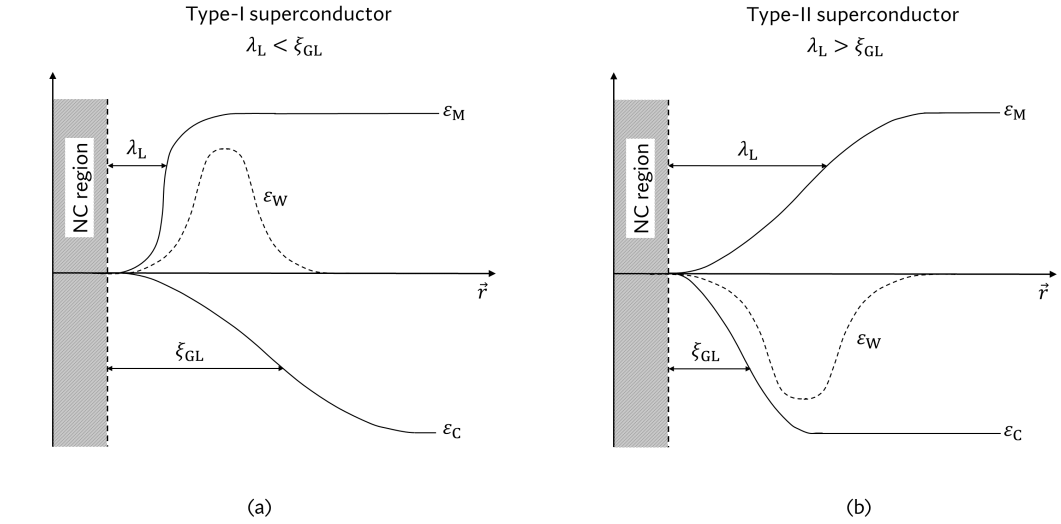

FIGURE 1.7: Schematic representation of the spatial variation of the magnetic expulsion energy and Cooper pair condensation energy at the interface between the normal conducting and superconducting regions for (a) a type-I superconductor, for which the resulting wall energy is positive, and (b) a type-II superconductor, for which the resulting wall energy is negative.

For type-I superconductors $\xi_{GL} > \lambda_L$, and the wall energy is positive, which means it must be supplied, at the expense of the magnetic field, in order for the normal to superconducting interface to be created. As a consequence, the size of the domains cannot become arbitrarily small, but depends on the optimal energy configuration allowing the free energy of the superconducting state to keep its minimum possible value.

For type-II superconductors, instead, $\xi_{GL} < \lambda_L$ and therefore the formation of an interface, represented here by the layer separating an Abrikosov vortex from the surrounding superconducting volume, is accompanied by an energy gain, reason why the penetration of flux lines is energetically favourable with respect to the complete disruption of the superconducting state. Since the magnetic field can penetrate the superconductor before the applied field becomes equal to B_{cth}, this must be taken into account by the condition given in Eq. 1.34, which becomes

$$\mathcal{E}_W = \xi_{GL} A \frac{B_{cth}^2}{2\mu_0} - \lambda_L A \frac{B_a^2}{2\mu_0} < 0 \,, \tag{1.35}$$

and therefore

$$\frac{B_{cth}^2}{B_a^2} < \frac{\lambda_L}{\xi_{GL}} \,. \tag{1.36}$$

As discussed earlier, the condition $\xi_{GL} < \lambda_L$ can always be realised by making the electron mean free path l sufficiently small (e.g. by alloying the superconductor with a small amount of impurities), also shown in Eqs. 1.25 and 1.26.

The plots in Fig. 1.6 are representative of the concept of interface layer discussed for type-I and type-II superconductors.

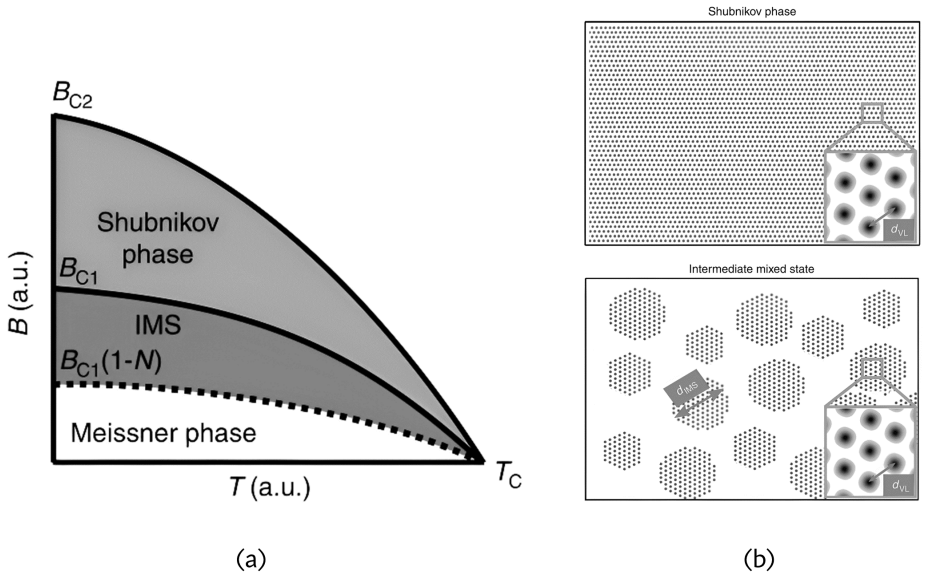

FIGURE 1.8: (a) Phase diagram of a type-II superconductor having $\kappa \approx 1/\sqrt{2}$ and a non-zero demagnetization coefficient N. The intermediate-mixed state (IMS), in which the Meissner and the Shubnikov phase coexist, is highlighted in darker gray. (b) Schematic representations of the Shubnikov phase and of the IMS, indicating the characteristic lengths of the inter-vortex distance in the Abrikosov lattice d_{VL} and IMS domain size d_{IMS}. (Both reproduced from [73]).

As for most relations derived within the GL theory, also the net distinction indicated in 1.27 is valid near T_c. In fact, for $T < T_c$ and κ slightly larger than $1/\sqrt{2}$ a type-II superconductor can enter a state in which both the Meissner and the Shubnikov phases coexist. For example, this is the case for niobium [73], the most commonly employed type-II superconductor. As long as the superconductors is in the Meissner state, the external field is expelled the same way as for a type-I superconductor. But if at the superconductor's surface the effective field ($N_M \neq 0$) reaches B_{c1}, macroscopic domains form, similar to the ones observed for a type-I superconductor in the intermediate state, in which the Shubnikov phase appears instead of the normal phase. These structures are referred to as the *intermediate-mixed state* and they are only observed for values of κ close to $1/\sqrt{2}$. The temperature dependence of the critical fields of a type-II superconductor represented in Fig. 1.2a is readapted in Fig. 1.8a to include the intermediate-mixed state, starting at $B_{c1}(1 - N_M)$. In 1966, L. Neumann and L. Tewordt [74] have extended the GL theory to temperatures below T_c to find that there is a narrow range of κ values near $1/\sqrt{2}$ for which the interaction between vortices becomes attractive. It is due to this attraction that domains in the Meissner state can coexist with domains featuring the Shubnikov phase.

1.2 RF superconductivity

1.2.1 The electrical conductivity of normal and superconductors in the harmonic regime

The following relations, whose derivation can be found in [30], [53], [75], are reported here as preparatory to the content of Section 1.2.2 and Section 1.2.3.

THE CLASSICAL DRUDE MODEL FOR NORMAL CONDUCTORS

In the classical Drude model, a conductor for which the Ohm law $\vec{j} = \sigma_0 \vec{E}$ is satisfied will exhibit a static (or DC) electric conductivity equal to:

$$\sigma_0 = \frac{n' e^2 \tau}{m} , \tag{1.37}$$

with n' being the electron density and τ the electron relaxation time. The Drude model also predicts the complex conductivity of a conductor exposed to a time-dependent electromagnetic field of the type $\vec{E}(t) = \vec{E} e^{i\omega t}$:

$$\sigma' = \sigma_1' + i\sigma_2' = \frac{\sigma_0}{1 - i\omega\tau} = \sigma_0 \left(\frac{1}{1 + (\omega\tau)^2} + i\omega\tau \frac{1}{1 + (\omega\tau)^2} \right) . \tag{1.38}$$

THE TWO-FLUID MODEL FOR SUPERCONDUCTORS

As anticipated in the previous Section, the electrical conductivity of a superconductor in the harmonic regime is expressed within the two-fluid model as the sum of the conductivities associated to the normal and superfluid components (Eq. 1.9). The normal component is known to correspond to the Drude conductivity given in Eq. 1.38, while the superfluid component can be directly calculated from Eq. 1.1 by implying the harmonic regime with $\vec{E}(t) = \vec{E} e^{i\omega t}$. This way, the total conductivity takes the explicit expression:

$$\sigma = \sigma_n + \sigma_s = \sigma' - i \frac{1}{\mu_0 \omega \lambda_L^2} = \sigma_1 + i\sigma_2 . \tag{1.39}$$

In this case, one must not forget that the relaxation time τ and the mass m included in σ' via Eq. 1.37 refer to the quasiparticles and do not necessarily coincide with the quantities associated to the normal electrons. The same is valid for n' appearing in Eq. 1.37, which is here replaced by n_n from Eq. 1.5.

In the low-frequency limit $\omega\tau \ll 1$, Eq. 1.39 takes the form of two parallel impedances, which can be expressed as a resistivity

$$\sigma_1^{-1} = \frac{1}{\sigma_0} = \frac{m}{n_\mathrm{n} e^2 \tau} , \tag{1.40}$$

and an inductivity

$$\sigma_2^{-1} = \mu_0 \omega \lambda_\mathrm{L}^2 . \tag{1.41}$$

This is representative of common approximation according to which, at low frequency, the superconducting electrons "short-circuit" the quasiparticles/normal conducting ones.

1.2.2 Surface impedance of normal conductors

An external electromagnetic field with magnetic field component $\vec{H}(t) = \vec{H}\mathrm{e}^{i\omega t}$ oriented parallel to the surface of a non magnetic, normal conductor, is known to decay within the conductor surface according to [30]:

$$\vec{H}(x) = \vec{H}_0 \mathrm{e}^{-\gamma x} , \tag{1.42}$$

where x represents the direction inside the conductor perpendicular to its surface and $\vec{H}_0$ the initial field amplitude at the conductor's surface. This is valid in the limit where the wavelength of the field is large compared to the electron mean free path. The complex attenuation constant γ is then expressed as:

$$\gamma = i\omega \sqrt{\mu_0 \varepsilon \left(1 - i\frac{\sigma'}{\omega\varepsilon}\right)} , \tag{1.43}$$

where ε is the conductor permittivity. For a good conductor the approximation $\sigma' \gg \omega\varepsilon$ can be made, so that Eq. 1.43 becomes:

$$\gamma \simeq (1+i)\sqrt{\frac{\omega\mu_0\sigma'}{2}} = (1+i)\frac{1}{\delta} . \tag{1.44}$$

Equation 1.44 defines the complex skin depth

$$\delta = \sqrt{\frac{2}{\omega\mu_0\sigma'}} , \tag{1.45}$$

representing the distance the harmonic field penetrates inside the conductor. Note how the skin depth scales as $\delta \propto (\omega\sigma')^{-1/2}$. Within the skin depth, currents flow at the conductor surface, screening the electromagnetic field from the bulk. For those cases when only the real part of the conductivity is relevant, σ' in Eq. 1.45 is replaced by σ_0 given in Eq. 1.37.

The response function of the conductor to the field propagation within its surface is known as the surface impedance, which can be expressed as:

$$Z_\mathrm{S} = R_\mathrm{S} + iX_\mathrm{S} , \tag{1.46}$$

with the real part R_S representing the resistance of the conductor in the harmonic regime, and the imaginary part X_S giving the reactance and arising from the surface currents not being in phase with the field.

By also considering the decay of the electric field component $\vec{E}(x) = \vec{E}_0 e^{-\gamma x}$ it can be found that:

$$Z_S \simeq (1+i)\sqrt{\frac{\omega\mu_0}{2\sigma'}} = (1+i)\frac{1}{\sigma'\delta}\,, \tag{1.47}$$

where again the approximation $\sigma' \gg \omega\varepsilon$ was made. When the conductivity has only a real component, R_S and X_S are found to coincide, yielding the following final expression for the surface resistance for a normal conductor:

$$R_S = X_S = \sqrt{\frac{\omega\mu_0}{2\sigma'}} = \frac{1}{\sigma'\delta}\,. \tag{1.48}$$

The relations discussed so far apply as long as the skin depth stays much larger than the electron mean free path ($\delta \gg l$), condition which grants the locality of the Maxwell equations and the validity of the conductor's constitutive relations. However, in the moment one has $l \gg \delta$, the relation between the field and the current density is no longer local and one finds, in this case, that $\delta \propto (\omega\sigma')^{-1/3}$, known as the "anomalous" skin depth [76].

1.2.3 Surface impedance of superconductors

A similar description can be applied to the case of superconductors, although a more complicated behaviour is expected due to the coexistence of paired and unpaired electrons. Even though the Cooper pairs can move without friction, they exhibit a certain inertia in responding to the field oscillations[3]. This results in a non-perfect screening of the field, which can penetrate the material's skin depth and couple to the unpaired electrons, leading to the appearance of the electrical resistance. The complex surface impedance of a superconductor depends on the two-fluid conductivity given by Eq. 1.9, so that in general takes the form:

$$Z_S = \sqrt{\frac{i\omega\mu_0}{\sigma_1 - i\sigma_2}}\,. \tag{1.49}$$

However, by considering that even at temperatures slightly smaller than T_c the condition $\sigma_2 \gg \sigma_1$ is verified, Eq. 1.49 can be further manipulated to extract the real and imaginary components of the surface impedance, given respectively by:

$$R_S \simeq \frac{1}{2}\sigma_n\omega^2\mu_0^2\lambda_L^3 \tag{1.50}$$

and

$$X_S \simeq \mu_0\omega\lambda_L\,. \tag{1.51}$$

Equation 1.50 represents the surface resistance of a superconductor, and shows the quadratic frequency scaling which makes the resistive losses of a superconductor drop much faster than the ones of a normal conductor in the same frequency regime.

[3]This is also the case for electrons in a normal conductor: their inertia contributes to the electrical resistance but becomes negligible compared to the contribution from scattering phenomena.

For $T \ll T_c$, for which $\lambda_L \approx \lambda_L(0)$, σ_n is proportional to the density of unpaired electrons and is known from the BCS theory to decrease with temperature according to a Boltzmann law, with Δ_0 as characteristic energy. This dependency can be approximated to:

$$R_{BCS} = A(\lambda_L^4, \xi_0, l, \sigma_n^{-1/2})\omega^2 e^{-\Delta_0/k_B T}. \tag{1.52}$$

The term $A \propto T^{-1/2}$ weakly depends on the temperature, so that R_{BCS} is dominated by the exponential term. The explicit dependencies of A on the material parameters can be calculated in the BCS framework and are found in [77]. From Eq. 1.52 one can again see the quadratic dependence of superconductor surface resistance on the field frequency.

Based on the purity of the material, a relation is found between the R_{BCS} and the electron mean free path l, which extends the definition of clean and dirty superconductor given in Eq. 1.24 so that:

$$\begin{aligned} &\textit{clean} \text{ superconductor:} \quad l \gg \xi_0 \quad \Rightarrow \quad R_{BCS}^{clean} \propto l, \\ &\textit{dirty} \text{ superconductor:} \quad l \ll \xi_0 \quad \Rightarrow \quad R_{BCS}^{dirty} \propto \frac{1}{\sqrt{l}}. \end{aligned} \tag{1.53}$$

Between the clean and dirty limits, R_{BCS} takes a minimum value when the electron mean free path becomes comparable to the coherence length [77]. In Fig. 1.9 the measured temperature dependence of the surface resistance of a 1.5 GHz niobium resonant cavity is plotted with the theoretical prediction. It is possible to see that below a certain temperature the data deviate from theory and approach a constant value. This behaviour is taken into account with the residual resistance R_{res} so that:

$$R_S = R_{BCS} + R_{res}. \tag{1.54}$$

While R_{BCS} correspond to energy dissipation due to unpaired electrons, the term R_{res} refers to the residual resistance of the material at very low temperatures.

1.2.4 Residual resistance of SRF materials

The causes for the residual resistance of superconducting materials in the radio-frequency regime can be diverse. Some are intrinsic material factors, like lattice structure imperfections and surface defects, which are known to play a role, as well as impurities (e.g. hydrides and oxides are known to be an issue for RF applications of niobium). In practical objects such as RF resonant cavities, assembly joints, seams and welds, although they do not strictly affect the quality of the superconducting surface, are also known to contribute significantly to R_{res} when placed at high-field regions. Some other causes are extrinsic to the material, such as trapped magnetic flux, and can be avoided by, e.g., practicing magnetic hygiene [78], [79].

A measure of the defects in a metal, and therefore an indication of its purity level, is given by the residual resistivity ratio (RRR), defined as:

$$\text{RRR} = \frac{\rho(300\text{K})}{\rho_0}\,, \tag{1.55}$$

where $\rho(300\text{K})$ is the electrical resistivity of the material at room temperature and ρ_0 is the residual resistivity measured at low temperature, usually 4.2 K for normal metals or right above T_c for superconductors. Since the room temperature resistivity is dominated by phonon scattering, one has RRR $\propto 1/\rho_0$ and hence proportional to

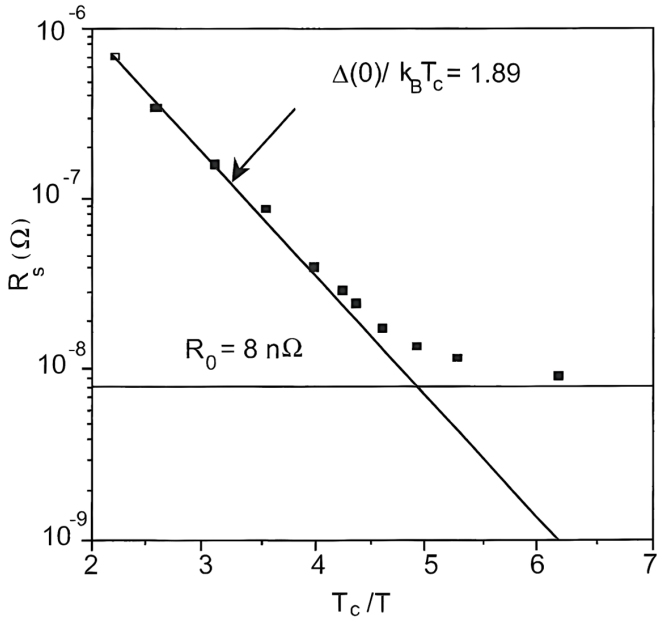

FIGURE 1.9: Temperature dependence of the surface resistance for a single-cell 1.5 GHz niobium cavity (reproduced from [32] with permission of John Wiley and Sons).

the electron mean free path l. Nevertheless, a direct relationship between R_{res} and RRR is not yet established.

Pure metals, such as niobium, and pure intermetallic compounds with a well defined stoichiometric composition, like Nb_3Sn, commonly employed in SRF applications, are usually clean superconductors, provided that they exhibit a low amount of crystalline defects. However, in most practical cases R_{BCS} cannot be neglected, and to limit its weight in the total R_{S} is therefore important, when choosing the superconducting material, to find the right compromise which maximizes T_{c} and minimizes λ_{L}. Since the order parameter is sensitive to defects that are larger or of comparable size to ξ_0, materials with a large BCS coherence length will be less affected in terms of increase of surface resistance. Type-II superconductors can have a large T_{c} and a reasonably small λ_{L}, so that their R_{BCS} can be small, even at rather high cryogenic temperature. On the other hand, their BCS coherence length is small, so type-II superconductors tend to display rather high R_{res}, unless they are prepared "defect-free".

	Superconducting property				
Material	T_{c} (K)	λ_{L} (nm)	ξ_0 (nm)	H_{c} (A/m)	H_{sh} (A/m)
Pb	7.2	39	83 – 92	6.4×10^4	8.4×10^4
Nb	9.2	32 – 44	30 – 60	1.6×10^5	1.9×10^5
Nb_3Sn	18	110 – 170	3 – 6	2.5×10^5	3.2×10^5
YBCO	94	140	0.2 – 1.5	$6 \times 10^5 - 10^6$	$6 \times 10^5 - 8 \times 10^5$

TABLE 1.1: Superconducting properties of lead (type-I), niobium (type-II with $\kappa \approx 1/\sqrt{2}$), Nb_3Sn (type-II with $\kappa > 1/\sqrt{2}$) and YBCO (high temperature superconductor). (Source [80]).

The development of SRF cavities has made it possible to identify several factors influencing R_{res}, which have been systematically understood and partly controlled. These are discussed into more detail in Section 2.3.1.

1.2.5 The superheating field

As observed by Bean and Livingston [81], a surface barrier exists against the nucleation of fluxons inside type-II superconductors, which can be observed when an applied external field H_a is oriented parallel to the surface of the superconductor. This barrier can prevent fluxons from nucleating inside the material even in those cases when H_a exceeds the field of first flux entry H_{c1} of the material. Under this condition, the superconductor can exist in a metastable Meissner state when exposed to fields $H_a > H_{c1}$, up to a field $H_a = H_{sh} > H_{c1}$, addressed as superheating field, at which the superconductor will enter the mixed state and fluxons will start nucleating. In the case of SRF cavities, the existence of the Bean-Livingston barrier is ensured by the field configuration. Although the metastable state can be achieved, the presence of defects on the surface of a cavity will make the parallel-field condition fail at these spots and promote flux entry. The dependence of H_{sh} on the GL parameter is calculated to be [82], [83]:

$$\begin{aligned} H_{sh} &\approx \frac{0.89}{\sqrt{\kappa}} H_c \qquad \text{for} \quad \kappa \ll 1, \\ H_{sh} &\approx 1.2 H_c \qquad \text{for} \quad \kappa \approx 1, \\ H_{sh} &\approx 0.75 H_c \qquad \text{for} \quad \kappa \gg 1. \end{aligned} \tag{1.56}$$

Typical values of the relevant parameters for different superconductors are given in Table 1.1 [80].

Chapter 2

Superconducting RF cavities

SRF resonant cavities are the devices responsible for the acceleration of the beam in particle accelerators and particle colliders. The specifications of a cavity strongly depend on the type and final scope of the accelerator it is developed and built for, and on the involved particle species. In this Chapter, the basics of SRF cavity design are given in Section 2.1. The figures of merit of cavity performance are presented and discussed in Section 2.2. Section 2.3 will focus on the properties, pros and cons of Nb/Cu cavities. Some considerations on the power consumption, a central topic in the planning of the future accelerator projects, are presented in Section 2.4, with emphasis on the possible role of Nb_3Sn. Finally, the current guidelines for cavity development are briefly discussed in Section 2.5.

2.1 The geometry trade-off

A resonant cavity can be described as a structure consisting of an enclosure made of conductor material, within which electromagnetic radiation conveys energy to the charged particles passing through it. The simplest structure of this kind is given by a hollow cylinder with closed ends, as shown in Fig. 2.1, and takes the name of "pillbox" cavity. The possible electromagnetic field configurations inside the pillbox cavity are obtained as the solutions to the field wave eigenvalue equation [32]. Two different sets of solutions can be obtained, which depend on the imposed boundary conditions and represent the cavity modes. These sets are denoted as the transverse magnetic (TM) and the transverse electric (TE) modes. For more complicated geometries than the pillbox, performing the calculation of the cavity modes does not change conceptually, although it can become a highly complicated task for which it often becomes necessary to turn to numerical methods. The electric and magnetic field distribution for the TM_{010} mode of a pillbox cavity are depicted in Fig. 2.1 in the cylindrical coordinate system.

The energy gain of a particle traveling across the cavity is proportional to the frequency of the field oscillation, usually in the radio-frequency (RF) range. In order to be accelerated, for half the RF period a charged particle travels a distance inside the cavity along which it experiences the accelerating electric field pointing in the forward direction. This distance, which defines the optimal cell length and addressed as the cavity's accelerating gap, is expressed as:

$$d = \beta \frac{\lambda_{\mathrm{RF}}}{2}\,, \tag{2.1}$$

with $\beta = v/c$ being the ratio of the particle speed v to the speed of light c, $\lambda_{\mathrm{RF}} = c/f$ the RF wavelength and f the RF frequency. For particles with $\beta \approx 1$ the accelerating gap equals half a wavelength, and the cavity is typically built to operate at RF frequencies between several hundreds of MHz and several GHz. For slower particles,

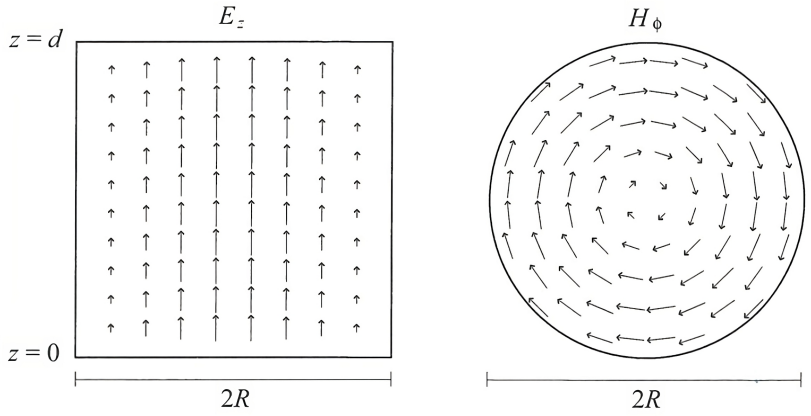

FIGURE 2.1: Electric and magnetic vector fields inside the pillbox cavity for the TM_{010} mode. Left: the electric field E_z on the $\rho - z$ plane. Right: the magnetic field H_ϕ on the $\rho - \phi$ plane. The cylinder height is given by z while $2R$ represents the cylinder diameter. (Reproduced from [32] with permission of John Wiley and Sons).

the cavity operation frequency must be chosen so that λ_{RF} is large, to compensate the small β and result into an accelerating gap yelding a satifying final accelerating voltage. Based on the speed of the particles, accelerating cavities can be classified into three major groups: high-, medium- and low-β cavities, the geometry of the cavity changing dramatically for each group. Fig. 2.2a shows four different cavity geometries, which cover wide cavity frequency and particle velocity ranges: quarter-wave resonators, employed for heavy-ion machines (low-β), are usually operated at frequencies between 50 and 200 MHz; elliptical resonators are employed for high-energy proton accelerators (medium- to high-β) and for electron/positron accelerators (high-β, usually multi-cell cavities), and cover frequencies in the 300 MHz – 3 GHz range; half-wave and spoke resonators cover the applications at intermediate particle velocity and accelerating frequency.

The comparison between the performances of different cavities is often not immediate. However, it can be shown [32] that the field equations for the cavity modes can be scaled by a scaling factor a, which accounts for the linear dimensions, without any loss of generality. It is also found that the spectrum of the cavity's modes ω_i is inversely proportional to the cavity's size, hence yielding the relation $\omega_i \propto a^{-1}$.

The most commonly employed quantities for the comparison of cavities of different material and shape, namely the geometrical factor G and the geometrical shunt impedance R_a/Q_0, are discussed in Section 2.2.4.

2.2 Figures of merit

The most crucial parameters describing the performance of an SRF cavity are given by the accelerating field, the dissipated power, the shunt impedance, the Q-value. These depend on the surface resistance R_S of the cavity's inner walls. In order to compare different cavity geometries, independently on the type of conductor employed for the production, some R_S-independent parameters are also of common use, such as the geometrical factor and the geometrical shunt impedance. The meaning of these parameters is briefly presented in the following, with the discussion

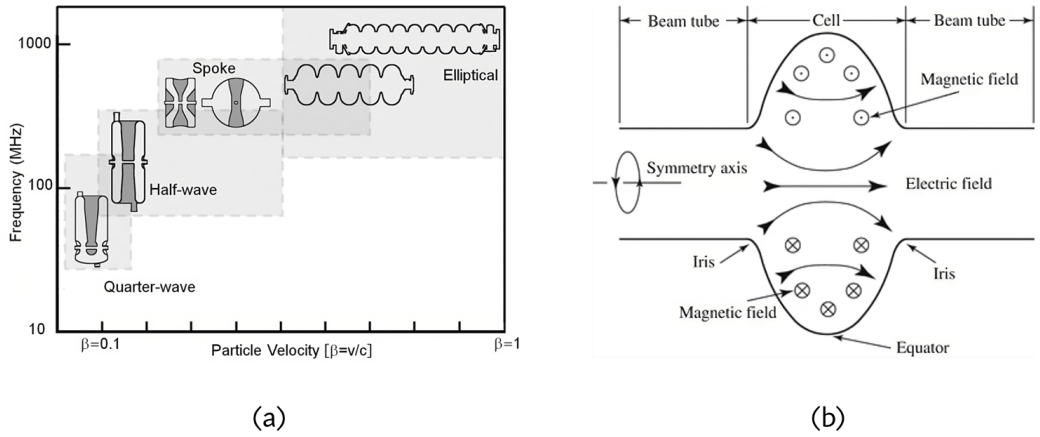

FIGURE 2.2: (a) Cavity geometry according to particle velocity (reproduced from [84] with permission of World Scientific Publishing). (b) Electric and magnetic field configuration in a single-cell SRF elliptical cavity (reproduced from [85] with permission of Springer Nature).

being limited to the case of elliptical cavities (single and multi-cell) whenever an explicit reference is made. A summary of the meaning of these parameters together with the desired optimization is given in Table 2.1.

2.2.1 Accelerating field

The energy received by a charged particle traversing the cavity depends on the electric field as "seen" by the particle itself along its path. If an electron is assumed to travel along the z-direction, one can define the accelerating voltage (per cell) of the cavity V_{acc} as the following path integral:

$$V_{\mathrm{acc}} = \left| \int_0^d E_{\mathrm{el}} \, \mathrm{d}z \right| , \tag{2.2}$$

where E_{el} is the electric field in the electron's reference frame and d is the distance travelled by it. Therefore, the average accelerating field E_{acc} experienced by the electron along its path, also called *gradient*, can be defined as:

$$E_{\mathrm{acc}} = \frac{V_{\mathrm{acc}}}{d} = \frac{2V_{\mathrm{acc}}}{\beta \lambda_{\mathrm{RF}}} , \tag{2.3}$$

where d has been replaced by the expression for the accelerating gap given in Eq. 2.1. The typical distributions of the TM_{010} electric and magnetic field in a $\beta = 1$, single cell elliptical SRF cavity are shown in Fig. 2.2b. The accelerating field E_{acc} is proportional to the peak electric field E_{pk}, as well as the peak magnetic field H_{pk} at the cavity inner surface. For an elliptical cavity, the magnetic field is maximum near the equator whereas the electric field is at a peak near the iris. Typical values for $E_{\mathrm{pk}}/E_{\mathrm{acc}}$ are 2.0 – 2.5 and for $H_{\mathrm{pk}}/E_{\mathrm{acc}}$ are 4 – 4.5 $\mathrm{mT}/(\mathrm{MV/m})$.

FIELD LIMITING FACTORS

Although there is no known theoretical limit to the value of E_{pk}, and therefore to E_{acc}, this is in reality limited by the phenomenon of field emission, usually starting

at values of $E_{pk} \approx 10 - 20\,\mathrm{MV/m}$. When this happens, electrons in the cavity material tunnel through the surface barrier, escape the cavity into the RF field region and move along different trajectories (depending on the RF phase at the moment of the emission) to eventually impact again on the cavity walls. These electrons absorb and release the energy stored in the cavity, thus limiting its RF performance. Typical signs of a cavity experiencing field emission are the observed temperature increase at the electron impact site and the emission of X-rays by Bremsstrahlung due to the electron curved trajectories [32]. Field emission is nowadays known to originate mostly from sites, called *emitters*, where impurities and contaminants are found. They occur in the form of particles whose size ranges between 0.3 µm and 20 µm, accidentally introduced during preparation/assembly procedures or brought to the surface during chemical etching (in the case of bulk niobium cavities). Not all impurities are emitters, that is, not all substances will affect the surface potential well in a way that field emission will take place. Whether an impurity will lead to field emission or not is found to depend, for example, on the particle shape, on its relative positioning with respect to the electric field, or on the possible presence of an insulating layer between the emitter and the cavity surface. To minimise the presence of emitters, strict cleaning procedures and clean-room assembly of RF cavities are an established routine, along with RF conditioning.

The limit imposed to the cavity gradient by H_{pk}, on the other hand, is known to be dictated by the superheating critical field H_{sh}, discussed in Section 1.2.5. Average values for the surface magnetic field of about 40 mT (and up to 90 mT peak values) are observed for accelerating gradients ranging from 5 to 20 MV/m in bulk niobium cavities. The two major limiting factors are given by the onset of thermal breakdown (also known as cavity *quench*) and by the phenomenon known as multipacting.

Thermal breakdown occurs at surface defects sporting electrical resistivity values much higher than the surface resistance of the superconductor. At these sites, typically sized < 1 mm, the surface reactance causes the RF currents to flow through the defect (not around it, as in the DC case) and dissipate heat. If the temperature at the defect area rises above T_c, the defect becomes normal conducting, power dissipation further increases and the size of the normal conducting area extends, leading to the thermal instability of the cavity. Experimental studies [86] demonstrated a quadratic dependence on the local magnetic field for the onset and extension of the thermal breakdown. According to a simplified thermal breakdown model based on a spherical defect embedded in a bulk niobium sheet [32], an effective way to prevent thermal breakdown at small defects is to increase the thermal conductivity of the niobium, in order to maximise the power that can be dissipated in the material (hence the tolerated magnetic field) before the transition to the normal state happens. The most commonly employed techniques to this aim are heat treatments such as solid-state gettering [87]. Coating niobium films on copper cavities, a technique developed at CERN for the 350 MHz accelerating cavities of LEP-II [88], is very effective preventing thermal breakdown (never observed on Nb/Cu cavities) because of the thermal stability granted by the copper due to its high thermal conductivity at low temperatures.

Multipacting takes place any time the impact of a stray electron with the cavity surface yields the emission of secondary electrons, which in turn hit the cavity walls producing more electrons. The electron build-up in the cavity absorbs the RF power, making it impossible to increase E_{acc} by increasing the input power. For a given secondary electron coefficient (SEC, material dependent), provided that the electric field points towards the cavity surface at the moment of impact, there is potentially no limit to the number of electron generations that can come in succession

when multipacting is triggered. A multipacting field barrier is usually overcome by allowing the phenomenon to progress, while gradually increasing the input power, until it stops. Often more barriers occur at higher fields. Tuning the SEC of the material and the geometry of the structure can be of great help in controlling the onset of multipacting, to a point where the phenomenon is nowadays nearly fully controlled in $\beta = 1$ cavities.

2.2.2 Dissipated power

The time averaged energy associated with the electric field in a cavity equals that associated with the magnetic field, leading to the expression

$$U = \frac{1}{2}\mu_0 \int_V |\vec{H}|^2 \, \mathrm{d}v = \frac{1}{2}\varepsilon_0 \int_V |\vec{E}|^2 \, \mathrm{d}v \tag{2.4}$$

for the total stored energy, where $\vec{H}$ and $\vec{E}$ are the local magnetic and electric peak fields. It will be seen later on how the energy stored in the cavity and the power dissipated by the cavity are related via the cavity's quality factor. The dissipated power P_c, generally addressed as *cavity losses*, is related to the surface resistance R_S of the cavity's inner walls via the following:

$$P_c = \frac{1}{2} R_S \int_S |\vec{H}|^2 \, \mathrm{d}s \, . \tag{2.5}$$

This dissipation, caused by the RF nature of the cavity field acting on the quasiparticles existing in the superconductor at $T > 0$, manifests itself in the form of Joule heating.

2.2.3 Shunt impedance

An estimate of the ability of a cavity to turn the RF input power into accelerating voltage is given by the shunt impedance R_a. The complex impedance $Z(\omega)$ associated to the cavity equals R_a at resonance, i.e. $Z(\omega_0) = R_a$, so that the shunt impedance can also be interpreted as the coupling strength of the cavity's main mode to the beam of charged particles. An expression for the cavity's shunt impedance is given by the ratio of the accelerating voltage to the power dissipated by the cavity, as follows:

$$R_a = \frac{V_{acc}^2}{P_c} \, . \tag{2.6}$$

2.2.4 Quality factor

The quality factor Q_0 of a resonant cavity represents an indication of the number of RF cycles (multiplied by 2π) required to dissipate the energy U stored in the cavity. It is expressed as:

$$Q_0 = \frac{\omega_0 U}{P_c} \, , \tag{2.7}$$

where ω_0 again represents the cavity's main resonance mode. Quality factors as high as 10^{11} have been observed in bulk-niobium elliptical cavities. By replacing U and P_c with their expressions given in Eq. 2.4 and 2.5 it is possible to express Q_0 as:

$$Q_0 = \frac{\omega_0 \mu_0 \int_V |\vec{H}|^2 \, \mathrm{d}v}{R_S \int_S |\vec{H}|^2 \, \mathrm{d}s} \, . \tag{2.8}$$

The geometrical factor G can be introduced at this point. Provided that R_S of the cavity is position and field independent, G does not depend on the surface resistance and is used to compare resonators with different geometries and materials. It is defined as:

$$G = \frac{\omega_0 \mu_0 \int_V |\vec{H}|^2 \, dv}{\int_S |\vec{H}|^2 \, ds} , \tag{2.9}$$

and therefore it represents the ratio of the cavity volume to its surface for a given frequency and field distribution. The quantity $\int_V |\vec{H}|^2 \, dv / \int_S |\vec{H}|^2 \, ds$ is found to scale like the scaling factor $a \propto \omega_0^{-1}$ (previously mentioned in Section 2.1), which makes G a constant factor. The ratio of the shunt impedance to the quality factor, called the geometrical shunt impedance, is also constant and does not depend on the surface resistance, allowing again the comparison between different RF structures:

$$\frac{R_a}{Q_0} = \frac{V_{acc}^2}{\omega_0 U} . \tag{2.10}$$

Due to the fact that the the quantity V_{acc}^2/U is found to scale like $1/a \propto \omega_0$, the geometrical shunt impedance is also constant.

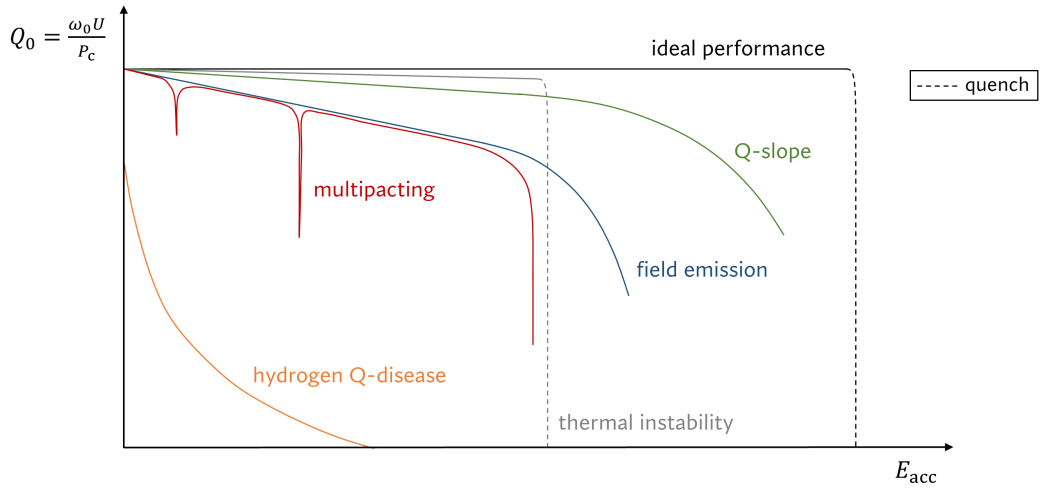

FIGURE 2.3: Qualitative dependency of Q_0 for bulk niobium as a function of the accelerating gradient E_{acc} for different cases, compared to the expected ideal performance (readapted from [8] with permission of IOP Publishing).

The ideal curve for the quality factor for bulk niobium as a function of E_{acc} is shown in Fig. 2.3, represented by the flat trend for increasing E_{acc} up to the theoretical superheating field limit H_{sh} [1].

The typical degradation due to the field limiting phenomena discussed above is shown case by case. The curve indicated as "hydrogen Q-disease" and not discussed in the text above, indicates the drop in quality factor which was commonly observed

[1] The assumption here is again that R_S is position and field independent and can be taken out of the integral defining the quality factor. The same assumption is often made when fitting the experimental data of the Q_0 vs. E_{acc} measurements. In reality, some slope is also observed in the ideal case, due to the decrease of the energy gap with increasing field (see Eq. 1.52). An example of discussion on how a more accurate calculation of R_S can be addressed, which generally involves complicated calculations and numerical methods, can be found in [89].

in the past in bulk niobium cavities [90]. The reason for this was found to be the presence of hydrogen in the cavity bulk, introduced by the chemical treatments, which would diffuse to the surface during cooldown and form niobium hydrides, known to be weak superconductors. Nowadays, this issue is considered to be fully controlled: high temperature cavity baking to reduce the amount of trapped hydrogen, and a fast cooldown between 300 and 100 K to minimize the "transit" time through temperatures at which the diffusivity of hydrogen into niobium is highest, are now standard procedures adopted to prevent the Q-disease.

Parameter	Description	Optimization
E_{acc}	Accelerating electrical field (or *gradient*)	Maximise
P_c	Power dissipated at cavity walls	Minimise
R_a	Shunt impedance	Maximise
Q_0	Quality factor	Maximise
G	Geometrical factor	Maximise
R_a/Q_0	Geometrical shunt impedance	Maximise

TABLE 2.1: Summary of cavity figures of merit.

2.3 Niobium-coated copper SRF cavities

In parallel with the development of SRF systems based on bulk niobium, the technique of sputtering niobium films onto the inner walls of copper cavities was pioneered at CERN for the upgrade of LEP-II [91], [92] and still is a well-established R&D branch at CERN and many different laboratories worldwide, such as INFN-LNL (Italy), JLAB (VA-USA), STFC (UK) and Cornell (NY-USA). Over the last three decades, high-β Nb/Cu cavities were developed and installed first at LEP-II (elliptical four-cell, 350 MHz) and subsequently at LHC (elliptical single-cell, 400 MHz) as they had already met the gradient requirements during the development for LEP; low-β structures were also successfully developed for ALPI (quarter-wave, 160 MHz) and HIE-ISOLDE (quarter-wave, 100 MHz). Depending on the application and on the coating technology progress status, different PVD techniques were applied for the coating of these cavities, with the ones more in focus being the bias diode sputtering in the early stages and DCMS in the more advanced phases of development.

The films studied in this thesis are developed with the long-term goal to improve the performance of the elliptical cavities. Extensive efforts are currently going on for the R&D of the Nb/Cu SRF system proposed at CERN for the FCC-ee, with HiPIMS being the coating technique of choice due to its capability of providing denser coatings [19], [93]. Both DCMS and HiPIMS techniques are introduced in Chapter 4.

Several reasons stood behind the choice to sputter-coat niobium on copper for SRF purposes, the first of all being the increased thermal stability of the cavity. At the time when the upgrade of LEP was in progress, the thermal breakdown of bulk niobium cavities still represented the main limit to the highest achievable gradient. As shown in Fig. 2.4, the thermal conductivity of OFE-grade copper (considering RRR = 150) is about 1 kW/m K [94] and a about factor 10^2 larger than the one of niobium at liquid-helium temperature, if compared to the data for RRR $\simeq$ 40, representing the typical niobium purity at the time of LEP-II. In order to screen the

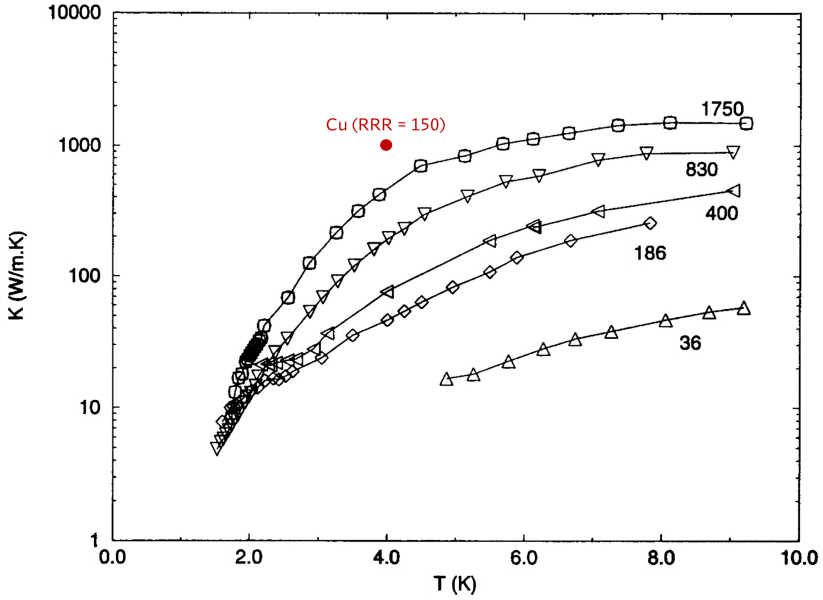

FIGURE 2.4: Thermal conductivity of bulk niobium at different RRR values (reproduced from [80]) with added data for OFE-grade copper [94].

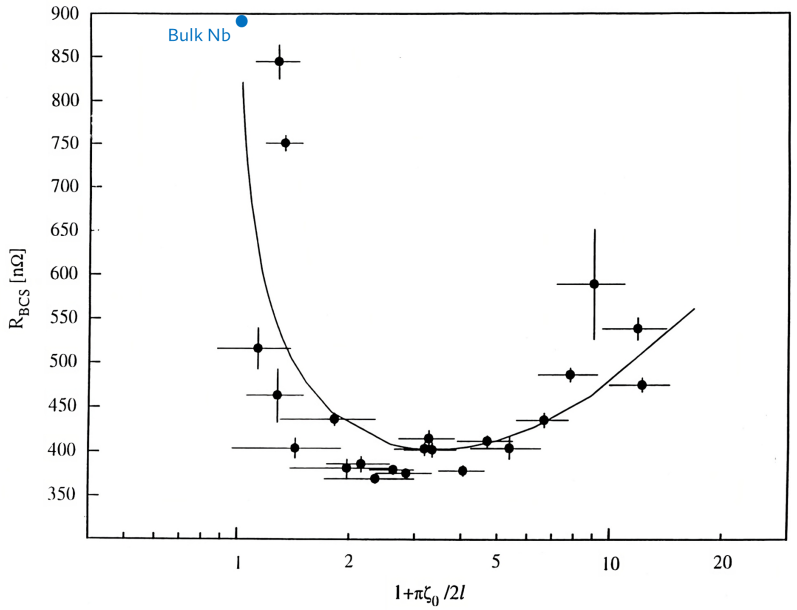

FIGURE 2.5: BCS resistance of niobium films as a function of the electron mean free path for a 1.5 GHz elliptical cavity at T = 4.2 K (reproduced from [14] with permission of Elsevier). Bulk niobium data added for comparison.

RF field, it is enough for the film thickness to be larger than the λ_L of niobium, so that a 1 µm thick film can already serve to the scope. The larger thermal conductivity of copper ensured the thermal stability of the niobium film during cavity operation to a point that thermal breakdown has not been observed in Nb/Cu cavities ever since. The cost mitigation introduced by the fact that copper is also much

cheaper than niobium was another driving factor for the development of Nb/Cu, especially considering the high number (288) of units needed for LEP-II. Furthermore, the sputtering route would leave open the possibility to investigate coatings of materials with higher T_c, such as A15 compounds (Nb_3Sn, V_3Si) or high-temperature superconductors, whose bulk form cannot be machined due to its brittleness. This option is discussed in Section 2.4.1.

During the development of a 500 MHz cavity tested and operated at PETRA [95], prior to the production of the LEP-II cavities, it was observed that Nb/Cu structures could provide higher Q_0 at low field than bulk niobium ones [92]. However, the same Q-value also decreased quickly with increasing field. Thanks to studies on 1.5 GHz single-cell elliptical cavity prototypes, the high Q_0 at low field for Nb/Cu was found to be related to the lower BCS surface resistance of the films with respect to bulk niobium [14]. In fact, the R_{BCS} of the films was found to be distributed mainly around the theoretical minimum expected between the clean and dirty limits discussed in Section 1.2, as shown in Fig. 2.5. Here the dependence from both the electron mean free path l and the coherence length ξ_0 is included in the abscissae. Advances in the chemical polishing procedures of the copper also provided smoother surfaces which resulted in the improved adhesion of the niobium film. Moreover, the surface resistance of the films was observed to be nearly unaffected by the Earth's magnetic field [14], allowing for the fabrication of simpler and cheaper cryostats which no longer needed magnetic shielding.

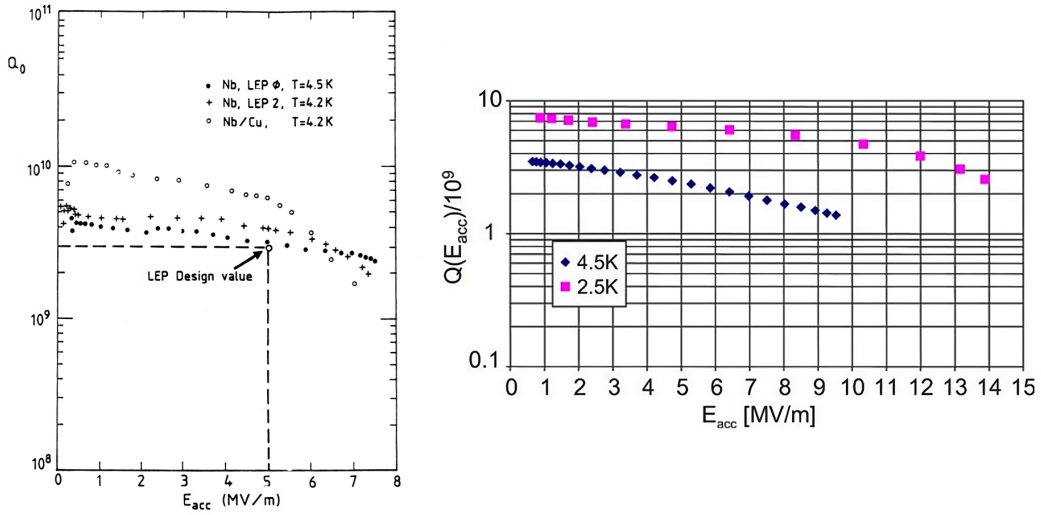

(a) (b)

FIGURE 2.6: Left: performance of the 352 MHz Nb/Cu prototype cavity for LEP compared to bulk niobium (reproduced from [96]). Right: performance of a 400 MHz Nb/Cu LHC cavity (reproduced from [10] with permission of Elsevier).

The newly acquired expertise resulted in an improved low-field Q_0 for the Nb/Cu cavities developed for LEP-II. These performed better than the bulk niobium counterpart up to a gradient of about 6 MV/m, after which the quality factor is again observed to decrease with increasing field. The same technology was later applied

for the production of the 400 MHz single-cell LHC elliptical cavities, although improvements in surface preparation and clean assembly procedures resulted in even increased accelerating fields, with the cavities reaching gradients of 10 MV/m. Also, the film superconducting properties, RRR and the low-field quality factor were observed to depend on the impinging angle of the target atoms during deposition [97], [98]. The RF performance of LEP-II and LHC Nb/Cu cavities compared to bulk niobium is shown in Fig. 2.6. Despite the significant advances in the development of the Nb/Cu technique, the decrease of the quality factor exhibited by these cavities is an unresolved matter and still represents a central research topic in the field. A summary of the main attempted explanations of the phenomenon, investigated causes and tackled experimental solutions is presented in the next Section.

2.3.1 Q-slope

The degradation of Q_0, today addressed as the "Q-slope", depends on the residual part of the surface resistance, which is thought to increase more strongly with increasing field in the case of films compared to bulk niobium. Several phenomena have been investigated and still are object of study, which might be connected to the increased resistance of the films. Some selected highlights from the theoretical and experimental research efforts made towards the understanding of the dissipative mechanism leading to the Q-slope are summarised and listed below.

- The Q-slope is treated as an intrinsic property of the film, due to its limited electron mean free path with respect to the bulk material, which can result in: a reduction of H_{c1} with consequent early nucleation of Abrikosov vortices [99]; a decrease in amplitude of the superconducting gap, as the supercurrent (and hence the RF field) increases, with the velocity at which the gap decreases depending on the film purity as indicated by the RRR [100]. Both mechanisms would lead to an increase of the film surface resistance.
- *Thermal runaway models:* the dissipated power is assumed to depend on the temperature difference between the inside (the RF side) and the outside (the liquid helium side) of the cavity and to increase proportionally to the thermal boundary resistance, with emphasis on localised film detachment or void areas at the Nb/Cu interface where the thermal resistance would increase and enhance the loss mechanism [101], [102].
- *Weak link models:* the polycrystalline niobium film is modeled as a network of intra-grain Josephson junctions, that is, the grain boundary is described as a weak superconducting link at which the supercurrent exceeds its critical value leading to dissipation [103], [104].
- *Trapped flux model:* possible film impurities represented by noble gas atoms trapped during the coating process are assumed to act as pinning centers for the magnetic flux lines [14], [105].

To this day, none of the proposed models has described completely the dependence of the quality factor on the field amplitude, nor the experimental methods have significantly controlled the issue, so that fixing the Q-slope is still an open task.

2.4 Materials and power consumption

The appeal of superconductors as RF materials mostly relates to their surface resistance: compared to the surface resistance of normal conductors, it can be up to a factor 10^5–10^6 smaller, resulting in quality factors which are 10^5–10^6 higher at typical accelerator RF frequencies. The employment of superconducting materials becomes beneficial for accelerators operating in continuous-wave (CW) mode or at high RF duty cycles, mitigating the power dissipated by the cavity during operation. Even so, when it comes to power consumption several efficiency factors must be taken into account for the mains to RF power conversion, which are different for normal conducting and superconducting cavities. For example, unlike normal conducting ones, superconducting cavities must be operated at cryogenic temperatures. This aspect increases the total required AC power, due to the additional one needed to run the cryogenic system, and introduces additional costs. The duty factor, shunt impedance and beam current also play a role.

In Table 2.2 the Q_0, dissipated power per unit length and AC power consumption are indicated for a 500 MHz superconducting and normal conducting resonator performing at 1 MV/m and 5 MV/m. Despite the power dissipation per meter is reduced by a factor 4×10^4 in the superconducting case, it is possible to notice that the power consumption is reduced by a factor ~ 200 by only taking into account the cryogenic efficiency.

In SRF based accelerators operated in CW mode, a major contribution to the power consumption is still coming from the wall-plug power needed to cool down the dissipated RF power. In good approximation, this power can be expressed as:

$$P = \frac{V_{\mathrm{acc}}^2}{(R_{\mathrm{a}}/Q_0)Q_0} N_{\mathrm{cav}} \eta_{\mathrm{cryo}}, \tag{2.11}$$

where N_{cav} is the number of cavities. The aforementioned cryogenic efficiency η_{cryo} results from the combined technical (η_{tech}) and Carnot (η_{C}) efficiencies, and can be explicitly expressed as:

$$\eta_{\mathrm{cryo}} = \eta_{\mathrm{tech}} \cdot \eta_{\mathrm{C}} = \eta_{\mathrm{tech}} \frac{T_{\mathrm{op}}}{300\,\mathrm{K} - T_{\mathrm{op}}}, \tag{2.12}$$

where T_{op} represents the operation temperature of the cavity. The technical efficiency can approach 0.3 for large, modern systems. The typical cryogenic efficiency of modern SRF systems corresponds to about $\eta_{\mathrm{cryo}} = 0.0042$ for operation at 4.2 K. The resulting power can be in the order of a few hundred MW for a lepton collider with a number of about 10^4 required cavities operated at 1.8 K (temperature at which $\eta_{\mathrm{cryo}} \simeq 0.0013$) and a target centre-of-mass energy of about 500 GeV, increased by a factor $10 - 10^2$ with respect to facilities involving a smaller number of cavities and targeting lower energies. Therefore, the need to limit the power consumption is pushing the interest toward those technologies for which operation at higher temperature ($\geq$ 4.2K) is envisaged, resulting in an increased Carnot efficiency. However, the focus must at the same time stay on the target performance in terms of Q_0 and maximum attainable gradient.

Highly valuable candidates toward this goal are compound materials like Nb_3Sn, NbN, NbTiN, V_3Si, Mo_3Re and MgB_2, the first three of them being the most studied to date. These materials, because of their mechanical properties, especially the brittleness, are only employable in the form of films. Although higher Q_0 values than 10^{10} are predicted for these materials at 4.4 K, early flux penetration at film defects is

currently limiting the resulting accelerating gradients. One possible way to bypass this issue is offered by multilayered (S'IS) coatings, in which a high-temperature superconductor (S') film of thickness ≤ 1 µm is deposited on a nm-thick insulator (I) layer, in turn deposited on a thick niobium (S) substrate [106].

For Nb_3Sn two are the main developed technologies: vapour diffusion [24] and sputtering techniques, both briefly discussed in the next Section. In the case of S'IS structures, Atomic Layer Deposition (ALD) [107] is a promising technique for the coating of materials like NbN, NbTiN and MgB_2 which allows to control precisely the growth process and the film thickness. Although the progress status is less advanced than for the other cavity coating techniques, it holds good long-term potential for the development of cavities operated at $T > 4.2$ K.

	Resonator type	
Parameter	Superconducting	Normal conducting
Q_0	2×10^9	2×10^4
R_a/Q_0 (Ω/m) at $f = 500$ MHz	330	900
P/L (W/m) at $E_{acc} = 1$ MV/m	1.5	5.6×10^4
AC-power (kW/m) at $E_{acc} = 1$ MV/m	0.54	112
AC power (kW/m) at $E_{acc} = 5$ MV/m	13.5	2.8×10^3

TABLE 2.2: Comparison between the typical AC power consumption of a normal conducting and a superconducting 500 MHz resonator (reproduced from [32] with permission of John Wiley and Sons).

2.4.1 The Nb_3Sn option

Nb_3Sn is an inter-metallic superconducting material belonging to the class of A15 compounds, which have always been of interest for SRF applications due to their high critical temperature, usually a factor 2 larger than the critical temperature of niobium (9.2 K).

The most common technique to form the Nb_3Sn phase is via high-temperature tin vapour diffusion into a bulk niobium substrate [24], [108], [109]. Nb_3Sn 1.3 GHz cavities produced by vapour tin diffusion are expected to have a Q_0 of about a factor ten larger than bulk niobium cavities (about 10^9) at T = 4.2 K [110], which makes the material attractive. For 650 MHz single-cell resonators this technique has delivered Q values $> 10^{10}$ at 20 MV/m. However, the repeatability of a precise stoichiometry and the control of known issues such as magnetic flux trapping, cracking due to brittleness and thermo-current generation during cooldown represent major challenges. On top of this, vapour diffusion is only suitable to bulk niobium substrates.

Advanced sputtering techniques, such as HiPIMS, are being applied [26], [27] to the deposition of Nb_3Sn in the attempt to introduce an alternative production technique to vapour diffusion. So far the technique has achieved promising results on small samples deposited on copper and dielectric substrate. The advantages of this technique are mainly found in the control of the stoichiometry and the possibility to deposit a wide range of compounds other than Nb_3Sn on different substrates. On the other hand, both the film quality and thickness depend on the complexity of the substrate geometry [19].

As mentioned in the previous Section, beyond Nb_3Sn, other A15 materials such as V_3Si, Nb_3Al, the Mo-Re systems, nitrides like NbN and NbTiN, or MgB_2 are of

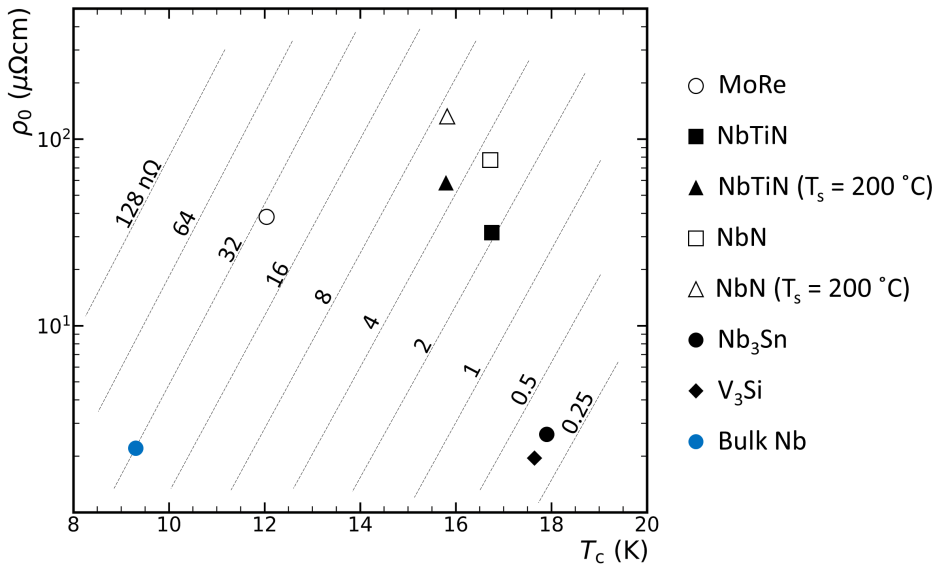

FIGURE 2.7: Lines of equal R_{BCS} calculated as a function of the residual resistivity ρ_0 and the critical temperature T_c at T = 4.2 K and 500 MHz. The substrate temperature T_s is indicated for the coatings produced at low temperature. (Reproduced from [111] with permission of Springer Nature).

interest for the application. It must be taken into account that, depending on the production technique, these materials might introduce further complications. A known example is given by the need, for A15 materials, to be deposited on a high-temperature substrate in order to properly form the A15 phase and limit the film granularity. When depositing on copper, this will most likely promote the diffusion of copper from the substrate into the growing film, when conventional sputter-coating techniques such as DCMS are applied. Also in this case the HiPIMS technique introduces some advantages, as it allows the transfer of the energy needed for the formation of the A15 phase via the impinging target ions in the form of kinetic energy, so that one can explore the possibility of coating on copper while circumventing the issue of copper inter-diffusion.

The typical values for some of these compounds are also shown so that it can be seen as, for a given operating temperature, the best RF performance are provided by the materials with both high T_c and low ρ_0, including Nb_3Sn. However, the BCS prediction for the surface resistance of a superconductor at low temperature can differ from the actual one due to the additional residual losses and depends on structural condition of the real surface, as previously discussed.

In Fig. 2.7 the calculated BCS surface resistance is shown as a function of T_c and of the residual electrical resistivity ρ_0 [111] at T = 4.2 K and 500 MHz.

2.5 General guidelines for cavity development

Following the requirements set by the accelerator specifications and by the beam characteristics, the final cavity design often results from a trade off among the choice of the optimal material, the fabrication technique, the geometry and the operating frequency. To different degrees, these aspects are all interconnected, making the design of the accelerating system of a particle accelerator all but a trivial task. The next

generation of particle accelerators will require RF systems whose specifications are beyond the state of the art, hence the R&D in the field is still advancing on both the normal conducting and the superconducting RF technologies. For the latter, the focus is on bulk niobium and thin-film (including high-temperature) superconductors, with the general goal to push the accelerating field delivered by a resonator at the highest possible quality factors, while limiting the power consumption.

In the past five decades, the advances in bulk niobium technology have made it possible to reach, at a high level of reproducibility, accelerating gradients of about 35 MV/m with Q values of $\sim 2 - 5 \times 10^{10}$ at 2 K operation temperature. Bulk niobium is approaching nowadays its limit performance [8], so that the search for cost-effective and reliable alternative technologies is vital for the advancement of the SRF accelerating systems. The pursued solutions all involve the development of thin-films, in the attempt to:

- **reduce the amount of employed superconducting material**: a film thickness in the order of 1 µm can theoretically replace the bulk material as the SRF performance is dominated by the properties of a surface layer a few penetration depths thick; combining this with the use of copper as a substrate increases the thermal stability of the cavity and allows easier chemical treatments in terms of hazardous substances and waste with respect to the ones needed for bulk niobium;
- **increase the operation temperature for same Q**: the employment of new superconductors such as alloys and A15 compounds also enables operation at higher temperatures ($\geq$ 4.2 K) and at the same time preserves a quality factor in the order of 10^{10} up to 22-24 MV/m on bulk niobium substrates; the major challenge is now to reproduce the same results on copper substrate;
- **increase the maximum operation gradient**: the development of multi-layer coatings showing higher critical fields than niobium represents a promising technique toward this end.

An ideal solution should combine all three goals. To this aim the priority should be given to film deposition techniques which can be scaled up from small, flat samples to complex cavity geometries, starting from the reproduction of the observed properties on 1.3 GHz prototypes. Promising methods are represented by plasma-assisted physical vapour deposition (PVD) methods (HiPIMS, DCMS), chemical vapour deposition (CVD), atomic layer deposition (ALD) and electro-deposition [112].

On top of these aspects, the optimisation of the fabrication and surface preparation of normal metal substrates, the development of high-efficient, cost-mitigating innovative cooling techniques and the establishment of specialised infrastructures and high-throughput testing methods and routines represent key factors for the success of the future development of the SRF accelerating technologies.

The state of the art is discussed in more detail in Chapter 3, for the specific case of the Future Circular Collider study.

Chapter 3

Future Circular Collider

In this Chapter, the Future Circular Collider study is introduced, with the project being summarized in Section 3.1. The requirements for the SRF cavities of the project's first stage, the FCC-ee, are then discussed in Section 3.2. Finally, Section 3.3 remarks on the sustainability aspects of the FCC-ee.

3.1 The project

The design studies for the Future Circular Collider (FCC), a lepton/hadron collider of 80-100 km circumference, started in 2014. The research activity within the FCC program focuses on the development of the technology needed to establish the next generation of particle colliders at CERN, with the goal to extend the fundamental research done at the LHC towards New Physics investigations [113].

Inspired by the success of the LEP and LHC consecutive programs, FCC builds on this legacy and on the experience of 60 years of operating colliding beam storage rings. The current phase, the FCC Feasibility Study [114] started in November 2020 and will last until the release of a Feasibility Study report in 2025/2026. The Feasibility Study addresses the key requests stated in the 2020 Update of the European Strategy for Particle Physics (ESPP) [115], stating that *"Europe, together with its international partners, should investigate the technical and financial feasibility of a future hadron collider at CERN with a centre-of-mass energy of at least* 100 TeV *and with an electron-positron Higgs and electroweak factory as a possible first stage. Such a feasibility study of the colliders and related infrastructure should be established as a global endeavour and be completed on the timescale of the next Strategy update."*.

The FCC integrated program covers an extensive, long-term physics research plan to be realised in two stages: an electron-positron collider, FCC-ee [15] as first stage, for the production of Z, W, Higgs bosons and top quarks at the highest luminosity, and a hadron collider (proton or heavy ion with electron-hadron option), FCC-hh [116] as second stage toward the high energy frontier. FCC-ee would operate at multiple centre-of-mass energies, spanning from 90 GeV to 400 GeV, while the goal of the FCC-hh is to reach 100 TeV as centre-of-mass collision energy (for comparison: LHC has reached 13.6 TeV during Run 3). A potential time frame to start the construction of the FCC is considered to be in the years 2026-2035.

Most of the R&D activities within the FCC program are currently mainly centered on the realisation of the FCC-ee, with focus on efficiency optimisation, development of precision diagnostic tools, and achievement of the end performance in terms of beam current and luminosity. Not only the pursue for highest efficiency, but also the mitigation of the costs and of the environmental impact of the project are central to the choice of technologies for the FCC-ee. Among these, high-Q superconducting RF cavities for the 400–800 MHz range are a crucial component.

The FCC-ee conceptual design report (CDR) [15], published in 2019, initially described the baseline accelerator design with a circumference of 97.75 km and two collision points. In 2021 the design was upgraded to a circumference of 91.2 km, due to an established lower-risk ring placement, which would be compatible with either two or four collision points. For this reason the CDR is under adaptation with the new re-optimised machine parameters.

A possible layout of the lepton collider is shown in Fig. 3.1. The green ring indicates the booster, while the collider ring is indicated in blue. Two experiment sites (PA and PG, with the two additional optional ones PD and PJ) and four technical sites (PB, PF, PL and PH) are foreseen, including the SRF systems. The main specifications of the FCC-ee, updated with respect to what presented in the CDR, are summarised in Table 3.1 with emphasis on the main RF requirements and accounting for the possibility of two or four (in parentheses) interaction points. In fact, the two experiment sites initially proposed in the CDR could also become four depending on the optimisation of design and costs.

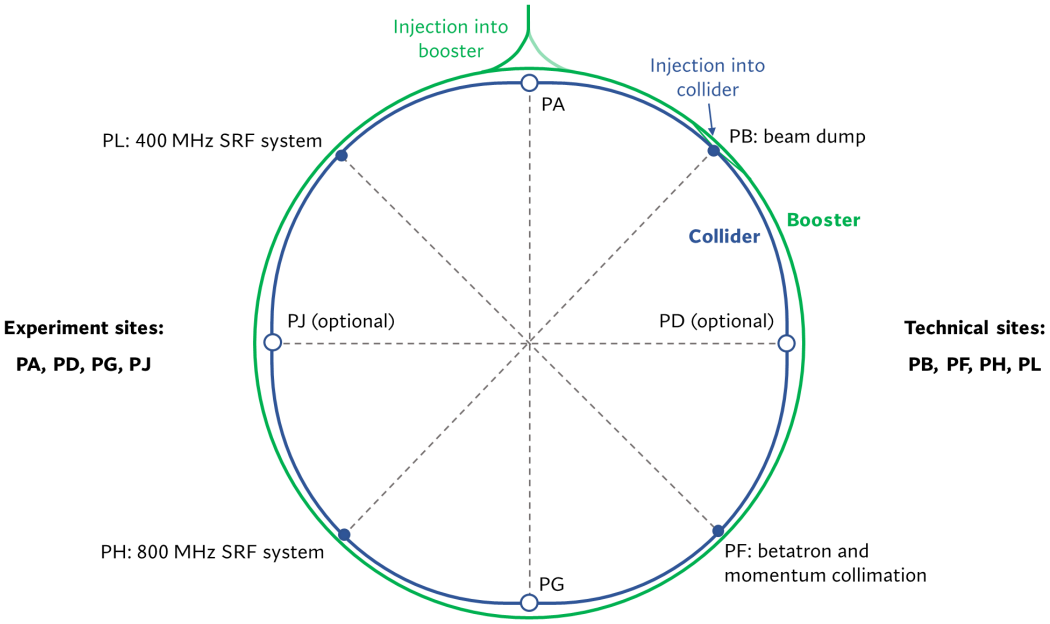

FIGURE 3.1: Schematics of a possible layout of the FCC-ee [117].

3.2 SRF cavities for the FCC

In the attempt to reach higher particle energies, it is essential to increase the accelerating gradient in order to keep the facility to a reasonable size. As discussed in Section 2.4, as a general guideline, pushing the quality factor of the cavities could lower the electric power required for the cryogenic plants and/or decrease the size of the system. The synchrotron losses are expected to be in the order of 50 MW per beam for the FCC-ee [15] and must be compensated by the SRF system at affordable energy consumption. Affordable RF systems at industrial scale must also be pursued via the optimisation of the fabrication costs.

The design of an efficient and cost effective system of high Q-value SRF cavities for the 400-800 MHz range represents one of the major challenges for the completion

of the FCC-ee, for which covering the different physics scenarios is also a challenge. Three sets of elliptical cavities are planned to be developed, with the dedicated R&D directed towards the production of:

- 56 single-cell 400 MHz Nb/Cu cavities to be installed at PL, for high-current low-voltage beam operation at the Z production energy;
- 112 and 280 two-cell 400 MHz Nb/Cu cavities to be installed at PL, at the W and Higgs operation energies respectively;
- a complement of 280 - 400 two to five-cell 800 MHz bulk niobium cavity system to be added at PH, for low-current high-voltage operation at the top-quark operation energy.

Alternative designs are also being explored, such as novel 600 MHz slotted waveguide elliptical (SWELL) cavities [118], which might have the advantage of mitigating the intervention activities between operating points.

	Operation mode			
Parameter	**Z**	**W**	**H**	**$t\bar{t}$**
Circumference (km)	91.2			
SR power/beam (MW)	50			
Luminosity/IP (10^{34}/cm^2 s)	181	19.5 (17.3)	7.5 (7.2)	1.3 (1.25)
Beam energy (GeV)	45.6	80	120	182.5
Beam current (mA)	1400	135	26.7	5
Bunches/beam	16600 (8800)	1120	380 (336)	44 (42)
Energy loss/turn (GeV)	0.039	0.37	1.87	10
SRF system parameter	**One RF site**			**Two RF sites**
RF frequency (MHz)	400	400	400	400 – 800
RF voltage (GV)	0.12	1	2.48	4 – 7.76
Accelerating field (MV/m)	5.72	11.9	2	2 – 5
Cavities	56	112	280	280 – 400
Cells/cavity [Material]	1 [Nb/Cu]	2 [Nb/Cu]	2 [Nb/Cu]	2 – 5 [bulk Nb]
Total number of cryomodules	14	28	70	70 – 100
Operation temperature (K)	4.5	4.5	4.5	4.5 – 2

TABLE 3.1: Main specifications of FCC-ee as presented at FCC Week 2022 [119] (updated with respect to the CDR) with emphasis on RF specifications.

3.2.1 R&D on thin-film coated copper cavities

The Accelerator R&D Roadmap of the ESPP 2022 [120] has clearly defined the goals for the thin-film research oriented to the development of SRF cavities [112]. They can be summarised into the following areas:

- **Nb/Cu**: reduce fabrication costs and reach bulk niobium RF performances on Nb/Cu cavities via R&D based on 1.3 GHz prototypes, with a target performance of $Q_0 = 10^{10}$ at $E_{acc} = 20$ MV/m first and 30 MV/m later on;

- **thin-films beyond Nb**: advance the performance of new superconductors (A15, MgB_2) thin films on copper for saving of operational costs, and reach a performance of $Q_0 = 10^{10}$ at $E_{acc} = 15$–$18\,MV/m$ and 4.2 K for Nb_3Sn/Cu 1.3 GHz prototype cavities, whose proof of principle has been already demonstrated for Nb_3Sn on bulk niobium; demonstrate the feasibility of MgB_2 coatings on 1.3 GHz cavities; test the influence of mechanical deformations on the RF performance of the coatings;

- **multi-layer coatings**: push the multi-layer coating on copper technology to demonstrate improved performance on a 1.3 GHz cavity, in the order of 30–50% increase in the maximum E_{acc} and a factor of two in Q_0;

- **substrate refinement**: optimise the production techniques of copper cavities via the development of seamless 1.3 GHz copper substrate (machined from a monoblock, hydroformed or electroformed) to be scales down to 400 MHz structures; optimise air-stable chemical treatments, such as electropolishing (EP), buffered chemical polishing (BCP), heat treatments, passivation layers, etc., for the preparation of the copper surface prior to film deposition;

- **innovative substrate and cooling techniques**: develop copper-aluminium alloy-based 1.3 GHz prototype substrates toward optimal thermal and mechanical response (similar to niobium at 4.2 K) and controlled surface roughness within 1 µm; reach bulk niobium performance for niobium films first, and new superconductors (A15, MgB_2) later on, deposited on electroformed and 3D printed 1.3 GHz substrates at 4.2 K; demonstrate effectiveness of conduction cooling techniques;

- **infrastructures and high-throughput testing**: establish dedicated buildings for thin-film specific infrastructures (coating facilities, clean rooms, chemistry pools, rinsing facilities, assembly points, etc.); establish systematic methods for assessment of the superconducting properties (DC and RF), for surface characterisation and cold test diagnostics for both flat samples and prototype cavities; establish high-throughput RF test methodologies and facilities to ensure cavity performance repeatability in preparation to series production.

This plan must be pursued for the SRF needs of the future European projects to be met, included the FCC, and will require synergy between the existing R&D, testing and handling laboratories (DESY, CEA, CNRS, CERN, INFN, to name a few) for the coordination of activities toward the common goal.

3.2.2 Status of the Nb/Cu route at CERN

The advantages of choosing the Nb/Cu technology over the bulk niobium one, among which the material cost mitigation, lowered power consumption and improved thermal stability at cryogenic temperatures, as well as the issue represented by the Q-slope, are discussed in Section 2.3. The expertise built on the successful implementation of Nb/Cu SRF cavities for both LEP-II and the LHC is driving the R&D activities towards the goal of delivering a functional 400 MHz prototype by the year 2025.

The RF performance of the LHC spare cavities is shown in Fig. 3.2, where the required specification for a single-cell 400 MHz FCC cavity is also indicated [121] along with the state of the art R&D at CERN. In order to meet the specifications, it is imperative to cure the slope of the LHC cavities. The task is being tackled via parallel R&D

activities, including the optimization of the cavity design [122]; the study of seamless manufacturing processes (machining from monoblock, hydroforming, electroforming) for 1.3 GHz prototypes, the optimisation of welding techniques such as internal electron beam welding, the study of the influence of the manufacturing method on the copper substrate purity [123]; the optimization of EP as surface treatment prior to coating [124]; the optimization of the HiPIMS coating technique under study on small samples and on 1.3 GHz prototypes via the assessment of the film morphology, superconducting properties and RF performance [19], [119], [125]; the study of coating materials alternative to niobium such as Nb_3Sn [27]; the strengthening of cavity diagnostics tools and film quality assessment methods [126], [127].

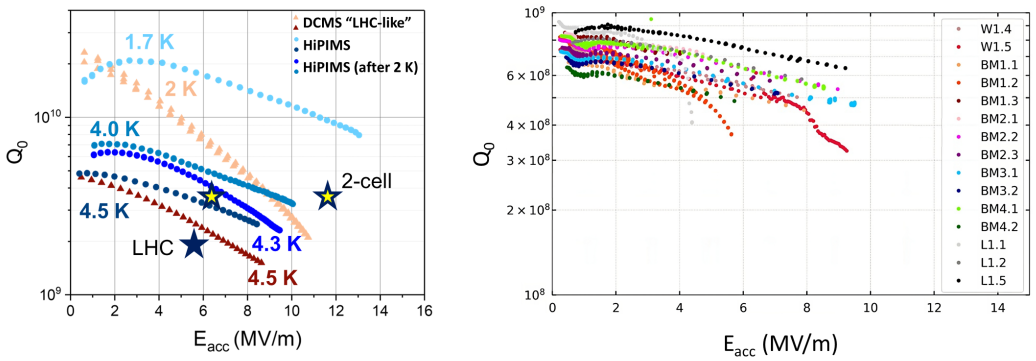

(a) (b)

FIGURE 3.2: (a) State of the art performance of single cell Nb/Cu 400 MHz elliptical cavities coated via DCMS and HiPIMS and tested at different temperatures. The stars indicate the required specifications for LHC and for FCC-ee (one and two-cell) [121]. (b) State of the art R&D for Nb/Cu 1.3 GHz prototypes [125].

3.2.3 R&D contribution within this thesis work

The work presented in this thesis is also framed into the R&D efforts ongoing at CERN. Its contribution is given by the establishment of a test station for the measurement of the critical temperature of superconducting thin-film small samples deposited on copper, for the quality assessment of the film on its substrate [128]; the demonstration of the reverse-coating concept, start from samples of simple geometry such as flat disks, toward the application to the production of seamless Nb/Cu cavities [28]; the study of the properties of small Nb_3Sn film samples deposited on copper via the HiPIMS coating technique.

3.3 Considerations on sustainability

Among all the proposed Higgs and electroweak factories, the FCC-ee is the most sustainable as it foresees the lowest energy consumption for a given total integrated luminosity [129]. Nevertheless, scarcity of resources and climate change caused by the excessive exploitation of fossil energy must be central aspects in the running of the existing scientific facilities and in the choice of technologies to establish the future ones. Until now, the electric power consumption relies primarily on fossil fuels, and since carbon-neutral sources are still under development it is mandatory

to focus on the realisation of sustainable concepts, as the increased performance of the future accelerators also anticipates an increased energy consumption.

The energy efficient technologies toward which the R&D efforts are investing cover several areas [130]: low loss superconducting resonators, efficient RF sources [131]–[133], low-dissipation (e.g. permanent) magnets [134], highly efficient cryogenic systems for heat removal caused by beam induced energy deposition such synchrotron radiation [135], superconducting electrical links [136] and use of heat pumps. Concerning the superconducting resonators, the focus is on the reduction of the cryogenic losses, which can become significant for accelerators in CW operation. High priority is given to the improvement of the quality factor and on the development of new superconductor coatings. As an example, Nb_3Sn which has shown good performance [137] at 4.5 K, temperature at which the cryogenic efficiency is greatly improved, still providing reasonable Q values.

Eventually, the analysis of the carbon footprint of a new accelerator facility during the design phase is vital to the assessment of the energy consumption for construction and operation. Actions toward the mitigation of water consumption, the choice of environmental-friendly materials, introduction and compliance with certifications of source materials and waste minimization must all be general guidelines, as thoroughly discussed in [138].

Chapter 4

Thin film deposition via magnetron sputtering

In the following, the PVD techniques of DC Magnetron Sputtering (DCMS) and High Power Impulse Magnetron Sputtering (HiPIMS) are briefly introduced. The thin film samples studied in this thesis are produced via HiPIMS, however, the basics of DCMS are given here as preparatory to the understanding of the HiPIMS technique.

4.1 General remarks

The vapour deposition techniques employed for the production of thin films can be categorised into two main groups, depending on the nature of the underlying process: chemical vapour deposition (CVD) and physical vapour deposition (PVD).

In CVD, the substrate is exposed to one or more precursors in the gaseous form, which react at the substrate's surface to produce the final material. Examples of CVD are thermal CVD, plasma enhanced CVD and atomic layer deposition (ALD).

The technique of PVD relies on solid or molten sources from which the atoms to be deposited are extracted via a variety of physical processes. Most commonly, either thermal energy is imparted to the source causing the atoms to leave the surface (evaporation) or kinetic energy is provided to the source atoms by bombarding with energetic ions so that they are ejected from the surface (sputtering). In both cases, thanks to the imparted energy, the source atoms are transferred to the substrate resulting in the film growth.

To initiate and sustain a sputtering process, a noble gas plasma must be generated to bombard the source material. The plasma is ignited by applying a cathodic potential to the source (also addressed as *target*), employed in solid bulk form: by doing so, primary and secondary electrons are emitted from the surface and ionize the gas atoms by colliding with them in an avalanche process. The gas ions impact the target surface and remove material in the form of atoms, ions or molecules, which travel toward the substrate in the low-pressure environment. The process must take place in a low-pressure environment, to facilitate the transfer of the sputtered target species. The effectiveness and stability of the process result from complex balance of several factors, such as the atomic masses of the gas and of the source material, the surface binding energy of the source material and the plasma regime. A comprehensive treatment of the details of thin film deposition techniques can be found in [139].

4.2 DC Magnetron Sputtering (DCMS)

In DCMS, a magnetron is placed below the target so that the free electrons, emitted when a DC cathodic potential is applied, are confined by the magnetic field to stay close to the surface after collision with the noble gas.

A graphical representation of a DCMS process with planar configuration is given in Fig. 4.1, where a planar target is placed in front of the substrate holder, usually at anode potential or grounded. The magnetic field can be either generated by permanent magnets or electromagnets, whose arrangement below the target defines the shape of the field lines. When the field lines are closed, the magnetron is said to be in the "balanced" configuration (which is the most commonly employed in DCMS) and create a field tunnel which confines the electrons emitted from the target close to its surface. In the region where the electric and magnetic fields are perpendicular to one another, electrons drift under the Lorentz force in a cycloidal hopping motion along the tunnel track length, which takes the name of "racetrack". Because ionization of the sputtering gas is most efficient above the racetrack, the plasma is most intense there.

In DCMS, electron confinement leads to an increased electron path length, which results into a more efficient gas ionization process hence higher deposition rate in DCMS with respect to other sputtering processes [139]. However, this also causes the selective erosion of the target, which will be more depleted in the areas corresponding to the plasma localisation, resulting in underutilisation of the target material and the typical "track" erosion. A Nb_3Sn target leaning on a circular magnetron is shown in Fig. 4.2a, with the localised plasma generated by the same magnetron visible in Fig. 4.2b (view from top). Fig. 4.2c shows the erosion track left on a niobium target by a plasma of the same kind as the one shown in Fig. 4.2b.

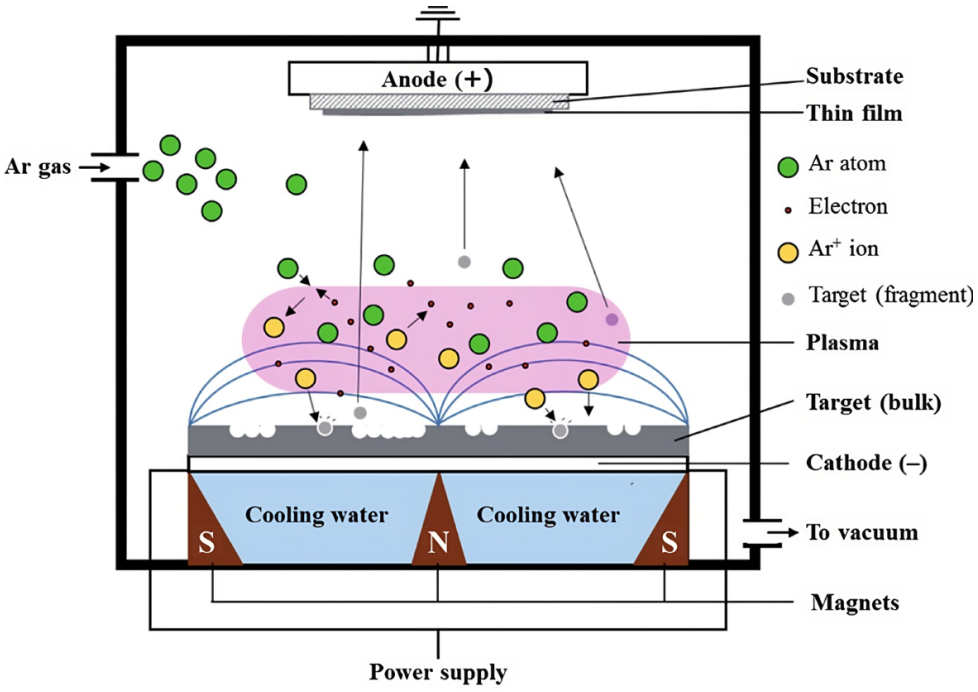

FIGURE 4.1: Planar DCMS configuration with elliptical field lines. Readapted from [140].

The sputtering process itself takes place when the energy of the gas ions passes a threshold energy (E_{th}) which depends on the surface binding energy (E_b) of the target material and on the atomic mass of the employed gas (M_i) and of the sputtered species (M_a). The threshold energy can be expressed as:

$$E_{th} = E_b \begin{cases} \frac{1+5.7(M_i/M_a)}{\Lambda} & \text{for } M_i \leq M_a \\ \frac{6.7}{\Lambda} & \text{for } M_i > M_a \end{cases} \tag{4.1}$$

where $\Lambda = \frac{4M_iM_a}{(M_i+M_a^2)}$ is the energy transfer factor. The number of atoms sputtered per impacting ion takes the name of sputter yield $Y(E)$, and mostly depends on the cathode/target voltage which determines the kinetic energy of the gas ions.

The energy of the sputtered material is independent on the energy of the incident ions, and is described by the Thompson formula [141], expressed in terms of differential sputtering yield $Y(E)$ of atoms sputtered with ejected energy E as:

$$Y(E)dE \propto \frac{1-\sqrt{(E_b+E)/\Lambda E_0}}{E^2(1+E_b/E)^3}dE\,, \tag{4.2}$$

for ions incoming with normal incidence. The sputtered atoms move to the substrate where they finally deposit as adatoms to form the thin film over time.

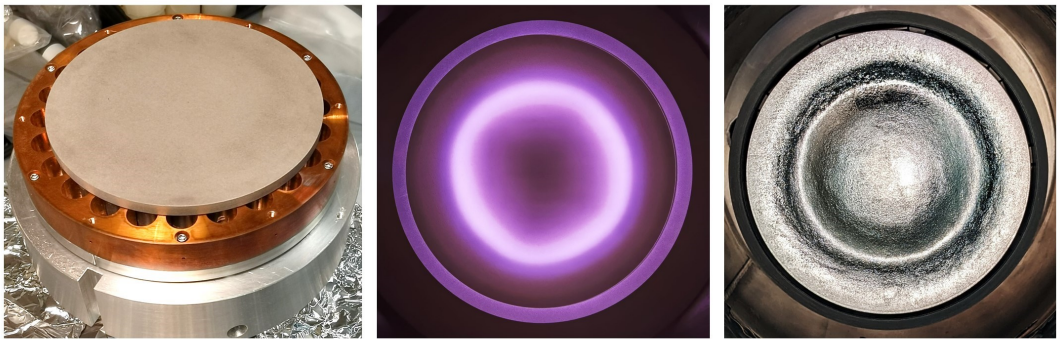

(a) (b) (c)

FIGURE 4.2: (a) Nb_3Sn target leaning on a circular magnetron employed for film production at INFN National Laboratories of Legnaro (INFN-LNL Italy). (b) Top view of an argon plasma generated by the same magnetron as in (a). (c) Erosion track on a niobium target, also courtesy of INFN-LNL.

4.3 High Power Impulse Magnetron Sputtering (HiPIMS)

Magnetron sputtering can also be performed in AC regime, as in the case of HiPIMS: instead of applying a DC potential to the target/cathode and the substrate/anode, the power is released in pulses of fixed length and frequency which also define the process duty cycle. The single pulse is addressed as "main pulse".

The time averaged power delivered in a HiPIMS process is comparable to that of a DCMS process, although the peak power and current at the cathode during the pulse can be a factor 10^2 larger than the average [142]. This peak current leads to an increase in the plasma density and a larger cross-section for collisions between the sputtered target atoms and the free electrons. Due to this, a large fraction of

the sputtered atoms is ionised, which is also known as one of the advantages of HiPIMS. In fact, the ionised atoms from the target can be accelerated towards the substrate [143], [144] by applying a bias to it. This causes thin films produced via HiPIMS to exhibit higher density and smoother surface than the ones produced via DCMS [145].

It is also shown that the addition of a positive voltage pulse immediately after the main pulse can further improve the film density and promote homogeneous deposition on substrates positioned at grazing angle with respect to the target surface [18], [19]. The positive pulse technique, also known as bipolar-HiPIMS, turns out to be a possible solution whenever applying a bias to the substrate is not possible, as in the case of large objects such as SRF cavities, which are typically grounded during the sputtering process.

A typical HiPIMS process with and without positive pulse is shown in Fig. 4.3. The voltage (full lines) and current (dashed lines) signals are shown in the case of HiPIMS without (blue) and with (red) positive pulse. Given the high power involved, typical HiPIMS duty cycles are small (i.e. 0.1 to 5% with pulse lengths of 10 – 200 µs) to prevent excessive heating of the target and magnet damage. As a consequence, a HiPIMS process will exhibit lower deposition rate than a DCMS process for the same average power [146]. Short pulse lengths and high current densities are found to increase the ionization efficiency [147], the ionised species mostly consisting of sputtering gas ions immediately after the application of the pulse, and of target material ions as the current approaches its peak [148].

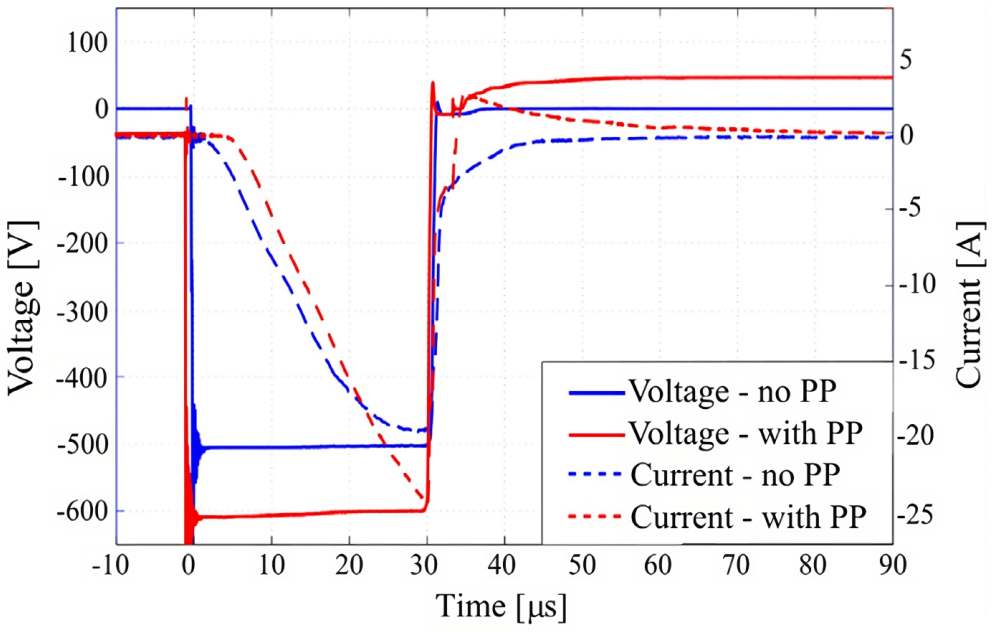

FIGURE 4.3: Applied voltage pulse (full line) of 30 µs and corresponding discharge current (dashed line) for HiPIMS without positive pulse or PP (blue), and with PP (red) of +50 V and 200 µs. Reproduced from [19].

4.4 Deposition parameters and film properties

The structure of the deposited film can be adapted by adjusting the deposition conditions. This is well represented in structure zone diagrams (SZD), the most recent of all being provided by Anders [149] and including the effects on the thin film structure by energetic PVD sputtering processes such as HiPIMS.

The diagram, shown in Fig. 4.4, chracterises the different growth zones of a thin film by the generalised temperatureT^* and the particle energy E^* as variable process parameters, as well as the relative film thickness t^* [149].

The generalised temperature $T^* = T_h + T'$ corresponds to the homologous temperature $T_h = T_s/T_m$ [150] plus a shift T' caused by the potential applied to the particles arriving on the surface, with T_s the substrate temperature and T_m the melting temperature of the deposited material. E^* is the energy including displacement and heating effects caused by the kinetic energy of bombarding particles and t^* is the relative film thickness, which can also go negative in case of ion etching.

Four zones can be identified in the diagram, each one corresponding to a different film morphology as described in Fig. 4.4.

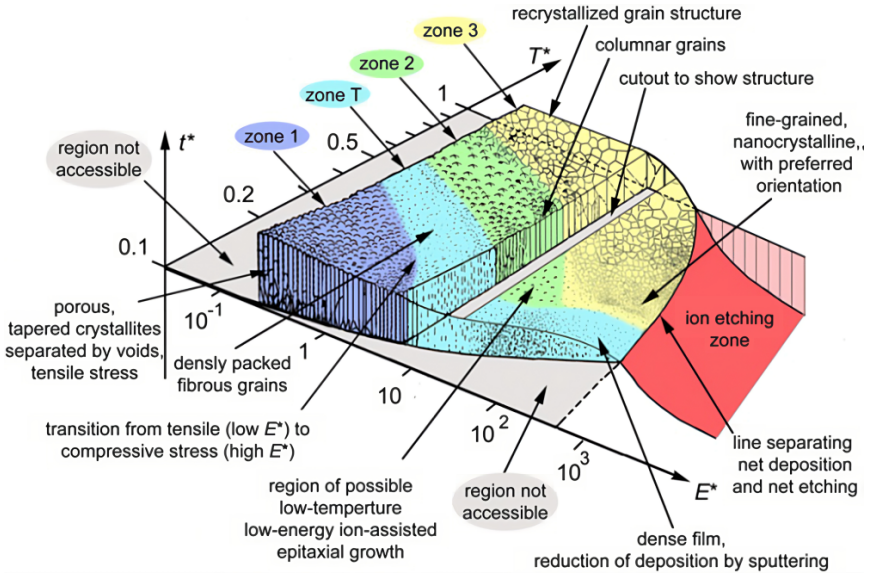

FIGURE 4.4: Structure zone diagram applicable to energetic deposition, the numbers on the axes are for orientation only. Reproduced from [149] with permission of Elsevier.

The influence of the deposition conditions on the film structure is briefly described in the following:

- **substrate temperature:** the adatom mobility increases as the process temperature is increased, promoting the diffusion of the deposited species and resulting in increased grain size and a denser film;
- **deposition pressure:** low base pressures in the coating system, prior to the start of the sputtering process, are preferred as they are generally an indication of a good vacuum and therefore small amount of impurities which could potentially contaminate the film. The pressure during the sputtering process, instead, directly affects the kinetic energy of the sputtered atoms by changing

their mean free path. Lower pressure corresponds to larger mean free path, hence the particle loses less kinetic energy in collisions with the sputtering gas atoms along its way to the substrate, reaching with enough energy for adatom rearrangement. On the contrary, at higher pressure the likelihood for collision increases and the particles will be less energetic when they reach the substrate;

- **sputtering gas:** noble gases which are inert, such as argon or krypton, are often chosen for non-reactive sputtering processes. A large atomic mass of the gas translates into a higher impact energy on the target, increasing the deposition rate. Furthermore, massive gases are less likely to be trapped in the film during growth;

- **substrate bias:** by applying a bias to the substrate the more energetic sputtering gas ions can release this energy on the film when impacting on it, affecting the surface properties such as roughness, texture and grain structure, to name a few, resulting in ion-assisted deposition. The formation of new defects in the film and their elimination arise as two competing mechanism when a substrate bias is applied. Re-sputtering can also occur in those cases when the ions are energetic enough to remove deposited material from the growing film. The substrate bias can be exploited with both DCMS and HiPIMS, although in the latter the target material ions are mostly involved. For HiPIMS, this also results into more conformal coatings on substrates with irregular structures, due to the attraction of the target ions to the substrate introduced by the substrate bias [19];

- **cathode power:** increased cathode power results into an increased sputter yield, hence higher deposition rate. Less gas ion inclusions are observed for higher power.

The stress level of thin films deposited via PVD is also known to depend on the process conditions [151], [152]. Two are the main contributions to the stress present in a thin film: the thermal stress, which originates from the difference in thermal expansion coefficients between the film and the substrate material, and the intrinsic stress, due to the cumulative effect of the crystallographic defects built in the film during growth. Intrinsic stress is known to prevail in high melting point materials such as niobium. Furthermore, the deposition pressure is known to play a role in the intrinsic stress of niobium thin films, with compressive stress becoming of tensile type when a certain threshold pressure, which depends on the material, is passed [153]. At high substrate biases however, the film stress is likely to remain in the compressive state [154].

Chapter 5

Test station for the measurement of the critical temperature

This chapter is dedicated to the description of the experimental station installed at the CERN Central Cryogenic Laboratory for the measurement of the critical temperature (T_c) of the thin films produced in the framework of the R&D for the SRF cavities of the Future Circular Collider. The test station was built, tested and commissioned within the scope of this thesis work. A conference proceeding on the test station [128] and an article on the first study relying on the measurement station [19] are the first publications resulting from this work. Section 5.1 will introduce the most commonly employed methods for the measurement of the critical temperature, with more emphasis given to the induction coil technique, which is also the one adopted for the measurement station. The experimental setup is described in Section 5.2, along with the measurement procedure. The simulation work and measurements performed to characterise the test station are presented in Section 5.3. The extraction method for T_c and an example of data analysis are given in Section 5.4. In Section 5.5 the measurements performed on reference samples of different materials are finally presented, along with a brief discussion of what is observed when, for example, damaged samples are measured.

5.1 Methods to infer the critical temperature

The reason to characterise the basic superconducting properties of a known superconductor is practical as many applications rely on those. The critical temperature T_c is one of the most important properties, along with the critical field and critical current, of a material exhibiting superconductivity. In the context of this research work, the emphasis is given to the measurement of T_c and to the shape of the superconducting transition as first assessment of the quality of the superconducting state of physical vapour deposited films. Measuring T_c also provides knowledge about the purity and residual stress of the films.

By definition, T_c is the temperature at which an abrupt change of well identified material properties, such as, for example, the electrical resistivity, can be observed due to the superconducting transition taking place. By measuring this change in properties as a function of temperature, one can extract or infer the critical temperature.

Many methods exist to measure T_c, including the resistance method, the induction coil method, magnetometry techniques, specific heat methods and so on. Some methods may be more suitable than others, depending, for example, on the homogeneity of the material or on whether the sample is in bulk, film or powder form. In the following, the most employed techniques are described, with more emphasis on the induction coil, the one chosen to build the test station presented in this work.

ELECTRICAL RESISTIVITY

The extraction of the critical temperature of a superconductor via the measurement of its electrical resistance across the transition point is done via a four-probe measurement. The work by Murase [155] describes this experimental technique exhaustively.

Two probes apply a small current at two opposite ends of the sample, while two more probes monitor the voltage drop at the same ends. The sample is either cooled down to its superconducting state before the measurement starts, without applying any current, or in some cases one might choose to perform the measurement directly during the cool-down process. A temperature sensor measures the sample's temperature at the same time. For warm-up measurements, the sample is often let warm up naturally. As long as it is superconducting, the current flows without resistance in it and no voltage drop is detected. As soon as the sample will turn normal conducting the electrical resistance becomes detectable. The temperature at which this is observed is interpreted as the critical temperature of the sample.

Due to the need to solder or press the probes against the sample, which can results in sample damage, and because electrical current often follows preferential paths especially in non-homogeneous materials, this method is preferred for homogeneous, bulk samples.

MAGNETOMETRY

The measurement of the magnetization also represents a method for determining the transition temperature T_c. This choice, unlike the four-probe method, preserves the sample's conditions, as it is contactless and does not require any physical intervention to perform the measurement.

After being cooled down in the absence of a magnetic field, the superconducting sample is magnetised by a static external magnetic field, and placed within a coil. The temperature is then increased and the self inductance of the coil, which increases as the sample turns normal conducting, is measured as a function of the temperature by exciting it with a small AC magnetic field. In modern systems, the change in self inductance is detected by a Superconducting Quantum Interference Device (SQUID) combined with the vibrating-sample technique (VSM with M standing for "magnetometry"): the dipole moment of the sample vibrated inside the coil is detected as changing magnetic flux by a SQUID inductively coupled to the coil.

Compared to the four-probe measurement, this method is sensitive to non-homogeneous samples: if superconductivity can be indicated by a single continuous current path in resistance measurements, despite the non homogeneity of the sample, the supercurrents must, instead, flow over the total surface of the sample in order to provide perfect shielding and indicate a homogeneous superconducting state in the magnetic measurement.

INDUCTION COIL

The measurement station built within this thesis work and described in this Chapter is based on this method, which also exploits the magnetic screening of an external field by the sample in the Meissner state. This contactless method to infer T_c is based on the detection of the mutual induction between two coaxial coils which are placed at the two opposite sides of the sample to be measured.

Figure 5.1 represents schematically the measurement principle. A usually flat sample (S), whose side cross section is depicted here, is placed between two coils and zero-field cooled well below its T_c to avoid magnetic flux trapping. One of the two coils, generally addressed as the *drive coil* (D), after the sample is cooled down,

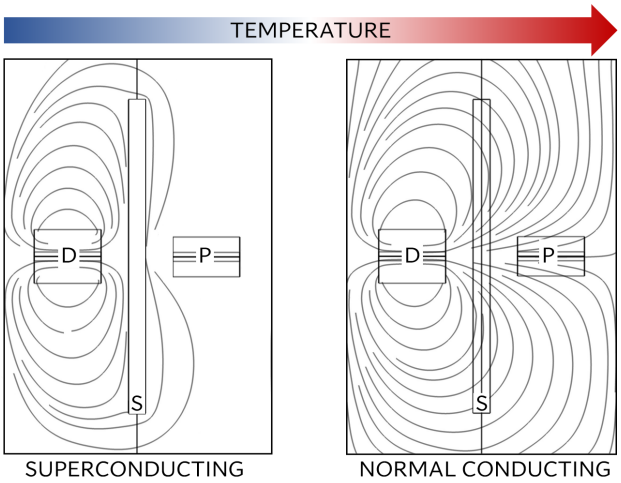

FIGURE 5.1: Measurement principle of the induction coil technique: the superconducting sample (S) is in the Meissner state, therefore screens the magnetic field generated by the drive coil (D) and prevents it from reaching the sensing or pickup coil (P); as the temperature is increased, the sample turns normal conducting and the field can pass through it, reaching the pickup coil and inducing a voltage signal in it from which it is possible to infer the critical temperature of the sample.

is excited with a sinusoidal current of constant amplitude to generate an alternating magnetic field. The second coil, placed at the other side of the sample, passively detects the voltage drop induced at its ends, according to Faraday's law of induction, by the alternating magnetic field generated by the drive coil. This second coil is addressed as *pickup coil* (P). Before the measurement starts, the sample is in the superconducting state and expels the magnetic field generated by the drive coil, preventing the field lines from entering the sample. By doing so, it also screens the pickup coil placed behind it from the magnetic flux lines. However, if the sample size is not extended enough to completely shield the pickup coil from the field generated by the drive coil, a background signal is detected at the pickup coil at this initial stage of the measurement, due to the existence of the field leaking around the sample. Starting from here, the sample's temperature is increased until it turns normal conducting. The transition of the sample to the normal conducting state results into a step-like voltage signal in the pickup coil, as described in Section 5.4, due to the sudden increase in the amount of magnetic flux lines becoming able to cross the sample, and consequently reach the pickup coil, as superconductivity breaks and the screening currents cease to exist. The T_c of the sample can hence be defined as the temperature at which the increase of the pickup voltage is observed.

This method of measuring T_c is well suited to flat samples and can measure bulk as well as thin film samples on dielectric or metallic substrate, depending on the frequency of the drive signal. It also has the advantage of being relatively cheaper and easier to set up than magnetometry measurements, on top of not requiring any physical intervention on or modification of the sample, contrarily to the case of standard magnetometry measurements, which are contactless but usually require the sample to be cut to a very small size (typically about 1×1 mm) in order to fit inside the sensing coil.

Generally, two-coil systems based on this principle can be employed for the measurement of the RRR, the penetration depth, the coherence length, the complex conductivity of the sample. However, depending on the quantity to be measured, the geometry of the setup, the needed instrumentation and read-out schemes might change considerably, so that building one two-coil system able to measure many different quantities can turn into a particularly complex task. Examples of the versatility of this method are found in the work by Fiory [156], Boloré [157], Claassen [158], [159], Turneaure [160], He [161], Kumar [162], Singer [87], Draskovic [163].

5.2 Description of the T_c test station

The description of the T_c measurement station presented here will follow a zoom-out approach. The cryostat hosting the measurement system and the core part of the measurement system itself, i.e. the two-coil experimental setup, are described first, with Fig. 5.2 being the reference figure for this part. The description of the instrumentation and the data readout system follows, referring to Fig. 5.4. Last, the description of the liquid helium circulation system is given, referring to Fig. 5.6.

THE HOST CRYOSTAT

The two-coil system for the measurement of the critical temperature is operated inside a large neck, vacuum insulated, liquid helium vessel cryostat. A schematic representation of the cryostat is given in Fig. 5.2 on the left. The vessel's inner height is 1.3 m, the inner diameter is 0.2 m.

The cryostat insert provides the support for the experimental chamber containing the two-coil system, the way of access for the samples to be measured, and, on the warm side, the support for the connections to the electronics and to the helium recovery system. Inside the cryostat, right below the insert, is a series of three copper shields to screen the cold side from the thermal radiation coming from the warm side of the vessel. The stainless steel insert tube is high-vacuum insulated and wrapped with a multi-layer insulation (MLI) sheet to maximise thermal decoupling with the surrounding cryostat environment. The experimental chamber and the vapour inlet are also wrapped in MLI.

The removable dip-stick consists of a hollow stainless steel tube, having the connections for the temperature sensors and the outgoing helium flow at the warm end, and the sample holder at the cold end, onto which the samples to be measured are mounted. The dip-stick can slide up and down the insert tube, to insert the sample into/extract the sample from the experimental chamber without removing the insert.

The experimental chamber is made of copper and is mounted, via a stainless steel flange, at the lower end of the insert tube. An indium seal between the chamber and the insert flanges ensures the tightness of the connection. The chamber lies above a liquid helium bath, in helium vapour environment. More details about the experimental chamber are given in the next Paragraph.

EXPERIMENTAL CHAMBER

A schematics of the cross-section of the experimental chamber hosting the two-coil system is depicted in the central part of Fig. 5.2. Four main parts can be identified: the experimental chamber, containing the coil setup, the cryostat insert tube above the chamber, to which the chamber is mounted, the inlet mounted below the chamber, which allows the helium vapour to flow into the chamber, and the dip-stick,

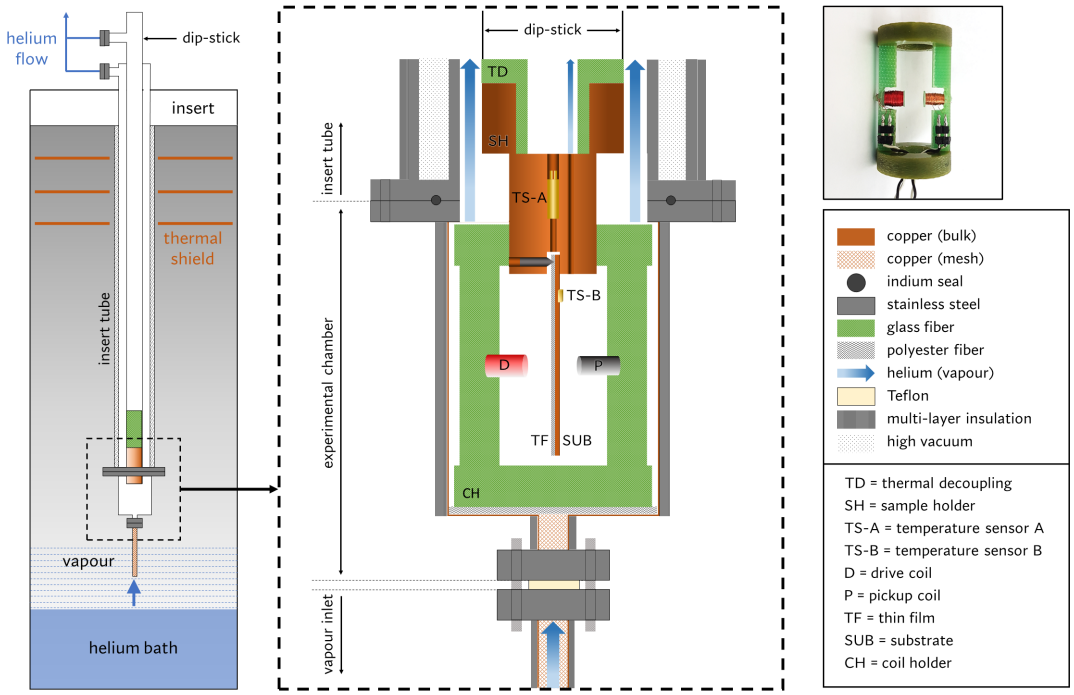

FIGURE 5.2: Schematic cross-section of the experimental chamber (central box) hosting the two-coil setup. On the left, a drawing of the cryostat inside which the two-coil setup is operated. On the top-right, a real-life image of the two-coil system on its glass-fiber support.

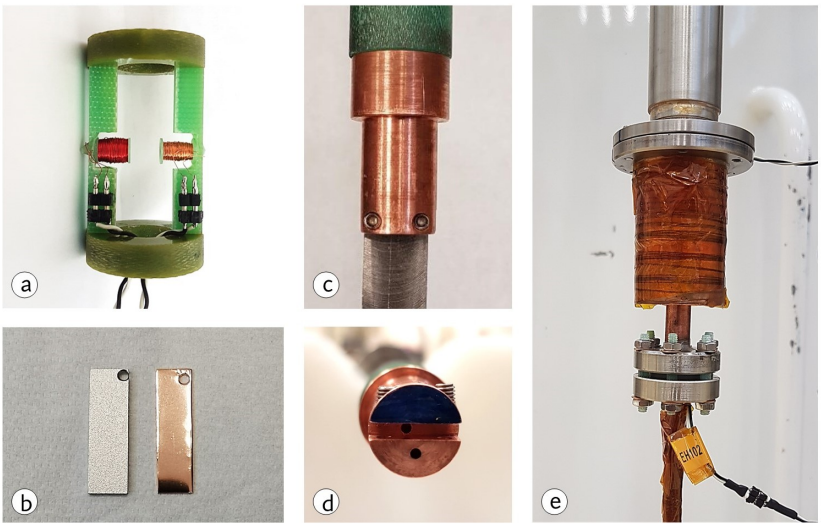

FIGURE 5.3: (a) Drive (red) and pickup coil mounted on the glass-fiber support. (b) Standard size bulk niobium sample (left) and copper substrate (right). (c) Sample holder front view. (d) Bottom view of the sample holder. (e) Experimental chamber mounted on the insert tube, with the vapour inlet at the bottom.

which holds the sample to be measured in place between the coils and can slide up and down the insert tube.

The chamber, a hollow copper cylinder of 35 mm diameter, has the role to create a separated environment where the temperature of the sample can be controlled via helium vapour flow. It is mounted at the cold end of the insert tube via indium-sealed stainless steel flanges.

The coils, placed inside the chamber, are mounted coaxially on a glass-fiber support, addressed as coil holder (CH). Both coils have the same length and inner diameter, respectively 7.46 mm and 1 mm. The outer diameter of the drive coil (D) is 6 mm and that of the pickup coil (P) is 4.4 mm. The distance between the coils is 8.1 mm.

The sample holder (SH) is made of bulk copper and is mounted to the end of the dip-stick. To thermally decouple the copper holder and the stainless steel dip-stick, a glass-fiber connector (TD) is installed between the two. The sample is mounted to the sample holder by pressing with screws its short edge against the inside wall of a 2.2 mm wide slit present at the holder's base, as shown in Fig. 5.2. The sample holder diameter (and therefore the length of the slit) is 13 mm. The measured samples have a standard rectangular shape, with surface size of 11×35 mm^2 and a thickness varying from 0.5 to 2 mm. All the dimensions indicated in the text are also listed in Table 5.1.

The orientation of the sample with respect to the coils is not relevant in the case of bulk samples. However, it is chosen by convention that, in case of thin film samples, the film (TF) side is placed in front of the drive coil, with the substrate (SUB) side facing the pickup coil, as shown in Fig. 5.2.

Two temperature sensors are used to measure the sample's temperature, depending on the sample type. The first one (TS-A), a Cernox ® AA-package, is placed in a custom socket inside the sample holder. A 1 mm diameter hole connects the bottom of the sensor socket to the slit where the sample is mounted, partly exposing the sensor to the environment surrounding the holder and the sample itself. When measuring thin-film samples on copper substrate, with the copper side of the sample in good thermal contact with the sample holder (ensured by the pressure applied by the screws), the sample's temperature is measured by TS-A. The second sensor (TS-B), a Cernox ® SD-package, is mounted at the sample's back, usually pressed against the sample via Teflon ® tape, and is used to measure the temperature of non-copper samples (e.g. bulk niobium, aluminium, Al_2O_3 substrates) as in this case the mismatch in thermal conductivity between the sample and the holder material does not ensure the accuracy of the measurement by TS-A.

To control the temperature of the sample, helium vapour flows into the chamber via the inlet at the bottom and leaves it via two parallel channels: the gap between the insert tube and the dip-stick, which is directly accessible at the upper part of the chamber, and the inside of the dip-stick tube itself, which the vapour can access via a 1 mm diameter duct across the sample holder. The helium flow into and out of the chamber is shown in Fig. 5.2 by the blue arrows. Two polyester pads are stacked at the bottom entrance of the chamber to serve as flow distributors, minimising the chances for laminar flow which would cause undesired temperature gradients inside the chamber volume.

The temperature of the vapour is regulated via a wire heater (26.5 Ω) wound around the inlet. The inlet is filled with copper mesh to facilitate the heat transfer from the inlet walls to the vapour. To ensure the complete thermal decoupling of the experimental chamber from the inlet heater, the connection is made with two stainless steel flanges separated by a Teflon ® gasket and held together via fiber

glass screws. To insulate the chamber, the insert tube and the vapour inlet from the surrounding environment, a wrapping of MLI is applied. Figure 5.3 shows real-life pictures of the parts described above.

MEASUREMENT STATION AND DATA ACQUISITION

A schematic representation of the measurement station with all the instrumentation and read-out system is given in Fig. 5.4. The connections are represented by arrows indicating the input direction.

To perform a measurement, the level of liquid helium inside the cryostat, monitored via a liquid helium gauge, is kept below the vapour inlet entrance. To produce vapour, a heater (heater 1) of 10.2 Ω resistance is placed inside the bath and activated as required. The temperature of the vapour entering the chamber is regulated via a LakeShore Model 335 temperature controller. A wire heater (heater 2) of 26.5 Ω resistance, wound around the inlet and connected to the temperature sensors via a PID control feedback loop is employed to set the vapour temperature.

Once the sample is inserted and cooled down, the magnetic field is turned on by exciting the drive coil with a sinusoidal current of constant amplitude and frequency (30 mA, 21 Hz), generated by a Keithley 4221 current source. A DSP Lock-In Amplifier Signal Recovery 7265 takes the drive current as input reference and and reads the pickup coil voltage to extract the amplitude and phase signals. The raw voltage signal of both coils (V_d and V_{pu}) is read out via an NI 9234 Analog Input Module. This is live monitored and logged, together with the detected temperature (T) and extracted pickup amplitude (A_{pu}), via a custom made LabView data acquisition software. All the connections between the experimental setup and the outer electronics are made via feed-throughs at the insert. For simplicity, this is not represented in Fig. 5.4, where a conceptual schematic of the connections is given. The arrows indicate the input direction.

The graphic user interface (GUI) of the acquisition software is shown in Fig. 5.5. It presents five live monitors showing the temperature read by the two sensors, the raw drive voltage signal, the raw pickup voltage signal (first row, left to right), and the pickup voltage amplitude and phase (second row, center and right). The panel

Part	**Size (**mm**)**
Cryostat inner height	1300
Cryostat inner diameter	200
Chamber inner diameter	35
Coil length	7.46
Coil inner diameter	1
Drive coil outer diameter	6
Pickup coil outer diameter	4.4
Coil to coil distance	8.1
Sample holder diameter / slit length	13
Slit width	2.2
Sample surface	11×35 (mm^2)
Sample thickness range	$0.5 - 2$

TABLE 5.1: List of relevant sizes of the parts of the experimental setup.

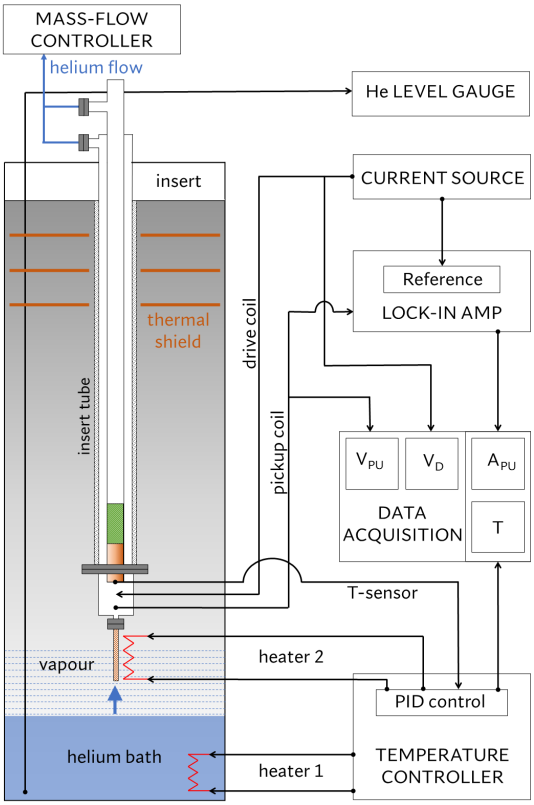

FIGURE 5.4: Schematics of measurement station. The connections to the instrumentation are represented by arrows indicating the input direction.

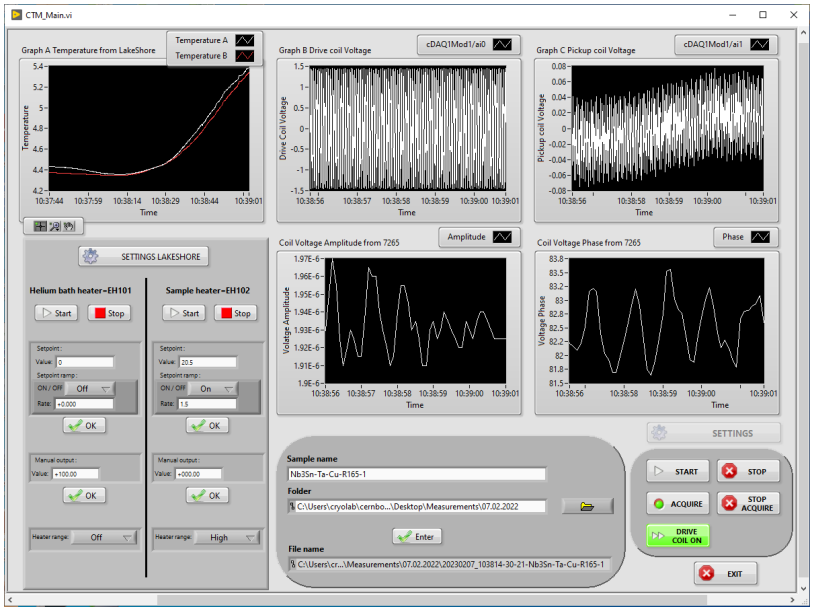

FIGURE 5.5: Graphic user interface of the LabView data acquisition system designed for the T_c measurement station.

on the left is to set the type of temperature control, the PID settings and the heater settings. The central panel at the bottom is for the file naming and saving. The last panel at the right bottom is to start and stop the measurement and data acquisition, and to turn on/off the magnetic field.

When the data acquisition is started, a log file is created in which all the measurement settings are stored. The logged data are: the drive and pickup coil raw voltage signals, the pickup voltage amplitude as extracted by the lock-in amplifier, the two temperature sensors and the time stamp. The extraction of the critical temperature is done offline by first combining the temperature and amplitude data via the common time stamp, then following the procedure described later on in Section 5.4.

HELIUM CIRCULATION SYSTEM

The helium circulation system to which the cryostat is connected is represented in Fig. 5.6, where the valves and pressure gauges are all mapped with their respective codes. The helium vapour flows into the chamber via the inlet at the bottom and leaves via two parallel channels: the gap between the fixed tube and the dip-stick, which is directly accessible at the top of the experimental chamber and the inside of the dip-stick tube itself, which the vapour can access via the 1 mm diameter duct across the sample holder, as shown in Fig. 5.2.

Three main parts can be identified in the helium circulation system for the T_c measurement station: the helium source, consisting of a 500 L Dewar were the liquid helium to fill the cryostat is stored; the cryostat housing the experiment; the helium recovery system to which both the gasometer and the helium balloon are connected. The stations with the connections to the helium recovery system, including the piping to the vacuum pumps (generally needed for purges or to pump helium to its superfluid state), take the name of *clarinet* according to the laboratory jargon.

The Dewar and the cryostat are usually not directly connected, unless a helium refill of the cryostat is needed, in which case they are connected via a transfer line as depicted in Fig. 5.6. The Dewar and the cryostat are always connected to the gasometer, which is at 30 mbar over-pressure with respect to ambient pressure. This way, in case of undesired small leaks in the vessels, the small over-pressure prevents the atmospheric gas (air) from entering and contaminating the helium. At the same time, the helium can be collected by the gasometer in case a pressure larger than 30 mbar builds inside the Dewar or the cryostat, e.g. during a helium transfer. The only case when the Dewar is not connected to the gasometer, is during the helium transfer, when building a small over-pressure inside the Dewar is of aid for the process and the outflow must all be directed to the cryostat. The transfer is also the only case when the connection to the helium bottles battery, represented in Fig. 5.6, is needed. The helium in the bottles is at a pressure of 50 bar and is in fact used to pressurise the Dewar to start the transfer. The amount of transferred liquid helium is monitored via a helium-level gauge, as explained in the previous Paragraph, but for convenience this is only shown in Fig. 5.4.

The connection between the cryostat and the helium balloon is only open during a measurement run, to allow the helium vapour to flow from the cryostat into the experimental chamber and up through the insert tube and dip-stick, then out to the balloon via the mass-flow controller. The vapour flow needed to perform the measurement is otherwise impeded, with the vapour staying in the cryostat or flowing into the gasometer in case of over pressure. Since it is at a pressure 25 mbar lower than ambient pressure, the balloon does not only serve as the recovery for the "dirty" helium used in the measurement, but it also keeps the vapour flow (hence the sample's temperature) stable.

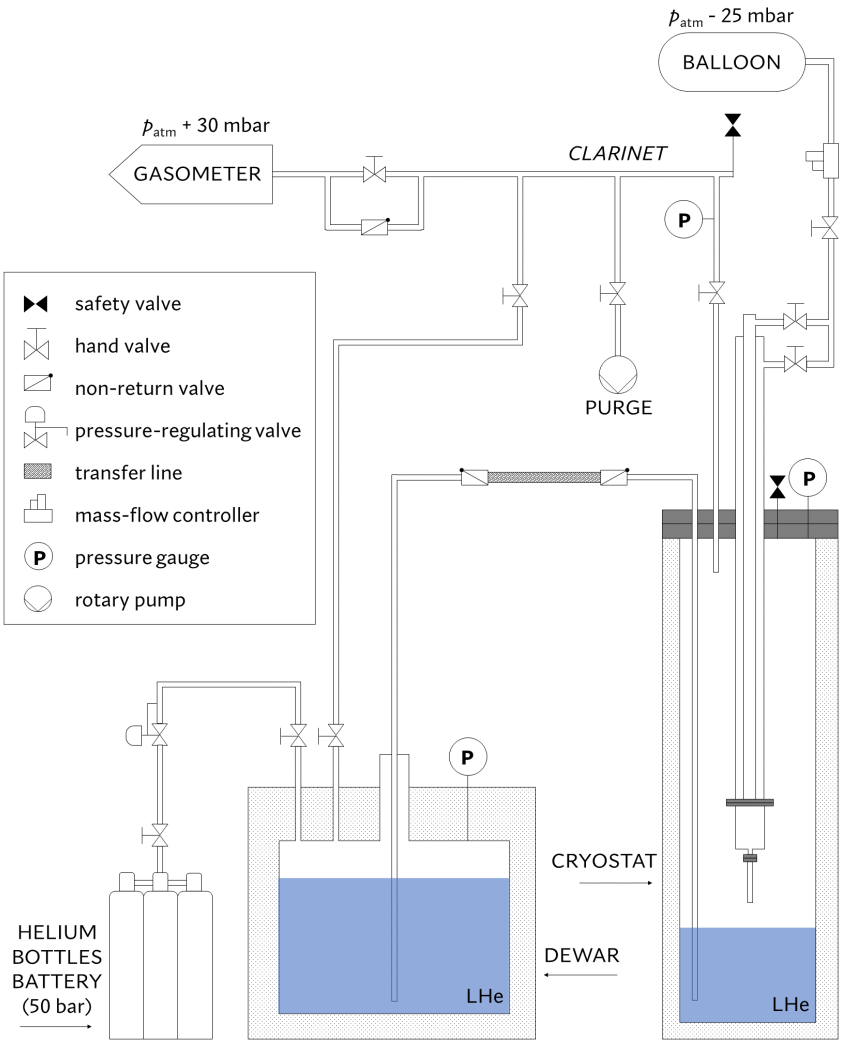

FIGURE 5.6: Helium circulation and recovery system for the T_c measurement station.

5.2.1 Measurement routine

It is recommended to follow a standardized routine to operate the test station and perform a measurement. In the following, the measurement settings and whole procedure are described in broad terms. For the future user of the test station, an accurate, step by step technical description of the measurement, to be followed while operating the system for the first times, is given in Appendix A.

The T_c measurement routine can be summarised by the following steps:

- fill the cryostat;
- start the helium flow to cool down the sample with the magnetic field off;
- turn on the magnetic field at the drive coil with the following settings:
  - drive coil current amplitude: 30 mA;

  - drive coil current frequency: 21 Hz;

- start the data acquisition;
- start the temperature ramp at 1.5 K/min;
- when the ramp is over stop the data acquisition;
- turn off the drive field;
- turn off the heaters.

5.3 Characterisation of the experimental setup (I)

The response of the measurement station was characterised by simulating its defining features, such as the pickup coil response to the drive coil signal and the magnetic field amplitude generated by the drive coil. The simulated data was then compared to the measured response under different conditions. COMSOL Multiphysics ® is the software employed for the simulations.

The experimental chamber is modeled according to its real geometry and size. The coils, a sample (bulk niobium, a niobium film on copper or a copper substrate, depending on the case) and the copper chamber itself are taken into account by the simulation. The coil and sample holders are neglected to avoid further complexity in the model.

The chamber model is shown in Fig. 5.7: (a) shows a 3D rendering of the copper chamber (1) with a bulk niobium sample (2) placed between the drive (3) and pickup (4) coil, and the hole for the vapour inlet (5) at the bottom of the chamber, while (b) and (c) show the view from the top and the side respectively. This represents the geometry used for all simulation studies, with the exception that, depending on the study, the sample is removed or replaced with a copper substrate or a Nb/Cu sample.

Only the electromagnetic response of the system is studied, with the temperature addressed as a static parameter, i.e. the transient thermal conditions of a measurement were not simulated. The superconducting state of the sample is considered only in terms of its magnetic properties, with the Meissner state reproduced by assigning to the magnetic permeability μ of niobium a parametric dependence on the temperature, so that:

$$\begin{aligned} \mu &= 1 && \text{for} \quad T \geq T_c \,, \\ \mu &= \left[\frac{T}{T_c}\right]^{100} && \text{for} \quad T < T_c \,. \end{aligned} \tag{5.1}$$

The resulting magnetic field expulsion is shown in Fig. 5.8, where the view is the same as the top view given in Fig. 5.7 (b). The Meissner state is simulated for a 1.9 mm thick bulk niobium sample (left column) and for a 25 µm niobium film on a 1 mm thick copper substrate (right column). The film faces the drive coil. The magnetic flux density lines, shown in red, cannot penetrate the niobium when superconducting at $T = 8$ K, hence they are forced to move around the sample. In both cases, one can notice the enhancement of the magnetic flux lines at the sample edges on the side facing the drive coil. In the normal conducting case, at $T = 10$ K, niobium can be considered transparent to the magnetic field, and the flux lines cross the material unperturbed. Only in the case of the Nb/Cu sample one can see that the field is partly attenuated inside the copper because of the induced eddy currents.

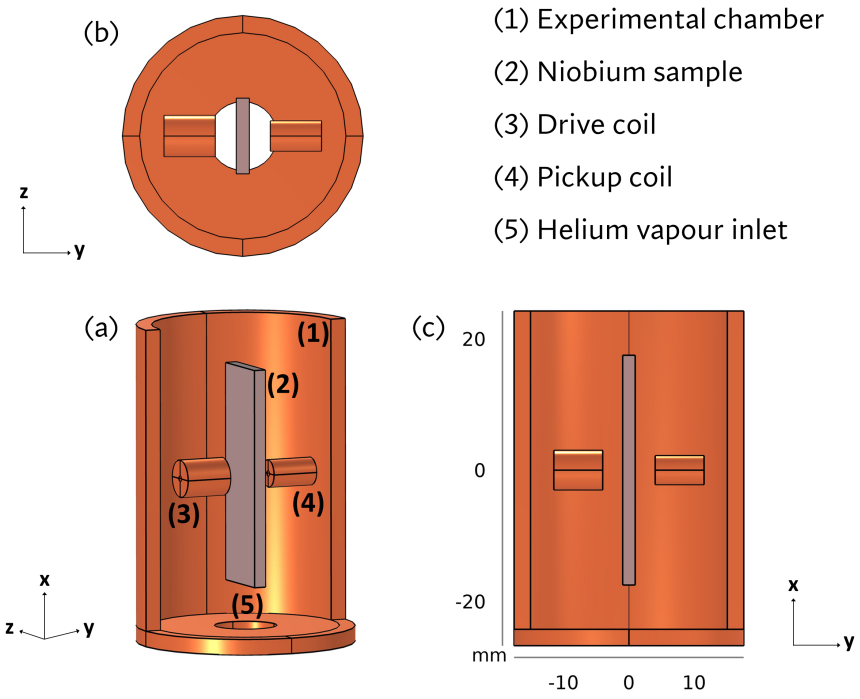

FIGURE 5.7: Model of the experimental chamber designed to simulate the two-coil system, including the chamber itself (1), the niobium sample (2), the drive and pickup coil (3 - 4). The inlet for the helium vapour (5) is visible at the bottom.

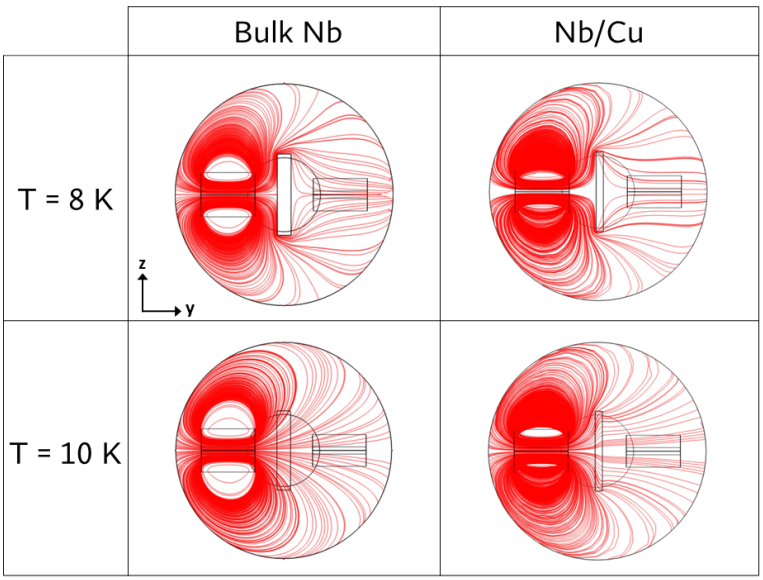

FIGURE 5.8: Top view of the simulated magnetic field lines inside the experimental chamber. Two cases are shown: a bulk niobium sample and a niobium film sample on copper for both the superconducting ($T = 8\,\mathrm{K}$) and the normal conducting ($T = 10\,\mathrm{K}$) states are shown.

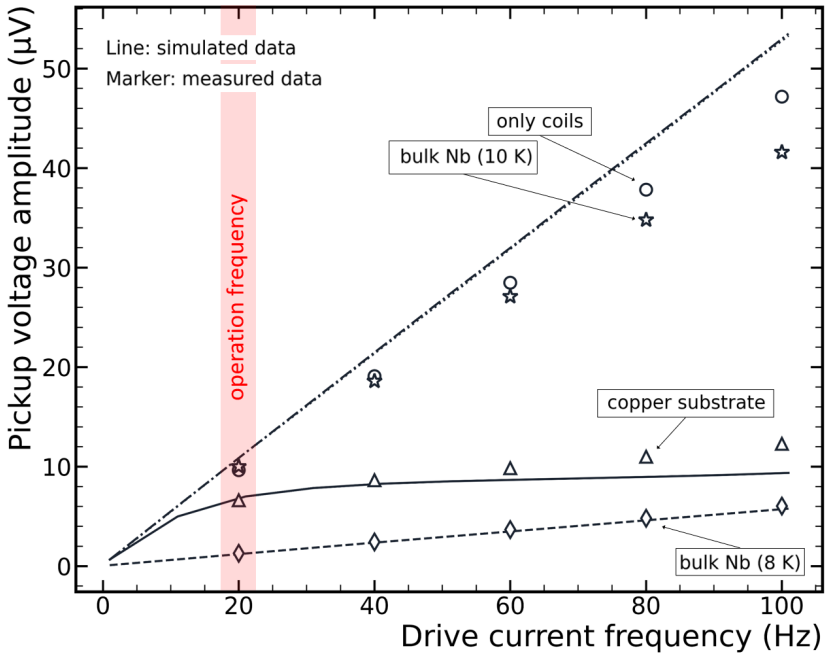

FIGURE 5.9: Response of the pickup coil as a function of the drive coil current frequency. The simulated and measured data are plotted for four different cases: without a sample (only coils), bulk niobium at 10 K, bulk niobium at 8 K and a copper substrate. The red band corresponds to the chosen operation frequency for the measurement system.

The pickup coil response to the drive field was then simulated for four different cases: in the absence of a sample (indicated as "only coils"), in the presence of a copper substrate, and for a bulk niobium sample in the superconducting ($T = 8$ K) and in the normal conducting ($T = 10$ K) state. Figure 5.9 shows the simulated and measured induced voltage amplitude in the pickup coil when a magnetic field generated by a fixed drive current of 30 mA is applied, as a function of the current frequency. The lines represent the simulated data, the markers represent the measurements.

The linear dependency of the signal amplitude in the pickup coil on the frequency of the drive signal, expected according to Faraday's law of induction, is immediately seen in both the simulated and the measured data for the coil system without sample. The reasons for the discrepancy between the simulated and experimental data toward higher frequencies can be different. Most likely, the mismatch between the real resistivity at low temperature of the wire employed for the coils, and of the copper of which the experimental chamber is made, and the value employed for the simulation plays a role. In the ideal case of pure niobium, the simulated data overlap the "only coils" case, where the normal conducting ($T = 10$ K) sample is unresponsive to the magnetic field. In the real case, the bulk niobium data separates from the ideal case even more with respect to the "only coils" case, due to the weak eddy currents developed at high frequency which have the effect of mildly screening the field from the pickup coil. In the superconducting state ($T = 8$ K), the bulk niobium sample screens the source field almost completely, with the increase towards higher frequencies being due to the field leaking around the sample and reaching the pickup coil (also shown in Fig. 5.8). With the copper substrate, the same behaviour as for the normal conducting niobium is observed, even though at

much lower frequencies. In fact, for the same frequency value, the skin depth of copper (see Eq. 1.45) is much smaller than the one of niobium, due to its much higher electrical conductivity[1], so that the signal is already attenuated by the eddy currents at about 20 Hz. The separation between the simulated and the measured data for increasing frequency is also in this case ascribed to the electrical conductivity assigned to the copper substrate in the simulations, likely higher than the real value. The red box indicates the frequency at which the test station is operated, for which all the simulated cases are in good agreement with the data.

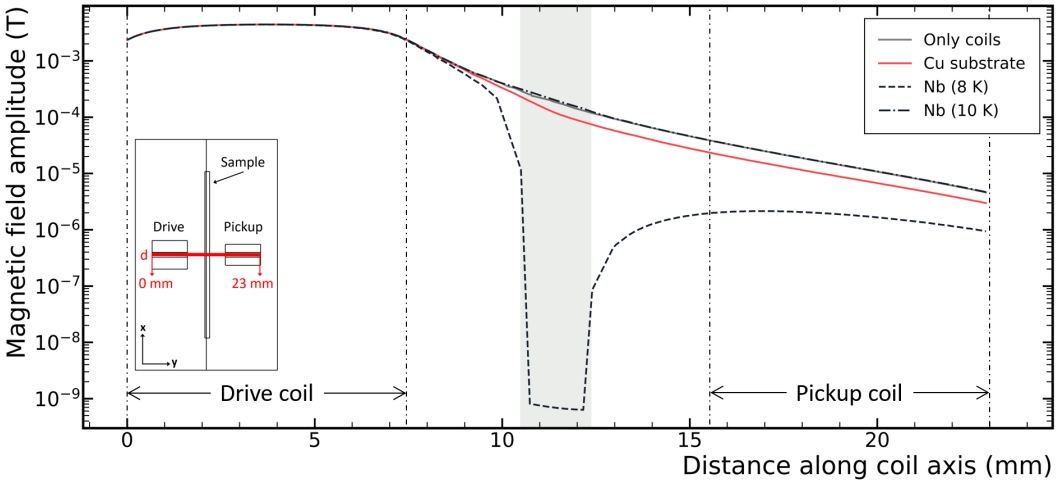

FIGURE 5.10: Simulated magnetic field amplitude along the coil axis. The line path of calculation is indicated in red in the inset box. The central gray band indicates the position of the bulk niobium sample.

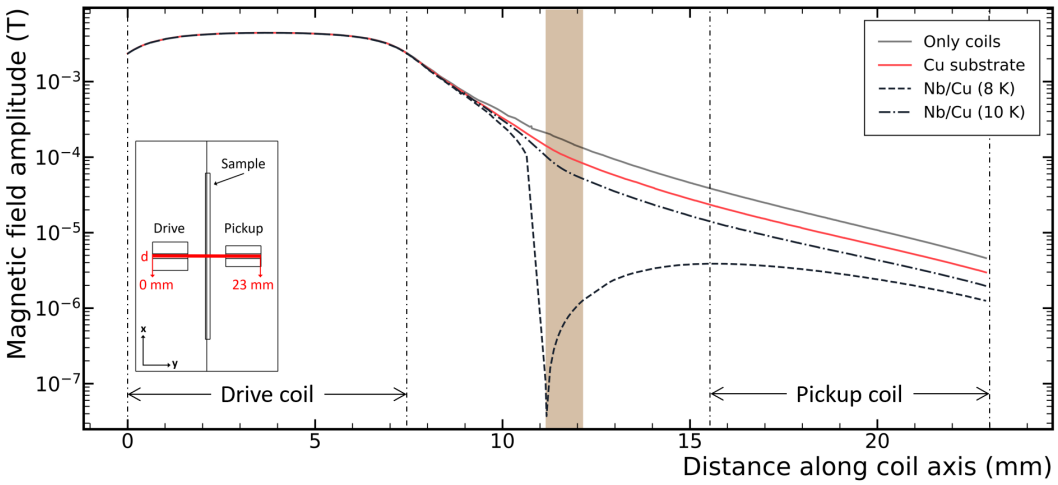

FIGURE 5.11: Simulated magnetic field amplitude along the coil axis. The line path of calculation is indicated in red in the inset box. The central brown band indicates the position of the Nb/Cu sample, with the film facing the drive coil.

[1] At 10 K and 21 Hz one gets a skin depth of approximately 2 mm for copper (RRR $\sim$ 50) and 9 mm for niobium (RRR $\sim$ 20).

Due to the impossibility to install a magnetic field probe inside the experimental chamber, the absolute value of the magnetic flux density is also simulated along the coil axis in order to ensure its value does not exceed the critical field of niobium at the sample surface. This was done in the presence of a bulk niobium and of a Nb/Cu sample in between the coils, as shown in Fig. 5.10 and Fig. 5.11 respectively. In both images, the modulus of the magnetic flux density generated by the drive coil for a fixed current of 30 mA and a frequency of 21 Hz is shown according to its values calculated along the coil axis d. In both pictures, the inset on the left shows the $x - y$ cross section of the experimental chamber with the distance d along which the magnetic flux modulus is calculated indicated as a red line. The vertical dashed lines represent the distance covered by the drive coil (on the left) and the pickup coil (on the right). In Fig. 5.10, the central gray area represents the position of the bulk niobium sample, while in Fig. 5.11 the central brown area represents the Nb/Cu sample. In both cases, the field was also calculated for the coils only and for the copper substrate cases. A field of about 4 mT is produced inside the drive coil, which decays by nearly one order of magnitude at the sample's surface. This field values are safely within the lower critical field of niobium (130 mT), so that it can be reliably assumed the presence of the field during the measurement does not have a detectable influence on the final T_c value. The screening of the field by the superconducting sample is visible in both the bulk niobium and the Nb/Cu case, resulting in a lower field reaching the pickup coil with respect to the signal in the normal conducting state.

5.3.1 A real measurement

The typical outcome of the T_c measurement of a bulk niobium sample, showing the raw data of the pickup coil voltage amplitude and the temperature, is given in Fig. 5.12a. It is possible to see the evolution of both quantities over time as the temperature ramp is started. After having cooled down the sample in zero field, the field is turned on, resulting in a stable signal of about 0.8 µV. A temperature ramp of 1.5 K/min, set to rise from 7 K to 11 K (not visible in the plot), is then started. While the temperature starts rising, the voltage amplitude in the pickup coil remains constant for as long as the sample is in the superconducting state. The transition to the normal conducting state is obvious as the temperature crosses T_c at about second 73 and results in the sharp jump in amplitude detected by the pickup coil as soon as the magnetic field is no longer screened by the sample. It will be seen later that the transition does not always appear as sharp, especially in the case of thin film samples. While the temperature keeps rising after the transition, the amplitude signal stays constant at about 10.2 µV. The choice of a temperature set-point (11 K) far from what the T_c is expected to be for the current measurement, is made in order to avoid disturbances likely caused by the temperature oscillations taking place around the set-point due to the PID settings.

The raw data as shown in Fig. 5.12a are then combined via the time stamp to plot the curves of the type shown in Fig. 5.12b and to extract the values of T_c and ΔT as explained later in Section 5.4.

The repeatability of a measurement performed with the test station is demonstrated in Fig. 5.12b. Here the same bulk niobium sample used for the measurement in in Fig. 5.12a is measured three times, on three different days, under the same drive coil and temperature ramp rate settings. It is possible to see that, except for some noise level depending on environmental factors, the three measurements fully overlap. Also, the maximum deviation in temperature from the mean value calculated

along the transition slope for the three measurements amounts to

$$\sigma(T) \leq 0.006\,\mathrm{K}\,, \tag{5.2}$$

which represents an indication of the precision achievable with this type of measurement. This should ensure the reliability of a T_c measurement performed with this test station, provided that the standard procedure described in Appendix A is followed carefully. On top of this, the typical root mean square noise observed for the temperature signal, calculated over a time interval of 10 s, corresponds to:

$$\epsilon(T) \simeq 0.004\,\mathrm{K}\,, \tag{5.3}$$

so that the choice is made to assume the uncertainty on the T_c measurement to be the transition width ΔT as defined later in Eq. 5.5.

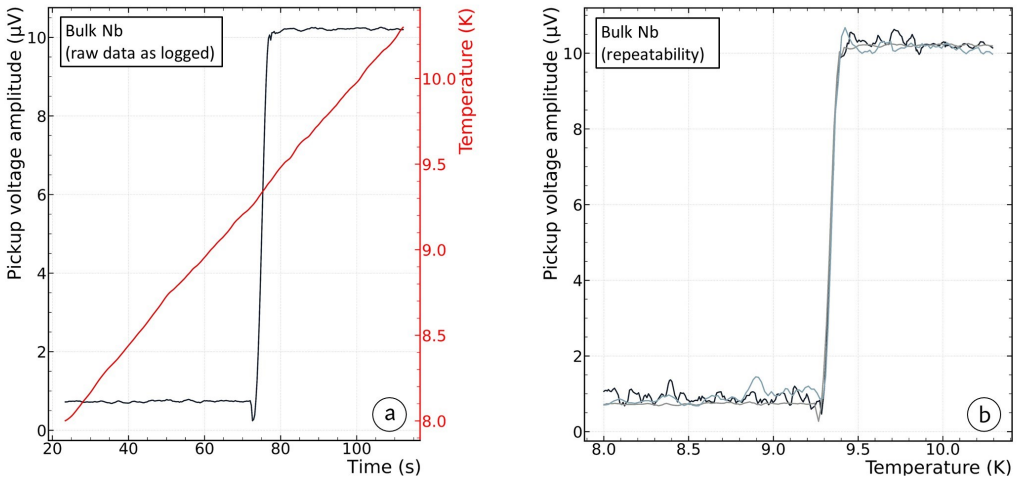

FIGURE 5.12: (a) Raw pickup voltage amplitude and temperature data plotted versus time as measured with the two-coil setup on a bulk niobium sample. (b) The same sample as in (a) measured three times on three different days to demonstrate the repeatability of the measurement.

5.4 Extraction of T_c from the superconducting transition curve

Since the remaining discussion on the characterisation of the test station will include the analysis of the superconducting transition curves measured for different samples, the explanation of the method of extraction for T_c and an introduction to the data processing is needed at this point. Section 5.5 will then complete the description of the characterisation procedures started in Section 5.3.

5.4.1 The 10% – 90% method

As anticipated in Section 5.1 with the description of the induction coil T_c measurement principle, a voltage signal is induced in the pickup coil whose amplitude shows a step-like behaviour when the sample transitions from the superconducting to the normal conducting state, as the temperature rises and crosses the sample's critical temperature.

An indicative example of how the curve would look like for a superconducting transition measured with the inductive method is given by the drawing in Fig. 5.13, where the trend of the amplitude of the voltage signal induced in the pickup coil is shown against the temperature[2]. A drawing is used here for ease of depiction of the involved quantities, with the real case described in the following Section.

Three main parts can be identified in the transition curve: the superconducting part, corresponding to the low temperature plateau, the normal conducting part, corresponding to the high temperature plateau, and the transition itself, represented by the step-like part in between the two plateaus.

To extract the critical temperature T_c, the choice is made here to apply the 10% – 90% method, although not the only possible one, as discussed later on. A linear fit is applied to each part of the curve, represented in Fig. 5.13 by the gray dashed lines. The intersection points between the transition and the plateau lines are indicated as 'A' and 'B', so that the height of the transition is defined by the quantity

$$\Delta A_{\mathrm{pu}} = |A_{\mathrm{pu}}(\mathrm{A}) - A_{\mathrm{pu}}(\mathrm{B})| \,. \tag{5.4}$$

Starting from this quantity one can calculate the voltage amplitudes corresponding to the 10% and the 90% of the total amplitude, $A_{\mathrm{pu}-10\%}$ and $A_{\mathrm{pu}-90\%}$ respectively. The points 'a' and 'b' are then extracted from the data set as the data points corresponding to these amplitude values. The temperature values corresponding to 'a' and 'b', labeled as $T_{10\%}$ and $T_{90\%}$ mark by definition the extremes of the transition, so that

$$\Delta T = |T_{10\%} - T_{90\%}| \tag{5.5}$$

represents the width of the transition. The critical temperature can be finally defined as the middle temperature within ΔT:

$$T_c = T_{10\%} + \frac{\Delta T}{2} \,. \tag{5.6}$$

Values of ΔT lower than 3% of T_c are considered acceptable when applying the 10% – 90% method [155]. A different method to extract T_c and ΔT leading to similar results as the 10% – 90% method is to calculate the derivative of the amplitude data. This way, T_c is extracted as the maximum of the derivative (corresponding to the inflection point in the transition curve) and ΔT as the FWHM of the derivative. The disadvantage of this approach lies in the fact that identifying the peak of the derivative becomes difficult if the initial data is noisy, requiring neat data filtering and sometimes fitting before proceeding with the peak identification and finally making the T_c extraction process needlessly lengthy. This method can be otherwise considered equivalent to the 10% – 90% method.

The use of the transition onset temperature, also indicated in Fig. 5.13, or of $T_{90\%}$, as value for T_c is often encountered in literature too. It is especially common in measurements of materials intended for superconducting magnets application. These are operated with high DC currents and with the superconductor in the mixed state, and for them the highest temperature above which the superconducting state of the sample is fully disrupted is of main interest.

Superconductors for SRF cavity application are operated in the pure Meissner state. Magnetic field penetration is undesirable as it leads to resistive losses in the RF regime, as discussed in Section 1.2. The 10% – 90% method for the extraction

[2]Similarly, one could choose to use the real and imaginary components of the voltage signal, also detected by the lock-in amplifier, for the extraction of T_c.

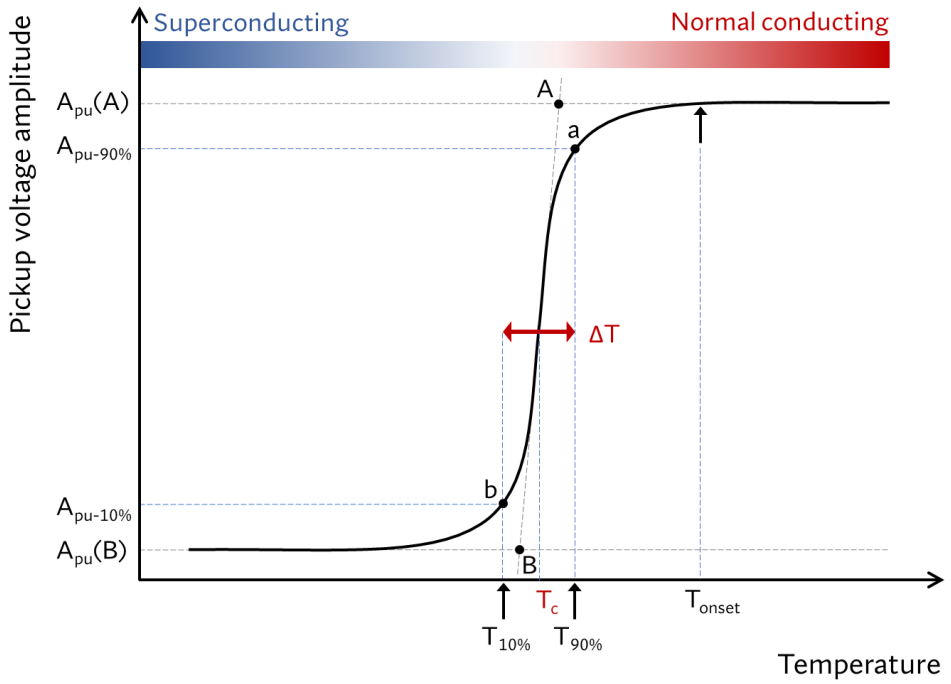

FIGURE 5.13: Example curve of the superconducting transition. The 10% – 90% method is used to extract the critical temperature T_c and the transition width ΔT.

of the T_c value is considered more conservative in this case, as it provides a value in between the temperature of first field penetration and the temperature at which the transition to the normal conducting state is completed. In addition, since the T_c value extracted with this method only has full meaning when accompanied by the associated transition width ΔT, it also provides information on the purity and homogeneity of the sample.

The extraction of T_c from real data according to this method is demonstrated in the next Section.

5.4.2 An example of data analysis

The application of the 10% – 90% method for the extraction of T_c to a real data set is demonstrated in Fig. 5.14. The measured sample is a Nb_3Sn thin film deposited on a copper substrate with a tantalum intermediate layer. All the data processing is done with Python.

The amplitude and temperature raw data are first combined via their common time stamp, as described earlier in Section 5.3.1, and plotted as pickup voltage amplitude versus temperature. To reduce the noise and facilitate the extraction of the quantities of interest, a basic filtering (of the Savitzky-Golay type) is applied. This is shown in Fig. 5.14a, where the raw data is represented by the blue line and the filtered data by the black line. The inset shows a zoom-in on the data to mark the small, yet visible difference before and after the filtering.

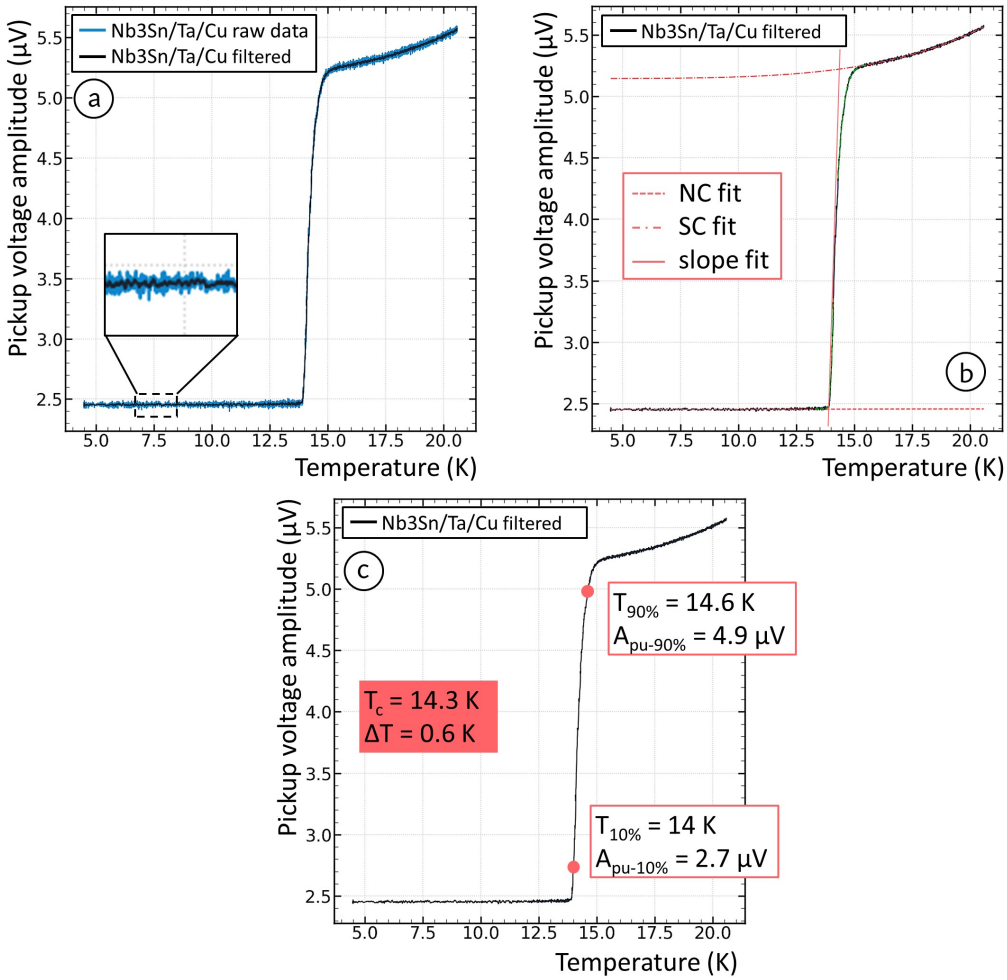

FIGURE 5.14: Example of routine data analysis for the extraction of T_c and ΔT, demonstrated for a measurement performed on a Nb_3Sn/Ta/Cu sample deposited at CERN via HiPIMS.

In Fig. 5.14b, the fitting of the superconducting, normal conducting and slope parts of the transition curve is shown. The superconducting and slope parts are here fitted with a linear function ('SC fit' and 'slope fit' respectively) as explained in the previous Section. However, in this case, it is not possible to apply a linear fitting to the normal conducting part of the curve. The OFE copper employed for the substrates is expected to have a RRR $\simeq 150 - 300$, reason why the resistivity of copper will start changing appreciably with temperature, starting from temperatures of about 10 - 12 K and above. This reflects on the intensity of the eddy currents induced in copper by the AC magnetic field generated by the drive coil, whose screening effect observed in the normal conducting part of the curve varies with temperature proportionally to the variation of resistivity. For this reason, when samples on copper which are expected to exhibit a T_c larger than 10 K are measured, the normal conducting part of the curve is fitted with the low temperature and RRR dependence function of the copper electrical resistivity as provided by [164]:

$$\rho(T, \mathrm{RRR}) = \rho_0 + \rho_i + \rho_{i0} \,, \tag{5.7}$$

where:

$$\rho_0 = \frac{1.553 \times 10^{-8}}{\mathrm{RRR}}\ ,\ \rho_\mathrm{i} = \frac{p_1 T^{p_2}}{1 + p_1 p_3 T^{(p_2 - p_4)} \exp[(-p_5/T)^{p_6}]}\ ,\ \rho_{\mathrm{i}0} = p_7 \frac{\rho_\mathrm{i}\rho_0}{\rho_\mathrm{i} + \rho_0}\ , \quad (5.8)$$

with the units being K for the temperature and VmA^{-1} for the resistivity, and the term $\rho_{\mathrm{i}0}$ representing the deviation from the Matthiessen rule. In the case of the resistivity of copper, all the p_{1-7} coefficients have a known value [164]. To fit the copper screening signal of the normal conducting part of the transition curve, the p_{1-7} coefficients and the RRR (hence the residual resistivity term ρ_0) are left as free parameters, resulting in the curve indicated in Fig. 5.14b as 'NC fit'.

Once the three components of the curve are fitted, the intersection points 'A' and 'B' can be found and used to calculate the values of $A_{\mathrm{pu}-10\%}$, $A_{\mathrm{pu}-90\%}$, $T_{10\%}$ and $T_{90\%}$ as indicated in Fig. 5.13, which finally represent the coordinates of the points indicated in light red in Fig. 5.14c and from which T_c and ΔT are calculated.

The data analysis just described is the same applied for the extraction of T_c and ΔT of the Nb_3Sn samples deposited on copper via HiPIMS which are object of the study presented later on in Chapter 7. It is always applied to all types of measured samples and materials, with the only difference being that, for copper substrates, the normal conducting part of the curve is fitted with a linear function or with the function in Eq. 5.7 depending on the RRR of the employed copper and on the temperature range at which the measurement must be performed.

5.5 Characterisation of the experimental setup (II)

5.5.1 Reference samples

The measurements to assess the response of the system are performed on five different reference samples, discussed in the following, whose size and properties are given in Table 5.2.

All the measurements are performed with the same settings and under the same conditions as described in Section 5.2.1 and Appendix A, and all the samples have the same standard surface size of 11×35 mm^2. The thickness of the bulk samples changes due to the size of the original sheet from which they were cut, that is 0.5 mm for the lead sample and 3.6 mm for the niobium sample. The latter is reduced to 1.9 mm by milling and buffered chemical polishing (BCP) to fit the size of the slit at the sample holder. The thickness of the film samples also changes, depending on the technique used to deposit them and on the study they were made for: the 45 µm thick niobium film on copper was coated via DCMS in the context of the thick films program [165] carried on at LNL-INFN (Italy); the 6 µm thick niobium film on copper was coated at CERN via HiPIMS specifically as a reference sample for the T_c measurement station; the 1 µm thick Nb_3Sn film on ceramic substrate was coated at CERN via DCMS as a reference sample to the Nb_3Sn films deposited on copper substrate [26]. The thickness of the copper substrate is of 1 mm in all cases. The copper employed for the substrate of the *thick* film sample is OFHC grade, while for the HiPIMS deposited sample OFE grade copper is used.

BULK LEAD

Lead is a type-I superconductor, hence the shape of the superconducting transition is expected to appear sharp at the known temperature of 7.2 K. The transition measurement shown in Fig. 5.15a shows a perfect correspondence to the literature value,

with critical temperature $T_c = 7.21\,\mathrm{K}$ and transition width $\Delta T = 0.03\,\mathrm{K}$, validating the good calibration of the measurement system. The slight broadening of the transition at the offset and onset points is likely due to the magnetic field at the surface (about 0.4 mT) exceeding the critical field of lead near T_c (about 0.2 mT as reported in [166]). This effect is also possibly promoted by the field enhancement at the sample edges, which could induce the intermediate state in small areas. The leak field in the superconducting state corresponds to a background signal of 1.5 µV, which is the minimum observed signal in case of a bulk sample and without applying any physical noise shielding to the experimental setup.

From the reference measurement on lead, and upon comparison to the accepted T_c value for lead of $T_c^{\mathrm{lit}}(\mathrm{Pb}) = 7.19\,\mathrm{K}$ found in literature [167], [168], a level of accuracy of

$$100 - \frac{|T_c^{\mathrm{lit}}(\mathrm{Pb}) - T_c(\mathrm{Pb})|}{T_c^{\mathrm{lit}}(\mathrm{Pb})} \times 100 \geq 99\% \tag{5.9}$$

can be safely stated for the measurement station.

BULK NIOBIUM

Niobium is a type-II superconductor, with critical temperature T_c typically between 9.2 K and 9.3 K. A broadening of the transition curve may be expected in case of type-II due to the fact that the sample will enter the intermediate-mixed state if the field at the surface approaches the critical field. This is not observed in this case, as it can be seen in Fig. 5.15b where the measurement of the superconducting transition of a bulk niobium sample is shown. The curve shows a sharp transition at $T_c = 9.38\,\mathrm{K}$ with $\Delta T = 0.01\,\mathrm{K}$. The field at the sample surface, estimated to be about 0.4 mT as already mentioned above, does not exceed the critical field of niobium close to T_c (about 9.8 mT as reported in [169]). Due to the absence of visible broadening of the transition at the offset and onset points, possible demagnetization effects due to field enhancement at the sample edges are also excluded in this case, so that the transition in bulk niobium is observed to be narrower than in lead. The higher critical temperature with respect to the literature value is ascribed to the stress induced in the material by the milling process applied to thin the niobium sheet from its initial

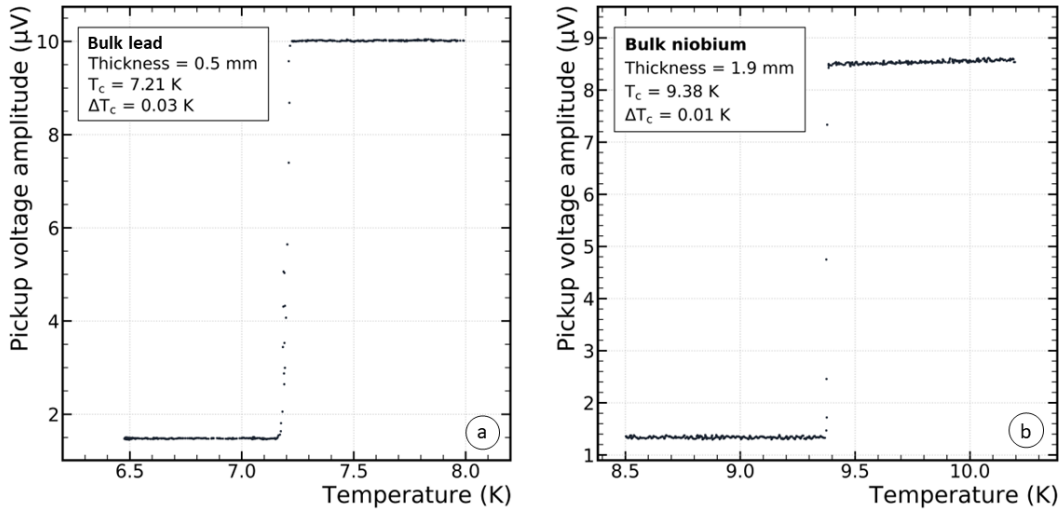

FIGURE 5.15: Inductive measurement of the superconducting transition of the bulk lead (a) and bulk niobium (b) reference samples.

thickness of 3.6 mm down to the required 1.9 mm thickness. The background (leak) signal level is the same as the one observed in lead, corresponding to 1.5 µV.

THICK NIOBIUM FILM ON COPPER

This sample consists of a thick niobium film deposited sequentially via DCMS technique. The final film thickness of 45 µm is reached by coating eight consecutive layers each 0.5 µm thick, followed by a final 5 µm thick layer. This approach is pursued in the attempt to reduce the residual stress of the final film [170] which would occur naturally due to the PVD process. The measured critical temperature $T_c = 9.33\,\mathrm{K}$ extracted from the measurement in Fig. 5.16a is indeed comparable to the one of the stressed bulk sample, with $\Delta T = 0.02\,\mathrm{K}$. The background signal at 2 µV is slightly larger than the one observed for the bulk samples as a consequence of the weaker screening currents forming in the film. The small signal rise observable just before the transition is due to early field penetration near T_c, most likely at the sample edges.

THIN NIOBIUM FILM ON COPPER

This 6 µm thick sample was coated at CERN via HiPIMS technique purposely as a reference sample for the T_c measurement station. The transition measurement of this sample is shown Fig. 5.16b. The extracted critical temperature $T_c = 9.44\,\mathrm{K}$ suggests a higher stress level than the thick film deposited sequentially. The broader transition with $\Delta T = 0.05\,\mathrm{K}$, in comparison to the thick film, is generally an indication of a poorer superconducting phase, as well as the larger background signal, here 2.5 µV, is an indication of weaker screening currents.

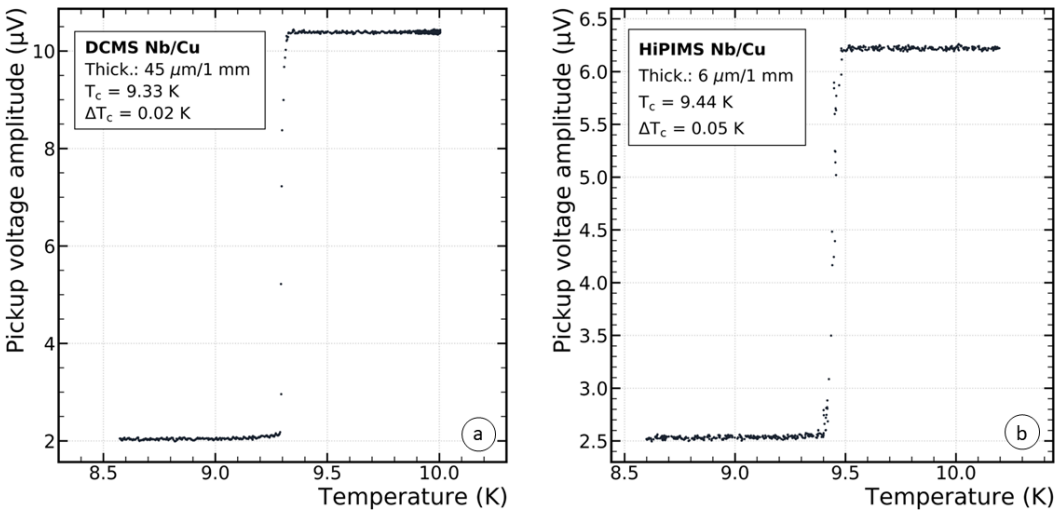

FIGURE 5.16: Inductive measurement of the superconducting transition of a thick (45 µm) niobium film on copper (a) and a thin (6 µm) niubium film con copper (b) as reference film samples.

THIN Nb_3Sn FILM ON CERAMIC

This film was deposited at CERN via DCMS as a reference to assess the influence of the substrate on Nb_3Sn films deposited on copper. It's critical temperature was already measured via four-probe to be 17.4 K [26], with the curve onset interpreted as T_c. The measurement performed here is shown in Fig. 5.17 and proves good

agreement with the four-probe measurement, with a T_c of 17.03 K (extracted with the 10% – 90% method) and $\Delta T = 0.29$ K. The broad transition is likely due to the non homogeneity of the film. A background signal of 3 µV is observed, the largest of all reference samples, indicating the weakest screening currents.

All the the samples on which these reference measurements were performed are carefully stored at CERN and available upon request for a reassessment of the measurement station response.

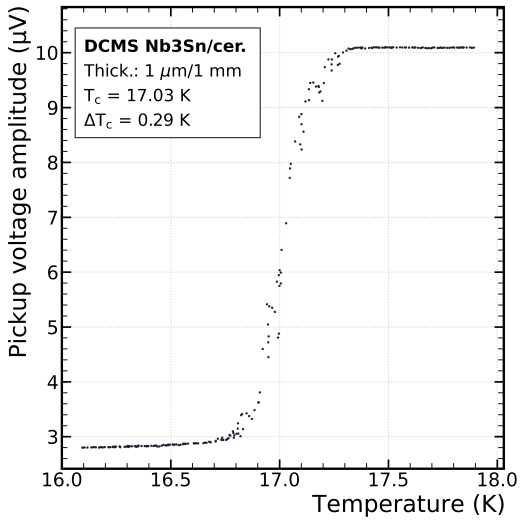

FIGURE 5.17: Inductive measurement of the superconducting transition of the DCMS coated Nb_3Sn film on Al_2O_3 ceramic substrate.

Material	**Sample thickness** (mm)	**Film/substrate thickness** (µm/mm)	T_c (K)	ΔT_c (K)
Bulk lead	0.5	–	7.21	0.03
Bulk niobium	1.9	–	9.38	0.01
Nb/Cu DCMS	–	45/1	9.33	0.02
Nb/Cu HiPIMS	–	6/1	9.44	0.05
Nb_3Sn/cer. DCMS	–	1/1	17.03	0.29

TABLE 5.2: List of reference samples for the T_c measurement station. All the samples have the same standard surface size of 11×35 mm^2, while the thickness is indicated in the table. The measured T_c and ΔT are also given.

Some general statements can be done at this point on the performance of the test station and what can be observed with the T_c measurements. Although it does not have a direct influence on the measured value of T_c, as a feature of these type of measurements it is worth noticing how the signal at the normal conducting part of the transition curve corresponds to different values for most samples. For lead and Nb_3Sn/ceramic a signal of about 10 µV is observed, corresponding to the only coil signal as shown in Fig. 5.9. This is expected as 0.5 mm of lead and Al_2O_3 are completely transparent to the magnetic field. Bulk niobium should also be transparent to the magnetic field, however the measured sample is thick enough to develop eddy currents which are visible in the signal, lowered to about 8.5 µV. The copper substrates also show a different behaviour: for the OFHC copper substrate a RRR of

about 100 – 150 is assumed, which is not enough for the induced eddy currents to cause a detectable screening at the involved temperatures. The observed signal of 10.4 µV is indeed compatible with the only coil signal. The OFE copper instead is expected to have a RRR of about 150 – 300, which is enough for the eddy currents to form a detectable shielding, resulting in a signal of about 6.2 µV, also compatible with what shown in Fig. 5.9.

5.5.2 Features of damaged or "non-standard" samples

For elemental materials, one can associate a T_c close to the literature value to a good purity level of the material. A higher value is always expected for thin films or for stressed bulk samples. This changes for compounds such as Nb_3Sn, as the T_c value also depends on the film stoichiometry and the stress level affects differently T_c depending on whether it is tensile or compressive [171]. A compact, homogeneous and pure sample is expected to show a sharp transition.

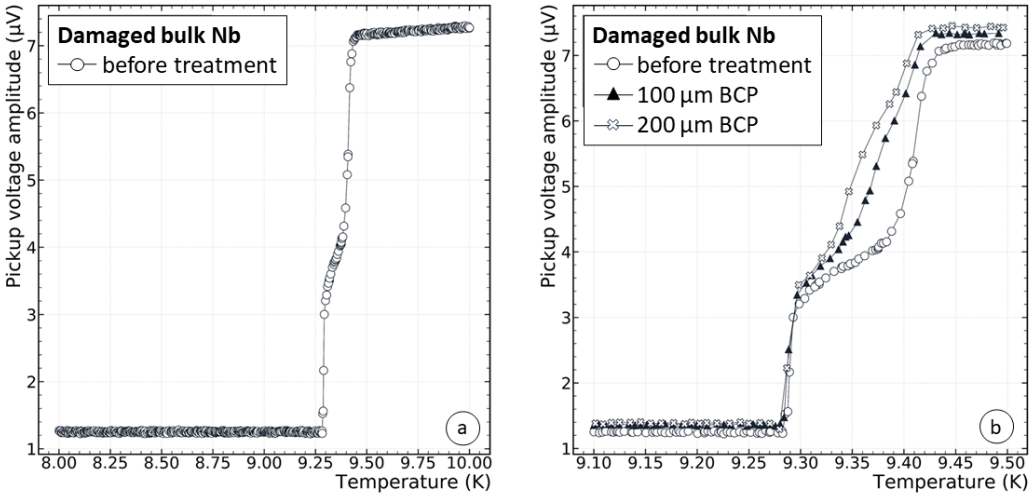

FIGURE 5.18: (a) Superconducting transition of a damaged bulk niobium sample sporting a bent shape towards higher temperatures due to the presence of mechanical stress in the surface layer. (b) Superconducting transition of the same sample measured again after each one of two consecutive runs of BCP, meant to remove about 100 µm of damaged material each time. The temperature axis is zoomed in around the transition to highlight the separation between the curves.

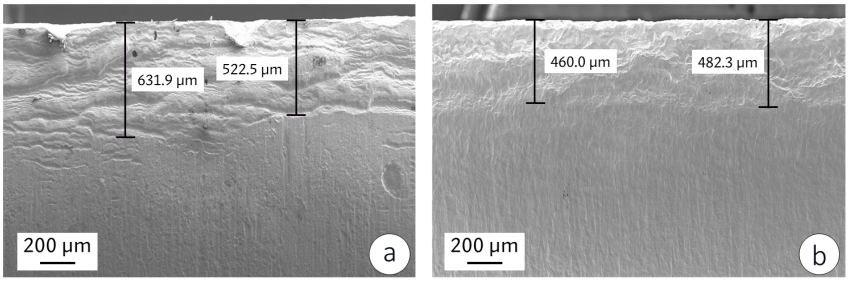

FIGURE 5.19: SEM images of the damaged niobium sample cross section, as measured for the first time (a) and after two runs of BCP (b).

As an example of what can be observed when this is not the case, the measurement of the superconducting transition of a bulk niobium sample which happened to be structurally damaged[3] is shown in Fig. 5.18a. The transition starts sharp at about 9.3 K but at approximately half-height, the curve appears to bend towards higher temperatures. Under the assumption that this behaviour was due to mechanical stress present at the sample surface, the sample was subjected to two separated runs of BCP to remove, at each run, approximately 100 µm of damaged material. The critical temperature of the sample was measured again after each BCP run and the results are shown in Fig. 5.18b together with the initial measurement for comparison. The temperature axis is zoomed in closer to the transition to highlight the difference between the three curves. From this graph it becomes clear how progressively removing damaged material has the effect, at each step, of gradually restoring the shape of the transition to the single step that would be expected to take place at the temperature where the transition starts. The observed behaviour is supported by the SEM images of the sample, where the initial damaged layer is clearly visible in Fig. 5.19a, and the same layer of reduced thickness following the two BCP runs is visible in Fig. 5.19b. The presence of the damaged layer, although reduced, after the chemical treatments explains that the transition curve is not fully restored.

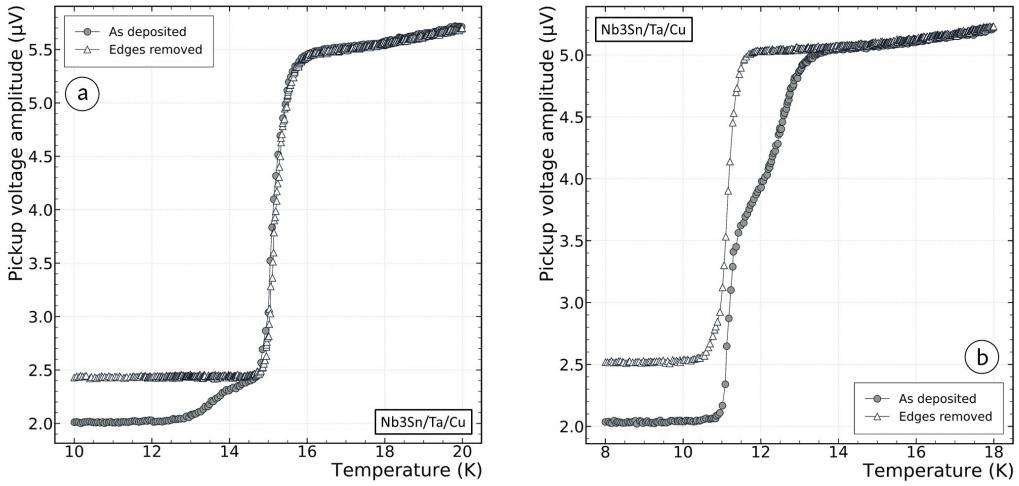

FIGURE 5.20: Superconducting transition of a Nb_3Sn/Ta/Cu sample with coating on the substrate edges sporting (a) a step-like feature at the base of the transition and (b) a bent shape towards higher temperatures as also observed in the case of a damaged bulk niobium sample (Fig. 5.18).

Another case of irregular transition curve is observed when a thin film sample is not only deposited on the main face of the substrate, but also covers the side edges. This is often observed to happen in samples coated with HiPIMS, as a high amount of the sputtered species is ionised and hence accelerated toward all sides of the substrate, unlike the neutral species in DCMS which fly ballistically toward the substrate and mainly deposit on the sample surface directly facing the material source. These dynamics of thin film physical vapour deposition processes are discussed more in detail in Chapter 4. The geometric effect of the position of the sample edges with respect to the magnetic field lines inside the experimental chamber (see Fig. 5.7) combined with the additional effect of a possible different film composition in the case of non-elemental samples such as Nb_3Sn can result in step-like features

[3]Possibly from the rolling or deep drawing process taking place during sheet production.

or irregular transition shapes. Examples of these are shown in Fig. 5.20, where the measurements of two different Nb_3Sn/Ta/Cu samples are presented. In Fig. 5.20a, a step-like feature appears at the base of the transition curve, while in Fig. 5.20b the transition is bent forward towards higher temperatures (similar to what observed in the case of the damaged bulk niobium sample in Fig. 5.18). In both cases, measuring the sample again after having removed the coating from the edges of the substrates results into a "fixed" transition curve.

A step-like feature similar to the one observed in Fig. 5.20a is also also observed in Fig. 6.6, the measured transition curves of the niobium control samples deposited on aluminium substrate for the reverse-coating study presented later on in Chapter 6.

Disclaimer: this work, in particular the part about the simulations and the design of the LabView user interface for the measurement station, was performed in collaboration with A. P. O. Vaaranta, who spent his Technical Studentship at the Central Cryogenic Laboratory at CERN during the time of the measurement station development, and is currently based at University of Helsinki. The commissioning of the test station was guided by T. Koettig and several mechanical parts for the test station were fabricated by A. Vacca, both from the CERN Central Cryogenic Laboratory's staff.

Chapter 6

Reverse-coating technique for a seamless copper substrate

In this Chapter, the first feasibility study of a new production method for seamless niobium-coated copper SRF cavities, already published on Superconductor Science and Technology [28], is presented and discussed. The method, addressed as 'reverse-coating', inherits from the original study for the production of non-evaporable getter (NEG) coated, small diameter beam vacuum chambers [29], [172]. In Section 6.1 the method is introduced conceptually. The preparation of the samples is presented in Section 6.2. Section 6.3 is dedicated to the characterisation measurements. Finally, the results are presented and discussed in Section 6.4.

6.1 The reverse-coating technique

The performance of niobium-coated copper superconducting radio-frequency (SRF) cavities is known to be closely related to the quality of the substrate [14]. While parameters such as surface roughness can be optimised to a certain degree, the presence of seams and welds cannot be completely avoided with standard cavity fabrication methods [21], [22], [91], [173], [174]. A possible way to avoid their presence is offered by the production of copper cavities via electroforming around a sacrificial aluminium mandrel, whose shape and size emulate the ones desired for the final cavity. The electroforming technique has already been shown to deliver cavities whose copper final properties are comparable to oxygen-free electronic (OFE) grade bulk copper [23], [175], and whose inner surface mirrors the mandrel finish.

Once the quality of the electroformed copper cavity structure has reached a satisfying level, the next step is to study the possibility of reproducing the process by also integrating the functional superconducting layer. In addition to the production of seamless niobium-coated copper cavities, a successful outcome of this process would lead to better adherence, with respect to their counterparts produced according to the standard methods, of the superconducting film to the copper substrate and make the non-trivial chemical treatment of the substrate in preparation to the coating, foreseen by the standard procedures (e.g. SUBU, EP), no longer needed as the substrate is directly formed on the film itself.

The general concept is represented in Fig. 6.1: the aluminium mandrel (A), which mimics the final cavity shape, is first coated with the niobium film (B), then with a copper film (C) which will serve as an adhesive layer for the final copper structure to be electroformed on it (D). Finally, the aluminium mandrel is etched (E) to deliver the complete structure consisting of the copper cavity with the film already included in it. This first study presented here is carried out on a simpler geometry than the elliptical cavity, such as a flat disk. The main process of sample production is repeated twice: in the first case, the niobium layer is coated directly on the aluminium

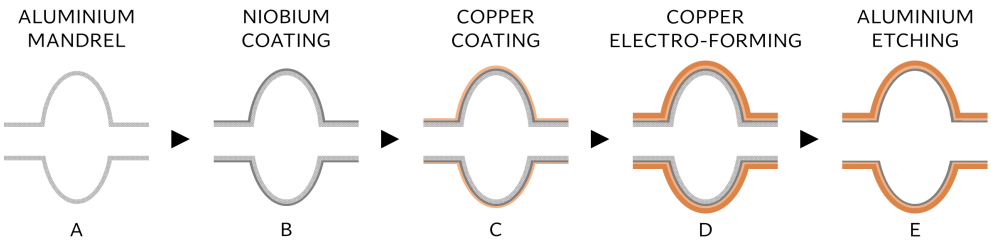

FIGURE 6.1: Schematic step sequence of the reverse-coating method for the production of seamless Nb/Cu cavities.

disk, while in the second case a copper layer is coated on the aluminium, prior to the deposition of the niobium film, for later protection of the niobium from possible damage caused by the final chemical removal of the mandrel.

6.2 Sample preparation

Two sets of samples where produced for this study: the control set and the reverse-coated set. The control samples, consisting of niobium-coated aluminium substrates, served as check for the reverse-coated samples. The reverse-coated samples are produced by electroforming copper on a sacrificial aluminium mandrel which has been pre-coated with a niobium thin film. The process consists of the following essential steps:

1. manufacturing of the aluminium mandrel;
2. niobium coating of the aluminium mandrel;
3. copper coating on top of the niobium layer, to improve the adhesion of the electroplated copper layer;
4. electroforming of the final copper structure on the coated copper layer;
5. chemical etching of the aluminium mandrel to obtain the final copper structure with internal niobium coating.

The next Paragraphs provide the details about each step.

MANDREL MANUFACTURING

In this study, the sacrificial mandrel is represented by a 150 mm diameter and 1.5 mm thick flat aluminium disk. The disks were machined in order to obtain a constant surface roughness (R_a) of 0.3 µm and degreased with a commercial detergent solution (60 °C, 30 min). The study was repeated identically with commercially pure aluminium (AW-1050, 99.5% pure) and with an aluminium alloy in the wrought aluminium-magnesium-silicon family (AW-6082) as base material, with the aim of evaluating the potential impact of impurities originating from the mandrel on the final niobium layer.

Two disks were prepared for each aluminium type: one for the control samples and one for the reverse-coated samples. For the control samples, a total amount of six substrates of size $11 \times 35 \times 1.5\,\text{mm}^3$ were cut from the aluminium disks (three per aluminium type) prior to the niobium coating.

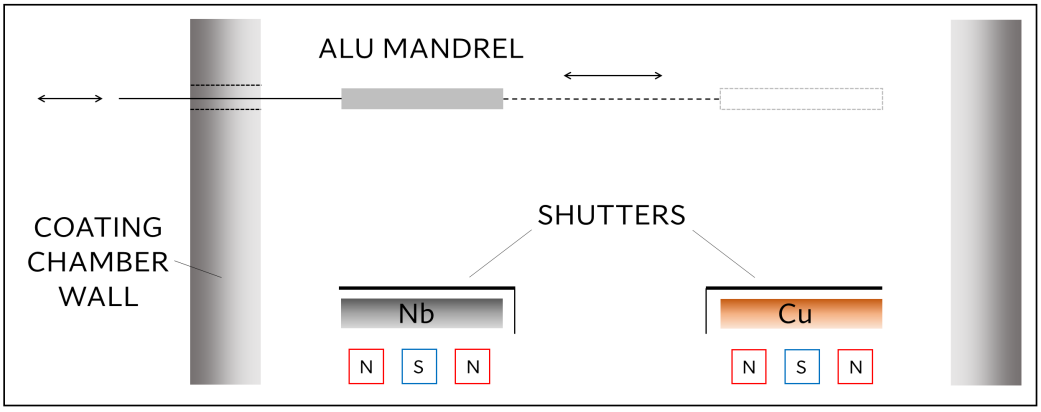

FIGURE 6.2: Readapted [172] schematics of the sputtering system used for the coating of the mandrels. The aluminium mandrel is mounted on a translation ultra-high vacuum (UHV) manipulator which allows its position to be adjusted without venting the system. The targets, niobium (left) and copper (right), are depicted with their magnet arrays providing the magnetron field. The shutters cover the targets when not in use.

	Material		
Coating parameter	Nb	Cu (A)	Cu (P)
P_{Kr} (mbar)	1.4×10^{-3}	1.4×10^{-3}	1.2×10^{-3}
MP amplitude (V)	-500	-760	-760
MP duration (µs)	50	50	50
Peak current (A)	33	22	20
Peak power (kW)	15	15	14
Average power (W)	280	350	310
PP amplitude (V)	130	130	130
PP duration (µs)	200	200	200
Delay (µs)	1	1	1
Frequency (kHz)	1	1	1
t_{coat} (min)	240	120	90

TABLE 6.1: Coating parameters for the deposition of the niobium film and copper adhesion film (A) in Run I and Run II, and for the deposition of the copper protective film (P) in Run II. All the coatings were performed in krypton atmosphere. MP and PP stand for main pulse and positive pulse respectively.

COATING OF NIOBIUM AND COPPER

The coating chamber is equipped with both the niobium and copper cathodes. The substrate/disk holder is placed at the extremity of a translation ultra-high vacuum manipulator, as shown in Fig. 6.2, so that the disk can be moved from the position on top of the niobium cathode to the one on top of the copper cathode (and vice versa) without the need to open the chamber. Thanks to this system, the niobium and copper films can be coated consecutively without venting the system in between, hence avoiding the risk of contamination due to contact with air.

Before the coatings, the bake-out of the system was performed at 120 °C for 24 hours. During the coatings, the equilibrium temperature reached by the system is 150 °C. All the coatings in this study were performed via bipolar-HiPIMS.

The control samples were coated first. A 1 µm thick niobium film was deposited on the aluminium substrates and analysed in order to establish a custom coating recipe and a reference to the structural and superconducting properties expected for niobium films deposited on aluminium via bipolar-HiPIMS [17], [19], [176].

To produce the reverse-coated samples two different approaches were applied, which are schematically represented in Fig. 6.3. In the first case (Run I), a 1 µm niobium film was deposited directly on the aluminium mandrel. In the second case (Run II), a 1 µm thick copper layer (addressed later on as protective layer (P)) is deposited on the aluminium mandrel *prior* to the niobium (i.e. between the aluminium and the 1 µm niobium layer deposited later on). In both cases, a 3 µm thick copper layer was finally deposited on top of the niobium film, to serve as adhesion layer (A) for the electroforming of the final copper structure. The parameters of the sputtering process are summarised in Table 6.1.

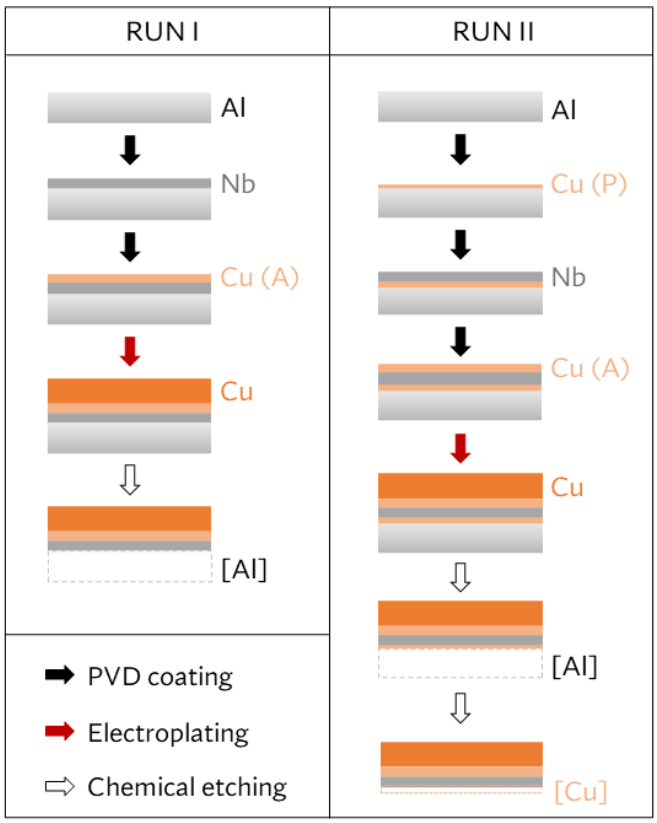

FIGURE 6.3: Schematics of the reverse coating technique steps for the case without a copper protective layer (Run I) and with copper protective layer (Run II). The etched layers are indicated in dashed contours and labeled in square brackets.

ELECTROFORMING OF COPPER

After the coating, in order to electroform the final copper structure, the mandrels were assembled on a special support which provides an electrical contact and, at

the same time, protects the mandrel from the undesired deposition of copper on the rear side. The electroplating of a 0.5 mm thick copper layer was performed in a copper sulphate ($CuSO_4\,5\,H_2O$) sulfuric acid (H_2SO_4) bath with the presence of a brightener, with an applied current of 200 A/m^2 for a duration of 20 h. The mandrel before and after the coating phase, and after the copper electroforming (with and without support) can be seen in Fig. 6.4.

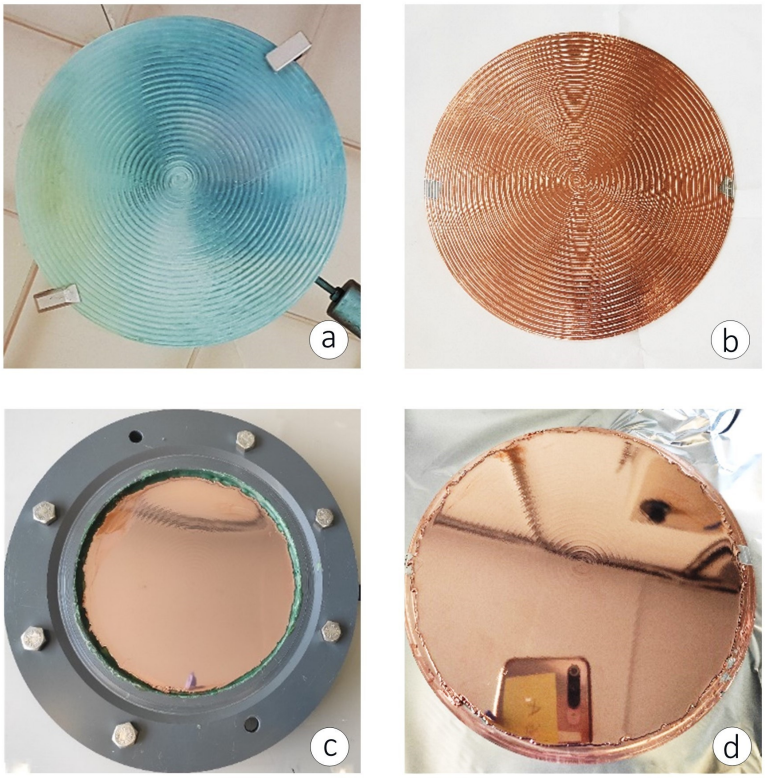

FIGURE 6.4: AW-1050 aluminium mandrel mounted inside the coating chamber before the coating of the niobium and copper adhesion films (a), after the coating (b) and after the electroplating of the final copper structure, still mounted on the special support for the electroplating (c) and without the support (d).

ETCHING OF THE MANDREL

Finally, the mandrels were dismounted from the support for the electroplating and samples of size $10 \times 35 \times 1.5\,mm^3$ were cut from them to proceed with the characterisation, which was done both with the aluminium mandrel still present (i.e. before etching) and after the aluminium mandrel removal.

The chemical etching of the aluminium mandrel was performed in a sodium hydroxide bath (NaOH $5 \times 10^3\,mol/m^3$, room temperature). For the samples having the protective copper layer on top of the niobium, ammonium persulfate ($(NH_4)_2S_2O_8$ 150 g/L, room temperature) was also used to chemically etch the protective copper layer after the aluminium removal. The etched layers are indicated enclosed in square brackets (e.g. [Al], [Cu]) in Fig. 6.3 and in the text to follow.

6.3 Sample characterization

After the production of every sample batch (control samples, reverse-coated samples without copper protective layer, reverse-coated samples with copper protective layer), the morphology and superconducting performance of the niobium films were evaluated. At this early stage of the study, it was important to assess the potential of the reverse coating technique to deliver suitable niobium films for an SRF end-use, exhibiting satisfying purity levels and regular morphology, free of porosities. Hence the characterisation phase focused on the measurement of the critical temperature T_c and on the imaging of the sample cross section. In the case of the reverse-coated samples, the measurement of T_c was performed before and after the mandrel removal and the results are presented together for comparison. Based on the outcome, the characterisation was carried further on with the measurement of the critical current density J_c for a selection of samples that showed the best properties. This physical quantity depends on the concentration of pinning centres [177], [178], provides insight into the amount of structural defects [179] which can be present in the material and is currently under investigation as a possible DC superconducting property that can potentially give early insight about the later RF performance of the film [121], [127].

The critical temperature was measured via the induction coil technique with the test station presented in Chapter 5.

The cross section of the films for morphology investigation was prepared via focused ion beam and analysed via scanning electron microscopy (FIB-SEM). The used equipment is located at the Materials and Metrology laboratory at CERN and consists of a Zeiss Crossbeam 540 SEM equipped with FIB. The imaging is performed by InLens and Secondary Electron Secondary Ion (SESI) detectors. In order to perform the milling needed for inspection of the sample cross section, a protective platinum layer ($20 \times 2 \times 1$ µm^3) is deposited with an ion beam current of 300 pA and accelerating voltage of 30 kV. This is a standard practice in FIB-SEM applications, as this additional layer protects the sample from high-energy ions during imaging and reduces charging effects caused by the ion beam. Platinum is usually chosen because of its high conductivity and contrast in electron microscopy. In this case, a $20 \times 10 \times 4$ µm^3 sample volume was then coarsely milled with an ion beam current of 3 nA and accelerating voltage of 30 kV. Prior to imaging, the cross sectional surface was smoothened with an ion beam current of 300 pA and accelerating voltage of 30 kV. The SEM imaging of the sample cross sections was performed at an accelerating voltage of 3 kV. Thanks to this technique it was also possible to infer the average film thickness.

The critical current density of the films was measured at the University of Geneva by means of a Superconducting QUantum Interference Device (SQUID) Vibrating Sample Magnetometer (VSM) by Quantum Design. The device is equipped with a superconducting coil able to generate magnetic fields up to 7 T and to cover the temperature range 1.8 K – 400 K. For these measurements, the standard sample size is 3×3 mm^2 with variable thickness: 1.5 mm for the aluminium substrate and 0.5 mm for the copper substrate. By measuring isothermal loops of the magnetic moment $m(B)$ in the field range - 7 T – 7 T it is possible to calculate J_c in the frame of the Bean critical state model [180] using the equation $J_c(T,B) = \frac{2\Delta m(T,B)}{Vt}$, which is valid for a slab geometry in parallel magnetic field, where $\Delta m(T,B)$ is given by the separation of the branches of the magnetic moment loop $m(B)$ measured with opposite field sweep directions at a given temperature T, and Vt is the product of the volume V of the superconducting sample and its thickness t. The temperature values at which

the loops $m(B)$ are measured range from 2.5 K to 9 K. This investigation also allows the estimation of the upper critical field B_{c2}, defined here as the intersection point of $J_c(B)$ with the $J_c = 0$ line.

6.4 Results and discussion

In the following sections the outcome of the characterisation of the Nb-Al control samples, the Cu-Nb-[Al] samples from Run I and the Cu-Nb-[Cu]-[Al] samples from Run II is presented and discussed in detail for each case. The results of the characterisation measurements are summarised in Table 6.2 for all the samples.

6.4.1 Nb-Al control samples

The niobium control samples deposited on the aluminium substrates were analysed first, in order to assess the quality of the coating recipe and the features presented by the film on the aluminium substrate. In Fig. 6.5 the substrates are shown mounted on the disk holder before (a) and after (b) the niobium coating. Aluminium AW-1050 was used for samples 1, 2 and 3, while AW-6082 was used for samples A, B and C.

The inductive measurement of the critical temperature lead $T_c = 9.33$ K and $T_c = 9.32$ K for the films on the AW-6082 and AW-1050 substrates respectively, as shown in Fig. 6.6. The width of the transition curve, $\Delta T_c \simeq 0.11$ K (AW-6082) and $\Delta T_c \simeq 0.1$ K (AW-1050). The shape of the superconducting transition curves obtained with the inductive measurement is shown in Fig. 6.6 and does not present any unusual feature, suggesting the absence of anomalies in the control films that could affect the superconducting state and the passage to the normal state. A higher value of T_c is normally observed for niobium films with respect to their bulk counterpart due to residual compressive stress induced during the sputtering process, and is expected to decrease with increasing sample thickness [181]. The measured values are nevertheless comparable to T_c of the pure bulk material [182], indicating a good level of purity of the control films. In addition to this, it is possible to observe

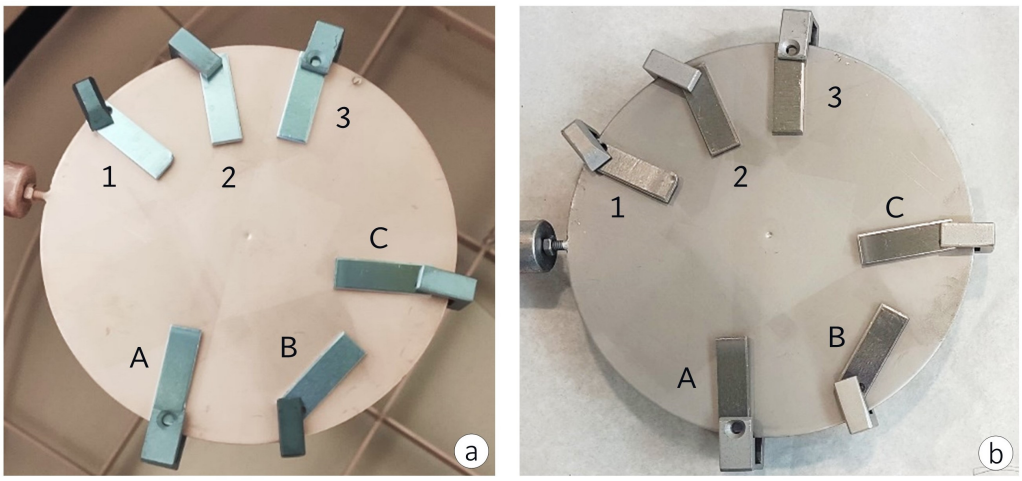

FIGURE 6.5: Aluminium substrates mounted on the disk holder before (a) and after (b) the coating of the niobium control film. The AW-1050 substrates are labeled as 1, 2, and 3; the AW-6082 substrates are labeled as A, B, and C.

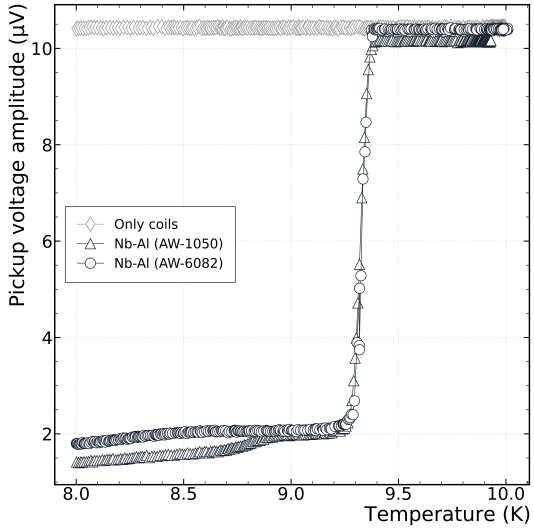

FIGURE 6.6: Inductive measurement of the superconducting to normal conducting state transition of the niobium control samples deposited on the AW-6082 (circles) and AW-1050 (triangles) aluminium substrates (black). The bare coil signal is also shown for comparison (triangles, grey). The sample T_c is extracted as the temperature corresponding to the half-height of the transition curve.

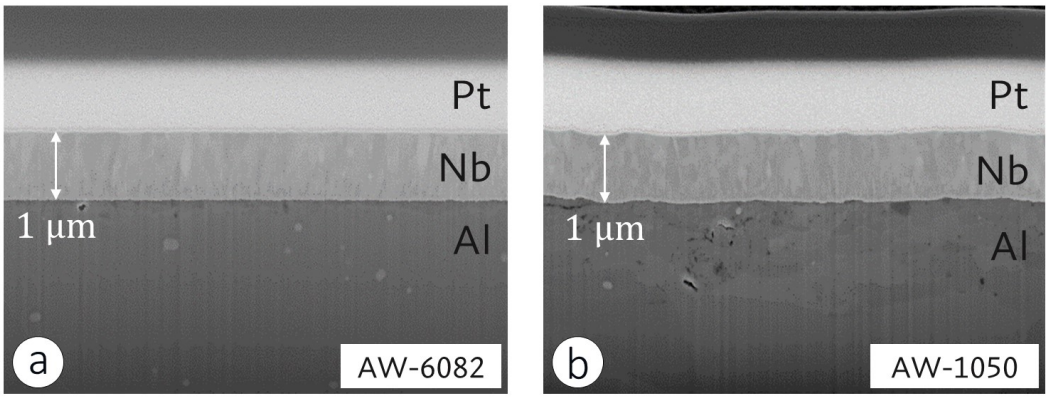

FIGURE 6.7: SEM micrographs of the FIB-milled cross section of the niobium control samples. The sample deposited on the AW-6082 substrate is shown in (a) and the one deposited on the AW-1050 substrate is shown in (b). In both images, the platinum (Pt) protective layer is visible on top, followed by the niobium film (Nb) in the middle and the aluminium substrate (Al) at the bottom. The indicated film thickness of 1 μm also provides the image scaling.

that films deposited on aluminium alloys of different purity show the same T_c, suggesting that the purity of the mandrel employed in the reverse coating process is not expected to be relevant for the purity of the functional niobium layer. The transition width ΔT_c is comparable to what is observed from typical inductive measurements of bulk niobium ($\Delta T_c \simeq 0.05\,\mathrm{K}$), also an indication of a low concentration level of impurities in the samples. The signal produced by the leak field when the samples are in the superconducting phase ($T < T_c$) is the same, as shown by the overlapping signal before the phase transition takes place, and differs towards lower temperatures due to effects of the coating on the sample edges, as previously discussed in

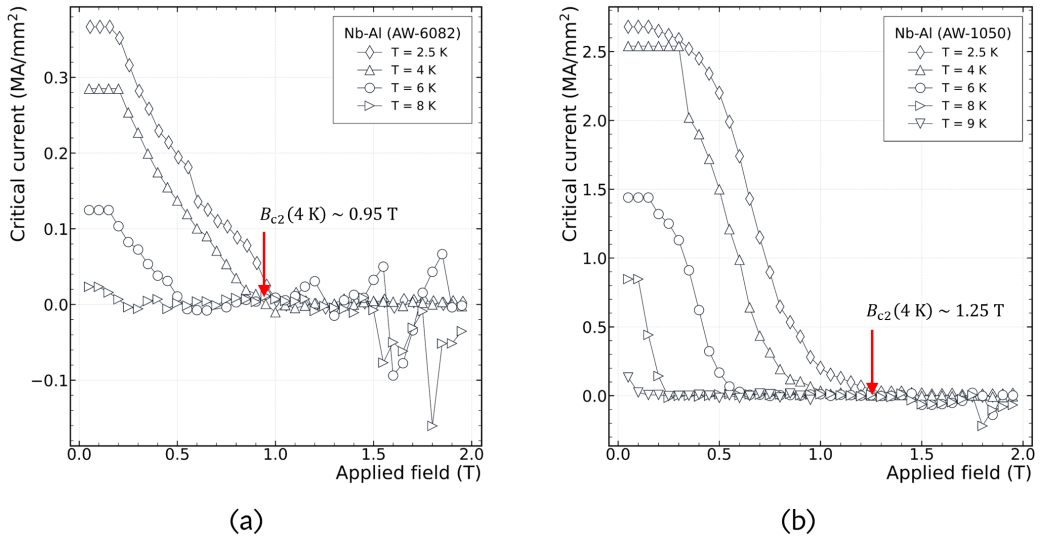

FIGURE 6.8: Critical current J_c of the niobium control samples calculated, in the framework of the Bean critical state model, from the VSM-SQUID measured sample magnetic moment loops $m(B)$ at different fixed temperatures. The upper critical field B_{c2} is taken as the field value at which $J_c(4\,\mathrm{K}) = 0$. The curves measured for the sample deposited on the AW-6082 and the AW-1050 substrates are shown in plot (a) and (b) respectively.

Section 5.5.2. The difference in amplitude between the signals on the normal conducting side of the curve (for $T > T_c$) does not depend on the films but rather on the different composition of the aluminium alloys used as substrate. For temperatures lower than 10 K, an electrical resistivity of $\rho > 0.1$ μΩ cm has to be expected for the AW-6082 and AW-1050 alloys [183], which results into a minimum skin depth of 3.5 mm for the aluminium substrates at the applied frequency of 21 Hz. Although this is more than a factor 2 larger than the substrate thickness, making it nearly transparent to the magnetic field, the difference in resistivity between the two alloys is such that the eddy currents induced in the aluminium by the magnetic field have higher intensity for the alloy with smaller resistivity (AW-1050). This finally leads to a stronger screening by the eddy currents induced into the AW-1050 substrate than the ones in the AW-6082: the latter are indeed not strong enough to separate the normal conducting signal from the signal induced into the pickup coil without a sample in between the coils (shown in light grey in Fig. 6.6), while in the lower resistivity alloy the currents are intense enough to partly screen the magnetic field and separate the signal from the bare-coils one.

The SEM images of the niobium film FIB-milled cross section are shown in Fig. 6.7, with the film coated on the AW-6082 substrate shown in Fig. 6.7a and the one on the AW-1050 substrate in Fig. 6.7b. In both images, the protective platinum layer (Pt) is visible as first layer on top, followed by the niobium film (Nb) below and the aluminium substrate last (Al). Both niobium films appear dense, free of voids and show good adhesion to the substrate. The columnar growth pattern typical of PVD thin films is also visible, with a coarser structure at the substrate interface, this being the first one to be deposited and therefore containing the initially nucleated film grains [139]. The SEM imaging of the film cross section made also possible to infer the average thickness of the niobium layer to be 1 μm along the milled length for both samples. The critical current density J_c extracted from the $m(T, B)$ loops is

shown in Fig. 6.8a for the film deposited on the AW-6082 substrate and in Fig. 6.8 b for the one deposited on the AW-1050 substrate. The $m(T, B)$ loops were measured at four different fixed temperatures: 2.5, 4, 6, and 8 K, and five different fixed temperatures: 2.5, 4, 6, 8 and 9 K for AW-6082 and AW-1050 respectively. The resulting J_c values at $B = 0.2$ T and $T = 4$ K are 0.29 MA/mm^2 for the sample on the AW-6082 substrate and 2.5 MA/mm^2 for the sample on the AW-1050 substrate. It is preferable that niobium films produced for SRF application exhibit critical current values which are as low as possible, and these values can be considered satisfying [179] for a niobium film of 1 µm thickness within the scope of this study. However, they still suggest the presence of high density of dislocations in the material [17]. One can also consider further reducing this J_c value especially when compared to currently used state-of-the-art bulk Nb that exhibits critical current density values in the order of 10 kA/mm^2[184]. From the measurements of J_c the upper critical field $B_{c2}(4\,\mathrm{K})$ was estimated to be $\simeq 0.95$ T and $\simeq 1.25$ T for the films deposited on the AW-6082 and the AW-1050 alloy substrates respectively.

Overall, the control niobium films exhibited good superconducting properties and classic structural defects, reason why the same coating recipe was also adopted for the next two coating runs for the production of the reverse-coated samples. In light of the results obtained with the characterisation measurements of the control samples, to avoid redundancy only the results obtained for the samples produced with the AW-1050 aluminium mandrel will be presented and discussed in the next subsections.

6.4.2 Run I: reverse Cu-Nb samples without Cu protective layer

The inductive measurement of the Run I samples, shown in Fig. 6.9, lead to a regular transition curve only for the Cu-Nb-Al (pre-etching) sample, while for the Cu-Nb-[Al] (post-etching) it revealed a poor-to-absent superconducting phase. From the measurement of the Cu-Nb-Al sample it is possible to extract a critical temperature of $T_c = 9.35$ K, with a width ΔT_c of about 0.16 K, while the post-etching measurement of the Cu-Nb-[Al] sample shows a poor-to-absent superconducting phase, as it can be seen in Fig. 6.9. The signal for $T > T_c$ corresponds to 9.2 µV and 9.6 µV for the samples with and without the aluminium mandrel respectively. For $T < T_c$ only the Cu-Nb-Al sample shows superconducting screening with a constant signal at about 2 µV. The Cu-Nb-[Al] sample signal is 7.6 µV already at $T = 8$ K and rises smoothly to its normal-conducting value showing an edge-like feature at a temperature of 9.35 K.

The fact that the Cu-Nb-Al sample showed a higher value for T_c than the control samples is likely an indication of a higher compressive residual stress level. This can be explained considering that in this case, not only the niobium film suffers from the residual stress caused by the growth process on the aluminium, but it is also constrained by the additional copper layer grown onto it which in turn adds up to the original stress introduced by the first coating. The increased transition width suggests the possibility of larger concentration of impurities with respect to the control samples. The signal for $T > T_c$ is about 1 µV smaller for this sample with respect to the control samples due to the presence of the copper layer. The copper electroformed according to the procedure described in Section 6.2 has been shown to have properties comparable to the OFE-grade copper [23] employed at CERN for the production of SRF cavities. One can assume RRR ≥ 50 and hence an electrical resistivity $\rho \leq 0.03$ µΩ cm for low temperatures (< 10 K). This results in eddy currents which are a factor 3 - 4 higher in intensity than in the aluminium mandrel and whose effect

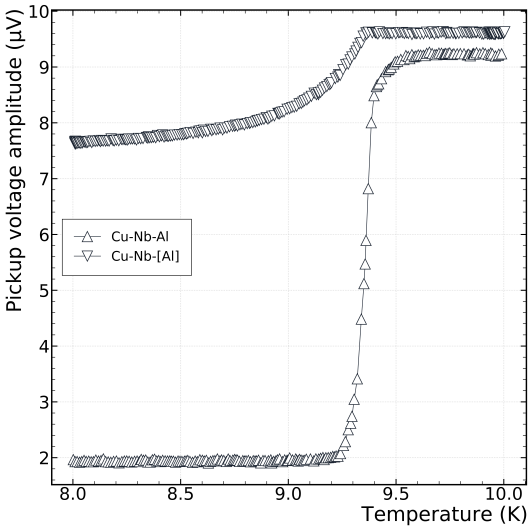

FIGURE 6.9: Inductive measurement of the superconducting transition of the Cu-Nb-Al sample (Run I) before and after the etching of the aluminium mandrel. The phase transition in the Cu-Nb-[Al] sample appears degraded by the mandrel removal process.

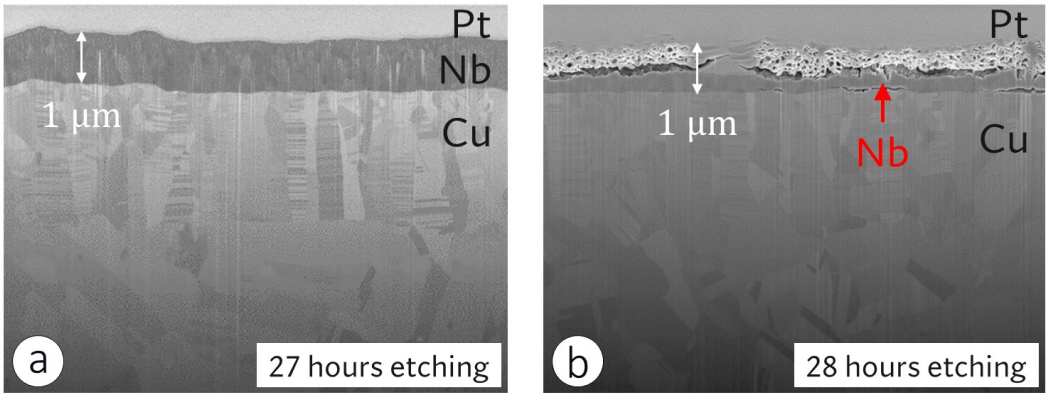

FIGURE 6.10: SEM micrographs of the FIB-milled cross section of the reverse coated Cu-Nb-[Al] samples. In (a) is the sample etched for 27 hours, time needed for the complete removal of the aluminium. In (b), the sample etched for 28 hours, showing the signs of damage from exposure to the etching solution.

results into a normal conducting signal which is about a factor 4 more damped for the reverse coated Cu-Nb-[Al] sample than for the Nb-Al (AW-1050) control sample. The normal conducting signal for the Cu-Nb-Al sample is even lower as the screening effect of the eddy currents generated into the aluminium adds up to the ones in the copper. The Nb-Cu-Al sample also shows, for $T < T_c$, a superconducting screening signal in full agreement with the screening levels observed in the control samples. The fact that after the mandrel removal the niobium sample no longer shows the signs of a superconducting phase (the screening is reduced by a factor ~ 4, absence of a step-like signal corresponding to the phase transition across T_c) suggested that the chemical etching process applied to remove the aluminium was detrimental to the functional film.

The SEM images of the FIB-milled cross section of two Cu-Nb-[Al] samples are

shown in Fig. 6.10 and support the interpretation that the observed degraded superconducting performance of the sample is due to the aluminium etching. Fig. 6.10a shows the sample also discussed above in the inductive measurements, which was left in the etching solution for as long as the etching process took place (27 hours) and removed as soon as it was finished. The main difference observable here with respect to the control film in Fig. 6.7 is that the first deposited niobium layer corresponds now to the upper part of the film, i.e. the former interface with the aluminium mandrel. The 3 µm thick coated copper adhesion layer is also visible as the large, columnar band structure below the niobium layer. Apart from these aspects, the sample does not appear appreciably different from the control samples. Fig. 6.10b instead was taken of a sample that was left in the etching solution for 1 hour longer after the etching process was finished (28 hours). Here the sample appears damaged, with the part exposed to the etching solution being porous and at intervals, detached from the material below.

Naturally niobium is protected by an air-formed oxide layer (Nb_2O_5) which is enough to prevent corrosion by the sodium hydroxide in short exposure times. However, the dissolution of the oxide layer and the activation of the underlying niobium surface have been observed for niobium in NaOH solution (at different concentrations and temperatures) with increasing exposure time [185]. In the case of the Cu-Nb-[Al] sample, the niobium film was deposited on aluminium and never exposed to air, which prevented the formation of the protective oxide layer on its surface. As soon as the aluminium layer was completely removed, two main processes are likely to have taken place resulting in the degradation of the niobium film: for the sample that was removed from the solution right at the end of the aluminium etching, the hydrogen produced in the reaction

$$2Al_{(s)} + 2NaOH_{(aq)} + 2H_2O_{(aq)} \rightarrow 2NaAlO_{2(aq)} + 3H_{2(g)} \tag{6.1}$$

started diffusing into the niobium; in addition to this, for the sample that was left in the solution for 1 hour longer than the end of the etching of the aluminium, the hydrogen diffused into the niobium creating enough defects to promote the propagation of the reaction from the surface into the film. Based on this, it was decided not to proceed with the measurement of the sample critical current, as it would have not provided additional insight on the interpretation of the effects of the mandrel etching on the niobium film, with respect to what was already obtained from the inductive and SEM measurements. Instead the choice was made to modify the manufacturing process adding a protective layer as presented in Section 6.2.

6.4.3 Run II: reverse Cu-Nb samples with Cu protective layer

The results of the inductive measurements performed for the samples from Run II are presented in Fig. 6.11. For these samples a copper protective layer (indicated as (P) in Fig. 6.3) was deposited on the aluminium mandrel prior to the deposition of the niobium film, differently from Run I in which the niobium film was deposited directly on the mandrel. At every production step (i.e. for Cu-Nb-Cu-Al, the sample as-deposited; Cu-Nb-Cu-[Al], after the etching of the mandrel; Cu-Nb-[Cu]-[Al], after the etching of the copper protective layer (P)) the niobium film shows a regular superconducting transition curve, which suggests the production process to be free from steps that can negatively affect the superconducting properties. All the measurements show values of the critical temperature T_c in accordance with the values measured for the control samples. The superconducting transition appears sharp

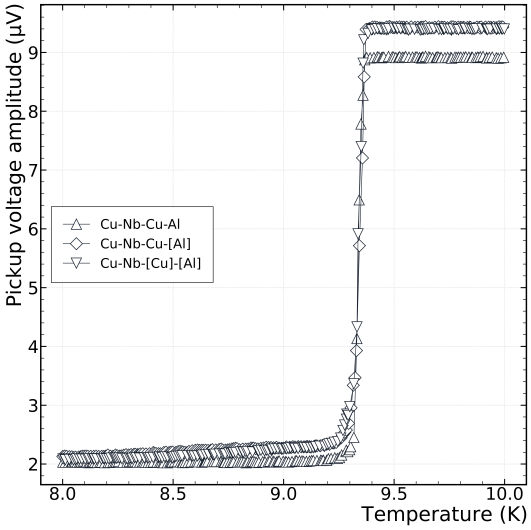

FIGURE 6.11: Inductive measurement of the superconducting transition of the reverse coated Cu-Nb-Cu-Al sample (Run II) before any etching, after the etching of the aluminium mandrel and after the etching of the copper protective layer.

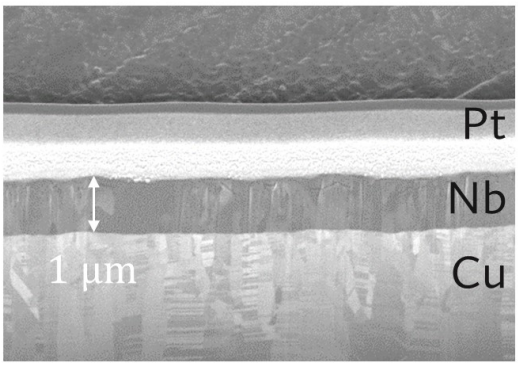

FIGURE 6.12: SEM images of the FIB-milled cross section of the reverse coated Cu-Nb-[Cu]-[Al] sample. The platinum (Pt) protective layer is visible on top, followed by the niobium film (Nb) in the middle and the copper (Cu) at the bottom.

for all the samples, with transition width ΔT_c values in the range $0.04 - 0.06$ K which are smaller than what observed for the control samples, $\Delta T_c = 0.07$ K.

The normal conducting signal (for $T > T_c$) for the Cu-Nb-Cu-Al sample is 0.5 μV smaller than the signal observed for the Cu-Nb-Cu-[Al] and Cu-Nb-[Cu]-[Al] samples, due to the screening effect introduced by the eddy currents in the aluminium layer, as previously explained in the discussion of the results from Run I. The signal for the Cu-Nb-Cu-[Al] and Cu-Nb-[Cu]-[Al] samples overlaps as the copper protective (P) layer is not thick enough (1 μm) for the eddy currents to result in a detectable screening effect. The superconducting screening signal (for $T < T_c$) for all three samples is consistent with what observed for the control samples and for the samples from Run I. The fact that the signal for $T < T_c$ remains flat for the Cu-Nb-Cu-Al sample while it presents a positive slope for the etched samples suggests that the sides of the niobium film (which are exposed to the etching solution along the cut sample edges) were damaged, facilitating early penetration of magnetic flux lines into the

sample as the temperature increased towards T_c. The slope remains unchanged from the Cu-Nb-Cu-[Al] sample to the Cu-Nb-[Cu]-[Al] sample, also suggesting that the mandrel etching process affected the exposed parts of the niobium film (introducing the slope), rather than the etching of the copper protective layer, after which the shape of the transition curve remains the same.

The effectiveness of the copper protective layer (P) is confirmed by the SEM images of the FIB-milled cross section of the Cu-Nb-[Cu]-[Al] sample shown in Fig. 6.12, where the niobium film is visible between the platinum and the copper layers. Other than the uppermost part of the film (the first one to be deposited), which might present a different nucleation pattern with respect to the niobium films deposited in Run I, which were deposited on aluminium and not on copper, there are no structural differences that can be observed between these samples and the ones coated previously. The film is dense, in good adhesion with the copper layer and overall appears healthy.

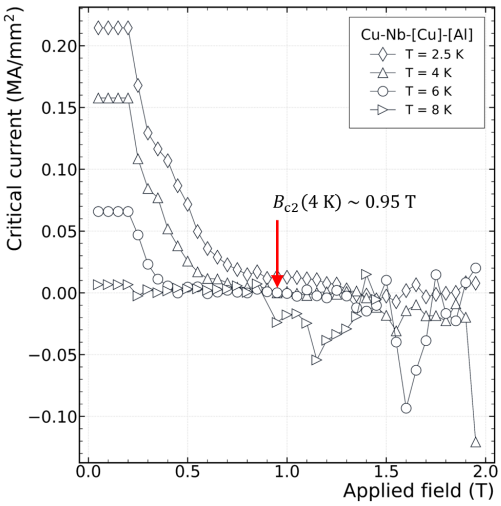

FIGURE 6.13: Critical current J_c of the reverse coated Cu-Nb-[Cu]-[Al] sample (Run II) calculated in the framework of the Bean critical state model, from the VSM-SQUID measured sample magnetic moment loops $m(B)$ at different fixed temperatures. The upper critical field B_{c2} is taken as the field value at which $J_c(4\,\mathrm{K}) = 0$.

The VSM-SQUID measurement of the critical current density J_c of the Cu-Nb-[Cu]-[Al] sample, from which the upper critical field B_{c2} is also extracted,is shown in Fig. 6.13. At a temperature of 4 K the low field value of J_c is about a factor 10 smaller than the average of what was measured for the control samples. As J_c and B_{c2} are both expected to increase with the sample disorder [179], these measurements prove that the procedure established in Run II for the production of the reverse-coated samples can provide niobium films whose performance is comparable to the control niobium samples deposited on the mandrel.

Given the above results, two advantages are to be underlined about the reverse coating technique with respect to standard fabrication methods: not only it represents a potential method for the production of seamless cavities, but also removes the surface chemistry (needed to prepare the substrate for the niobium coating) from the list of mandatory production stages, from which the quality of the film can depend strongly. The next natural step in the feasibility study is the assessment of the RF performance of the samples, but the way to proceed still has to be defined. The

	Characterisation results				
	T_c (K)	ΔT_c (K)	d (µm)	J_c (MA/mm^2)	B_{c2} (T)
Control samples					
AW-1050	9.32	0.07	1	2.5	1.25
AW-6082	9.33	0.07	1	0.29	0.95
Run I					
Cu-Nb-Al	9.35	0.11	-	-	-
Cu-Nb-[Al]	x	x	1	-	-
Run II					
Cu-Nb-Cu-Al	9.34	0.04	-	-	-
Cu-Nb-Cu-[Al]	9.34	0.06	-	-	-
Cu-Nb-[Cu]-[Al]	9.33	0.05	1	0.16	0.95

TABLE 6.2: Summary of the results of the characterisation measurements of the control and reverse-coated (Run I, Run II) samples. The material removed by chemical etching is indicated inside square brackets in the sample label. The measurements which were not performed are indicated by "-" while the measurements which were not conclusive are indicated by "x". The values for J_c are measured at 4 K and 0.2 T, and B_{c2} is given at 4 K.

manufacturing of a sample suitable for quadrupole resonator [17] (QPR) testing is not feasible. Loading a flat sample inside a high-frequency test resonator, or directly manufacturing a higher frequency, elliptical cavity (e.g. 1.3 GHz) will be considered as options. With regard to this, the treatment of the mandrel surface, which in principle could simply be machined with mirror-like surface finish, and the related consequences on the RF behaviour of the film are yet to be studied. Whether and how this will have an impact on the RF performance is currently an open question.

Disclaimer: this work was performed in collaboration with the CERN colleagues from the Surface-Coatings-Chemistry Section G. Rosaz and L. Lain Amador who provided assistance and the coatings, and from the Materials and Metrology Section S. Pfeiffer and A. Baris, who provided the FIB-SEM measurements. The critical current measurements were performed by M. Bonura at the Department of Quantum Matter Physics of the University of Geneva. All the contributors to this work are listed as authors of the resulting published article [28].

Chapter 7

Nb_3Sn coatings on copper via bipolar HiPIMS

To obtain Nb_3Sn films suitable to the final use as SRF coatings on copper cavities, a good control on the material stoichiometry and a balanced choice of the coating parameters must be mastered. Although promising results have been obtained so far on dielectric substrates (e.g. sapphire [186]), achieving comparable results on copper is all but straightforward. Employing copper as a substrate limits the temperature at which the coating process can take place, because of the low weakening point of copper (600 °C – 650 °C), and requires the presence of an intermediate layer to prevent copper-tin interdiffusion. In addition to this, porosities and voids in the film must be avoided at any cost while aiming at good RF performance. The deposition of dense Nb_3Sn films on copper may be achieved via the bipolar HiPIMS sputtering technique, although it can also be considered unexplored territory. In this Chapter, the preliminary results from the study of the properties of Nb_3Sn films deposited on copper via the bipolar HiPIMS technique are presented. In Section 7.1, the general properties of Nb_3Sn are recalled. Section 7.2 presents the main results from the study made at CERN, previous to this one, on Nb_3Sn coatings made via DCMS [26], [187]. The study on the Nb_3Sn on Cu coatings via bipolar HiPIMS, with the experimental and characterization techniques, the choice of data set and the film analysis results is finally presented in Section 7.3. The study is currently still ongoing at CERN, guided by G. Rosaz and S. Leith within the R&D activities of the Vacuum, Surfaces and Coatings group. The results presented here, for this reason, are not comprehensive and do not pretend to be conclusive, but rather to demonstrate the state of the art of the technique.

7.1 General properties of Nb_3Sn

As previously discussed in Section 2.4.1, Nb_3Sn is of significant interest to the SRF cavity community due to its high critical temperature (T_c = 18.3 K), which is nearly twice that of niobium, and its low BCS surface resistance ($R_{BCS} \sim 0.4\,n\Omega$ at 4.2 K and 500 MHz) [111].

The superconducting properties of Nb_3Sn are well known to be dependent on the relative Nb-Sn composition, grain size, and strain state of the material [188]. When niobium is alloyed with tin, it can form $Nb_{1-\beta}Sn_\beta$ or the line compounds Nb_6Sn_5 and $NbSn_2$ as illustrated in the Nb-Sn binary phase diagram by Charlesworth et al. [189] shown in Fig. 7.1. These line compounds are also superconductors, albeit not of practical interest, since they both exhibit a critical temperature below 3 K [190]. The phase of interest of the Nb-Sn system occurs when $0.18 \leq \beta \leq 0.25$, which can be formed at temperatures higher than 930 °C in the presence of a Sn-Nb melt or at lower temperatures through the reaction between niobium and Nb_6Sn_5 or $NbSn_2$. The critical temperature of this phase depends on the composition and can range

from 6 K to about 18 K [191]. The dashed line within the $Nb_{1-\beta}Sn_{\beta}$ stability range indicates a Sn-rich preferential A15 formation in that area, as suggested by some studies [191]. A graphic representation of the Nb_3Sn unit cell is given in Fig. 7.2. Due to the A15 crystal structure of the $Nb_{1-\beta}Sn_{\beta}$ system, the reduced distance in the niobium chains with respect to the distance between the atoms in *bcc* niobium is believed to result in the increased critical temperature. The primary cause of the significant variations in T_c is often interpreted in terms of long-range crystallographic order: tin vacancies in the A15 structure, which are considered thermodynamically unstable, will lead the niobium atoms to fill the vacancies, affecting the continuity of the niobium chain and resulting in those variations [192].

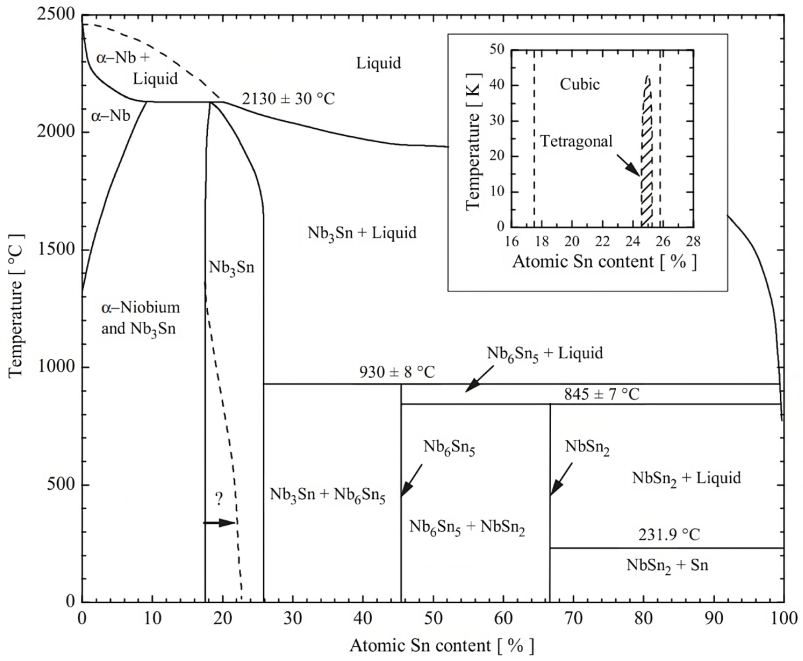

FIGURE 7.1: Binary phase diagram of the Nb-Sn system by [189]. The dashed line indicates the suggested area for Sn-rich A15 formation [191]. The low temperature data in the inset [192] show the stability range of the tetragonal phase. Reproduced from [188] with permission of IOP Publishing.

Nb_3Sn is generally referred to as a strong coupling superconductor, as in the electron-electron coupling is mediated by a strong phonon-mediated pairing interaction, which is dependent on the material composition. The BCS theory provides a weak-coupling approximation for the energy gap (and the critical temperature) of superconductors at zero temperature which relies on the assumption that the attractive interaction between the electrons is constant (i.e. independent of energy, direction or temperature), which in turn yields the weak coupling limit represented by the constant ratio given in Eq. 1.20. In strongly coupled superconductors, the expressions for the energy gap and the critical temperature derived within the BCS theory are no longer valid as they become dependent on the details of the electron-phonon interaction. This results in a rise of the ratio given in Eq. 1.20 above the weak coupling limit of 3.528.

By measuring the critical temperature via the inductive method and the superconducting gap via tunnelling I-V characteristics of Nb-Sn films, Moore et al. [193] have estimated this ratio as a function of the film composition, as shown in Fig. 7.3a.

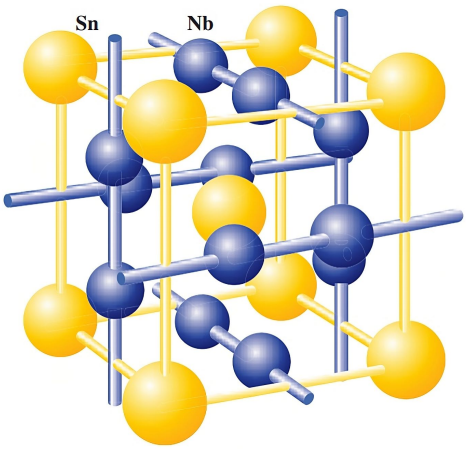

FIGURE 7.2: Nb_3Sn unit cell. The tin *bcc* lattice is represented in yellow, while the orthogonal chains of niobium atoms bisecting the *bcc* cube faces are shown in blue. Reproduced from [188] with permission of IOP Publishing.

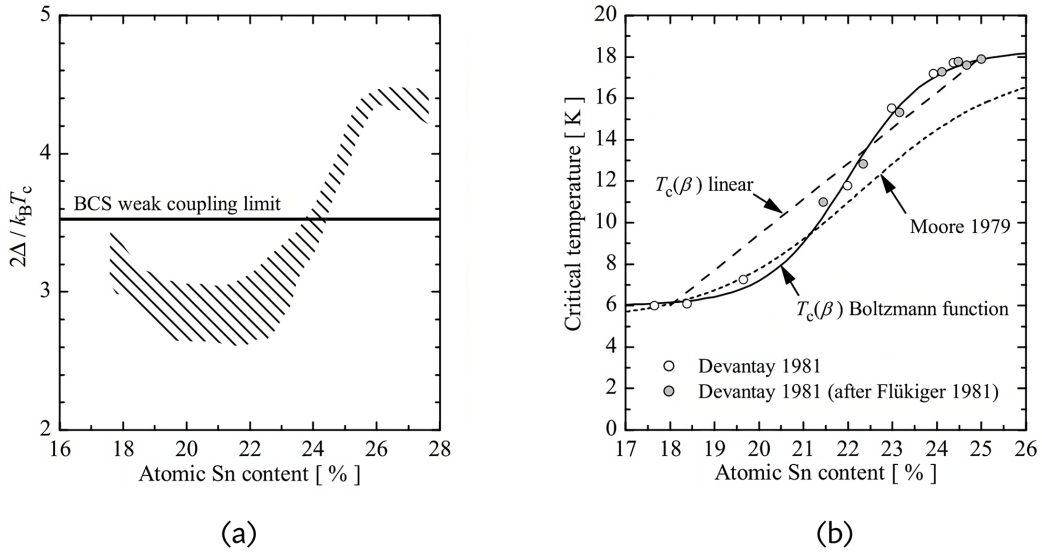

FIGURE 7.3: (a) Ratio $2\Delta_0/k_BT_c$ as a function of the film composition [193]. (b) Results from literature for the critical temperature of Nb_3Sn bulk (plain circles [191] and gray circles [191], [192]) and thin film (fine dashed line [193]) samples as a function of the composition. The coarse dashed line represents the $T_c(\beta)$ fit proposed by Devantay [191]. The full line represents the $T_c(\beta)$ Boltzmann fit, as proposed by Moore [193], applied to Devantay's data by Godeke [188]. For both fits, β represents the atomic tin content. Both figures are reproduced from [188] with permission of IOP Publishing.

The solid line in Fig.7.3a represents the BCS weak coupling limit of 3.528. For most of the composition range, the Nb-Sn films exhibit weak coupling, while becoming strongly coupled for compositions above 23% – 24% of tin, close to stoichiometry. Notably, Moore's composition range is wider than that generally accepted based on the Charlesworth phase diagram (Fig. 7.1). The critical temperature as a function of atomic tin content is shown in Fig. 7.3b, combining data from Moore et al. [193] on

Nb-Sn thin films and Devantay et al. on bulk samples [191] with additional data by Flükiger [192]. Moore's data systematically show a lower critical temperature for the same tin content, saturating at about 18 K at approximately 28% tin content. Devantay's data is more in agreement with the composition stability range proposed by Charlesworth, generally considered more accurate. However, the different nature of the samples probed should be kept in mind: electron-beam co-evaporated thin films on Al_2O_3 substrates in Moore's study [193] and bulk alloys prepared from Nb and Sn powders via a sintering-melting-annealing process in Devantay's study [191].

Moreover, De Marzi et al. [171] discussed the expected effect of applied uniaxial strain on the critical temperature of A15 Nb_3Sn based on their first principle calculations. The critical temperature of the bulk material is expected to decrease in both compressive and tensile directions relative to the maximum value to which the equilibrium state (absence of strain) corresponds.

7.2 DCMS coatings at CERN

Prior to the study presented here, research had already been conducted at CERN to investigate the potential use of Nb_3Sn on copper as SRF material[26], [187]. In these studies, thin films of Nb_3Sn were deposited on copper substrates via DCMS using a stoichiometric target, and their superconducting and morphological properties were evaluated to determine their suitability for use as the inner coating of SRF cavities.

Based on the known properties of the material [189] and on the experience gained through the R&D for Nb/Cu cavities, the starting point for the study was identified in the following key concepts:

- a precise control of the film stoichiometry is needed;
- high temperature treatments are needed for the formation of the A15 phase;
- applicable annealing temperatures are limited by the copper substrate.

To have control on the effects of the copper substrate, the films were deposited on both ceramic and copper substrates. Both krypton and argon were used as sputtering gases. The krypton-coated films were expected to have fewer residual gas inclusions than the argon-coated films [194], as the amount of gas included during coating depends on the relative masses of the gas and the target sputtered material. Two heat treatment routes were pursued, including post-coating annealing in a vacuum furnace at temperatures ranging from 600 to 800 °C (the coating was performed at the equilibrium temperature reached by the sputtering system during the process without additional heating) and *in situ* annealing by actively warming up the substrates during the coating process at temperatures from 600 to 735 °C. It was also found that additional post-coating annealing of films reacted during the coating process increased the critical temperature [26]. Furthermore, the benefits of an intermediate layer deposited between the substrate and the functional Nb_3Sn film were investigated, after copper diffusion from the substrate into the Nb_3Sn film at high temperatures was observed. Tantalum was chosen as an intermediate layer between the substrate and the functional Nb_3Sn film and proved effective in preventing copper diffusion.

The produced samples were analysed to assess their morphology, composition, critical temperature and microstrain state. The obtained critical temperature as a function of the tin content for the films on copper substrate produced without and

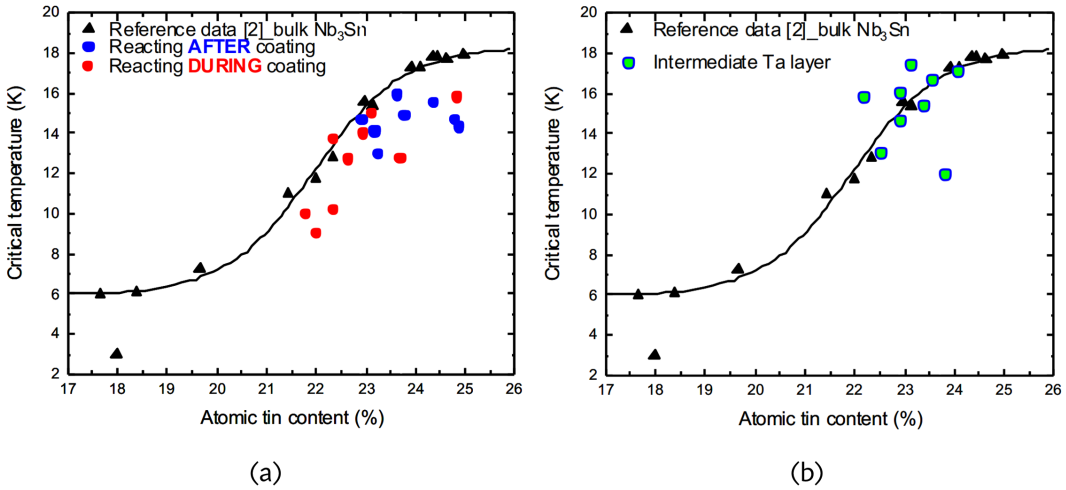

FIGURE 7.4: (a) Critical temperature measured for the Nb_3Sn DCMS coatings on copper substrate [26], [187]. The blue circles are for the samples annealed after the coating process. The red circles are for the the samples coated at high-temperature. The black triangles and the full line represent the reference bulk data reported by Godeke [188]. (b) Critical temperature measured for the Nb_3Sn DCMS coatings on copper substrate after the introduction of the tantalum intermediate layer to prevent copper diffusion. Both figures are reproduced from [187].

with the tantalum intermediate layer are shown in Fig. 7.4a and Fig. 7.4b respectively. The data is shown together with the bulk data by Devantay and Flükiger as reported by Godeke [188]. Although the best critical temperature achieved on ceramic substrate was found to be 17.5 K [26], the copper substrate seems to have a detrimental effect in the T_c. This can be seen in Fig. 7.4a, were the highest T_c corresponds to about 16 K. Although the samples which were post-coating annealed exhibited a higher critical temperature, as stated in [26], the SEM surface scans revealed the presence of cracks [187], likely due to the release of the residual stress built in the film during the coating process. However, this was not observed for the high-temperature coatings. A difference was also observed between the films sputtered in argon and krypton atmosphere: the latter did not show cracks following the annealing process, unlike the first ones. The introduction of the tantalum intermediate layer sensibly improved the results on the T_c, as reported in [187]. However, more information about these coatings is not availabe in literature. In summary, the above study [26], [187] yielded the following results:

- the films deposited with argon at high pressure exhibit a high tin content but a rough and porous morphology;
- the films deposited with krypton as sputtering gas demonstrated a higher atomic tin content under the same coating conditions, but increase in krypton pressure leads to a decrease of the tin content, likely due to re-sputtering;
- unlike the films deposited in argon atmosphere, the films deposited with krypton showed a crack free surface following post-coating annealing;
- the post-coating annealing step mitigates the high disorder levels shown by the films deposited with both gases, improving the critical temperature;

- the post-coating annealing step removes the undesired Nb_6Sn_5 or $NbSn_2$ phases which are present in the film before the annealing;
- the films annealed during the coating did not show unwanted Nb_6Sn_5 or $NbSn_2$ phases;
- the films annealed after the coating show a better critical temperature than the ones annealed during the coating, but also exhibit a cracked surface which is incompatible with RF operation;
- under the same conditions, films on copper systematically exhibit a lower critical temperature than the ones on a ceramic substrate;
- the introduction of a tantalum intermediate layer prevents the diffusion of copper into the Nb_3Sn layer and helps decreasing the lattice mismatch and reducing the residual stress in the Nb_3Sn film, with consequent improvement of the critical temperature.

7.3 HiPIMS coatings at CERN

Experimental evidence has demonstrated the efficacy of the bipolar HiPIMS technique in providing dense and void-free films, especially on surfaces oriented at grazing angles with respect to the target surface, as reported by Avino et al. in a study on niobium [19]. This finding is particularly relevant, as it makes bipolar HiPIMS an interesting candidate technique for compensating one of the main reasons which are thought to be behind the Q-slope observed in Nb/Cu cavities, as discussed in Section 2.3.1.

Based on the results obtained at CERN with the studies on the DCMS coatings, discussed in the previous section, the option of producing Nb_3Sn coatings for SRF cavities with the bipolar HiPIMS technique is guided by the following key elements:

- krypton is to be preferred as sputtering gas, due to the better performance with respect to argon in terms of residual gas inclusions, film composition and final surface morphology;
- a coating process performed at high temperature is to be preferred to avoid surface cracking due to post-coating annealing;
- a tantalum intermediate layer between the copper substrate and the Nb_3Sn film is to be implemented to prevent tin-copper interdiffusion and decrease the lattice mismatch between the film and the substrate, possibly leading to less stressed films and therefore a better T_c;
- the way to a correct stoichiometry, with tin atomic content in the 18% – 26% range, is to be explored further, with the target composition possibly playing a role in addition to the chosen film production technique.

7.3.1 Experimental procedure

From May 2021 to January 2023 (the time interval covered by the results presented here) a total of 104 coating runs were performed. Of these, a subset of runs was selected to define the samples to be included in this study. The selection criteria for the subset are discussed in Section 7.3.3. Although more runs have been done

afterwards or still are being performed, they are not included in this study as the characterization of the samples was not completed yet.

The coating system for the production of the Nb_3Sn samples is shown in Fig. 7.5. The open coating chamber can be seen in Fig. 7.5a, where the two targets (the tantalum target on the left and the stoichiometric Nb_3Sn target on the right) can be identified, with the sample holder mounted on top, 10 cm away from the target, and indicated by the red arrow. Similar to the coating system employed for the reverse-coating study and described in Section 6.2, also in this case the coating of the tantalum intermediate layer and of the Nb_3Sn film can be performed consecutively by moving the sample holder from one target to the next one without having to open the chamber. The sample holder placed above the tantalum target during the coating can be seen in Fig. 7.5b, where the plasma is also nicely visible. In Fig. 7.5c six samples can be seen arranged on the sample holder after the coating.

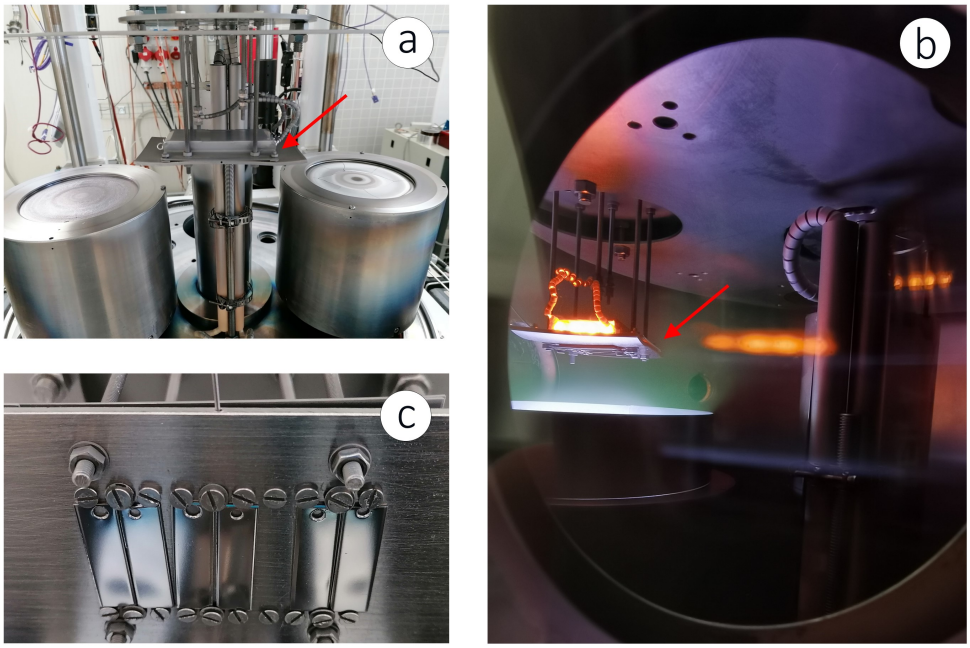

FIGURE 7.5: (a) Inside of the coating chamber. The tantalum target is visible on the left, the Nb_3Sn target on the right. The sample holder in the center, above the targets, is indicated by the red arrow. (b) Inside of the coating chamber seen from a view port during the coating process. The sample holder, indicated by the red arrow, is placed above the tantalum target. (c) Sample holder with six samples mounted on it, after the coating.

Substrate properties	
Material	OFE-grade copper
Size (mm^3)	$11 \times 35 \times 1$
Surface preparation	SUBU (20 min)
Ta interlayer coating parameters	**Value**
P_{Kr} (mbar)	1.0×10^{-3}
T_{coat} (°C)	750
t_{coat} (min)	40
MP amplitude (V)	-500
MP duration (µs)	50
MP Frequency (kHz)	1
PP amplitude (V)	50
PP duration (µs)	200
Delay (µs)	4
Average power (W)	350
T_{ann} (°C)	750
t_{ann} (min)	45
P_{ann} (mbar)	1.0×10^{-3}
Nb_3Sn film coating parameters	**Value or Range**
Target type	Stoichiometric or Sn-enriched
Gas type	Kr
P_{coat} (mbar)	7.0×10^{-4} – 5.0×10^{-2}
T_{coat} (°C)	210 – 750
t_{coat} (min)	90 – 240
MP amplitude (V)	-500
MP duration (µs)	50
MP Frequency (kHz)	1
PP amplitude (V)	35 – 130
PP duration (µs)	200
Delay (µs)	4
Average power (W)	350

TABLE 7.1: Summary table including the copper substrate properties and the coating parameters employed for the deposition of the tantalum intermediate layer and the Nb_3Sn films. The abbreviations MP and PP stand for "main pulse" and "positive pulse" respectively, and refer to the voltage pulses of the bipolar HiPIMS process described in Chapter 4.

7.3.2 Characterisation techniques

The following techniques were adopted for the characterisation of the Nb_3Sn samples:

- inductive measurement of the critical temperature;
- SEM scans of the film surface;
- SEM scans of the film FIB-milled cross section;
- EDS analysis of the film composition.

As already discussed in Section 6.3, the inductive measurement of the critical temperature provides an early insight into the superconducting performance of the film. In the case of Nb_3Sn films it also provides qualitative information about the relative Nb-Sn composition, as discussed in Section 7.1. One should take care that generally the coexistence of off-stoichiometry phases with the main Nb_3Sn phase having a lower critical temperature cannot be detected with the induction coil method as all the lower T_c phases are screened by the phase with higher T_c. As also discussed by Godeke [188], this may result into a systematic overestimation of the critical temperature of the films not having a single, homogeneous, stoichiometric phase.

The SEM scans of the film surface and FIB-milled cross section help assessing the surface morphology, the film density and granular structure and allow for the estimation of the film thickness. The experimental devices employed for the SEM/FIB-SEM scans are the same as described in Section 6.3.

The Energy Dispersive X-ray Spectroscopy (EDS) technique is used to estimate the Nb_3Sn film composition by bombarding its surface with the beam of energetic electrons produced by the SEM electron gun and detecting the characteristic X-rays emitted by the excited element. The detector associated to the SEM used in this study is a $50\,mm^2$ X-Max EDS detector by Oxford Instruments with AZtec software for chemical composition analysis.

7.3.3 Selection of the data set

Of the above mentioned 104 coating runs, a final subset of 58 runs was selected for this study, in order to have a homogeneous set of samples. The substrate properties and parameter space covered for the coatings of the Ta intermediate layer and of the Nb_3Sn films are given in Table 7.1 for the selected subset. The selection/exclusion criteria which led to the final sample group are listed below.

First, the following runs were excluded, in which:

- the coating process was aborted for technical reasons, or
- argon or xenon is used as sputtering gas instead of krypton, or
- the intermediate layer is niobium instead of tantalum, or
- the substrate is bulk niobium or ceramic instead of copper, or
- only the tantalum layer was deposited without the final Nb_3Sn film, or
- the Nb_3Sn film did not show a superconducting phase.

Among the remaining ones, were selected the runs in which:

- the coating parameters for tantalum intermediate layer were fixed to the ones indicated in Table 7.1, and
- the cathode power did not vary for the deposition of the Nb_3Sn film and kept a constant value of 350 W for all the runs.

The complete list of chosen runs with the corresponding parameters is given in Appendix B. The analysis of the final data set is presented in the next Section.

7.3.4 Results and discussion

DATA OVERVIEW

An example of typical transition curves measured for this study is given in Fig. 7.6, where a typical 'broad' (Fig. 7.6a) and 'narrow' (Fig. 7.6b) transition is shown. The $T_c \pm \frac{\Delta T}{2}$ corresponding values are (9.5 ± 0.5) K and (16.3 ± 0.2) K for run 71 and 139 respectively.

An overview on the time progress of the main quantities associated to the selected subset of samples is given in Fig. 7.7. The coating runs appear in chronological order and are labeled by the run number along the x-axis. Stacked vertically is given the time evolution of the quantities involved in the data analysis: the critical temperature of the Nb_3Sn films, the width of the superconducting transition, the coating parameters such as the positive pulse, the coating pressure and coating temperature, as well as the tin atomic content and the film thickness. The plain markers flag those runs for which a Sn-enriched target was used instead of the stoichiometric one. The full grid lines indicate those runs for which a post-coating annealing was applied.

For the runs in which the critical temperature was measured on more than one sample, the average value of T_c and ΔT is plotted with the standard deviation as error bar. In all the graphs shown after Fig. 7.7, the critical temperature is plotted with error bars. These represent the width ΔT associated with the transition, as discussed in Section 5.4. For this reason a different style is chosen for the bars, to distinguish them from the error bars shown in Fig. 7.7 representing the standard deviation.

Toward the later runs, some data for the tin content and the film thickness is missing, due to the characterization measurements not being completed yet at the time of the analysis being presented. The involved samples were anyway kept for the study not to exclude the information on the measured critical temperature.

The critical temperature of the samples is seen to improve over time with some oscillations, with the highest and lowest values of $T_c \pm \frac{\Delta T}{2} = (16.6 \pm 0.3)$ K and $T_c \pm \frac{\Delta T}{2} = (15.5 \pm 0.4)$ K recorded for the runs 147 and 113 respectively. The transition width ΔT, after some strong variations, stabilised on values ranging from about 0.5 K to 1 K.

The effect of the coating parameters on the critical temperature is difficult to evaluate separately for each parameter, as the final T_c is rather the result of the combined effects of all the parameters. At a first look, it is possible to notice that the highest T_c values were reached at 50 V positive pulse, with some obvious T_c degradation corresponding to higher positive pulse voltages. A similar consideration can be made about the coating pressure, with the high pressure values generally corresponding to a better T_c. Not much can be stated at this point on the influence of the coating temperature if not in combination with the post-coating annealing, which seemingly leads to higher T_c when applied to the coatings performed at lower temperature.

Due to the missing data, it is not yet possible to know if the best T_c values systematically correspond to the highest tin content. Surely a correct stoichiometry has a

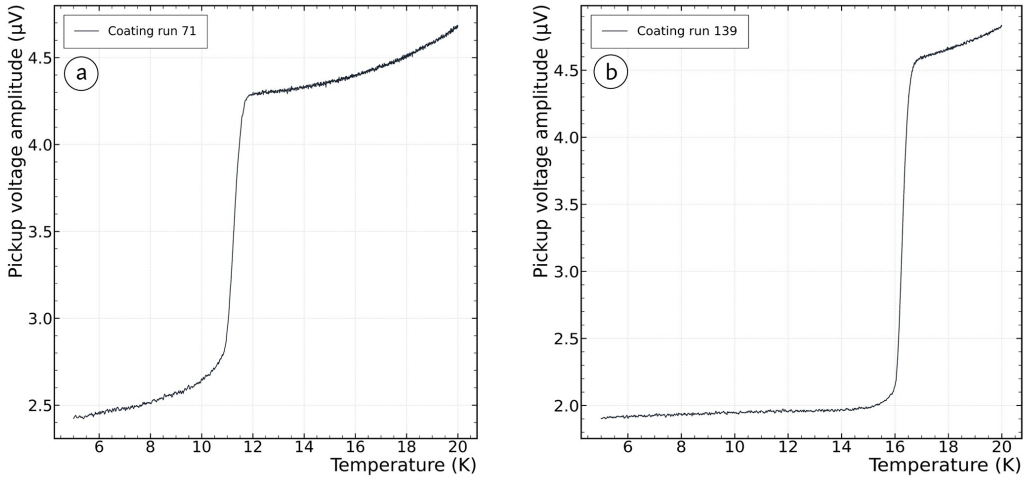

FIGURE 7.6: Typical transition curves for $Nb_3Sn/Ta/Cu$ samples deposited via bipolar HiPIMS. Run 71 (a) represents a typical broad curve with $T_c \pm \frac{\Delta T}{2} = (9.5 \pm 0.5)$ K, run 139 (b) represents a typical narrow curve with $T_c \pm \frac{\Delta T}{2} = (16.3 \pm 0.2)$ K.

positive influence on the final T_c, although a good critical temperature results from a combination of factors. It is to be verified whether the introduction of a Sn-enriched target may be of help or not in reaching and maintaining the desired stoichiometry. What can be already seen is that it does not appear to have a detrimental effect.

The information on the thickness is given for completeness, and from the present data it does not seem to play a leading role on the film critical temperature.

OBSERVED DEPENDENCIES

In order to have a consistent set of data, the following analysis only includes the coatings performed at high temperature (750 °C) with the stoichiometric target. Also, the two most commonly occurring values of the coating pressure (7×10^{-4} mbar and 2.5×10^{-2} mbar) and the positive pulse (50 V and 100 V) were chosen in order to investigate any relevant trend.

First, the dependence of the critical temperature on the positive pulse and the coating pressure is analysed. In fig. 7.8a the critical temperature is seen to decrease with increasing positive pulse voltage. This can be interpreted as the more energetic particles degrading the film quality in terms of critical temperature. This effect is visible at both pressures but is worsened at low pressure. One possible explanation to this is that, at low pressure and at the given temperature, the mean free path of the sputtered particles is in the order of the meter, which implies that no collisions take place along the path from the target to the substrate, placed 10 cm away. In the high pressure case, the mean free path is estimated to be roughly 5 cm, for which on average a few (1 – 2) collisions may occur, decreasing the energy of the particle before it lands on the substrate.

Since at higher pressure the likelihood for the sputtered particles to lose some energy by undergoing collisions along their path is higher, the worsening of the critical temperature observed for the more energetic particles is mitigated with respect to the case at low pressure. This reasoning is supported by the plot in Fig. 7.8b,

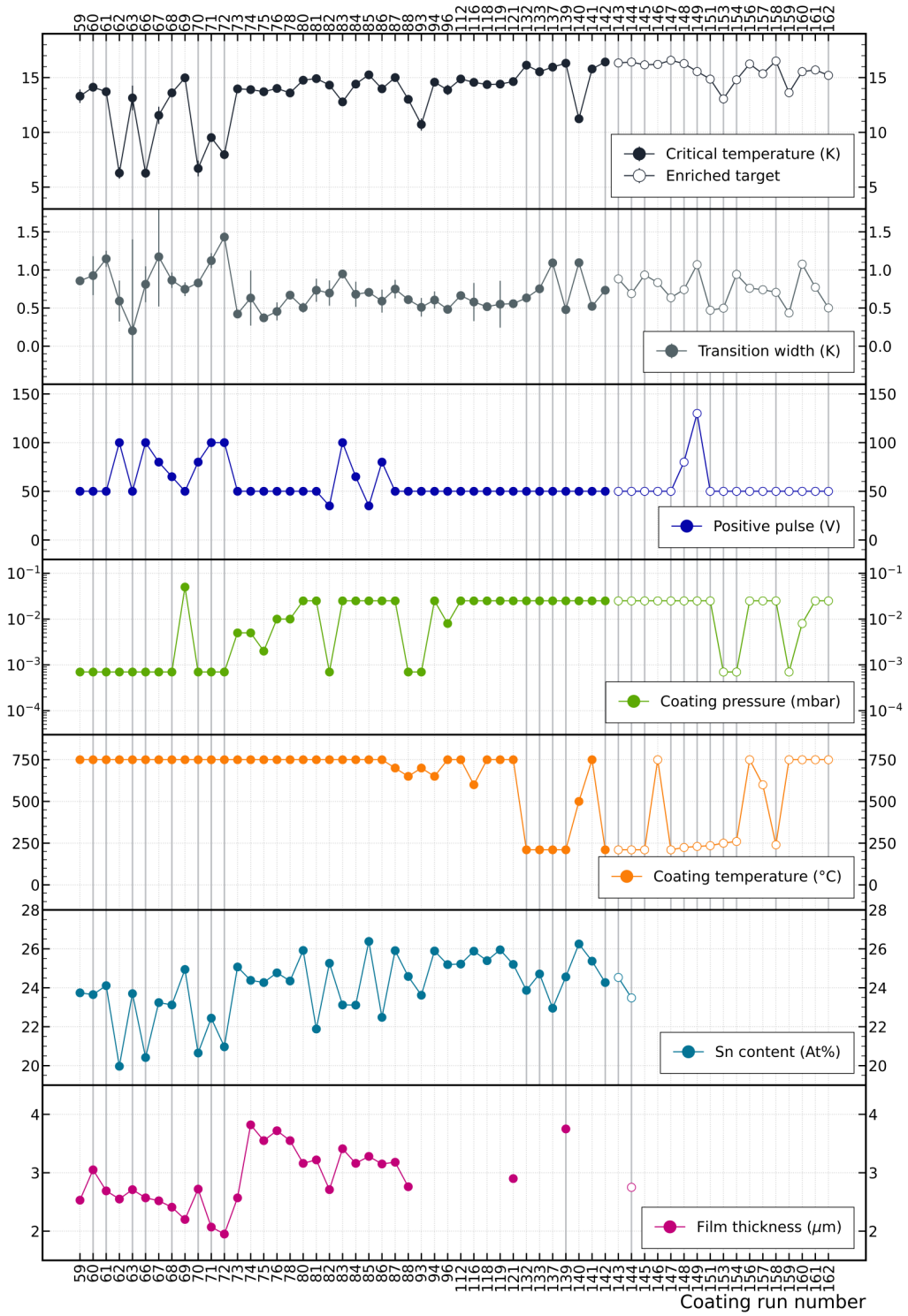

FIGURE 7.7: Time progress of the main quantities involved in the analysis of the Nb_3Sn coatings. Along the x-axis the numbers associated to each coating run are given. The quantity name and the unit are given in each plot's legend. The measured tin content and thickness are also given, although the latest data is still missing. The plain markers indicate the runs for which a Sn-enriched target was employed instead of a stoichiometric one. The full grid lines indicate the runs for which a post-coating annealing was performed.

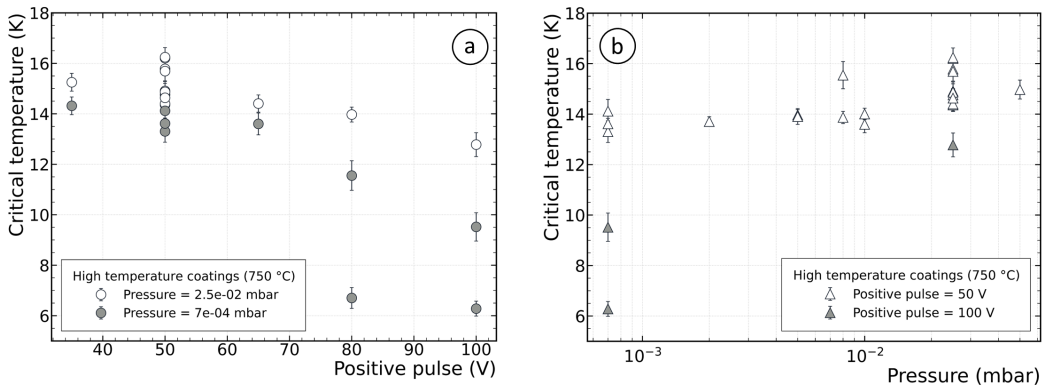

FIGURE 7.8: Critical temperature of the Nb_3Sn coatings as a function of the positive pulse (a) and coating pressure (b).

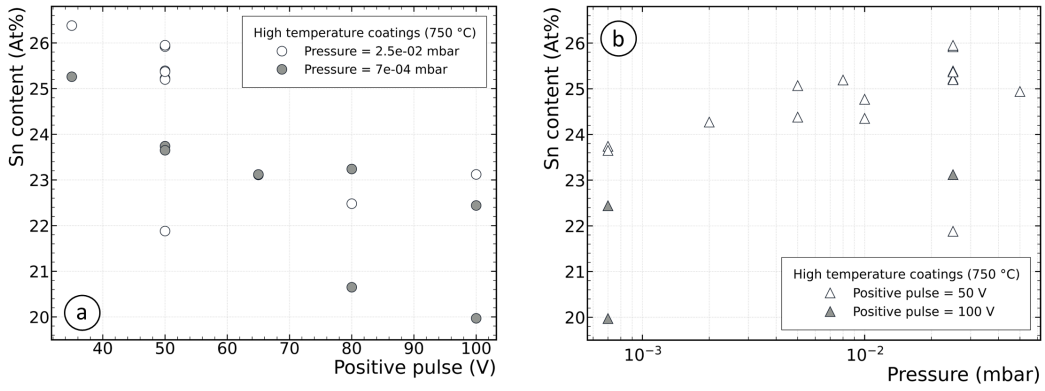

FIGURE 7.9: Atomic tin content of the Nb_3Sn coatings as a function of the positive pulse (a) and coating pressure (b).

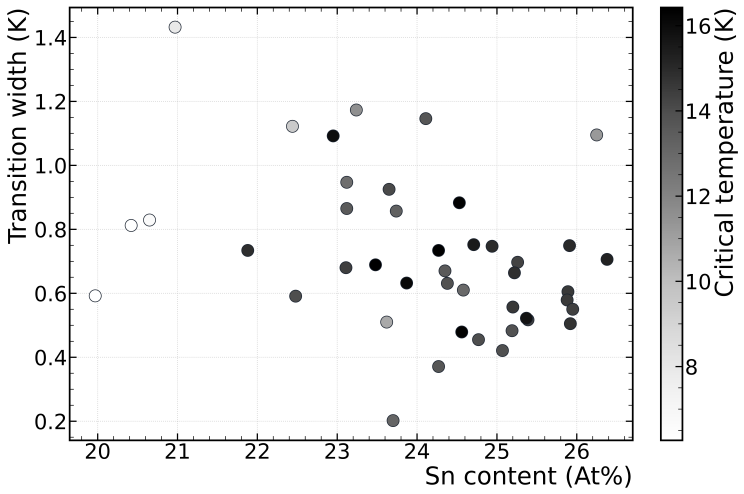

FIGURE 7.10: Transition width of the Nb_3Sn coatings as a function of the tin content. The critical temperature is indicated in gray-scale.

where the critical temperature is plotted against the coating pressure. It is observable how the increasing pressure has a positive effect on the critical temperature, with a more evident effect on the more energetic particles (those for which the positive pulse is set at 100 V) for which the degradation of the critical temperature at low pressures is more effectively mitigated with increasing pressure.

Second, it is useful to analyse the dependence of the tin content on the same variables under the same conditions. The data set appears reduced due to the missing data about the tin content of the latest coatings. In Fig. 7.9a a decrease in tin content is observed as the positive pulse is increased, suggesting that re-sputtering takes place by means of the more energetic particles, with again a slightly stronger dependence observed at low pressure, for which, as discussed earlier, the sputtered species are expected to reach the substrate with higher energy due to the larger mean free path. A dependence which is almost mirroring the one observed for the critical temperature is also observed in Fig. 7.9b for the tin content versus the coating pressure, explaining the degradation of the T_c against the positive pulse as the film stoichiometry moves away from the ideal Nb-Sn ratio. Also here, the effect is generally stronger for higher positive pulse. Overall both the pressure and the positive pulse are observed to have an effect on the critical temperature, with a similar effect observed for the tin content. However, the pressure seems to have a stronger influence on the tin content and this can be reasonably connected to the effect on the T_c values.

The width of the transition, in Fig. 7.10, also exhibits a dependence on the tin content. In this case the data set is larger as all the pressure, positive pulse and coating temperature values have been included. A general trend can be noticed, according to which the higher the tin content the narrower the transition. This appears to be also associated to higher values of the critical temperature. Although this observation is in agreement with what has been discussed so far, it cannot be considered conclusive. If on one hand it is possible to rely on the assumption that a good stoichiometry contributes to a sharp transition (and, at the same time, to a satisfactory T_c), on the other hand the sharpness of the superconducting transition results from a combination of factors rather than from the tin content only. This reasoning is immediately applied to the critical temperature as well.

Comparison to known dependencies

To understand whether the data trends observed by Devantay and Flükiger for bulk Nb_3Sn [191], [192] and by Moore for thin Nb_3Sn films [193] (readapted by Godeke [188]) are reproduced by the HiPIMS coatings, the critical temperature of the films is plotted against the tin content, together with the fit curves by Godeke and Moore. In Fig. 7.11 the plot is reproduced three times, each time with the data being color-flagged according to the coating pressure, positive pulse and coating temperature values. The distribution of the T_c can be generally considered to be in accordance with the data already presented in literature. The color flagging again confirms the advantage of choosing high coating pressures, with the best samples in terms of T_c all being coated at 2.5×10^{-2} mbar, and a medium-low positive pulse voltage, with the best samples being the ones deposited at 50 V positive pulse. Concerning the coating temperature, the best samples seem to be delivered by both the coatings performed at 750 °C and at the system equilibrium temperature (or "room"

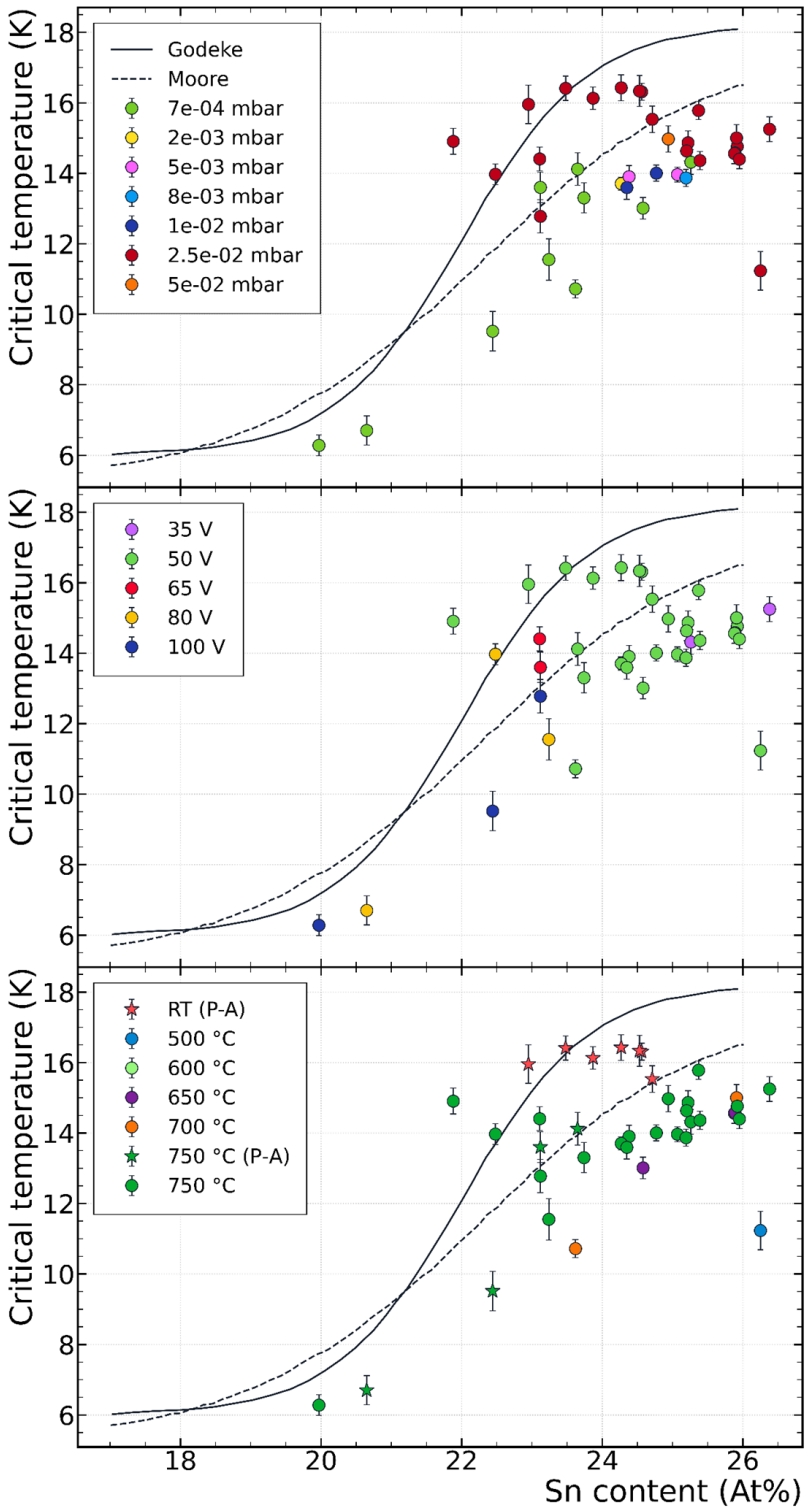

FIGURE 7.11: Critical temperature of the Nb_3Sn bipolar-HiPIMS coatings versus tin content. The trend curves for the Nb_3Sn bulk data by Godeke (full line) [188] and thin film data by Moore (dashed line) [193] found in literature are reported. The data are flagged by (from top to bottom) coating pressure, positive pulse and coating temperature. The abbreviation RT (P-A) stands for room-temperature (RT) coated and post-coating annealed (P-A).

temperature, RT) coatings which have been post-coating annealed (P-A) for 24 h at 750 °C. At the same time, the post-coating annealing performed on the films deposited at 750 °C does not seem to improve the film T_c sensibly. Although the RT-deposited, post-coating annealed films exhibit the best critical temperature, it will be shown in the next Paragraph that this is not the only parameter to rely on, as these coatings will exhibit a morphology which is not RF compatible.

FILM MORPHOLOGY

As just anticipated in the previous Paragraph, the samples exhibiting the best T_c in the T_c versus tin content distribution appear to have a morphology that is not RF compatible. This can be seen in Fig. 7.12, where the SEM images of the surface of the films coated in run 141 and run 142 are shown. The two runs are coated at 750 °C without P-A and at RT with P-A respectively. It is immediately seen that, although the coating from run 142 exhibited a higher T_c of 16.4 K, the surface appears cracked, with smaller grains and a non-homogeneous grain size distribution. This was observed for all the coatings performed at RT with P-A. The presence of cracks, also observed in the DCMS coatings [26], is especially adverse for RF applications. On the contrary, for the coating from run 141 a lower T_c of 15.8 K is measured, yet the surface morphology appears dense, the grains are bigger and their size more homogeneously distributed. The cracking of the films is most likely due to the release of the compressive stress during the annealing process, built in the film during the RT deposition, which also results in the higher T_c. It is known, in fact, that compressive stress lowers the T_c of A15 superconducting structures [171]. The measured transition width is helpful for weighing the information conveyed by the critical temperature, as the damaged film from run 142 shows a ΔT of 0.7 K, 0.2 K larger than the one measured for the film from run 141 exhibiting a better morphology.

The analysis of the effects of the positive pulse, coating pressure and coating temperature on the film morphology is also investigated, in Fig. 7.13, Fig 7.14 and

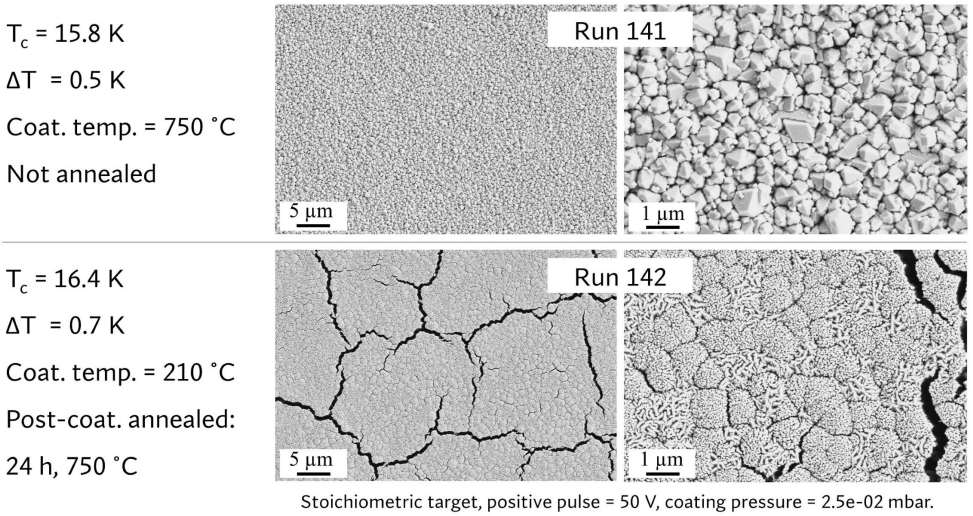

FIGURE 7.12: Comparison of surface morphology between a coating performed at 750 °C without annealing and a coating performed at low temperature and post-coating annealed.

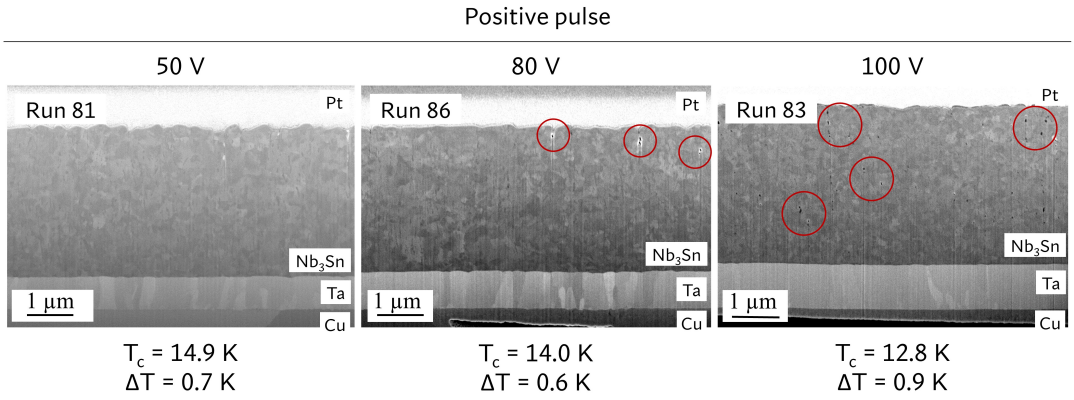

FIGURE 7.13: Effect of the positive pulse on the bulk morphology of the Nb_3Sn films. The red circles indicate possible voids.

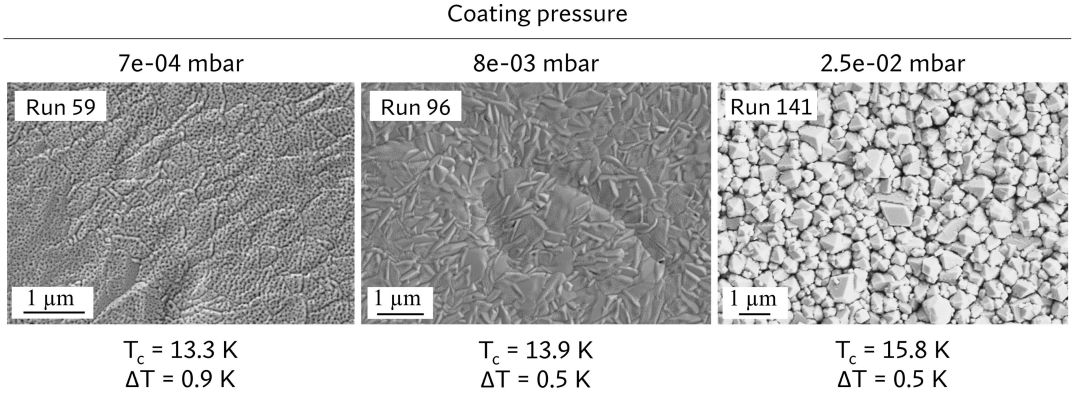

FIGURE 7.14: Effect of the coating pressure on the surface morphology of the Nb_3Sn films.

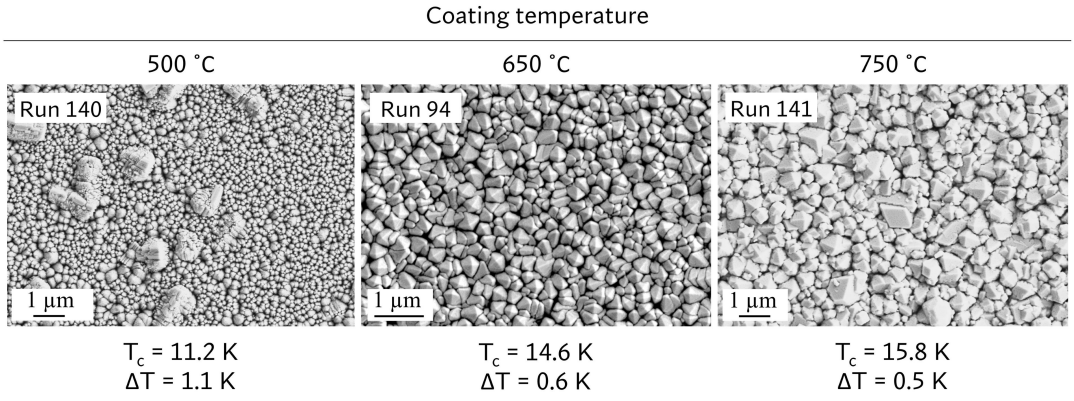

FIGURE 7.15: Effect of the coating temperature on the surface morphology of the Nb_3Sn films.

Fig. 7.15 respectively. For each of these quantities, a film coated at three different values is shown, with all the other coating parameters not varying.

The value of the positive pulse did not appear to affect the morphology of the film surface, but an effect can be observed in the bulk. The FIB-milled cross sections of the coatings from run 81, run 86 and run 83 are shown in Fig. 7.13 to which a positive pulse of 50 V, 80 V and 100 V correspond respectively. The grain size seems to slightly decrease with increasing positive pulse, but mostly voids in the film bulk appear, resulting in a less homogeneous film texture.

In Fig. 7.14 the surfaces of the films from run 59, run 96 and run 81 are shown, deposited at a coating pressure of 7×10^{-4} mbar, 8×10^{-3} mbar and 2.5×10^{-2} mbar respectively. It can be seen as increasing the coating pressure results in the formation of bigger and better defined grains. The origin of the *pores* appearing all over the surface in all three cases is not yet explained.

The surfaces of the films from run 140, run 94 and run 81, deposited at 500 °C, 650 °C and 750 °C respectively, are shown in Fig. 7.15. It can be seen also here how the higher coating temperatures result in a larger grain size. The *pores* mentioned earlier are also visible here, although only in the high temperature coating.

It is worth commenting that it is encouraging to notice how the film morphology reflects that described by Anders [149] in his phase diagram for the structure of films deposited by energetic physical deposition processes such as HiPIMS.

FINAL REMARKS

Although the analysis presented here is not conclusive, several considerations can be carefully made at this stage of the study. In terms of the critical temperature, it seems better to limit the kinetic energy provided to the sputtered species by adjusting the positive pulse around medium-low values (50 V) and the coating pressure toward higher values (2.5×10^{-2} mbar), with the exact values depending on the experimental setup[1]. These two quantities are seen to have an effect on the critical temperature possibly via their effect on the film composition, with the film tin content showing a dependency on the positive pulse and the coating pressure which is very similar to the one observed for the T_c. In fact, the tin content is seen to decrease for increasing positive pulse, possibly due to re-sputtering by the high-energetic particles. The tin content also appears to increase with increasing pressure, due to the smaller mean free path of the sputtered particles.

The critical temperature as a function of the tin content of the HiPIMS coatings follows the distribution found in literature [188]. When combined with the information about the positive pulse and the coating pressure, these data validate the statement for which low positive pulse and high pressure are the preferable options toward a high T_c film. These statements are supported by the observed film morphology too, which also demonstrated the possibility of producing dense Nb_3Sn films via bipolar HiPIMS.

Concerning the coating temperature, a specific trend of the T_c value could not be found. The coatings performed at 750 °C exhibited a wide range of critical temperatures. Annealing the samples after the coating did not bring an improvement in this sense. However, the coatings performed at room temperature and annealed after the coating displayed the highest T_c values. It later became clear from the surface morphology that these coatings cannot be RF compatible as they exhibit severe cracks,

[1] The same study performed with a coating setup having different geometry, magnetron configuration etc. might reproduce the trends observed here but report different absolute values for the coating parameters.

analogous to what was previously observed for the DCMS coatings [26]. If the transition temperature is an indicator of a high purity, homogeneous and stress-free material for elemental superconductors like niobium, the interpretation for a compound such as Nb_3Sn is less univocal. As discussed in Section 7.1, T_c is definitely related to the stoichiometry of the material (i.e. the niobium-tin content ratio), but the long-range order, mainly affected by the tin vacancies in the A15 structure and the grain structure also play a role. These are also related to the stoichiometry, as a tin-poor film would necessarily present more vacancies than a close-to-stoichiometry one. A stoichiometric film will likely show a high T_c yet will not necessarily exhibit a sharp transition, even though the two quantities are likely to evolve in the same direction, as observed earlier. The analysis of the morphology of the HiPIMS coatings suggested that homogeneity of the film, large and homogeneously distributed grain size as well as a dense and void-free morphology are all factors contributing positively to a sharp transition. Adding information about the possible presence of spurious Nb-Sn phases would help in validating/rejecting these observations.

Disclaimer: this work was performed in collaboration with S. Leith and G. Rosaz from the Surface-Coatings-Chemistry Section at CERN, who provided the coatings and exchanged knowledge in support of this study, and A. Baris, S. Pfeiffer and B. Ruiz Palenzuela from the Materials-Metrology Section at CERN, who provided the SEM, FIB-SEM and EDS characterisation measurements.

Conclusions

In the context of this thesis, three R&D activities for the advancement of the SRF cavity system of the FCC have been carried out, all having in focus the development and characterisation of superconducting thin films on copper. The materials considered in this thesis are niobium and Nb_3Sn, in the form of thin films deposited via the energetic physical vapour deposition technique of bipolar HiPIMS. The performed activities are wrapped up in the following.

TEST STATION FOR T_c MEASUREMENT

A test station for the measurement of the critical temperature (T_c) of superconducting thin films produced in small samples has been commissioned and permanently installed at the CERN Central Cryogenic Laboratory. The measurement of T_c performed with this station is now the first step in the characterization routine of the superconducting films produced at CERN for SRF cavity development.

The measurement of T_c represents a simple and relatively cheap way for a first assessment of the quality of the thin film: from the value of T_c itself it is possible to, e.g., infer the purity of an elemental superconductor such as niobium or about the stoichiometry of a compound such as Nb_3Sn.

The measurement system of choice for the test station is the induction-coil technique, which exploits the screening effect of a superconducting sample placed in between two coils when in the Meissner state. This is a contactless technique, and as such does not need probe contact or soldering, with the advantage to leave the measured film intact and in good conditions for additional characterisation measurements. For this particular test station, the two coil system is installed inside a helium bath cryostat and run in helium vapour environment, with the vapour temperature regulation implemented via a PID control loop. The system is built so that the whole experimental apparatus needs minimal handling and only the samples must be inserted/extracted for the measurement via a dip-stick. A user-friendly LabView interface was designed to set, run and control the measurement.

The measurement station was tested and characterised before the final commissioning. In the characterization phase, the magnetic field produced for the measurement was simulated to have an estimate of the field lines distribution around the sample and of the field values inside the experimental chamber, especially at the sample surface, where the field is expected to be around 0.4 mT. The pickup coil response to the magnetic field was also simulated and found in good agreement with the measurements.

Measurements on five different reference samples were also performed to assess the response of the system. The samples were lead, bulk niobium, niobium thin film on copper deposited via HiPIMS, niobium thick multi-layer film on copper deposited via DCMS and Nb_3Sn thin film on ceramic deposited via DCMS.

Based on the measurement for lead, an accuracy level of at least 99% can be stated for the measurement station. The error on the measured critical temperature is chosen to be the width of the superconducting transition ΔT as extracted via the

10% – 90% method, since the temperature fluctuations are estimated to be as small as 4 mK over an acquisition period of 10 s.

Reverse-coating study for seamless Nb/Cu cavities

The reverse-coating technique, conceived for the production of non-evaporable getter (NEG) coated, small diameter beam vacuum chamber, was implemented for the first time for the production of a seamless copper substrate for Nb/Cu SRF cavities having the niobium layer already present at the end of the fabrication process.

The study, thought to address the feasibility of the technique, was performed on a simpler geometry than an elliptical cavity, such as flat disk samples. According to the method, a niobium film is first coated via bipolar HiPIMS onto an aluminium mandrel which emulates the shape of the final desired object (the disk in this case, the elliptical cavity as final aim). A copper layer is then coated onto the niobium film, to serve as a root layer for the final copper structure which is electro-formed on it. Once the copper structure is formed the aluminum mandrel can be removed chemically, so that the final product will have the niobium layer left in it.

The study on disk samples demonstrated that the possibility of obtaining healthy niobium films (in terms of T_c, purity and morphology) via this technique is real, provided that an additional copper protective layer is also applied between the niobium film and the mandrel prior to the deposition of the niobium. In fast, the protective layer was observed to protect the film from possible degradation introduced by the chemical etching of the mandrel. The future step foreseen for the assessment of the technique is the study of the performance of the reverse-coated niobium films in RF conditions.

Nb_3Sn thin films on copper via bipolar HiPIMS

Nb_3Sn is still an option under investigation for coatings on copper for SRF cavities, as alternative material to niobium.

The fact that HiPIMS was never used before for the production of Nb_3Sn coatings and the extended coating parameter space with respect to DCMS makes it not an easy task to find a good coating recipe. The quality of the produced coatings was studied in terms of T_c, composition and morphology, and an initial investigation of the possible correlations between the film features and the coating parameters was performed. It was observed that a choice of parameters leading to a lower energy of the sputtered species, such as low voltage pulses and high coating pressures, results into improved film quality in terms of T_c, composition and morphology. No particular dependency was observed with respect to the coating temperature although, as previously observed for the DCMS coatings, applying a post-coating annealing to coating performed at equilibrium temperature improved the Nb-Sn composition ratio of the films but resulted in a cracked surface which cannot be considered compatible with RF use. Not all the coatings for which a high T_c was measured exhibited a sharp superconducting transition, confirming that the right stoichiometry is only one of the required conditions for good Nb_3Sn films. In fact, the coatings which exhibited a homogeneous, dense and void-free texture, with large grain size, were the ones that also showed a sharp transition. The production of these coatings is still ongoing and this study cannot be conclusive. Further investigation is needed to make a final statement on whether the choice of bipolar HiPIMS can lead to a satisfying coating recipe for Nb_3Sn films on copper.

Appendix A

User guide for the T_c measurement station at CERN

It is recommended to follow a standardized routine to operate the test station and perform a measurement. This Appendix is meant as a friendly guide to the users approaching the test station for the first time. It includes the instructions for the operation of the cryostat, the dipstick (*Excalibur* for friends), the data acquisition system and to run a measurement of T_c from the beginning to the next sample. At the risk of stating the obvious, the most basic operations will be also mentioned, with the hope of saving the user time- and helium-consuming oversights. However, it is important to bear in mind that the following instructions only apply to the specific system described in Chapter 5.

Preparation of the cryostat

- If the cryostat was exposed to air or inactive for a long time, it is good practice to purge it before the first fill. This is done by pumping vacuum in the cryostat with the purge pump (box 1, Fig. A.1) and then flushing with helium by re-connecting it to the gasometer. Repeating this operation for three consecutive times should ensure only a few ppm of air are left inside the cryostat before filling it with helium, provided that no leaks occur during the procedure.
- If the cryostat is completely warm, the first fill should transfer between 200 and 250 mm of liquid helium, which will likely evaporate soon completely due to the strong heat load from the cryostat.
- The helium level gauge should be turned on when the transfer has started.
- If the cryostat is cold, it is enough to fill 200 mm of liquid helium, to safely ensure the helium level is below the entrance of the vapour inlet.
- Before starting any other activity, make sure that: the cryostat connection to the gasometer is open (box 2, Fig. A.1) and that the cryostat has reached the equilibrium pressure (P_{atm} + 30 mbar); that the cryostat and the dewar are disconnected, hence there is no transfer line (box 3, Fig. A.1) connecting the two, with the respective connections being sealed.

Mounting of the sample

- The sample must be mounted at the slit of the sample holder. It is good practice to ensure it is as centered as possible, in order to have a symmetrical arrangement of the sample-coils relative position, to achieve approximately the same amount of leak field on each side of the sample.

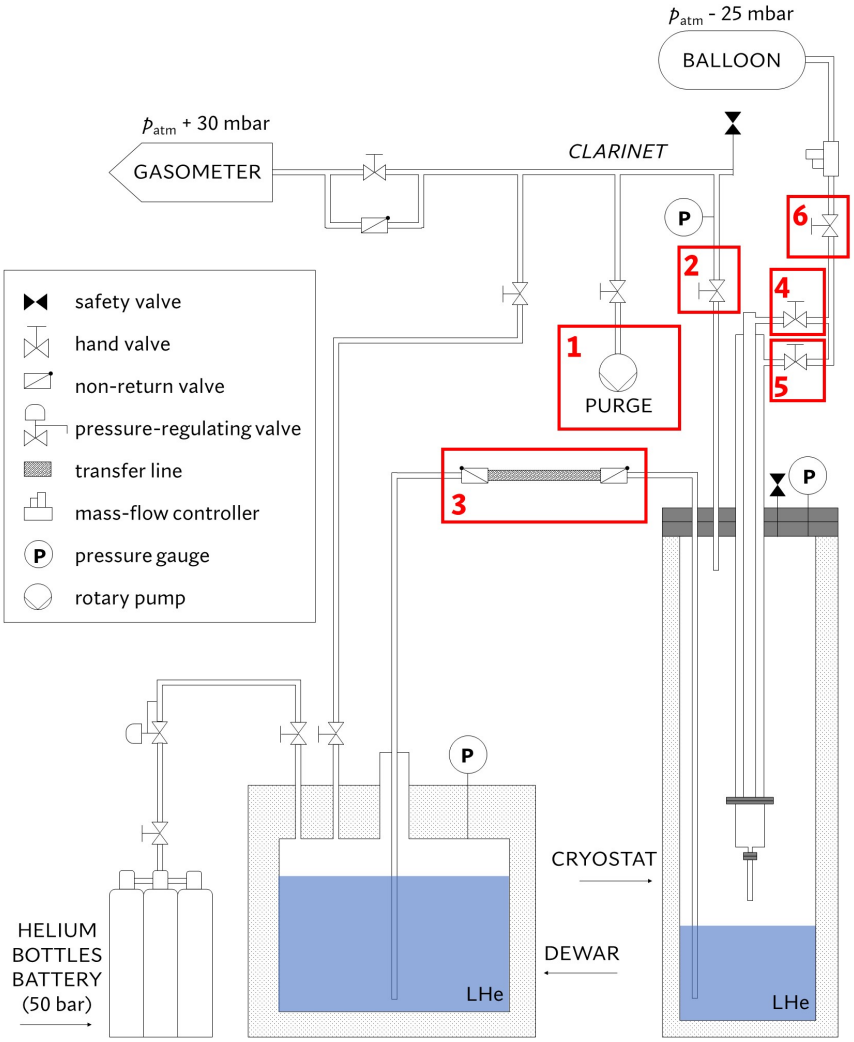

FIGURE A.1: Helium circuit for the T_c measurement station. All the parts of the system are explained in detail in Chapter 5.

- If the sample consists of a film+substrate sample, by routine it is mounted so that the film faces the drive coil. Given the system geometry described in Chapter 5, this is done so that the screws at the holder slit press on the film side when tightened, to ensure the copper side is pressed against the holder.
- The outer temperature sensor (TS-B) can now be secured to the back of the sample by tightening it with Teflon tape. One must be careful when doing so on a copper substrate, especially is annealed, as they are soft and bend easily. Although this sensor is not used for measurements on films, it is recommended to do so not to have any free hanging object while inserting the sample in the experimental chamber.
- Open the helium flow valve at the top of the dipstick (box 4, Fig. A.1), so that the vapour can flow up in when inserting the stick, pushing out any possible residual air.

- Carefully lower the dipstick down the cryostat insert tube, paying special attention not to hit and bend (or damage) the sample. Follow the guide so that the dipstick is aligned with the custom positioning block when completely down. This will ensure the correct position of the sample between the coils.
- Seal the dipstick to the insert and connect the flow tube to the mass flow meter and the connector with the electrical connections to the temperature sensors at the top of the dipstick.

PREPARATION OF THE MEASUREMENT (HARDWARE)

- Turn off the helium level gauge, otherwise it will be a noise source during the measurement.
- Open the hand valves connecting the helium flow from the insert tube and from the dipstick to the mass flow meter (box 5 and 6 respectively, Fig. A.1).
- Check that the NI acquisition cards are ON and all the devices are correctly connected.
- Turn on the mass flow meter, the temperature controller, the amplifier and the current source.

PREPARATION OF THE MEASUREMENT (SOFTWARE)

- Open the data acquisition program `CTM_Main.vi` with LabView and start the `.vi` ('CTM' stands for Critical Temperature Measurement). The GUI in Fig. A.2 will appear (from now on the boxes mentioned in the following refer to it).
- Insert the settings:
  - **Box 1 – sample name**: indicate the material, coating run number and sample number, e.g. "Nb-Cu-Run37-1";
  - **Box 1 – folder**: click on the folder icon, select the folder where to store the data, then click "current folder"; click "enter";
  - **Box 2 – acquisition channels**: click "settings" then open the "DAQmx channel" scroll menu, click "browse"; select the acquisition channels `ai0` and `ai1` (both at the same time) and click "OK"; do not close the menu yet;
  - **Box 2 – measurement settings**: still in the "settings" menu, and fill the fields as follows: "current" = 30 mA; "frequency" = 21 Hz; "compliance voltage" = 10 V; "acquisition time" is to be set depending on the measurement duration; "acquisition rate A" = 10 Hz; "acquisition rate B+C" = 10 Hz[1](A, B and C refer to the names of the three live monitors at the top row of the `.vi`, highlighted by box 5 in Fig. A.2); click "OK";
  - **Box 3 – temperature controller settings**: click "settings LakeShore" and the settings menu will pop up; then, depending on the helium level, the amount of vapour left in the cryostat and the number of measurements already performed before the current run, one might need to either cool down (1) or warm up (2) the system to the starting temperature desired for the next measurement:

[1]The actual acquisition rate here is the default one provided by the NI cards, but due to an unresolved bug in the LAbView program it needs to be set to the same value as the acquisition rate for the temperature and amplitude data.

1. **Step A**: go to the second column from the left in the settings menu, "Device EH101" is the heater in the helium bath to produce helium vapour (always set in open loop as it is not PID controlled): must be turned on from the scroll menu at the bottom and "heater range" must be set as "high"; **Step B**: go to the third column from the left, "Device EH102" is the heater around the helium vapour inlet to regulate the vapour temperature (PID controlled): the start point of the temperature ramp must be set at "Set point" $\rightarrow$ "Value" $\rightarrow$ insert desired start value in Kelvin, then "Ramp" must be set ON and "Rate" on 0 K/min (when the ramp rate is set to zero it directly goes to the set-point temperature without running a ramp); **Step C**: click "Save";
2. skip **Step A** from above and keep EH101 off; execute **Step B** and, after that, EH102 must be turned on from the scroll menu at the bottom and "heater range" must be set as "high"; proceed with **Step C**.

RUN THE MEASUREMENT

- **Box 4**: click "START" on the main panel.
- Wait for the temperature to stabilize at the setpoint value. For the system to be considered thermalised it is good practice to wait until the temperature difference between TS-A and TS-B is smaller than 50 mK.
- Wait for the EH102 heater power to stabilise below 30%.
- **Box 4**: the magnetic field can now be turned on by clicking on "DRIVE COIL OFF" (OFF/ON stand for the current status of the coil); the button should turn green, as shown in Fig. A.2.
- **Box 4**: the data acquisition can be started by clicking on "ACQUIRE"; the indicator light on the button should turn green, as shown in Fig. A.2.
- **Box 3**: on the LakeShore settings, without clicking on the settings button (i.e. staying on the current window), the temperature ramp can now be set on the "Sample heater = EH102" column: "Set point" $\rightarrow$ "Value" $\rightarrow$ insert desired final temperature value in Kelvin, then "Ramp" is set at 1.5 K/min. Operation in helium vapour makes the available temperature range to be limited to 4.2 K – 20 K for stable measurements.
- **Box 3**: start the ramp by clicking "OK".
- **Box 4**: when the final temperature is reached and the ramp is over, the data acquisition can be stopped by clicking on "STOP ACQUIRE"; the indicator light on the button should turn red.
- **Box 4**: the magnetic field can now be turned off by clicking on "DRIVE COIL ON"; the button should turn back to gray.
- **Box 3**: heater EH102 can be turned off by setting "heater range" to "off".
- The measured data is stored in a `.tdms` file, containing all the measurement settings and the logged data for both temperature sensors, both coils raw voltages, pickup coil voltage amplitude and phase as extracted by the lock-in amplifier and the clock time stamp for the temperature and amplitude acquisition. The data analysis for the extraction of T_c is performed offline according to what discussed in Section 5.4.2.

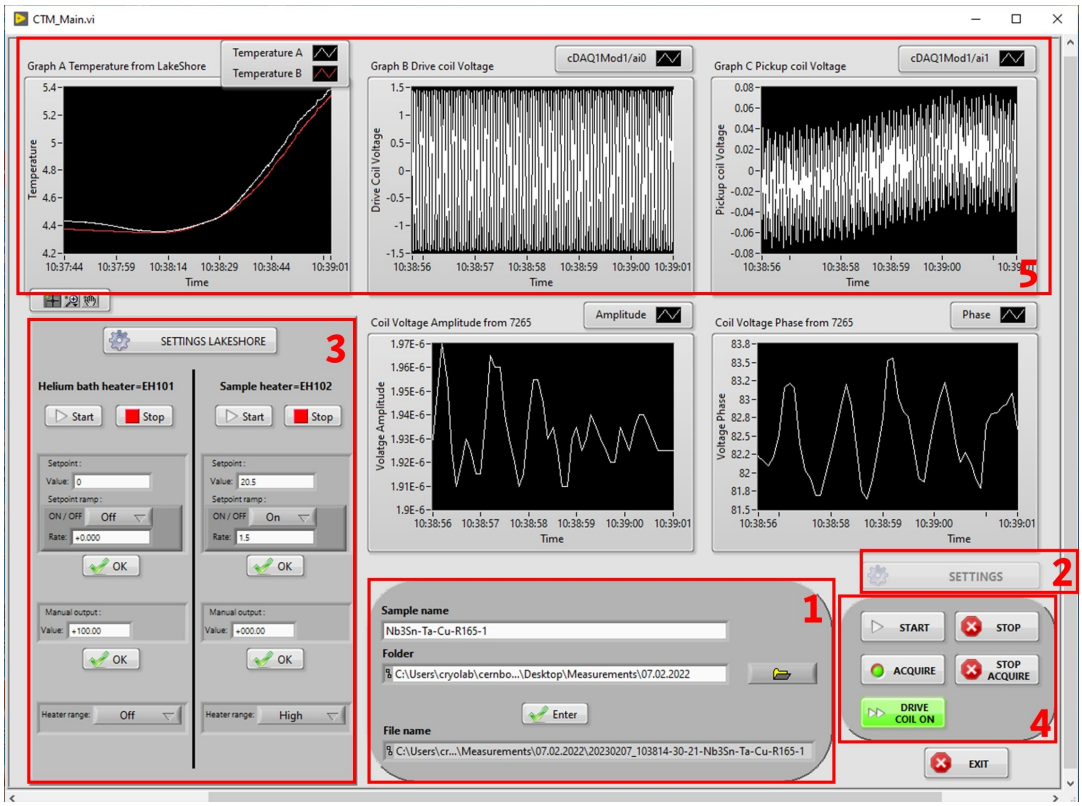

FIGURE A.2: GUI of the LabView data acquisition program for the measurement of T_c. The details of the instrumentation employed for the measurement station are discussed in Chapter 5.

PREPARATION OF THE NEXT MEASUREMENT

- The mass flow controller must be turned off and the hand valve connecting it to the dipstick and insert tube flows closed (box 6, Fig. A.1).
- After having turned off the LakeShore controller, the connector to the temperature sensors can be disconnected from the dipstick.
- Disconnect the flow tube from the dipstick (box 4, Fig. A.1).
- Lift the dipstick up while leaving it inside the cryostat. Lock it in position and leave it warm up slowly before taking it out, to avoid air condensation on the coils and connections taking place if taken out when too cold. Slow warm up (as well as slow cool down) is also recommended to avoid damage to any soldered electrical connections.
- When the dipstick is warm, can be taken out of the insert. A new sample to be measured can now be mounted.

Appendix B

Nb_3Sn coatings data selection

Run no.	T_c (K)	ΔT_c (K)	PP (V)	P_{Kr} (mbar)	T_{coat} (°C)	Sn (At%)	d (µm)	Post-ann. (Y/N)	Enr. targ. (Y/N)
59	13.3	0.9	50	7×10^{-4}	750	23.7	2.5	N	N
60	14.1	0.9	50	7×10^{-4}	750	23.7	3	Y	N
61	13.7	1.1	50	7×10^{-4}	750	24.1	2.7	Y	N
62	6.3	0.6	100	7×10^{-4}	750	20	2.6	N	N
63	13.1	0.2	50	7×10^{-4}	750	23.7	2.7	Y	N
66	6.3	0.8	100	7×10^{-4}	750	20.4	2.6	Y	N
67	11.6	1.2	80	7×10^{-4}	750	23.2	2.5	N	N
68	13.6	0.9	65	7×10^{-4}	750	23.1	2.4	Y	N
69	15	0.7	50	5×10^{-2}	750	25	2.2	N	N
70	6.7	0.8	80	7×10^{-4}	750	20.7	2.7	Y	N
71	9.5	1.2	100	7×10^{-4}	750	22.4	2.1	Y	N
72	8	1.4	100	7×10^{-4}	750	21	2	Y	N
73	14	0.4	50	5×10^{-3}	750	25.1	2.6	N	N
74	13.9	0.6	50	5×10^{-3}	750	24.4	3.8	N	N
75	13.7	0.4	50	2×10^{-3}	750	24.3	3.6	N	N
76	14	0.5	50	1×10^{-2}	750	24.8	3.7	N	N
78	13.6	0.7	50	1×10^{-2}	750	24.4	3.6	N	N
80	14.8	0.5	50	2.5×10^{-2}	750	26	3.2	N	N
81	14.9	0.7	50	2.5×10^{-2}	750	21.9	3.2	N	N
82	14.3	0.7	35	7×10^{-4}	750	25.3	2.7	N	N
83	12.8	0.9	100	2.5×10^{-2}	750	23.1	3.4	N	N
84	14.4	0.7	65	2.5×10^{-2}	750	23.1	3.2	N	N
85	15.3	0.7	35	2.5×10^{-2}	750	26.4	3.3	N	N
86	14	0.6	80	2.5×10^{-2}	750	22.5	3.2	N	N
87	15	0.7	50	2.5×10^{-2}	700	25.9	3.2	N	N
88	13	0.6	50	7×10^{-4}	650	24.6	2.8	N	N

TABLE B.1: Data set employed for the data analysis presented in Chapter 7. Continued in Table B.2.

Run no.	T_c (K)	ΔT_c (K)	PP (V)	P_{Kr} (mbar)	T_{coat} (°C)	Sn (At%)	d (µm)	Post-ann. (Y/N)	Enr. targ. (Y/N)
93	10.7	0.5	50	7×10^{-4}	700	23.6	–	N	N
94	14.6	0.6	50	2.5×10^{-2}	650	25.9	–	N	N
96	13.9	0.5	50	8×10^{-3}	750	25.2	–	N	N
112	14.9	0.7	50	2.5×10^{-2}	750	25.2	–	N	N
116	14.6	0.6	50	2.5×10^{-2}	600	25.9	–	N	N
118	14.4	0.5	50	2.5×10^{-2}	750	25.4	–	N	N
119	14.4	0.6	50	2.5×10^{-2}	750	26	–	N	N
121	14.6	0.6	50	2.5×10^{-2}	750	25.2	2.9	N	N
132	16.1	0.6	50	2.5×10^{-2}	210	23.9	–	Y	N
133	15.5	0.8	50	2.5×10^{-2}	210	24.7	–	Y	N
137	16	1	50	2.5×10^{-2}	210	23	–	Y	N
139	16.3	0.5	50	2.5×10^{-2}	210	24.6	3.8	Y	N
140	11.2	1.1	50	2.5×10^{-2}	500	26.3	–	N	N
141	15.8	0.5	50	2.5×10^{-2}	750	25.4	–	N	N
142	16.4	0.7	50	2.5×10^{-2}	210	24.3	–	Y	N
143	16.3	0.9	50	2.5×10^{-2}	210	24.5	–	Y	Y
144	16.4	0.7	50	2.5×10^{-2}	210	23.5	2.8	Y	Y
145	16.2	0.9	50	2.5×10^{-2}	210	–	–	Y	Y
146	16.2	0.8	50	2.5×10^{-2}	750	–	–	N	Y
147	16.6	0.6	50	2.5×10^{-2}	210	–	–	Y	Y
148	16.3	0.7	80	2.5×10^{-2}	224	–	–	Y	Y
149	15.5	1.1	130	2.5×10^{-2}	230	–	–	Y	Y
151	14.9	0.5	50	2.5×10^{-2}	235	–	–	Y	Y
153	13.2	0.5	50	7×10^{-4}	250	–	–	Y	Y
154	14.8	0.9	50	7×10^{-4}	260	–	–	Y	Y
156	16.2	0.76	50	2.5×10^{-2}	750	–	–	N	Y
157	15.3	0.7	50	2.5×10^{-2}	600	–	–	N	Y
158	16.5	0.7	50	2.5×10^{-2}	240	–	–	Y	Y
159	13.6	0.4	50	7×10^{-4}	750	–	–	N	Y
160	15.5	1.1	50	8×10^{-3}	750	–	–	N	Y
161	15.7	0.8	50	2.5×10^{-2}	750	–	–	N	Y
162	15.2	0.5	50	2.5×10^{-2}	750	–	–	Y	Y

TABLE B.2: Data set employed for the data analysis presented in Chapter 7. Continues from Table B.1.

Bibliography

[1] L. W. Alvarez, H. Bradner, J. V. Franck, *et al.*, "Berkeley Proton Linear Accelerator," *Review of Scientific Instruments*, vol. 26, no. 2, pp. 111–133, 1955, Publisher: American Institute of Physics, ISSN: 0034-6748. DOI: 10.1063/1.1771253.

[2] M. Vretenar, *Radio frequency for particle accelerators: Evolution and anatomy of a technology*, arXiv.org, 2012. DOI: 10.48550/arXiv.1201.2345.

[3] A. Nassiri, B. Chase, P. Craievich, *et al.*, "History and Technology Developments of Radio Frequency (RF) Systems for Particle Accelerators," *IEEE Transactions on Nuclear Science*, vol. 63, no. 2, pp. 707–750, 2016, Publisher: IEEE, ISSN: 1558-1578. DOI: 10.1109/TNS.2015.2485164.

[4] A. P. Banford and G. H. Stafford, "The feasibility of a superconducting proton linear accelerator," *Journal of Nuclear Energy. Part C, Plasma Physics, Accelerators, Thermonuclear Research*, vol. 3, no. 4, p. 287, Jan. 1961, ISSN: 0368-3281. DOI: 10.1088/0368-3281/3/4/308.

[5] E. Chiaveri, "Superconducting RF cavities: Past, present and future," *IEEE Transactions on Applied Superconductivity*, vol. 13, no. 2, pp. 1199–1204, 2003, Publisher: IEEE, ISSN: 1558-2515. DOI: 10.1109/TASC.2003.812631.

[6] H. Podlech, *Superconducting versus normal conducting cavities*, arXiv.org, 2013. DOI: 10.48550/arXiv.1303.6552.

[7] H. Padamsee, *Design Topics for Superconducting RF Cavities and Ancillaries*, arXiv.org, 2014. DOI: 10.48550/arXiv.1501.07129.

[8] H. Padamsee, "50 years of success for SRF accelerators - a review," *Superconductor Science and Technology*, vol. 30, no. 5, 2017, Publisher: IOP Publishing, ISSN: 0953-2048. DOI: 10.1088/1361-6668/aa6376.

[9] D. Bafia, A. Grassellino, O. Melnychuk, A. Romanenko, Z.-H. Sung, and J. Zasadzinski, "Gradients of 50 MV/m in TESLA Shaped Cavities via Modified Low Temperature Bake," in *Proceedings of the 19th International Conference on RF Superconductivity*, Publisher: JACoW Publishing, Geneva, Switzerland, vol. SRF2019, 2019. DOI: 10.18429/JACOW-SRF2019-TUP061.

[10] S. Calatroni, "20 Years of experience with the Nb/Cu technology for superconducting cavities and perspectives for future developments," *Physica C: Superconductivity*, Proceedings of the 12th International Workshop on RF Superconductivity, vol. 441, no. 1-2, pp. 95–101, 2006, Publisher: Elsevier, ISSN: 0921-4534. DOI: 10.1016/j.physc.2006.03.044.

[11] V. Arbet-Engels, C. Benvenuti, S. Calatroni, *et al.*, "Superconducting niobium cavities, a case for the film technology," *Nuclear Instruments and Methods in Physics Research Section A: Accelerators, Spectrometers, Detectors and Associated Equipment*, vol. 463, no. 1, pp. 1–8, May 2001, ISSN: 0168-9002. DOI: 10.1016/S0168-9002(01)00165-6.

[12] J. P. H. Sladen, "Status of Superconducting Cavities in LEP," in *Proceedings of 8th International Workshop on RF Superconductivity*, vol. 60, Abano-Terme, Italy: Part. Accel., 1998, pp. 15–25.

[13] T. L. S. Group, "The Large Hadron Collider : Conceptual design," Tech. Rep. CERN-AC-95-05-LHC, 1995, CERN Document Server.

[14] C. Benvenuti, S. Calatroni, I. Campisi, *et al.*, "Study of the surface resistance of superconducting niobium films at 1.5 GHz," *Physica C: Superconductivity*, vol. 316, no. 3-4, pp. 153–188, 1999, Publisher: Elsevier, ISSN: 0921-4534. DOI: 10.1016/S0921-4534(99)00207-5.

[15] The FCC Collaboration, A. Abada, M. Abbrescia, *et al.*, "FCC-ee: The Lepton Collider: Future Circular Collider Conceptual Design Report Volume 2," *The European Physical Journal Special Topics*, vol. 228, no. 2, pp. 261–623, 2019, ISSN: 1951-6355, 1951-6401. DOI: 10.1140/epjst/e2019-900045-4.

[16] W. Venturini Delsolaro, M. Garlasche, F. Peauger, *et al.*, "Progress and R/D challenges for FCC-ee SRF," en, *EPJ Techniques and Instrumentation*, vol. 10, no. 1, pp. 1–13, Dec. 2023, Publisher: SpringerOpen, ISSN: 2195-7045. DOI: 10.1140/epjti/s40485-023-00094-5.

[17] M. Arzeo, F. Avino, S. Pfeiffer, *et al.*, "Enhanced radio-frequency performance of niobium films on copper substrates deposited by high power impulse magnetron sputtering," *Superconductor Science and Technology*, vol. 35, no. 5, 2022, Publisher: IOP Publishing, ISSN: 0953-2048. DOI: 10.1088/1361-6668/ac5646.

[18] F. Avino, A. Sublet, and M. Taborelli, "Evidence of ion energy distribution shift in HiPIMS plasmas with positive pulse," *Plasma Sources Science and Technology*, vol. 28, no. 1, 2019, ISSN: 1361-6595. DOI: 10.1088/1361-6595/aaf5c9.

[19] F. Avino, D. Fonnesu, T. Koettig, *et al.*, "Improved film density for coatings at grazing angle of incidence in high power impulse magnetron sputtering with positive pulse," *Thin Solid Films*, vol. 706, 2020, ISSN: 00406090. DOI: 10.1016/j.tsf.2020.138058.

[20] A. Miyazaki and W. V. Delsolaro, "Two different origins of the Q-slope problem in superconducting niobium film cavities for a heavy ion accelerator at CERN," *Physical Review Accelerators and Beams*, vol. 22, no. 7, p. 073 101, Jul. 2019, Publisher: American Physical Society. DOI: 10.1103/PhysRevAccelBeams.22.073101.

[21] V. Palmieri, "Seamless cavities : The most creative topic in RF superconductivity," in *Proceedings of 8th International Workshop on RF Superconductivity*, vol. 3, Abano Terme (Padova), Italy, 1997.

[22] V. Palmieri, "Review of Fabrication of SC Cavity Structures," in *LINAC98 Papers*, Chicago, Illinois, USA, 1998, pp. 697–700.

[23] L. Lain Amador, P. Chiggiato, L. M. A. Ferreira, *et al.*, "Electrodeposition of copper applied to the manufacture of seamless superconducting rf cavities," *Physical Review Accelerators and Beams*, vol. 24, no. 8, 2021, ISSN: 2469-9888. DOI: 10.1103/PhysRevAccelBeams.24.082002.

[24] S. Posen, J. Lee, D. N. Seidman, *et al.*, "Advances in Nb3Sn superconducting radiofrequency cavities towards first practical accelerator applications," *Superconductor Science and Technology*, vol. 34, no. 2, 2021, ISSN: 0953-2048. DOI: 10.1088/1361-6668/abc7f7.

[25] G. Ciovati, J. Anderson, S. Balachandran, *et al.*, "Development of a prototype superconducting radio-frequency cavity for conduction-cooled accelerators," *Physical Review Accelerators and Beams*, vol. 26, no. 4, Apr. 2023, ISSN: 2469-9888. DOI: 10.1103/PhysRevAccelBeams.26.044701.

[26] E. A. Ilyina, G. Rosaz, J. B. Descarrega, *et al.*, "Development of sputtered Nb3Sn films on copper substrates for superconducting radiofrequency applications," *Superconductor Science and Technology*, vol. 32, no. 3, 2019, ISSN: 0953-2048. DOI: 10.1088/1361-6668/aaf61f.

[27] S. Leith, *Progress with bipolar HiPIMS-deposited Nb3Sn films on Cu for SRF applications*, FCC Week 2022, Paris, France, May 2022.

[28] D. Fonnesu, A. Baris, S. Calatroni, *et al.*, "Reverse coating technique for the production of Nb thin films on copper for superconducting radio-frequency applications," *Superconductor Science and Technology*, vol. 35, no. 12, 2022, Publisher: IOP Publishing, ISSN: 0953-2048. DOI: 10.1088/1361-6668/ac9c99.

[29] L. Lain Amador, P. Chiggiato, L. M. A. Ferreira, *et al.*, "Development of copper electroformed vacuum chambers with integrated non-evaporable getter thin film coatings," *Journal of Vacuum Science & Technology A: Vacuum, Surfaces, and Films*, vol. 36, no. 2, 2018, ISSN: 0734-2101. DOI: 10.1116/1.4999539.

[30] J. D. Jackson, *Classical Electrodynamics*, 3rd. Wiley, 1998, ISBN: 978-0-471-30932-1.

[31] W. Buckel and R. Kleiner, *Superconductivity: Fundamentals and Applications*, 2nd edition. WILEY-VCH, 2004, ISBN: 978-3-527-40349-3. DOI: 10.1002/9783527618507.

[32] H. Padamsee, J. Knobloch, and T. Hays, *RF Superconductivity for Accelerators*, 2nd edition. WILEY-VCH, 2008, ISBN: 978-3-527-40842-9.

[33] H. K. Onnes, "Further experiments with liquid helium. C. On the change of electric resistance of pure metals at very low temperatures etc. IV. The resistance of pure mercury at helium temperatures," in *Through Measurement to Knowledge: The Selected Papers of Heike Kamerlingh Onnes 1853–1926*, ser. Boston Studies in the Philosophy of Science, H. K. Onnes, K. Gavroglu, and Y. Goudaroulis, Eds., Dordrecht: Springer Netherlands, 1991, pp. 261–263, ISBN: 978-94-009-2079-8. DOI: 10.1007/978-94-009-2079-8_15.

[34] H. K. Onnes, *Communications from the Physical Laboratory at the University of Leiden*. 1914, vol. 133a, Original from Harvard University.

[35] W. Meissner and R. Ochsenfeld, "Ein neuer Effekt bei Eintritt der Supraleitfähigkeit," *Naturwissenschaften*, vol. 21, no. 44, pp. 787–788, 1933, ISSN: 1432-1904. DOI: 10.1007/BF01504252.

[36] A. M. Forrest, "Meissner and Ochsenfeld revisited," *European Journal of Physics*, vol. 4, no. 2, pp. 117–120, 1983, ISSN: 0143-0807. DOI: 10.1088/0143-0807/4/2/011.

[37] F. London, H. London, and F. A. Lindemann, "The electromagnetic equations of the supraconductor," *Proceedings of the Royal Society of London. Series A - Mathematical and Physical Sciences*, vol. 149, no. 866, 1935, Publisher: Royal Society. DOI: 10.1098/rspa.1935.0048.

[38] C. J. Gorter, "On supraconductivity I," *Physica*, vol. 1, no. 1-6, 1934, Publisher: North-Holland, ISSN: 0031-8914. DOI: 10.1016/S0031-8914(34)90037-9.

[39] J. McLennan, H. Smith, and J. Wilhelm, "XIV. The scattering of light by liquid helium," *The London, Edinburgh, and Dublin Philosophical Magazine and Journal of Science*, vol. 14, no. 89, pp. 161–167, 1932, Publisher: Taylor & Francis, ISSN: 1941-5982. DOI: 10.1080/14786443209462044.

[40] W. H. Keesom and A. P. Keesom, "New measurements on the specific heat of liquid helium," *Physica*, vol. 2, no. 1, pp. 557–572, 1935, ISSN: 0031-8914. DOI: 10.1016/S0031-8914(35)90128-8.

[41] W. H. Keesom and A. P. Keesom, "On the heat conductivity of liquid helium," *Physica*, vol. 3, no. 5, pp. 359–360, 1936, ISSN: 0031-8914. DOI: 10.1016/S0031-8914(36)80312-7.

[42] J. F. Allen, R. Peierls, and M. Z. Uddin, "Heat Conduction in Liquid Helium," *Nature*, vol. 140, no. 3532, pp. 62–63, 1937, Publisher: Nature Publishing Group, ISSN: 1476-4687. DOI: 10.1038/140062a0.

[43] E. F. Burton, "Viscosity of Helium I and Helium II," *Nature*, vol. 135, no. 3407, pp. 265–265, 1935, Publisher: Nature Publishing Group, ISSN: 1476-4687. DOI: 10.1038/135265a0.

[44] P. Kapitza, "Viscosity of Liquid Helium below the λ-Point," *Nature*, vol. 141, no. 3558, pp. 74–74, 1938, Number: 3558 Publisher: Nature Publishing Group, ISSN: 1476-4687. DOI: 10.1038/141074a0.

[45] J. F. Allen and A. D. Misener, "Flow of Liquid Helium II," *Nature*, vol. 141, no. 3558, pp. 75–75, 1938, Publisher: Nature Publishing Group, ISSN: 1476-4687. DOI: 10.1038/141075a0.

[46] A. Einstein, "Quantentheorie des einatomigen idealen Gases," in *Albert Einstein: Akademie-Vorträge (1925)*, John Wiley & Sons, Ltd, 2005, pp. 237–244, ISBN: 978-3-527-60895-9. DOI: 10.1002/3527608958.ch27.

[47] Bose, "Plancks Gesetz und Lichtquantenhypothese," *Zeitschrift für Physik*, vol. 26, no. 1, pp. 178–181, 1924, ISSN: 0044-3328. DOI: 10.1007/BF01327326.

[48] F. London, "On the Bose-Einstein Condensation," *Physical Review*, vol. 54, no. 11, pp. 947–954, 1938, Publisher: American Physical Society. DOI: 10.1103/PhysRev.54.947.

[49] F. London, "The λ-Phenomenon of Liquid Helium and the Bose-Einstein Degeneracy," *Nature*, vol. 141, no. 3571, pp. 643–644, 1938, Publisher: Nature Publishing Group, ISSN: 1476-4687. DOI: 10.1038/141643a0.

[50] L. Tisza, "Transport Phenomena in Helium II," *Nature*, vol. 141, no. 3577, pp. 913–913, 1938, Publisher: Nature Publishing Group, ISSN: 1476-4687. DOI: 10.1038/141913a0.

[51] L. Tisza, "The Theory of Liquid Helium," *Physical Review*, vol. 72, no. 9, pp. 838–854, 1947, Publisher: American Physical Society. DOI: 10.1103/PhysRev.72.838.

[52] A. B. Pippard, "High-Frequency Resistance of Superconductors," *Nature*, vol. 158, no. 4007, pp. 234–235, 1946, Publisher: Nature Publishing Group, ISSN: 1476-4687. DOI: 10.1038/158234c0.

[53] C. J. Gorter, "Chapter I The Two Fluid Model for Superconductors and Helium II," in *Progress in Low Temperature Physics*, vol. 1, Elsevier, 1955, pp. 1–16. DOI: 10.1016/S0079-6417(08)60076-1.

[54] L. D. Landau and V. L. Ginzburg, "On the theory of superconductivity," *Zhurnal Eksperimental'noi i Teoreticheskoi Fiziki*, 1950.

[55] L. D. Landau, "On the theory of phase transitions. I," *Physikalische Zeitschrift der Sowjetunion*, 1937.

[56] L. D. Landau and E. M. Lifshitz, *Statistical Physics: Volume 5*. Elsevier, 2013, ISBN: 978-0-08-057046-4.

[57] J. R. Clement and E. H. Quinnell, "The Atomic Heat of Lead in the Region of its Transition to Superconductivity," *Physical Review*, vol. 85, no. 3, pp. 502–503, Feb. 1952, Publisher: American Physical Society. DOI: 10.1103/PhysRev.85.502.

[58] A. B. Pippard and W. L. Bragg, "An experimental and theoretical study of the relation between magnetic field and current in a superconductor," *Proceedings of the Royal Society of London*, A, vol. 216, no. 1127, pp. 547–568, 1953. DOI: 10.1098/rspa.1953.0040.

[59] L. V. Shubnikov, V. I. Khotkevich, Y. D. Shepelev, and Y. N. Ryabinin, "Magnetic properties of superconducting metals and alloys," *Ukrainian Journal of Physics - Special Issue*, vol. 53, p. 11, 2008, Translated and reprinted from Zh. Eksper. Teor. Fiz. 7, pp. 221–237 (1937), ISSN: 2071-0194.

[60] T. Kinsel, E. A. Lynton, and B. Serin, "Magnetic and Thermal Properties of Second-Kind Superconductors. I. Magnetization Curves," *Reviews of Modern Physics*, vol. 36, no. 1, pp. 105–109, 1964, Publisher: American Physical Society. DOI: 10.1103/RevModPhys.36.105.

[61] A. A. Abrikosov, "The magnetic properties of superconducting alloys," *Journal of Physics and Chemistry of Solids*, vol. 2, no. 3, pp. 199–208, 1957, ISSN: 0022-3697. DOI: 10.1016/0022-3697(57)90083-5.

[62] R. P. Feynman, "Chapter II Application of Quantum Mechanics to Liquid Helium," in *Progress in Low Temperature Physics*, C. J. Gorter, Ed., vol. 1, Elsevier, 1955, pp. 17–53. DOI: 10.1016/S0079-6417(08)60077-3.

[63] B. S. Deaver and W. M. Fairbank, "Experimental Evidence for Quantized Flux in Superconducting Cylinders," *Physical Review Letters*, vol. 7, no. 2, pp. 43–46, 1961, Publisher: American Physical Society. DOI: 10.1103/PhysRevLett.7.43.

[64] I. Giaever, "Flux Pinning and Flux-Flow Resistivity in Magnetically Coupled Superconducting Films," *Physical Review Letters*, vol. 16, no. 11, pp. 460–462, 1966, Publisher: American Physical Society. DOI: 10.1103/PhysRevLett.16.460.

[65] H. Fröhlich, "Theory of the Superconducting State. I. The Ground State at the Absolute Zero of Temperature," *Physical Review*, vol. 79, no. 5, pp. 845–856, 1950, Publisher: American Physical Society. DOI: 10.1103/PhysRev.79.845.

[66] J. Bardeen, "Wave Functions for Superconducting Electrons," *Physical Review*, vol. 80, no. 4, pp. 567–574, 1950, Publisher: American Physical Society. DOI: 10.1103/PhysRev.80.567.

[67] E. Maxwell, "Superconductivity of the Isotopes of Tin," *Physical Review*, vol. 86, no. 2, pp. 235–242, 1952, Publisher: American Physical Society. DOI: 10.1103/PhysRev.86.235.

[68] B. Serin, C. A. Reynolds, and C. Lohman, "The Isotope Effect in Superconductivity. II. Tin and Lead," *Physical Review*, vol. 86, no. 2, pp. 162–164, 1952, Publisher: American Physical Society. DOI: 10.1103/PhysRev.86.162.

[69] J. M. Lock, A. B. Pippard, and D. Shoenberg, "Superconductivity of tin isotopes," *Mathematical Proceedings of the Cambridge Philosophical Society*, vol. 47, no. 4, pp. 811–819, 1951, Publisher: Cambridge University Press, ISSN: 1469-8064. DOI: 10.1017/S0305004100027250.

[70] J. Bardeen, L. N. Cooper, and J. R. Schrieffer, "Theory of Superconductivity," *Physical Review*, vol. 108, no. 5, pp. 1175–1204, 1957, Publisher: American Physical Society. DOI: 10.1103/PhysRev.108.1175.

[71] P. Schmüser, "Superconductivity," Hamburg, Germany, CAS - CERN Accelerator School CERN-96-03, 1995, ISBN: 9789290830849 Publisher: CERN. DOI: 10.5170/CERN-1996-003.

[72] M. Tinkham, *Introduction to superconductivity*, 2nd edition. Mineola, N.Y.: Dover Publications, 2004, ISBN: 978-1-62198-598-3.

[73] T. Reimann, S. Mühlbauer, M. Schulz, *et al.*, "Visualizing the morphology of vortex lattice domains in a bulk type-II superconductor," *Nature Communications*, vol. 6, no. 1, p. 8813, 2015, Publisher: Nature Publishing Group, ISSN: 2041-1723. DOI: 10.1038/ncomms9813.

[74] L. Neumann and L. Tewordt, "Temperature dependence of the magnetization in the mixed state of superconducting alloys," *Zeitschrift für Physik*, vol. 191, no. 1, pp. 73–80, 1966, ISSN: 0044-3328. DOI: 10.1007/BF01362470.

[75] D. C. Mattis and J. Bardeen, "Theory of the Anomalous Skin Effect in Normal and Superconducting Metals," *Physical Review*, vol. 111, no. 2, pp. 412–417, 1958, Publisher: American Physical Society. DOI: 10.1103/PhysRev.111.412.

[76] G. E. H. Reuter, E. H. Sondheimer, and A. H. Wilson, "The theory of the anomalous skin effect in metals," *Proceedings of the Royal Society of London*, A, vol. 195, no. 1042, pp. 336–364, 1948, Publisher: Royal Society. DOI: 10.1098/rspa.1948.0123.

[77] A. Gurevich, "Theory of RF superconductivity for resonant cavities," *Superconductor Science and Technology*, vol. 30, no. 3, 2017, Publisher: IOP Publishing, ISSN: 0953-2048. DOI: 10.1088/1361-6668/30/3/034004.

[78] K. Saito, H. Ao, B. Bird, *et al.*, "FRIB Solenoid Package in Cryomodule and Local Magnetic Shield," in *Proceedings of the 19th International Conference on RF Superconductivity*, ISBN: 9783954502110 Publisher: JACoW Publishing, Geneva, Switzerland, vol. SRF2019, Dresden, Germany, 2019. DOI: 10.18429/JACOW-SRF2019-MOP072.

[79] J. Völker, A. Frahm, A. Jankowiak, *et al.*, "A Superconducting Magnetic Shield for the Photoelectron Injector of BERLinPro," in *Proceedings of the 19th International Conference on RF Superconductivity*, ISBN: 9783954502110 Publisher: JACoW Publishing, Geneva, Switzerland, vol. SRF2019, Dresden, Germany, 2019. DOI: 10.18429/JACOW-SRF2019-MOP105.

[80] B. Bonin, "Materials for Superconducting Cavities," in *CAS - CERN Accelerator School: Superconductivity in Particle Accelerators*, ser. CERN Yellow Reports: School Proceedings, Stuart Turner, 1996, pp. 191–200, ISBN: 92-9083-084-0. DOI: 10.5170/CERN-1996-003.191.

[81] C. P. Bean and J. D. Livingston, "Surface Barrier in Type-II Superconductors," *Physical Review Letters*, vol. 12, no. 1, pp. 14–16, Jan. 1964, Publisher: American Physical Society. DOI: 10.1103/PhysRevLett.12.14.

[82] J. Matricon and D. Saint-James, "Superheating fields in superconductors," *Physics Letters A*, vol. 24, no. 5, pp. 241–242, 1967, ISSN: 0375-9601. DOI: 10.1016/0375-9601(67)90412-4.

[83] M. K. Transtrum, G. Catelani, and J. P. Sethna, "Superheating field of superconductors within Ginzburg-Landau theory," *Physical Review B*, vol. 83, no. 9, 2011, Publisher: American Physical Society. DOI: 10.1103/PhysRevB.83.094505.

[84] M. Kelly, "Superconducting Radio-Frequency Cavities for Low-Beta Particle Accelerators," *Reviews of Accelerator Science and Technology*, vol. 5, pp. 185–203, Jan. 2012, Publisher: World Scientific Publishing Co., ISSN: 1793-6268. DOI: 10.1142/S1793626812300071.

[85] J. Knobloch, "Superconducting RF: Enabling Technology for Modern Light Sources," in *Synchrotron Light Sources and Free-Electron Lasers: Accelerator Physics, Instrumentation and Science Applications*, E. J. Jaeschke, S. Khan, J. R. Schneider, and J. B. Hastings, Eds., Cham: Springer International Publishing, 2016, pp. 505–559, ISBN: 978-3-319-14394-1. DOI: 10.1007/978-3-319-14394-1_13.

[86] H. Padamsee, D. Proch, P. Kneisel, and J. Mioduszewski, "Field strength limitations in superconducting cavities-multipacting and thermal breakdown," *IEEE Transactions on Magnetics*, vol. 17, no. 1, pp. 947–950, 1981, ISSN: 1941-0069. DOI: 10.1109/TMAG.1981.1061065.

[87] W. Singer, A. Brinkmann, D. Proch, and X. Singer, "Quality requirements and control of high purity niobium for superconducting RF cavities," *Physica C: Superconductivity*, Proceedings of the topical conference of the International Cryogenic Materials Conference (ICMC 2002). Superconductors for Practical Applications, vol. 386, pp. 379–384, 2003, ISSN: 0921-4534. DOI: 10.1016/S0921-4534(02)02208-6.

[88] C. Benvenuti, M. Minestrini, D. Bloess, N. Hilleret, W. Weingarten, and E. Chiaveri, "Status report on CERN activities aiming at the production of sputter-coated copper superconducting rf cavities for LEP," in *4th Workshop on RF Superconductivity*, CERN Document Server Number: CERN-EF-89-013, National Laboratory for High Energy Physics, Tsukuba, Japan: Y. Kojima, 1989, pp. 377–396.

[89] D. Longuevergne, "Geometrical corrections for accurate fitting of the field dependent surface resistance for superconducting accelerating cavities," *Nuclear Instruments and Methods in Physics Research Section A: Accelerators, Spectrometers, Detectors and Associated Equipment*, vol. 910, pp. 41–48, 2018, ISSN: 0168-9002. DOI: 10.1016/j.nima.2018.08.005.

[90] J. Knobloch, "The "Q disease" in Superconducting Niobium RF Cavities," *AIP Conference Proceedings*, vol. 671, no. 1, pp. 133–150, 2003. DOI: 10.1063/1.1597364.

[91] C. Benvenuti, N. Circelli, and M. Hauer, "Niobium films for superconducting accelerating cavities," *Applied Physics Letters*, vol. 45, no. 5, pp. 583–584, 1984, ISSN: 0003-6951, 1077-3118. DOI: 10.1063/1.95289.

[92] G. Arnolds-Meyer and W. Weingarten, "Comparative measurements of niobium sheet and sputter coated cavities," *IEEE Transactions on Magnetics*, vol. 23, no. 2, pp. 1620–1623, Mar. 1987, Conference Name: IEEE Transactions on Magnetics, ISSN: 1941-0069. DOI: 10.1109/TMAG.1987.1064948.

[93] A. Ramiere, C. Z. Antoine, and J. Amrit, "Model for hot spots and Q -slope behavior in granular niobium thin film superconducting rf cavities," *Physical Review Accelerators and Beams*, vol. 25, no. 2, p. 022 001, Feb. 2022, ISSN: 2469-9888. DOI: 10.1103/PhysRevAccelBeams.25.022001.

[94] *Cryogenic Properties of Copper*, Information compiled for the International Copper Association, Ltd. by C.A. Thompson, W. M. Manganaro and F.R. Fickett of the National Institute of Standards and Technology (NIST), Boulder, Colorado, July 1990. [Online]. Available: https://copper.org/resources/properties/cryogenic/.

[95] P. Bernard, D. Bloess, P. Marchand, *et al.*, "Operation of the CERN 5-cell superconducting acceleration cavity in PETRA," Tech. Rep. CERN-EF-83-012, 1983, CERN Document Server.

[96] G. Arnolds-Meyer, C. Benvenuti, P. Bernard, *et al.*, "Radiofrequency Superconductivity at CERN: A status report," en, in *Proceedings of the Third Workshop on RF Superconductivity*, vol. 1, ANL-PHY-88-1, Argonne National Laboratory, IL, USA: K. W. Shepard, Jan. 1988, pp. 55–79. [Online]. Available: https://www.osti.gov/servlets/purl/5095772.

[97] O. Aberle, D. Boussard, S. Calatroni, *et al.*, "Technical developments on reduced-beta superconducting cavities at CERN," en, in *Proceedings of the 1999 Particle Accelerator Conference*, vol. 2, New York, NY, USA: IEEE, 1999, pp. 949–951, ISBN: 978-0-7803-5573-6. DOI: 10.1109/PAC.1999.795410.

[98] D. Tonini, C. Greggio, G. Keppel, *et al.*, "Morphology of Niobium Films Sputtered at Different Target-Substrate Angle," in *Proceedings of the 11th Workshop on RF Superconductivity*, Lübeck/Travemünder, Germany, 2003.

[99] J. Halbritter, "Granular superconductors and their intrinsic and extrinsic surface impedance," *Journal of Superconductivity*, vol. 8, no. 6, pp. 691–703, 1995, ISSN: 1572-9605. DOI: 10.1007/BF00727492.

[100] I. A. Kulik and V. Palmieri, "Theory of Q-degradation and nonlinear effects in Nb-coated superconducting cavities," *Part. Accel.*, vol. 60, pp. 257–264, 1998.

[101] J. Halbritter, "Transport in superconducting niobium films for radio frequency applications," *Journal of Applied Physics*, vol. 97, no. 8, p. 083 904, 2005, Publisher: American Institute of Physics, ISSN: 0021-8979. DOI: 10.1063/1.1874292.

[102] V. Palmieri and R. Vaglio, "Thermal contact resistance at the Nb/Cu interface as a limiting factor for sputtered thin film RF superconducting cavities," *Superconductor Science and Technology*, vol. 29, no. 1, 2015, Publisher: IOP Publishing, ISSN: 0953-2048. DOI: 10.1088/0953-2048/29/1/015004.

[103] C. Attanasio, L. Maritato, and R. Vaglio, "Residual surface resistance of polycrystalline superconductors," *Physical Review B*, vol. 43, no. 7, pp. 6128–6131, 1991, Publisher: American Physical Society. DOI: 10.1103/PhysRevB.43.6128.

[104] B. Bonin and H. Safa, "Power dissipation at high fields in granular RF superconductivity," *Superconductor Science and Technology*, vol. 4, no. 6, p. 257, 1991, ISSN: 0953-2048. DOI: 10.1088/0953-2048/4/6/008.

[105] C. Benvenuti, S. Calatroni, P. Darriulat, M. A. Peck, and A. M. Valente, "Fluxon pinning in niobium films," *Physica C: Superconductivity*, vol. 351, no. 4, pp. 429–437, 2001, ISSN: 0921-4534. DOI: 10.1016/S0921-4534(00)01646-4.

[106] A. Gurevich, "Maximum screening fields of superconducting multilayer structures," *AIP Advances*, vol. 5, no. 1, 2015, Publisher: American Institute of Physics. DOI: 10.1063/1.4905711.

[107] T. Proslier, "3.5 Atomic Layer Deposition," in *Ametis*, EDP Sciences, Dec. 2021, pp. 285–289, ISBN: 978-2-7598-2588-2. DOI: 10.1051/978-2-7598-2588-2.c017.

[108] B. Hillenbrand, H. Martens, H. Pfister, K. Schnitzke, and G. Ziegler, "Superconducting Nb3Sn-cavities," *IEEE Transactions on Magnetics*, vol. 11, no. 2, pp. 420–422, Mar. 1975, Conference Name: IEEE Transactions on Magnetics, ISSN: 1941-0069. DOI: 10.1109/TMAG.1975.1058735.

[109] S. Posen and M. Liepe, "Advances in development of Nb3Sn superconducting radio-frequency cavities," *Physical Review Special Topics - Accelerators and Beams*, vol. 17, no. 11, 2014, Publisher: American Physical Society. DOI: 10.1103/PhysRevSTAB.17.112001.

[110] S. Posen and D. L. Hall, "Nb3Sn superconducting radiofrequency cavities: Fabrication, results, properties, and prospects," *Superconductor Science and Technology*, vol. 30, no. 3, p. 033 004, Jan. 2017, Publisher: IOP Publishing, ISSN: 0953-2048. DOI: 10.1088/1361-6668/30/3/033004.

[111] R. Vaglio, "RF Superconducting Cavities for Accelerators," in *Microwave Superconductivity*, ser. NATO Science Series, H. Weinstock and M. Nisenoff, Eds., Dordrecht: Springer Netherlands, 2001, pp. 447–471, ISBN: 978-94-010-0450-3. DOI: 10.1007/978-94-010-0450-3_17.

[112] S. Bousson, H. Weise, G. Burt, *et al.*, "Chapter 3: High-gradient RF structures and systems," *CERN Yellow Reports: Monographs*, vol. 1, pp. 61–61, 2022, ISSN: 2519-8076. DOI: 10.23731/CYRM-2022-001.61.

[113] The FCC Collaboration, A. Abada, M. Abbrescia, *et al.*, "FCC Physics Opportunities: Future Circular Collider Conceptual Design Report Volume 1," *The European Physical Journal C*, vol. 79, no. 6, p. 474, 2019, ISSN: 1434-6044, 1434-6052. DOI: 10.1140/epjc/s10052-019-6904-3.

[114] M. Benedikt and F. Zimmermann, "Future Circular Collider: Integrated Programme and Feasibility Study," *Frontiers in Physics*, vol. 10, 2022, ISSN: 2296-424X. DOI: 10.3389/fphy.2022.888078.

[115] *2020 Update of the European Strategy for Particle Physics (Brochure)*, Number: CERN-ESU-015 Publisher: CERN, 2020. DOI: 10.17181/CERN.JSC6.W89E.

[116] The FCC Collaboration, A. Abada, M. Abbrescia, *et al.*, "FCC-hh: The Hadron Collider: Future Circular Collider Conceptual Design Report Volume 3," *The European Physical Journal Special Topics*, vol. 228, no. 4, pp. 755–1107, 2019, ISSN: 1951-6355, 1951-6401. DOI: 10.1140/epjst/e2019-900087-0.

[117] A. Faus-Golfe, G. H. Hoffstaetter, Q. Qin, and F. Zimmermann, *Accelerators for Electroweak Physics and Higgs Boson Studies*, arXiv.org, 2022. DOI: 10.48550/arXiv.2209.05827.

[118] I. Syratchev, F. Peauger, I. Karpov, and O. Brunner, "A Superconducting Slotted Waveguide Elliptical Cavity for FCC-ee," Zenodo, Tech. Rep., Jun. 2021. DOI: 10.5281/zenodo.5031953.

[119] G. Rosaz, *The Ell Cavities Program at CERN: Short Intro (Strategy and Goals)*, FCC Week 2022, Paris, France, May 2022.

[120] "European Strategy for Particle Physics - Accelerator R&D Roadmap," vol. 1, Mar. 2022, CERN Yellow Reports: Monographs. DOI: 10.23731/CYRM-2022-001.

[121] C. Pereira Carlos, *HIPIMS Nb coatings, from 1.3 GHz to 400 MHz*, FCC Week 2023, London, UK, Jun. 2023.

[122] S. G. Zadeh, "Accelerating cavity and higher order mode coupler design for the Future Circular Collider," Doctoral Thesis, Universität Rostock, 2020. DOI: 10.18453/rosdok_id00003023.

[123] M. Garlasche, *Elliptical Cavities Production Technology*, FCC Week 2022, Paris, France, May 2022.

[124] G. Bellini, L. Ferreira, and P. H. Hugon, *Electropolishing 1300 & 400 MHz SRF copper substrates*, FCC Week 2022, Paris, France, May 2022.

[125] L. Vega-Cid, *RF Tests of Nb/Cu 1.3 GHz Elliptical Cavities*, FCC Week 2022, Paris, France, May 2022.

[126] A. Bianchi, *Temperature Mapping System For Niobium Coated Copper Cavities*, FCC Week 2022, Paris, France, May 2022.

[127] C. Pereira Carlos, *Nb/Cu thin film HiPIMS coatings optimization for SRF applications*, FCC Week 2022, Paris, France, May 2022.

[128] D. Fonnesu, J. Bremer, T. Koettig, *et al.*, "CERN Based Tc Measurement Station for Thin-Film Coated Copper Samples and Results on Related Studies," in *Proceedings of the 20th International Conference on RF Superconductivity*, ISSN: 2673-5504, vol. SRF2021, FRIB, MSU, MI, USA: JACoW Publishing, 2021, p. 4, ISBN: 978-3-95450-233-2. DOI: 10.18429/JACOW-SRF2021-SUPFDV018.

[129] M. Benedikt, A. Blondel, P. Janot, M. Mangano, and F. Zimmermann, "Future Circular Colliders succeeding the LHC," *Nature Physics*, vol. 16, no. 4, pp. 402–407, 2020, Publisher: Nature Publishing Group, ISSN: 1745-2481. DOI: 10.1038/s41567-020-0856-2.

[130] T. Roser and M. Seidel, "Chapter 8: Sustainability considerations," in *European Strategy for Particle Physics - Accelerator R&D Roadmap*, vol. 1, CERN Yellow Reports:Monographs, CERN-2022-001, N. Mounet, 2022. DOI: 10.23731/CYRM-2022-001.245.

[131] C. Lingwood, I. Syratchev, M. Jensen, and R. Ruber, *EnEfficient RF Sources*, Workshop at Cockroft Institute, UK EuCARD2 - Enhanced European Coordination for Accelerator Research & Development, Jun. 2014. [Online]. Available: https://indico.cern.ch/event/297025/.

[132] C. Marchand, D. Dancila, J. Plouin, and R. Ruber, *ARIES Workshop on Energy Efficient RF*, Workshop at Ångström Laboratory, Uppsala, Sweden ARIES - Horizon2020 GA730871, Jun. 2019. [Online]. Available: https://indico.uu.se/event/515/.

[133] M. Seidel, *Proton Driver Efficiency Workshop*, Workshop at Paul Scherrer Institut (PSI), Switzerland EuCARD2, Feb. 2016. [Online]. Available: https://indico.psi.ch/event/3848/.

[134] *Workshop on Special Compact and Low Consumption Magnet Design*, Workshop at CERN, Geneva, Switzerland EuCARD2, Nov. 2014. [Online]. Available: https://indico.cern.ch/event/321880/.

[135] Y. Mori, A. Taniguchi, Y. Kuriyama, *et al.*, "Intense Negative Muon Facility with MERIT Ring for Nuclear Transmutation," in *Proceedings of the 14th International Conference on Muon Spin Rotation, Relaxation and Resonance*, ser. JPS Conference Proceedings, vol. 21, Journal of the Physical Society of Japan, 2017, p. 9. DOI: 10.7566/JPSCP.21.011063.

[136] A. Ballarino, "Development of superconducting links for the Large Hadron Collider machine," en, *Superconductor Science and Technology*, vol. 27, no. 4, 2014, Publisher: IOP Publishing, ISSN: 0953-2048. DOI: 10.1088/0953-2048/27/4/044024.

[137] M. Liepe, "Superconducting RF for the Future: Is Nb3Sn Ready for Next-generation Accelerators?" In *Proc. of International Particle Accelerator Conference IPAC19*, Melbourne, Australia, 2019, ISBN: 978-3-95450-208-0.

[138] M. Seidel, *5th Workshop Energy for Sustainable Science at Research Infrastructures*, Workshop at Paul Scherrer Institute (PSI), Switzerland, Nov. 2019. [Online]. Available: https://indico.psi.ch/event/6754/.

[139] M. Ohring, *Materials Science of Thin Films*, en. Elsevier, 2002, ISBN: 978-0-12-524975-1. DOI: 10.1016/B978-0-12-524975-1.X5000-9.

[140] P. N. Hishimone, H. Nagai, M. Sato, P. N. Hishimone, H. Nagai, and M. Sato, "Methods of Fabricating Thin Films for Energy Materials and Devices," in *Lithium-ion Batteries - Thin Film for Energy Materials and Devices*, IntechOpen, Jul. 2020, ISBN: 978-1-78985-464-0. DOI: 10.5772/intechopen.85912.

[141] D. Depla, S. Mahieu, R. Hull, R. M. Osgood, J. Parisi, and H. Warlimont, Eds., *Reactive Sputter Deposition* (Springer Series in Materials Science). Berlin, Heidelberg: Springer, 2008, vol. 109, ISBN: 978-3-540-76662-9. DOI: 10.1007/978-3-540-76664-3.

[142] A. Anders, "Discharge physics of high power impulse magnetron sputtering," *Surface and Coatings Technology*, PSE 2010 Special Issue, vol. 205, S1–S9, Jul. 2011, ISSN: 0257-8972. DOI: 10.1016/j.surfcoat.2011.03.081.

[143] V. Kouznetsov, K. Macák, J. M. Schneider, U. Helmersson, and I. Petrov, "A novel pulsed magnetron sputter technique utilizing very high target power densities," *Surface and Coatings Technology*, vol. 122, no. 2, pp. 290–293, Dec. 1999, ISSN: 0257-8972. DOI: 10.1016/S0257-8972(99)00292-3.

[144] J. Bohlmark, J. Alami, C. Christou, A. P. Ehiasarian, and U. Helmersson, "Ionization of sputtered metals in high power pulsed magnetron sputtering," *Journal of Vacuum Science & Technology A*, vol. 23, no. 1, pp. 18–22, Nov. 2004, ISSN: 0734-2101. DOI: 10.1116/1.1818135.

[145] D. Lundin and K. Sarakinos, "An introduction to thin film processing using high-power impulse magnetron sputtering," *Journal of Materials Research*, vol. 27, no. 5, pp. 780–792, Mar. 2012, Publisher: Cambridge University Press, ISSN: 2044-5326, 0884-2914. DOI: 10.1557/jmr.2012.8.

[146] A. Anders, "Deposition rates of high power impulse magnetron sputtering: Physics and economics," *Journal of Vacuum Science & Technology A*, vol. 28, no. 4, pp. 783–790, Jun. 2010, ISSN: 0734-2101. DOI: 10.1116/1.3299267.

[147] G. Terenziani, S. Calatroni, and A. Ehiasarian, "Niobium coatings for superconducting RF applications by HiPIMS," Jun. 2012. DOI: 10.13140/2.1.2837.9846.

[148] A. P. Ehiasarian, Y. A. Gonzalvo, and T. D. Whitmore, "Time-Resolved Ionisation Studies of the High Power Impulse Magnetron Discharge in Mixed Argon and Nitrogen Atmosphere," *Plasma Processes and Polymers*, vol. 4, no. S1, S309–S313, 2007, ISSN: 1612-8869. DOI: 10.1002/ppap.200730806.

[149] A. Anders, "A structure zone diagram including plasma-based deposition and ion etching," *Thin Solid Films*, vol. 518, no. 15, pp. 4087–4090, May 2010, ISSN: 0040-6090. DOI: 10.1016/j.tsf.2009.10.145.

[150] J. A. Thornton, "High Rate Thick Film Growth," *Annual Review of Materials Science*, vol. 7, no. 1, pp. 239–260, 1977. DOI: 10.1146/annurev.ms.07.080177.001323.

[151] J. A. Thornton and D. W. Hoffman, "Stress-related effects in thin films," *Thin Solid Films*, vol. 171, no. 1, pp. 5–31, Apr. 1989, ISSN: 0040-6090. DOI: 10.1016/0040-6090(89)90030-8.

[152] H. Windischmann, "Intrinsic stress in sputter-deposited thin films," *Critical Reviews in Solid State and Materials Sciences*, vol. 17, no. 6, pp. 547–596, Jan. 1992, Publisher: Taylor & Francis, ISSN: 1040-8436. DOI: 10.1080/10408439208244586.

[153] C. T. Wu, "Intrinsic stress of magnetron-sputtered niobium films," *Thin Solid Films*, International Conference on Metallurgical Coatings, San Diego, 1979-Part III, vol. 64, no. 1, pp. 103–110, Nov. 1979, ISSN: 0040-6090. DOI: 10.1016/0040-6090(79)90549-2.

[154] D. W. Hoffman, "Perspective on stresses in magnetron-sputtered thin films," *Journal of Vacuum Science & Technology A*, vol. 12, no. 4, pp. 953–961, Jul. 1994, ISSN: 0734-2101. DOI: 10.1116/1.579073.

[155] S. Murase, K. Itoh, H. Wada, *et al.*, "Critical temperature measurement method of composite superconductors," *Physica C: Superconductivity*, vol. 357-360, pp. 1197–1200, Aug. 2001, ISSN: 0921-4534. DOI: 10.1016/S0921-4534(01)00483-X.

[156] A. T. Fiory, A. F. Hebard, P. M. Mankiewich, and R. E. Howard, "Penetration depths of high Tc films measured by two-coil mutual inductances," *Applied Physics Letters*, vol. 52, no. 25, pp. 2165–2167, Jun. 1988, ISSN: 0003-6951, 1077-3118. DOI: 10.1063/1.99757.

[157] M. Boloré, B. Bonin, Y. Boudigou, *et al.*, "A New Inductive Method for Measuring the RRR-Value of Niobium," in *Proceedings of 7th International Workshop on RF Superconductivity*, Gif-sur-Yvette, France, 1995.

[158] J. H. Claassen, M. E. Reeves, and R. J. Soulen, "A contactless method for measurement of the critical current density and critical temperature of superconducting films," *Review of Scientific Instruments*, vol. 62, no. 4, pp. 996–1004, Apr. 1991, ISSN: 0034-6748, 1089-7623. DOI: 10.1063/1.1141991.

[159] J. H. Claassen, M. L. Wilson, J. M. Byers, and S. Adrian, "Optimizing the two-coil mutual inductance measurement of the superconducting penetration depth in thin films," *Journal of Applied Physics*, vol. 82, no. 6, pp. 3028–3034, Sep. 1997, Publisher: American Institute of Physics, ISSN: 0021-8979. DOI: 10.1063/1.366287.

[160] S. J. Turneaure, A. A. Pesetski, and T. R. Lemberger, "Numerical modeling and experimental considerations for a two-coil apparatus to measure the complex conductivity of superconducting films," *Journal of Applied Physics*, vol. 83, no. 8, pp. 4334–4343, Apr. 1998, ISSN: 0021-8979, 1089-7550. DOI: 10.1063/1.367193.

[161] X. He, A. Gozar, R. Sundling, and I. Božović, "High-precision measurement of magnetic penetration depth in superconducting films," *Review of Scientific Instruments*, vol. 87, no. 11, p. 113 903, Nov. 2016, Publisher: American Institute of Physics, ISSN: 0034-6748. DOI: 10.1063/1.4967004.

[162] S. Kumar, C. Kumar, J. Jesudasan, V. Bagwe, P. Raychaudhuri, and S. Bose, "A two-coil mutual inductance technique to study matching effect in disordered NbN thin films," *Applied Physics Letters*, vol. 103, no. 26, p. 262 601, Dec. 2013, Publisher: American Institute of Physics, ISSN: 0003-6951. DOI: 10.1063/1.4858402.

[163] J. Draskovic, T. R. Lemberger, B. Peters, *et al.*, *Measuring the superconducting coherence length in thin films using a two-coil experiment*, arXiv:1403.6856 [cond-mat], Mar. 2014. DOI: 10.48550/arXiv.1403.6856.

[164] N. J. Simon, E. S. Drexler, and R. P. Reed, "Properties of copper and copper alloys at cryogenic temperatures," National Institute of Standards and Technology, Gaithersburg, MD, Tech. Rep. NIST MONO 177, 1992. DOI: 10.6028/NIST.MONO.177.

[165] V. Garcia Diaz, O. Azzolini, E. Chyhyrynets, *et al.*, "Thick Film Morphology and SC Characterizations of 6 GHz Nb/Cu Cavities," *Proceedings of the 20th International Conference on RF Superconductivity*, vol. SRF2021, 5 pages, 2.496 MB, 2022, Artwork Size: 5 pages, 2.496 MB ISBN: 9783954502332 Medium: PDF Publisher: JACoW Publishing, Geneva, Switzerland, ISSN: 2673-5504. DOI: 10.18429/JACOW-SRF2021-SUPCAV007.

[166] G. Chanin and J. P. Torre, "Critical-Field Curve of Superconducting Lead," *Physical Review B*, vol. 5, no. 11, pp. 4357–4364, Jun. 1972, Publisher: American Physical Society. DOI: 10.1103/PhysRevB.5.4357.

[167] B. T. Matthias, T. H. Geballe, and V. B. Compton, "Superconductivity," *Reviews of Modern Physics*, vol. 35, no. 1, pp. 1–22, Jan. 1963, ISSN: 0034-6861. DOI: 10.1103/RevModPhys.35.1.

[168] J. Eisenstein, "Superconducting Elements," *Reviews of Modern Physics*, vol. 26, no. 3, pp. 277–291, Jul. 1954, ISSN: 0034-6861. DOI: 10.1103/RevModPhys.26.277.

[169] C. Chou, D. White, and H. L. Johnston, "Heat Capacity in the Normal and Superconducting States and Critical Field of Niobium," *Physical Review*, vol. 109, no. 3, pp. 788–796, Feb. 1958, Publisher: American Physical Society. DOI: 10.1103/PhysRev.109.788.

[170] V. Palmieri, "The Way of Thick Films toward a Flat Q-curve in Sputtered Cavities," in *Proceedings of the 18th International Conference on RF Superconductivity*, Lanzhou, China: JACOW, Geneva, Switzerland, Jan. 2018, pp. 378–381, ISBN: 978-3-95450-191-5. DOI: 10.18429/JACoW-SRF2017-TUYBA03.

[171] G. D. Marzi, L. Morici, L. Muzzi, A. d. Corte, and M. B. Nardelli, "Strain sensitivity and superconducting properties of Nb3Sn from first principles calculations," *Journal of Physics: Condensed Matter*, vol. 25, no. 13, p. 135 702, Mar. 2013, Publisher: IOP Publishing, ISSN: 0953-8984. DOI: 10.1088/0953-8984/25/13/135702.

[172] L. Lain Amador, "Production of ultra-high-vacuum chambers with integrated getter thin-film coatings by electroforming," Doctoral Thesis, U. Bourgogne Franche-Comte, 2019. DOI: 10.17181/CERN.A2EJ.YIS2.

[173] W. Singer, "Fabrication of elliptical SRF cavities," *Superconductor Science and Technology*, vol. 30, no. 3, 2017, Publisher: IOP Publishing, ISSN: 0953-2048, 1361-6668. DOI: 10.1088/1361-6668/30/3/033001.

[174] J.-F. Croteau, G. Robin, E. Cantergiani, *et al.*, "Characterization of the Formability of High-Purity Polycrystalline Niobium Sheets for Superconducting Radiofrequency Applications," *Journal of Engineering Materials and Technology*, vol. 144, no. 2, Oct. 2021, ISSN: 0094-4289. DOI: 10.1115/1.4052557.

[175] G. Rosaz, *Cu electrodeposition for the manufacturing of seamless SRF cavities*, 19th International Conference on RF Superconductivity, Dresden, Germany, 2019.

[176] F. Avino, F. Manke, T. Richard, and A. Sublet, "Afterglow dynamics of plasma potential in bipolar HiPIMS discharges," *Plasma Sources Science and Technology*, vol. 30, no. 11, 2021, Publisher: IOP Publishing, ISSN: 0963-0252. DOI: 10.1088/1361-6595/ac2aed.

[177] T. Matsushita, *Flux Pinning in Superconductors*. Berlin, Heidelberg: Springer, 2007, ISBN: 978-3-642-07945-0. DOI: 10.1007/978-3-540-44515-9.

[178] C. Z. Antoine, "Influence of crystalline structure on rf dissipation in superconducting niobium," *Physical Review Accelerators and Beams*, vol. 22, no. 3, p. 034 801, Mar. 2019, ISSN: 2469-9888. DOI: 10.1103/PhysRevAccelBeams.22.034801.

[179] S. Casalbuoni, E. A. Knabbe, J. Kötzler, *et al.*, "Surface superconductivity in niobium for superconducting RF cavities," *Nuclear Instruments and Methods in Physics Research Section A: Accelerators, Spectrometers, Detectors and Associated Equipment*, vol. 538, no. 1, pp. 45–64, Feb. 2005, ISSN: 0168-9002. DOI: 10.1016/j.nima.2004.09.003.

[180] Y. Iwasa, "Magnetization," in *Case Studies in Superconducting Magnets: Design and Operational Issues*, Boston, MA: Springer US, 2009, pp. 1–38, ISBN: 978-0-387-09800-5. DOI: 10.1007/b112047_5.

[181] S. Bose, P. Raychaudhuri, R. Banerjee, P. Vasa, and P. Ayyub, "Mechanism of the Size Dependence of the Superconducting Transition of Nanostructured Nb," *Physical Review Letters*, vol. 95, no. 14, 2005, ISSN: 0031-9007. DOI: 10.1103/PhysRevLett.95.147003.

[182] A. Inaba, "Superconductive Transition Point of Tantalum and Niobium as a Reference Temperature," *Japanese Journal of Applied Physics*, vol. 19, no. 8, pp. 1553–1559, Aug. 1980, ISSN: 0021-4922, 1347-4065. DOI: 10.1143/JJAP.19.1553.

[183] J. Ekin, *Experimental Techniques for Low-Temperature Measurements: Cryostat Design, Material Properties and Superconductor Critical-Current Testing*, 1st ed. Oxford University PressOxford, Oct. 2006, ISBN: 978-0-19-857054-7. DOI: 10.1093/acprof:oso/9780198570547.001.0001.

[184] A. S. Dhavale, P. Dhakal, A. A. Polyanskii, and G. Ciovati, "Flux pinning characteristics in cylindrical niobium samples used for superconducting radio frequency cavity fabrication," *Superconductor Science and Technology*, vol. 25, no. 6, p. 065 014, Jun. 2012, ISSN: 0953-2048, 1361-6668. DOI: 10.1088/0953-2048/25/6/065014.

[185] A. Robin, "Corrosion Behaviour of Niobium in Sodium Hydroxide Solutions," *Journal of Applied Electrochemistry*, vol. 34, no. 6, pp. 623–629, Jun. 2004, ISSN: 0021-891X. DOI: 10.1023/B:JACH.0000021924.82854.71.

[186] M. N. Sayeed, U. Pudasaini, C. E. Reece, G. V. Eremeev, and H. E. Elsayed-Ali, "Properties of Nb3Sn films fabricated by magnetron sputtering from a single target," en, *Applied Surface Science*, vol. 541, p. 148 528, Mar. 2021, ISSN: 01694332. DOI: 10.1016/j.apsusc.2020.148528.

[187] K. Ilyina-Brunner, *A15 sputtered thin films for SRF applications*, FCC Week 2018, Amsterdam, Netherlands, 2018.

[188] A. Godeke, "A review of the properties of Nb $_3$ Sn and their variation with A15 composition, morphology and strain state," *Superconductor Science and Technology*, vol. 19, no. 8, R68–R80, Aug. 2006, ISSN: 0953-2048, 1361-6668. DOI: 10.1088/0953-2048/19/8/R02.

[189] J. P. Charlesworth, I. Macphail, and P. E. Madsen, "Experimental work on the niobium-tin constitution diagram and related studies," *Journal of Materials Science*, vol. 5, no. 7, pp. 580–603, Jul. 1970, ISSN: 1573-4803. DOI: 10.1007/BF00554367.

[190] J. P. Charlesworth, "The superconducting transition temperatures of Nb6Sn5 and NbSn2," *Physics Letters*, vol. 21, no. 5, pp. 501–502, Jun. 1966, ISSN: 0031-9163. DOI: 10.1016/0031-9163(66)91272-8.

[191] H. Devantay, J. L. Jorda, M. Decroux, J. Muller, and R. Flükiger, "The physical and structural properties of superconducting A15-type Nb-Sn alloys," *Journal of Materials Science*, vol. 16, no. 8, pp. 2145–2153, Aug. 1981, ISSN: 1573-4803. DOI: 10.1007/BF00542375.

[192] R. Fluekiger, "Atomic ordering, phase stability and superconductivity in bulk and filamentary A15 type compounds," Institut für Technische Physik (ITEP), Karlsruhe, Germany, University publication KFK-4204, 1987, KITopen-ID: 200024395. DOI: 10.5445/IR/200024395.

[193] D. F. Moore, R. B. Zubeck, J. M. Rowell, and M. R. Beasley, "Energy gaps of the A15 superconductors Nb3Sn, V3Si, and Nb3Ge measured by tunneling," *Physical Review B*, vol. 20, no. 7, pp. 2721–2738, Oct. 1979, Publisher: American Physical Society. DOI: 10.1103/PhysRevB.20.2721.

[194] S. Amorosi, M. Anderle, C. Benvenuti, *et al.*, "Study of the discharge gas trapping during thin-film growth," *Vacuum*, The Sixth European Vacuum Conference, vol. 60, no. 1, pp. 89–94, Jan. 2001, ISSN: 0042-207X. DOI: 10.1016/S0042-207X(00)00359-6.

Acknowledgements

I wish to begin by expressing my gratitude to my advisor, Jens Knobloch, for kindly accepting to provide his academic support and scientific expertise for my work at CERN. I am thankful for the care with which he reviewed this thesis and for his guidance throughout the years, both in times of ease and difficulty.

A deep and sincere thank you goes to Sergio Calatroni, my CERN supervisor. This thesis found its shape and meaning under his guidance, and would have not been possible without his constantly available expertise. The warm welcome I received upon joining his group marked a turning point in my PhD journey, offering me the support I needed to bring this work to completion. Words cannot adequately express my gratitude for this.

I am grateful to Oliver Kugeler for his assistance in this work's progress, his consistently insightful ideas, constructive critiques, and engaging discussions.

My gratitude also goes to Guillaume Rosaz, for proposing the projects that resulted in the content of this thesis work, for his expertise, advice and for closely following the development of this work.

I would like to extend my sincere gratitude to Claire Z. Antoine for kindly accepting the role of second reviewer for this thesis. I would also like to express a warm thank you to Xin Jiang, Alexander Lenz and Roberto Passante for kindly agreeing to be part of the PhD Committee.

My sincere gratitude also goes to all the individuals whose support and contributions have played a role in the completion of this thesis: the CERN Central Cryogenic Laboratory team, especially Johan Bremer, for affording me the opportunity to spend my EASITrain[1] scholarship within his laboratory, Torsten Koettig, Agostino Vacca, Laetitia Dufay-Chanat, and Sebastien Prunet for their assistance during the establishment and operation of the T_c measurement station, and Erwan Reches, my first successor in operating the measurement station and my *Verlan* teacher (it has been a pleasure, *Waner*!); Antti Olavi Pekka Vaaranta, for his assistance with the calibration measurements, the design of the data acquisition system and the simulations during the commissioning of the T_c test station; Lucia Lain Amador, for the production of the samples and sharing her knowledge in the reverse-coating study; Stewart Leith, for the production of the Nb_3Sn HiPIMS samples, the constant availability and the always stimulating discussions; Fabio Avino, the first real user of the T_c test station, for his support and encouragement during its development; Vanessa Garcia Diaz from INFN-LNL, for the production of the niobium thick films used as reference samples; Marco Bonura and Carmine Senatore from the University of Geneva, for providing the sample magnetization measurements and expertise; Stephen Pfeiffer and Adrienn Baris, for providing sample SEM imaging and EDS analysis, and Ana Teresa Perez Fontenla, for her advice in the field; Walter Venturini-Delsolaro, for his expertise, support and guidance; Alick Macpherson, for providing source material for the bulk niobium reference samples and insightful conversations; Carlo Petrone, for making available his instrumentation and for sharing his knowledge about sensing coils; Simon Barriere, for the preparation of the bulk niobium reference samples; Serge Forel, for the chemical treatments of the substrates and bulk samples; Marco Morrone, for his advice about COMSOL simulations; the personnel of the CERN Human Resources, especially Anne-Laure Tantot, Oxana Goponova, Celine Delieutraz, Stefano Fattori, for their professionalism, kindness, and support, which have been indispensable in keeping my project on track; last but not least, Paolo Chiggiato, for giving me the opportunity to join his group of PhD students. I am truly thankful to each and everyone of them.

[1]European Advanced Superconductivity Innovation and Training. This Marie Sklodowska-Curie Action (MSCA) Innovative Training Networks (ITN) has received funding from the European Union's H2020 Framework Programme under Grant Agreement no. 764879.

Kirtana Puthran, for our shared passion for science, for her tireless support, love, understanding, for the fun and tears, for the small dances across the lab when nobody's watching (well, now they know...), for our sisterhood; Antonio Bianchi, for the physics discussions at the whiteboard, the coffee breaks, the shared fun and frustration, for that time a *crogiolo* was made, for his friendship; Maria Asuncion Barba Higueras, for her genuineness and curiosity, for her contagious motivation and optimism, because everything was more fun with her around, for her support and friendship; Andrea Vitrano and Linn Kretzschmar, met as project fellows and then turned into friends, neighbours and family, for their lovely presence, support, friendship, for all the food, card/board games and incredible fun; my dearest friends Marianna Fontana and Roberto Mulargia, for sharing time, space, joys and sorrows, hopes and discouragement, food and fun and love, and a bond that goes way beyond our shared love for physics and nerdish things; Antti Vaaranta, for his patience as I tutored him during his technical studentship (*"I appreciate that, Ma'am!"*), because working with him has probably taught me more than I was able to teach him, for the nice physics talks, the countless nerd jokes, for the CTRL+FO command, because buying him with cookies was so easy, for the Italian-Finnish twinning, for pairing up with Lise Murberg against the summer-loving part of the world, it was real fun to have *'em northlings* around; Flory Ten Broeke, for her presence and support; Lennard Busch, for his friendship and all the surprising life developments that followed our paths crossing at CERN; Remy Kriboo, lovely office mate, endless source of smiles and happiness; Tim Mulder, for all the coffee breaks and nice talks, for the shared love for plants, for the actually good Italian-certified homemade pizza; Patrick Krkotic, Kristof Brunner and all the colleagues who made me feel home since day zero when I joined their group; Cecilia, Miezi-Miezi, Mia and Ami. Because of all of the above my heart is filled with beautiful memories of my time at CERN, and I wish to thank them all from the bottom of my heart.

My gratitude also goes to the group of people I had the privilege of meeting within the EASITrain program, including my fellow researchers, supervisors and project managers. That experience provided me with invaluable professional and life training.

To all those who made my journey more pleasant by sprinkling it with small moments of joy each day, often without even realizing it. In particular to Mamadou and Natasha from Restaurant 1, as well as Fatima from the cafeteria at Building 30: warmly thank you!

Thank you also to the two persons who mostly helped me in navigating the stormy seas of German bureaucracy with infinite patience: Frau Zizka and Frau Schabardin.

A big thanks to my current team leader Cristian Pira, for having allowed me to finish writing my thesis, even if at times it meant subtracting time to my postdoc activities. To my current lab mates Davide Ford, Giovanni(-no) Marconato(/nello), Alessandro Salmaso, Roberta Caforio, Alisa Kotliarenko, Eduard Chyhyrynets and Mourad El Idrissi, for creating all together a friendly and supportive environment which gave me the boost I needed in the last months when things got tough. You guys are just the best group of people one can ever hope to work with. Thank you so much with all my heart.

A big thank you to my dearest friends Anna Garau, Elena Piras, Matteo Casula, Federica Mantegazzini, Felix Ahrens, Steffen Allgeier, Lina Norton, Melanie Schmidt, Valentin Sauter and Diego Macis for their presence and support over these years. I hope they know it meant a lot to me, even when I forgot to tell them.

A warm thank you to Maria Anna Fonnesu, for her presence, love and support, and for enduring the challenging task of being my sister.

A mia madre Barbara Piras e mio padre Gian Paolo Fonnesu, per l'affetto e i tanti sacrifici, un grazie di cuore anche a voi.